



**Mariya Hristova
Kostova**

**Síntese e caracterização de novos silicatos
lamelares e microporosos fotoluminescentes**

**Synthesis and characterization of new layered and
microporous photoluminescent silicates**

UA-SD



279407



**Mariya Hristova
Kostova**

**Síntese e caracterização de novos silicatos
lamelares e microporosos fotoluminescentes**

**Synthesis and characterization of new layered and
microporous photoluminescent silicates**

Dissertação apresentada à Universidade de Aveiro para cumprimento dos requisitos necessários à obtenção do grau de Doutor em Química, realizada sob a orientação científica do Doutor João Carlos Matias Celestino Gomes da Rocha, Professor Catedrático do Departamento de Química da Universidade de Aveiro e do Doutor Luís António Ferreira Martins Dias Carlos, Professor Catedrático do Departamento de Física da Universidade de Aveiro.

Apoio financeiro da FCT e do FSE no âmbito do III Quadro Comunitário de Apoio.

o júri

presidente

Reitora da Universidade de Aveiro

Prof. Dr. José Manuel Gaspar Martinho
professor Catedrático do Instituto Superior Técnico da Universidade Técnica de Lisboa

Prof. Dr. João Paulo Gil Lourenço
professor auxiliar da Faculdade de Ciências e Tecnologia no Departamento de Química e Bioquímica da Faculdade da Universidade do Algarve

Prof. Dr. João Carlos Matias Celestino Gomes da Rocha
professor catedrático do Departamento de Química da Universidade de Aveiro

Prof. Dr. Luís António Ferreira Martins Dias Carlos
professor catedrático do Departamento de Física da Universidade de Aveiro

Prof. Dr. Maria Rute de Amorim e Sá Ferreira André
professor auxiliar convidado do Departamento de Física da Universidade de Aveiro

Dr. Filipe Alexandre Almeida Paz
investigador auxiliar do CICECO da Universidade de Aveiro

palavras-chave

Silicatos, lantanídeos, terras raras, lamelar, microporoso, fotoluminescência, síntese hidrotérmica, estrutura

resumo

Esta tese tem como principal objectivo a síntese, a caracterização estrutural e o estudo das propriedades de fotoluminescência de novos silicatos, lamelares e microporosos de terras raras.

As técnicas de caracterização utilizadas foram a difracção de raios-X de pós e de mono-cristal, a microscopia electrónica de varrimento, as análises térmica e elementar, e as espectroscopias de fotoluminescência, ressonância magnética nuclear, Raman e infravermelho. Os silicatos de terras raras cristalinos foram obtidos por síntese hidrotérmica em condições de temperatura e pressão moderadas.

Os silicatos lamelares AV-22, $K_3[(RE)Si_3O_8(OH)_2]$, $RE^{3+}=Y^{3+}$, Eu^{3+} , Er^{3+} , Tb^{3+} , Gd^{3+} e Ce^{3+} são sistemas hóspede-hospedeiro convenientes para criar materiais multifuncionais com um amplo leque de propriedades. A estrutura dos materiais AV-22 foi determinada por difracção de raios-X de mono-cristal. Os materiais Tb- e Eu-AV-22 são emissores de luz visível (verde e vermelho, respectivamente), com eficiências comparáveis à dos padrões usados em lâmpadas comerciais, enquanto que Er-AV-22 é um emissor de infravermelho, à temperatura ambiente. A incorporação de Ce^{3+} e Tb^{3+} no mesmo silicato lamelar cria um efectivo canal de transferência da energia do primeiro para o segundo.

Após calcinação a 650 °C, os materiais AV-22 sofrem uma transformação de fase, convertendo-se em uma estrutura de poros estreitos, conhecida como AV-23, $K_3[RESi_3O_9]$, $RE^{3+}=Y^{3+}$, Eu^{3+} , Er^{3+} e Tb^{3+} . O valor da radiância da amostra Tb-AV-23 é semelhante à do padrão ($Gd_2O_2S:Tb$) verde de Tb^{3+} . O processo de calcinação aumenta a intensidade da emissão de Er^{3+} (essencialmente devido à remoção de grupos OH) e a importância das interacções $Er^{3+}-Er^{3+}$ como um mecanismo de extinção da fotoluminescência.

Os silicatos microporosos AV-24, $K_7Ln_3Si_{12}O_{32}\cdot 3H_2O$, $Ln^{3+}=Eu^{3+}$, Sm^{3+} , Tb^{3+} e Gd^{3+} constituem o primeiro sistema que possui dímeros Ln-O-Ln isolados em uma matriz silicosa, exibindo uma emissão característica: o tempo de vida do estado excitado 5D_0 é notavelmente longo, ca. 10 ms a 10 K.

A estrutura de todos estes silicatos admite a inclusão de um segundo (ou até mesmo um terceiro) tipo de ião Ln^{3+} na rede cristalina, permitindo um ajuste (muitas vezes fino) das propriedades de fotoluminescência.

keywords

Silicates, lanthanides, rare-earths, layered, microporous, photoluminescence, hydrothermal synthesis, structure

abstract

This thesis reports the synthesis, structural characterization and photoluminescence properties of new layered and microporous rare-earth silicates.

These materials have been characterized by powder and single crystal X-ray diffraction, scanning electron microscopy, thermal analysis, elemental analysis, nuclear magnetic resonance, infrared, Raman and photoluminescence spectroscopies. The crystalline rare-earth silicates were obtained by hydrothermal synthesis at moderate temperatures and pressures.

Layered rare-earth silicates AV-22, $K_3[(RE)Si_3O_8(OH)_2]$, $RE^{3+}=Y^{3+}$, Eu^{3+} , Er^{3+} , Tb^{3+} , Gd^{3+} and Ce^{3+} are host-guest systems suitable for engineering multifunctional materials with tuneable properties. The structure of AV-22 was solved by single crystal X-ray diffraction. The Tb- and Eu-AV-22 samples are visible emitters (green and red, respectively) with output efficiency comparable to that of standards used in commercial lamps, while Er-AV-22 is a room-temperature infrared phosphor. The incorporation of Ce^{3+} and Tb^{3+} in the same layered silicate induces an effective Ce^{3+} to Tb^{3+} energy transfer channel.

Upon calcination at 650 °C, AV-22 materials undergo a phase transformation to small-pore framework AV-23, $K_3[RESi_3O_9]$, $RE^{3+}=Y^{3+}$, Eu^{3+} , Er^{3+} and Tb^{3+} . The radiance values of Tb-AV-23 and standard Tb^{3+} green phosphors ($Gd_2O_2S:Tb$) are similar. The calcination process increases the intensity of the Er^{3+} emission (essentially due to the removing of OH groups) and the importance of the Er^{3+} - Er^{3+} interactions as a quenching emission channel.

Microporous lanthanide silicates AV-24, $K_7Ln_3Si_{12}O_{32}\cdot 3H_2O$, $Ln^{3+}=Eu^{3+}$, Sm^{3+} , Tb^{3+} and Gd^{3+} are the first reported to contain Ln-O-Ln dimmers isolated in a siliceous matrix and exhibiting a unique emission feature: the lifetime of the 5D_0 excited state is remarkably long, ca. 10 ms at 10 K.

The structure of all these silicates allows the inclusion of a second (or even third) type of Ln^{3+} ion in the framework and, therefore, the fine-tuning of their photoluminescence properties.

Index

Chapter 1 - Introduction

1.1	Introduction	2
1.2	Microporous framework materials	2
1.2.1	Zeolites and molecular sieves	2
1.2.2	Microporous metalosilicates	4
1.2.3	Microporous materials encompassing rare-earth elements	7
1.3	Layered materials	14
1.3.1	Clays	14
1.3.2	Layered titanosilicates	16
1.3.3	Layered rare-earth silicates	19
1.4	References	20

Chapter 2 - Lanthanide ions

2.1	Introduction	26
2.2	Electronic configurations	28
2.3	The Hamiltonian for the free ion	31
2.4	The ions in a chemical environment	32
2.5	$4f^n \rightarrow 4f^n$ transitions	36
2.6	$4f^n \rightarrow 4f^{n-1}5d$ (<i>fd</i>) transitions	38
2.7	Lifetimes	40
2.8	Energy transfer	42
2.9	Applications	47
2.10	References	52

Chapter 3 - Experimental techniques

3.1	Introduction	56
-----	--------------	----

3.2	Luminescence	56
3.2.1	Excitation sources	57
3.2.2	Light dispersing elements	60
3.2.3	Detectors	64
3.2.4	Experimental conditions	68
3.3	Other techniques	72
3.3.1	Single-crystal X-ray diffraction	72
3.3.2	Powder X-ray diffraction	72
3.3.3	Solid-state nuclear magnetic resonance	72
3.3.4	Raman spectroscopy	73
3.3.5	Scanning electro microscopy / Energy dispersive spectrometry	73
3.3.6	Elemental analysis	73
3.3.7	Thermal analyses	74
3.4	References	75

4 Chapter 4 - Layered lanthanide silicates ($K_3[M_{1-a}Ln_aSi_3O_8(OH)_2]$, $M^{3+}=Y^{3+}, Tb^{3+}$; $Ln^{3+}=Eu^{3+}, Er^{3+}, Tb^{3+}, Gd^{3+}$ and Ce^{3+}), $1 \geq a > 0$

4.1	Introduction	78
4.2	Synthesis	78
4.3	Structural characterization	80
4.4	Photoluminescence spectroscopy	92
4.5	Conclusions	113
4.6	References	115

5 Chapter 5 - Small-pore rare-earth silicates ($K_3LnSi_3O_9$, $RE^{3+}=Tb^{3+}, Eu^{3+}, Y^{3+}$ and Er^{3+})

5.1	Introduction	118
5.2	Synthesis	118
5.3	Structural characterization	119

5.4	Transformation of AV-22 to AV-23	123
5.5	Photoluminescence spectroscopy	129
5.6	Conclusions	138
5.7	References	139

Chapter 6 - Microporous lanthanide silicates ($K_7M_{3-a}Ln_aSi_{12}O_{32}\cdot 3H_2O$, $M^{3+} = Tb^{3+}, Gd^{3+}$; $Ln^{3+} = Eu^{3+}, Sm^{3+}, Tb^{3+}$ and Gd^{3+}), $3 \geq a > 0$

6.1	Introduction	142
6.2	Synthesis	142
6.3	Structural characterization	144
6.4	Photoluminescence spectroscopy	154
6.5	Conclusions	167
6.6	References	169

Chapter 7 - Final conclusions and further work 171

Appendices 175

Appendix I	– Crystal data and structure refinement information for Tb-AV-22	177
Appendix II	– Crystal data and structure refinement information for Tb-AV-23	181
Appendix III	– Crystal data and structure refinement information for Sm-AV-24	185

List of figures

Chapter 1

1.1 – Projection of zeolite A down b axis.	4
1.2 – Projection of the ETS-10, polymorph B.	6
1.3 – Crystal structure of montregianite-type materials.	9
1.4 – Crystal structure of sazhinite-type materials.	11
1.5 – Crystal structure of Eu-AV-20.	12
1.6 – Layered structures of selected clays and their interrelationships via isomorphous or non-isomorphous substitution. a) Kaolinite; b) Pyrophyllite; c) Montmorillonite; d) Muscovite (mica); e) Vermiculite.	15
1.7 – Polyhedral representation of the layered structure of JDF-L1 and AM-1.	16
1.8 – Polyhedral representation of the layered structure of AM-4.	17
1.9 – Polyhedral representation of the layered structure of jonesite.	18
1.10 – Polyhedral representation of the layered structure of AMH-3.	19

Chapter 2

2.1 – Chronology and dendrology of the isolation of rare-earth elements.	27
2.2 – Radial charge distribution $P^2(R)$ as a function of R for the $4f$, $5s$, $5p$, and $6s$ orbitals of Gd^+ .	30
2.3 – Partial energy diagram for Eu^{3+} ion, presenting the approximate values of the energies associated to different Hamiltonians, which influences the $4f^6$ configuration.	35
2.4 – Energy levels of the $4f^n$ configurations of the trivalent lanthanide ions in crystals of LnF_3 , representing the fundamental level of each ion.	36
2.5 – Schematic representation of the electronic configuration for the ground state, the lowest-energetic high-spin $4f^7 5d$ state and the higher-energetic low-spin $4f^7 5d$ state for Tb^{3+} .	40
2.6 – Principles of time-resolved spectroscopy.	42
2.7 – Energy transfer from a donor to an acceptor.	43
2.8 – Energy level schemes and the interaction H_{DA} between a donor and an acceptor.	43
2.9 – Ranges of interaction in Förster's and Dexter's models.	46
2.10 – Schematic diagram of a fluorescent lamp illustrating the light generation process.	48
2.11 – Emission spectrum of a tricolor fluorescent lamp (CHINT®) excited at 254 nm.	48

2.13 – Principles of heterogeneous and homogeneous immunoassays.	51
--	----

Chapter 3

3.1 – Spectral distribution of tungsten filament lamp at different temperatures.	58
3.2 – Spectral distribution of high-pressure xenon, mercury and deuterium lamps.	59
3.3 – Czerny-Turner configuration of a grating monochromator ($\lambda_1 > \lambda_2$).	61
3.4 – Mechanisms of diffraction from an echellette-type grating.	62
3.5 – Schematic representation of photomultiplier tube.	64
3.6 – Schematic representation of a silicon photodiode.	65
3.7 – Schematic representation of the operation of a CCD.	67
3.8 – Schematic representation of the configuration used for steady-state measurements.	69
3.9 – Schematic representation of the configuration used for time-resolved and lifetime measurements.	70

Chapter 4

4.1 – Schematic representation of the synthesis of AV-22 materials.	79
4.2 – Perspective view of a portion of the $[\text{TbSi}_3\text{O}_8(\text{OH})_2]^{3-}$ anionic layer of Tb-AV-22.	82
4.3 – Polyhedral representation of the unit cell contents of Tb-AV-22 viewed along the <i>c</i> axis.	83
4.4 – Experimental and simulated powder XRD patterns of Er-AV-22.	85
4.5 – Experimental and simulated powder XRD patterns of Eu-AV-22.	85
4.6 – Experimental powder XRD patterns of pure AV-22 samples.	86
4.7 – Experimental powder XRD patterns of mixed Y/Er-AV-22 samples.	86
4.8 – Scanning electron micrographs of pure and mixed AV-22 compositions.	87
4.9 – TG and DTA curves for Er-AV-22.	88
4.10 – Experimental and simulated ^{29}Si MAS NMR spectra of Y-AV-22.	89
4.11 – Si local environments in the structure of Y-AV-22.	89
4.12 – ^{29}Si MAS and high-power ^1H decoupling (HPDEC) MAS NMR spectra of Y-AV-22 recorded with a 5 kHz spinning rate and 60 s recycle delay.	90
4.13 – ^{29}Si MAS NMR spectra of $\text{K}_3[\text{Y}_a\text{Er}_{1-a}\text{Si}_3\text{O}_8(\text{OH})_2]$ recorded with a 15 kHz spinning rate and 60 s recycle delay.	91
4.14 – Raman spectrum of Tb-AV-22.	92

4.15 – Excitation spectra of $K_3[Y_{a-1}Tb_aSi_3O_8(OH)_2]$ ($a=1, 0.1$) monitored at the $Tb^{3+} {}^5D_4 \rightarrow {}^7F_5$ transition (540.5 nm) at room temperature. The inset shows the excitation spectrum of a pure Tb^{3+} sample monitored at the $Tb^{3+} {}^5D_4 \rightarrow {}^7F_5$ transition (540.5 nm) at 10 K, showing the region in which the transition to the high-spin and low-spin fd states are observed.	93
4.16 – Room temperature emission spectra of Tb-AV-22 and a commercial save-energy 18W CHINT® lamp excited at 254 nm.	94
4.17 – Lifetime of the 5D_4 level of Tb^{3+} detected at the strongest 7F_5 manifold and excited at 377 nm, as a function of Tb^{3+} content, a in $K_3[Y_aEr_{1-a}Si_3O_8(OH)_2]$, $a=0.05-1$.	95
4.18 – Room temperature 5D_4 decay curve of Tb-AV-22 monitored at 540.5 nm, under 377 nm excitation.	95
4.19 – Room temperature excitation spectrum of Eu-AV-22 monitored at the 7F_2 manifold (610.5 nm).	97
4.20 – Room temperature emission spectrum of Eu-AV-22 excited at 5L_6 manifold (394 nm). The inset shows an expansion of the $Eu^{3+} {}^5D_0 \rightarrow {}^7F_1$ transition collected at 10 K.	98
4.21 – Room temperature 5D_0 decay curve of Eu-AV-22 monitored at 610.5 nm under 394 nm excitation.	99
4.22 – Room temperature excitation spectra of Eu-AV-22 and $K_3[Tb_{0.95}Eu_{0.05}Si_3O_8(OH)_2]$, monitored at the 7F_2 manifold (610.5 nm).	100
4.23 – Room temperature emission spectrum of $K_3[Tb_{0.95}Eu_{0.05}Si_3O_8(OH)_2]$ excited at 5D_3 manifold (377 nm).	101
4.24 – Room temperature 5D_4 and 5D_0 decay curves of $K_3[Tb_{0.95}Eu_{0.05}Si_3O_8(OH)_2]$ detected at 540.5 nm (Tb^{3+}) and 610.5 nm (Eu^{3+}). Tb^{3+} and Eu^{3+} were excited at 377 nm. The inset shows the “grow-in” component of the $K_3[Tb_{0.95}Eu_{0.05}Si_3O_8(OH)_2]$ luminescence emission profile.	103
4.25 – Room temperature excitation and emission spectra of $K_3[Gd_{0.67}Tb_{0.28}Eu_{0.05}Si_3O_8(OH)_2]$. The excitation was performed at 377 nm, while emission was monitored at 540.5 nm (Tb^{3+} levels).	104
4.26 – Room temperature excitation spectra of Tb/Ce-AV-22 monitored at 543 nm, and Y/Ce-AV-22 monitored at 420 nm; 14 K excitation spectra of Tb/Ce-AV-22 monitored at 543 nm and 420 nm, and Y/Ce monitored at 420 nm.	105
4.27 – Room temperature and 14 K emission spectra of Tb/Ce-AV-22 excited at 342 nm. The inset shows the Y/Ce-AV-22 room temperature emission spectrum recorded at 342 nm.	106
4.28 – Room temperature and 14 K 5D_4 decay curves of as-prepared Tb/Ce-AV-22, monitored at 543 nm under 377 and 342 nm excitation.	108
4.29 – CIE chromaticity diagram showing the room temperature (x,y) color coordinates, measured at the excitation wavelengths depicted in Table 4.5.	111

4.30 – FT-Raman spectra of $K_3[Y_{1-a}Er_aSi_3O_8(OH)_2]$ $a=0.1$ and 1.0 . The insets depict the normalized integrated intensity of the $1.54 \mu m$ photoluminescence as a function of the Er^{3+} content for the samples with a in the range 0.005 to 1 .	112
4.31 – Infrared emission spectra of Er-AV-22 excited at 514.5 nm , recorded at 75 and 300 K . The inset shows the normalized integrated intensity of the $1.54 \mu m$ PL as a function of temperature.	113

Chapter 5

5.1 – Schematic representation of the synthesis of AV-23 materials.	119
5.2 – Polyhedral representation of the crystal packing in Tb-AV-23 viewed along the b axis.	122
5.3 – Schematic representation of the condensation ($Si-OH + Si-OH \rightarrow Si-O-Si + H_2O$) of adjacent anionic layers of AV-22 yielding the framework of AV-23.	124
5.4 – Experimental powder XRD patterns of pure AV-23 samples.	125
5.5 – Experimental powder XRD patterns of mixed Y/Er-AV-23 samples.	125
5.6 – Scanning electron micrograph of Tb-AV-23 crystals.	126
5.7 – Experimental and simulated ^{29}Si MAS NMR spectra of Y-AV-23.	126
5.8 – Si local environments in the structure of Y-AV-23.	127
5.9 – Powder XRD spectra illustrating the changes of the structure of Y-AV-23 with the time of hydration.	127
5.10 – ^{29}Si MAS NMR spectra recorded with 5 kHz MAS illustrating the changes of the structure of Y-AV-23 with the time of hydration.	128
5.11 – Raman spectrum of Tb-AV-23.	129
5.12 – Excitation spectrum of Tb-AV-23, monitored at the 7F_5 manifold (542 nm).	130
5.13 – Emission spectrum of Tb-AV-23, excited at the 5D_3 manifold (377 nm).	130
5.14 – Room temperature and 10 K 5D_4 decay curves of Tb-AV-23, monitored at 542 nm under 283 and 377 nm excitation.	131
5.15 – Excitation spectrum of Eu-AV-23, monitored at the 7F_2 manifold (609.5 nm).	132
5.16 – Emission spectrum of Eu-AV-23, excited at the 5L_6 manifold (392 nm).	133
5.17 – Photoluminescence steady-state and time-resolved emission spectra of Eu-AV-23 acquired at 14 K and excited at the 5L_6 manifold (392 nm).	133
5.18 – Room temperature and 10 K 5D_0 decay curves of Eu-AV-23, monitored at 609.5 and 615 nm under 392 nm excitation.	134

5.19 – Emission spectra of Eu-AV-22 and Eu-AV-23 acquired at 14 K and excited at the 5L_6 manifold (392 nm). The inset shows the FWHM deconvolution for the three Eu sites.	135
5.20 – FT-Raman spectra of $K_3(Y_{1-a}Er_aSi_3O_9)$, $a=0.05$ and 0.005 . The inset depicts the normalized integrated intensity of the 1.54 μm photoluminescence as a function of the Er^{3+} content for the samples with a in the range 0.005 to 1.	137

Chapter 6

6.1 – Schematic representation of the synthesis of AV-24 materials.	143
6.2 – Distorted octahedral $\{SmO_6\}$ coordination environments of Sm(1) and Sm(2) centers present in the crystal structure of Sm-AV-24.	145
6.3 – Perspective views along a) the a direction of Sm-AV-24, showing the two six-membered rings ($R_6^{1,2}$), an eight-membered ring (R_8) and a highly distorted twelve-membered ring (R_{12}) and b) the c direction; showing the packing of adjacent two-dimensional $(Si_{12}O_{32})_n^{16n-}$ anionic layers.	148
6.4 – Crystal packing of Sm-AV-24 viewed along the a axis.	149
6.5 – Experimental powder XRD patterns of pure AV-24 samples.	150
6.6 – Scanning electron micrographs of pure and mixed AV-24 compositions.	151
6.7 – Experimental and simulated ^{29}Si MAS NMR spectra of Sm-AV-24.	152
6.8 – Si local environments in the structure of Sm-AV-24.	153
6.9 – Raman spectrum of Eu-AV-24.	154
6.10 – Excitation spectrum of Tb-AV-24, monitored at the 7F_5 manifold (541 nm).	155
6.11 – Emission spectrum of Tb-AV-24, excited at the 5D_3 manifold (377 nm).	155
6.12 – Room temperature and 10 K 5D_4 decay curves of Tb-AV-24, monitored at 542 nm under 377 nm excitation.	156
6.13 – Excitation spectra of Eu-AV-24, recorded at room temperature and at 10 K, monitored at the 7F_2 manifold (610.8 nm).	157
6.14 – Excitation spectra of $K_7(Gd_{2.7}Eu_{0.3})Si_{12}O_{32}\cdot 3H_2O$, recorded at room temperature and at 10 K monitored at the 7F_2 manifold (610.8 nm).	157
6.15 – Emission spectra of Eu-AV-24 recorded at room temperature and 10 K, excited at the 5L_6 manifold (393 nm).	158
6.16 – Emission spectra of $K_7(Gd_{2.7}Eu_{0.3})Si_{12}O_{32}\cdot 3H_2O$ recorded at room temperature and 10 K, excited at the 5L_6 manifold (393 nm).	159
6.17 – Emission spectra of Eu-AV-24 recorded at 10 K excited at 393 nm, 5L_6 manifold and at 525.5 nm, 5D_1 manifold.	159

6.18 – Time-resolved emission spectra of Eu-AV-24 recorded at 10 K, with an initial delay of 0.05 and 25 ms. The excitation was performed at 393 nm.	160
6.19 – Eu(2)-Eu(2) dimmer decay curve of Eu-AV-24 and $K_7(Gd_{2.7}Eu_{0.3})Si_{12}O_{32} \cdot 3H_2O$ detected at 10 K on the $^5D_0 \rightarrow ^7F_1$ transition (589.8 nm) and excited at 229 nm. The inset shows the “grow-in” component of the luminescence emission profile.	161
6.20 – Decay curves of $K_7(Gd_{2.7}Eu_{0.3})Si_{12}O_{32} \cdot 3H_2O$ detected at different temperatures (10-300 K) on the $^5D_0 \rightarrow ^7F_2$ transition (609 nm) and excited at 393 nm.	162
6.21 – Temperature dependence of Eu(2)-Eu(2) lifetime for samples $K_7Eu_3Si_{12}O_{32} \cdot 3H_2O$ and $K_7(Gd_{2.7}Eu_{0.3})Si_{12}O_{32} \cdot 3H_2O$. The full lines correspond to the best fit of the experimental lifetimes using the Mott-Seitz temperature-dependence.	163
6.22 – Excitation spectra of Eu-AV-24, recorded at 10 K, monitored at the 7F_2 manifold (610.8 nm) and at the 7F_1 manifold (589.8 nm) (isolated dimmer line). The insets show the phonon-assisted anti-Stokes ($^7F_0 \rightarrow ^5D_2$) and Stokes vibronic components ($^7F_1 \rightarrow ^5D_3$).	164
6.23 – Time-resolved emission spectra of Eu-AV-24 with initial delay of 25 ms recorded at 10 K and at 50 K. The excitation was performed at 393 nm.	165
6.24 – Room temperature emission spectra of $K_7Tb_{2.94}Eu_{0.06}Si_{12}O_{32} \cdot 3H_2O$, excited at the 5D_3 manifold (377 nm).	166
6.25 – CIE chromaticity diagram showing the RT (x,y) color coordinates, measured at 270 nm for $Gd_2O_3:S:Tb$, 264 nm for $Y_2O_3:Eu$, 393 nm for Eu-AV-24 and 377 nm for Tb-AV-24 and mixed Tb/Eu samples.	167

List of tables

Chapter 2

- 2.1 – Normal electronic configuration of the neutral lanthanides, the first three stages of ionization and the Ln^{3+} radii. 29
- 2.2 – The number of energy J-sublevels for the 32 point symmetry groups versus the quantum number J. 34

Chapter 3

- 3.1 – Different luminescence types. 57

Chapter 4

- 4.1 – Characteristics of the used reagents. 80
- 4.2 – Unit cell parameters of AV-22 materials. 84
- 4.3 – Molar ratios obtained by EDS. 88
- 4.4 – $^5\text{D}_4$ lifetimes (ms) of Tb/Ce-, Tb/Eu- and Tb-AV-22 monitored at 543 nm; measured for different excitation wavelengths (342 and 377 nm) at 14 and 300 K. 109
- 4.5 – Room-temperature radiance ($\mu\text{W}/\text{cm}^2$) and (x,y) CIE color coordinates for the standard green phosphor $\text{Gd}_2\text{O}_2\text{S}:\text{Tb}$, Tb-AV-22 and Tb/Ce-AV-22 measured for different excitation wavelengths. 110

Chapter 5

- 5.1 – $^5\text{D}_4$ lifetimes of Tb-AV-22 and Tb-AV-23 measured at 300 and 10 K. 132
- 5.2 – $^5\text{D}_0$ lifetimes of Eu-AV-22 and Eu-AV-23 measured at 300 and 10 K. 134
- 5.3 – Room temperature radiance for the standard green $\text{Gd}_2\text{O}_2\text{S}:\text{Tb}$ and red $\text{Y}_2\text{O}_2:\text{Eu}$ phosphors, Tb- and Eu-AV-22, Tb- and Eu-AV-23 measured at different excitation wavelengths. 136
- 5.4 – Room temperature $^4\text{I}_{13/2}$ lifetimes of $\text{K}_3(\text{Y}_{1-a}\text{Er}_a\text{Si}_3\text{O}_9)$ ($a=0.01-0.20$) excited at 376 nm. 137

Chapter 6

- 6.1 – Characteristics of the used reagents. 143
- 6.2 – Unit cell parameters of AV-24 materials. 149

- 6.3** – Dimmer Eu(2)-Eu(2) lifetimes as a function of the temperature for $K_7Eu_3Si_{12}O_{32} \cdot 3H_2O$ and $K_7Gd_{2.70}Eu_{0.30}Si_{12}O_{32} \cdot 3H_2O$ samples monitoring the ${}^5D_0 \rightarrow {}^7F_1$ transition (589.8 nm) excitation of 229 nm. 161
- 6.4** – The normalized integrated intensity of the ${}^5D_4 \rightarrow {}^7F_{5,6}$ Tb^{3+} transitions for $K_7Tb_{3-a}EuaSi_{12}O_{32} \cdot 3H_2O$ samples, $a = 0.06-1.50$. 166

1 Introduction

Index

1.1	Introduction	2
1.2	Microporous framework materials	2
1.2.1	Zeolites and molecular sieves.....	2
1.2.2	Microporous metalosilicates.....	4
1.2.3	Microporous materials encompassing rare-earth elements	7
1.3	Layered materials	14
1.3.1	Clays	14
1.3.2	Layered titanosilicates	16
1.3.3	Layered rare-earth silicates.....	19
1.4	References	20

1.1 Introduction

Microporous framework materials and layered materials are involved in many aspects of science and technology. The synthesis and characterization of new microporous framework materials is not only driven by pure academic interest but also by the broad range of useful and unique physicochemical and catalytic properties they possess [1-4]. The current rate of publications related to microporous materials is about 2000 per year and new materials are regularly discovered. Layered materials exhibiting ability to pillar or establish permanent intra-crystalline porosity within layers and are an important field in development [5].

The aim of this chapter is to briefly discuss microporous zeolite-type materials and layered materials containing lanthanide elements, exhibiting photoluminescence properties.

1.2 Microporous framework materials

Microporous framework materials, often referred to as molecular sieves or open framework materials, are a class of inorganic solids with regular pores or voids with a size in the range of 5-30 Å. Zeolites are the most known family of such materials. Other families are the aluminophosphates (AlPOs), silicoaluminophosphates (SAPOs), metal-aluminophosphates (MeAPOs), transition metal silicates, in which the metal can be penta- or hexa-coordinated and, recently, the lanthanides silicates.

1.2.1 Zeolites and molecular sieves

Zeolites were the first materials identified as a class of minerals with uniform distribution of pore size. Reversible dehydration without loss of structural integrity as well as absorption of liquids and gasses imply a microporous continuous framework in zeolites. The word zeolite derives from the Greek words *zein*, "to boil" and *lithos*, "stone", and it was coined by the Swedish mineralogist Alex Fredric Cronstedt in 1756. Cronstedt

found that stilbite (the first zeolite he discovered) released large amounts of water when heated in a blowpipe flame, giving the impression that the solid was boiling [6].

Zeolites are hydrated, crystalline, naturally occurring aluminosilicates formed by TO_4 tetrahedra, (where, T represents Si^{4+} or Al^{3+} in tetrahedral coordination) with a three-dimensional, framework, structure. The frameworks, generally, are very open and enclose cavities and channels occupied by large cations and water molecules. Each tetrahedron has four oxygen positions, and each oxygen is bound to two T (Si or Al) atoms. The pure silica frameworks are not charged since silicon is a tetravalent ion. However, aluminosilicate materials have one negative charge per framework Al^{3+} ion which is balanced by extra-framework cations. Typical cations in natural zeolites include alkali, *e.g.* Na^+ , K^+ , Rb^+ and Cs^+ , and alkaline-earth, *e.g.* Mg^{2+} , Ca^{2+} , Sr^{2+} , Ba^{2+} ions. Synthetic zeolites may contain cations such as La^{3+} , Cu^{2+} , Ln^{3+} and NH_4^+ . A representative empirical formula for a zeolite is written usually as: $\text{M}_{2/n}\text{O} \cdot [\text{Al}_2\text{O}_3 \cdot x\text{SiO}_2] \cdot y\text{H}_2\text{O}$, where, M represents the non-framework exchangeable cations of valence n . y is the number of non-framework water molecules. As a result of the open structure, cations are not free to leave the crystals unless they are replaced by other cations because neutralization of the anionic charge of the aluminosilicate framework must be maintained. The bracketed term represents the framework composition. x has to be equal or greater than 2 because of the Löwenstein rule [7], which rationalizes the absence of Al-O-Al linkages in tectoaluminosilicates on the basis that negatively charged tetrahedral clusters are less stable than isolated negative charges.

Zeolites possess relevant chemical properties due to their structure. The most important physico-chemical characteristics they have are: well defined pore size; reversible dehydration capacity; gas absorption ability; ion-exchange; catalytic activity; high and tunable acidity.

There are more than 40 natural zeolites and their specific properties make them important materials to study. As a result of a systematic work, synthetic analogues of natural zeolites and synthetic zeolites without any natural counterparts were synthesized. The Structure Commission of the International Zeolite Association provides structural information on all zeolite structure types. This includes crystallographic data and drawings for all zeolite framework types, simulated powder patterns for representative materials and

relevant references [8]. The zeolites are represented by a three-letter code *e.g.* zeolite A (Figure 1.1) is designated LTA.

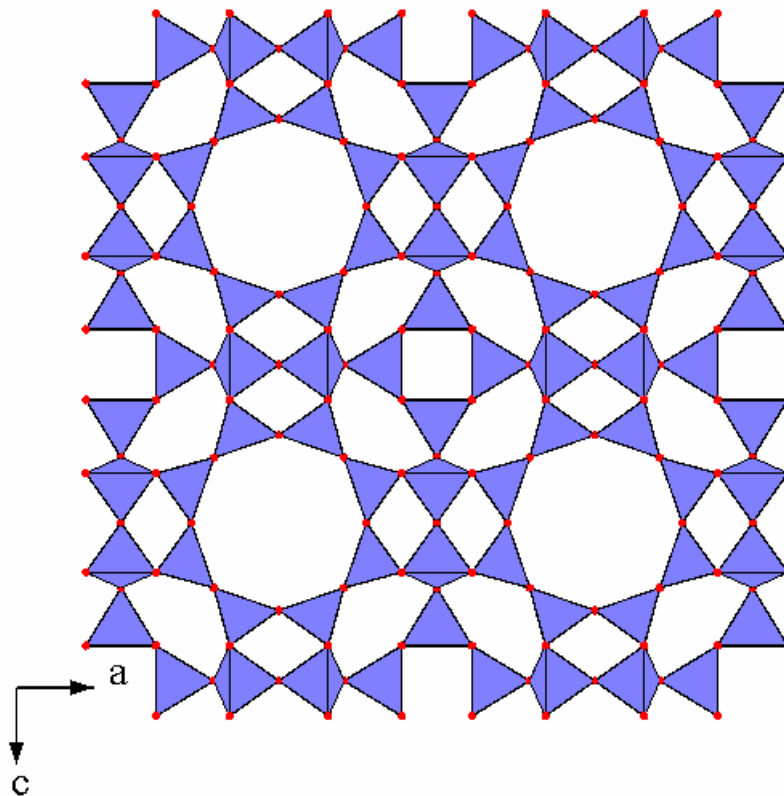


Figure 1.1 – Projection of zeolite A (LTA) down the b axis. Blue SiO_4 and AlO_4 tetrahedra, red O.

The term “molecular sieves” was proposed by J. W. McBain [9] in 1932 to describe porous materials which can separate components of a mixture based on the difference of their molecular size and shape. Molecular sieves are microporous crystalline solids having a three-dimensional structure built up of tetrahedra (SiO_4 , AlO_4 , PO_4 , GaO_4 , TiO_4), octahedra (TiO_6 , MoO_6 , MnO_6 , BiS_6 , VO_6) or pentaedra (TiO_5 , VO_5) [1-4].

1.2.2 Microporous metalosilicates

Since zeolites are unstable under certain conditions, a large effort was devoted to prepare materials that do not present this limitation. The first materials to be prepared were porous aluminophosphates (AlPOs), followed by the silico-aluminophosphates (SAPOs)

and the metalsilicoaluminophosphates (MeSAPOs). In all these materials the framework atoms are in tetrahedral coordination.

Microporous structures comprised entirely of octahedral sites are also known: octahedral molecular sieves (OMS) encompassing mixed-valence manganese oxides, (Mn^{2+} , Mn^{3+} and Mn^{4+}) and phases with composition $\text{Na}_2\text{Nb}_{2-x}\text{M}_x\text{O}_{6-x}(\text{OH})_x\cdot\text{H}_2\text{O}$, where $\text{M}=\text{Ti}$, Zr , and $0 < x \leq 0.4$ (Sandia octahedral molecular sieves (SOMS)). Transition metals play here an important role since they can usually be in different coordination environments and adopt different oxidation states. Mixed octahedral-pentahedral-tetrahedral microporous siliceous frameworks have been much studied since the early 1990s [10-12]. The chemistry of metalosilicates (MeSOs) [10-12] is of particular interest, because the materials reported in this thesis belong to this class. The most representative microporous metalosilicates obtained in laboratories are the titanosilicates. Among the already large family of titanosilicates, the most important material is the one first discovered by Kuznicki in 1989 [13], denominated ETS-10. At about the same time another material, which appeared to mimic the mineral zorite was patented by the Engelhard Corporation and called ETS-4 [14]. At the same time, independently, Chapman and Roe [15,16] reported on the synthesis of a microporous titanosilicate, whose structure resembles the structure of the mineral zorite.

Owing to its thermal stability and wide-pore nature, ETS-10 is the most important octahedral-tetrahedral framework microporous titanosilicate. The structure of ETS-10 was solved and reported briefly in 1994 by Anderson *et al.* [17] and described fully by the same authors in the following year [18]. A single crystal study (crystals up to 45 μm) of ETS-10 has refined and confirmed all of the previous structural work [19].

The structure of ETS-10 consists of a three-dimensional framework formed by SiO_4 tetrahedra and TiO_6 octahedra interlinked through bridging oxygen atoms. The negative charge of the crystalline net is compensated by exchangeable Na^+ and K^+ cations. ETS-10, with the formula $(\text{Na}_{2-x}\text{K}_x)\text{TiSi}_5\text{O}_{13}\cdot 4\text{H}_2\text{O}$, has a three dimensional wide-pore channel system, consisting of 12-rings in all three dimensions, 7-rings, 5-rings and 3-rings. The structure is highly disordered, which could be explained in terms of different stacking sequences of the same $[\text{Si}_{40}\text{Ti}_8\text{O}_{108}]_{16}$ unit, giving origin to several polymorphic forms. One of the most relevant polymorphs described is B, represented in Figure 1.2.

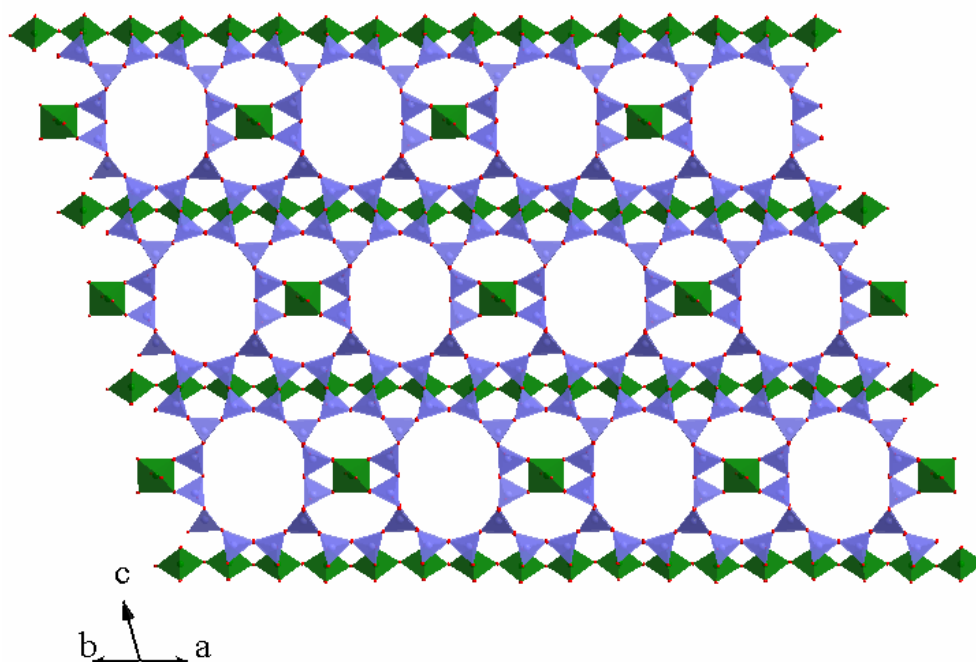


Figure 1.2 – Projection of the ETS-10 structure, polymorph B along the [110] direction. Green TiO_6 octahedra, blue SiO_4 tetrahedra, red O.

The most interesting aspect of the structure of ETS-10 is that it contains infinite $-\text{O}-\text{Ti}-\text{O}-\text{Ti}-\text{O}-$ chains (with alternating long-short bonds) which are surrounded by a silicate ring structure. These combine to make up a rod and because of this rod nature ETS-10 has interesting physical properties. Adjacent layers of rods are stacked orthogonal to each other.

In 1973 a naturally occurring alkaline titanosilicate identified as zorite was discovered [20] in trace quantities on the Siberian Tundra. As noted above, ETS-4 is the synthetic analogue of the mineral zorite, possessing a mixed tetrahedral (Si)-pentahedral (Ti2)-octahedral (Ti1) framework. The structure of ETS-4 presents a high degree of disorder, and in contrast to ETS-10, ETS-4 is small-pore. The single-crystal X-ray data, presented by Nair and collaborators [21], suggests that the titanium in the connection units (Ti2) is penta-coordinated in square pyramidal geometry.

Although most of the research has been focused on ETS-4 and ETS-10, many other titanosilicate microporous materials are now known, most of which are synthetic counterparts of rare minerals. Importantly, these solids are in general small-pore silicates or tunnel structures, with porosity accessible only to small molecules. As a result, the studies exploring their potential applications concentrate on ion-exchange properties.

The search for octahedral-pentahedral-tetrahedral microporous siliceous frameworks of metals other than Ti such as Zr, Nb, V, Sn, In and Ca, has been reported [10-12]. Following the synthesis and structural characterization work, the potential applications of these novel materials have been evaluated, particularly in the areas of catalysis, separation and ion-exchange.

1.2.3 Microporous materials encompassing rare-earth elements

Microporous materials hosting rare-earth elements were recently intensively researched. These photoluminescent lanthanide materials encompass [22]:

- 1) Zeolites doped via ion exchanging the extra-framework cations by lanthanide ions (Ln^{3+}).
- 2) Lanthanide complexes with organic ligands, enclosed in the zeolitic pores and channels.
- 3) Open-framework coordination polymers (organic-inorganic hybrids).
- 4) Novel lanthanide silicates, which contain stoichiometric amounts of framework Ln^{3+} .

In this thesis I will describe in detail the first and last materials.

1.2.3.1 Zeolites doped with lanthanide ions via ion-exchange

The conventional ion-exchange methods normally used consist of stirring for several hours a zeolite suspension in an aqueous solution of lanthanide salt, at adequate pH and room, or moderate, temperature. Ln^{3+} ions exchange for the charge-compensating cations (Na^+ , K^+ , Mg^{2+} , Ca^{2+} ...) residing in the intra-crystalline cavities and channels of zeolites and related materials. The photoluminescence of Ln^{3+} cation-exchanged zeolites has been investigated to evaluate the potential of this materials used as phosphors and as a probe to obtain information on the cations local environment inside the cages [23-27].

Rocha and co-workers ion-exchanged ETS-10 with Eu^{3+} [28] and Er^{3+} [29], substituting Na^+ and K^+ , and studied the photoluminescence properties of the resultant materials. In the hydrated state only Eu^{3+} -doped ETS-10 is optically active, even at 300 K. However, the presence of a significant number of water molecules inside the channels of

ETS-10, coordinated to Eu^{3+} , partially increases the non-radiative process, reducing the photoluminescence [28]. Photoluminescence indicates the presence of, at least, two local environments for the Eu^{3+} ions in ETS-10. A way to overcome the quenching of photoluminescence by water molecules and hydroxyl ions in zeolites consists of collapsing the microporous framework into more dense structures. Borgmann and co-workers prepared efficiently emitting Ln^{3+} (e.g. Eu^{3+}) sodalites by calcination of zeolite X at 1000 °C [30]. At 700 °C Eu^{3+} and Er^{3+} -doped ETS-10 phase transforms into the dense titanosilicate analog of the mineral narsarsukite, with interesting photoluminescence properties. Er^{3+} -doped narsarsukite, in particular, exhibits a high and stable room temperature emission in the visible and in the infrared spectral regions [29].

1.2.3.2 Microporous rare-earth silicates

Embedding rare-earth ions in the framework is a novel approach proposed by Rocha and co-workers for preparation of photoluminescent microporous materials, which contain stoichiometric amounts of RE^{3+} . One of the first studied systems was AV-1, a sodium yttrium silicate possessing the structure of the mineral montregianite [31,32]. Montregianite (also known as UK-6) is a very rare hydrous sodium potassium yttrium silicate ($\text{Na}_4\text{K}_2\text{Y}_2\text{Si}_{16}\text{O}_{38}\cdot 10\text{H}_2\text{O}$), from Mont St. Hilaire, Québec, Canada, where it occurs in miarolitic cavities and thermally metamorphosed inclusions and rheomorphic breccias in nepheline syenite [33,34]. The structure of montregianite (AV-1) is very unusual because the sodium (and yttrium) cations are an integral part of the framework. In contrast, in zeolites and zeolite-type materials the charge-balancing sodium cations usually reside within the channels and, thus, are not part of the framework. Later, the same group reported Ce^{3+} (AV-5) [35], Eu^{3+} and Tb^{3+} (AV-9) [36] montregianite-type materials.

The structures of AV-9 and related materials containing Er^{3+} and Nd^{3+} [37,38], and montregianite are related. The tetrahedral layers of AV-9 solids and montregianite are similar. The octahedral layers are different because montregianite, AV-1 and AV-5 contain a single kind of RE^{3+} , facing the pores, while AV-9 contains two kinds of RE^{3+} : one is isolated by $[\text{NaO}_4(\text{H}_2\text{O})_2]$ octahedral, while the other is facing the pores (Figure 1.3).

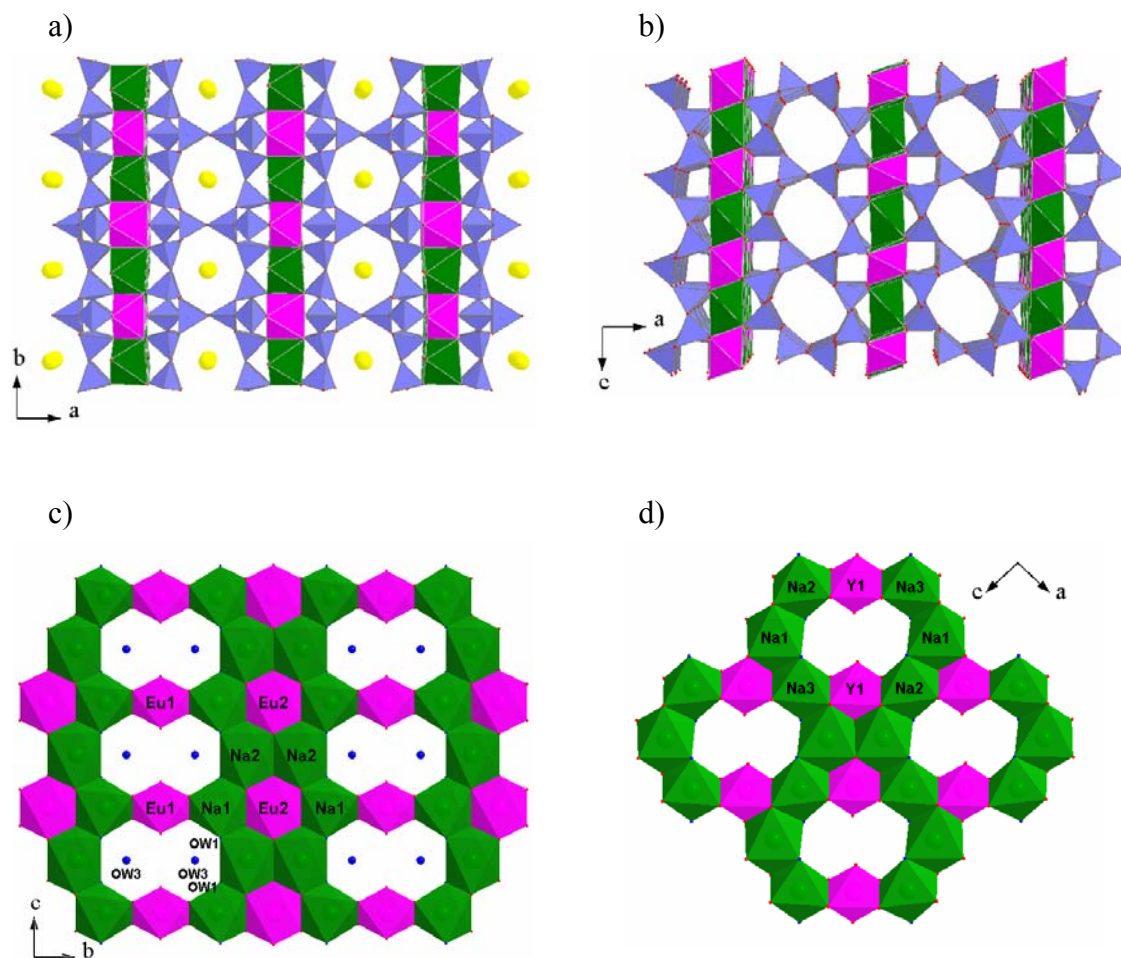


Figure 1.3 – Crystal structure of montregianite-type materials showing: a) the alternating octahedral sheet and double-silicate layer; b) the channels along the b axis which are defined by eight-membered rings and are free from any cations; c,d) an open octahedral sheet composed of REO_6 and $[NaO_4(H_2O)_2]$ octahedra; c) AV-9 materials contain two types of RE^{3+} , one is isolated by $[NaO_4(H_2O)_2]$ octahedra and the other faces the pores; d) montregianite, AV-1 and AV-5 contain a single type of RE^{3+} facing the pores. Polyhedra: purple REO_6 , green $[NaO_4(H_2O)_2]$, blue SiO_4 ; spheres: yellow K^+ , dark blue H_2O , red O.

Eu- and Tb-AV-9 are photoluminescent in the visible region, while dehydrated Er-AV-9 and Nd-AV-9 are room temperature infrared emitters [37,38]. Tb-AV-9 is the first example of a microporous siliceous X-ray scintillator, it emits in the visible region when excited with X-ray, $CuK\alpha$, radiation (integrated intensity 60% of that of standard material $Gd_2O_3:S:Tb$) [37].

Montregianite-type materials are important because they combine in a single, stable, solid microporosity and photoluminescence. Fine tuning of optical (and other) properties

may be achieved by adjusting the structure, the chemical composition and the oxidation state of the elements (for example $\text{Ce}^{3+}/\text{Ce}^{4+}$ in AV-5 [35]).

Another interesting system is based on mineral sazhinite $\text{Na}_2(\text{CeSi}_6\text{O}_{14})(\text{OH})\cdot n\text{H}_2\text{O}$ $n \geq 1.5$ [39] and its synthetic analogues: AV-21 $[\text{Na}_3(\text{EuSi}_6\text{O}_{15})\cdot 2\text{H}_2\text{O}]$ [40], $\text{Na}_{4.8}\text{Ce}_2\text{Si}_{12}\text{O}_{30}\cdot 4\text{H}_2\text{O}$ [41], α and β forms of $\text{K}_3(\text{NdSi}_6\text{O}_{15})\cdot x(\text{H}_2\text{O})$, [42,43] and $\text{Na}_3\text{NdSi}_6\text{O}_{15}\cdot 2\text{H}_2\text{O}$ [44]. All structures are formed by undulated $[\text{Si}_2\text{O}_5^{2-}]_\infty$ layers (in the bc plane, for AV-21; Figure 1.4b) in which all the SiO_4 tetrahedra are formed by three bridging O-atoms (to neighboring intra-layer Si-atoms) and one terminal O-atom coordinated to one Ln^{3+} ion (tetrahedral vertices pointing “upwards” and “downwards” in Figure 1.4). In all structures the layers are formed by the condensation of adjacent xonotlite-type ribbons. The way they coalesce in AV-21 and $\text{Na}_{4.8}\text{Ce}_2\text{Si}_{12}\text{O}_{30}\cdot 4\text{H}_2\text{O}$ is different from what is observed for sazhinite, α and β forms of $\text{K}_3(\text{NdSi}_6\text{O}_{15})\cdot x(\text{H}_2\text{O})$. In the mineral (and related structures) the coalescence of xonotlite-type ribbons is purely parallel, leading to the formation of alternating 4- and 6-membered rings in the interface between ribbons (Figure 1.4a). In AV-21 and $\text{Na}_{4.8}\text{Ce}_2\text{Si}_{12}\text{O}_{30}\cdot 4\text{H}_2\text{O}$ only 5-membered rings are observed in the interface due to an $[\text{ABAB}\cdots]$ alternating fashion for the linked ribbons (Figure 1.4b).

Adjacent $[\text{Si}_2\text{O}_5^{2-}]_\infty$ layers are pillared by the Eu^{3+} ions, connected through coordinative interactions to the terminal SiO_4 oxygen atoms, forming a porous three-dimensional network (Figure 1.4c,d). Sazhinite contains channels running along each crystallographic direction of the unit cell [39]. The largest channels are formed by the hills and valleys of the corrugated $[\text{Si}_2\text{O}_5^{2-}]_\infty$ sheets, which lead to the formation of two different types of irregular 8-membered tunnels [39]. The same structural type of 8-membered channel is also observed for AV-21 (Figure 1.4d), $\text{Na}_{4.8}\text{Ce}_2\text{Si}_{12}\text{O}_{30}\cdot 4\text{H}_2\text{O}$, α and β forms of $\text{K}_3(\text{NdSi}_6\text{O}_{15})\cdot x(\text{H}_2\text{O})$. Na^+ ions and water molecules are located within the channels of the open $[(\text{EuSi}_6\text{O}_{15})]_n^{3n-}$ anionic framework of AV-21.

Our group has recently studied the structure of AV-21 $[\text{Na}_3(\text{EuSi}_6\text{O}_{15})\cdot 2\text{H}_2\text{O}]$ which contains two crystallographically unique Eu^{3+} centers coordinated to six different SiO_4 tetrahedra. The Eu-AV-21 photoluminescence in the visible region has also been reported [40].

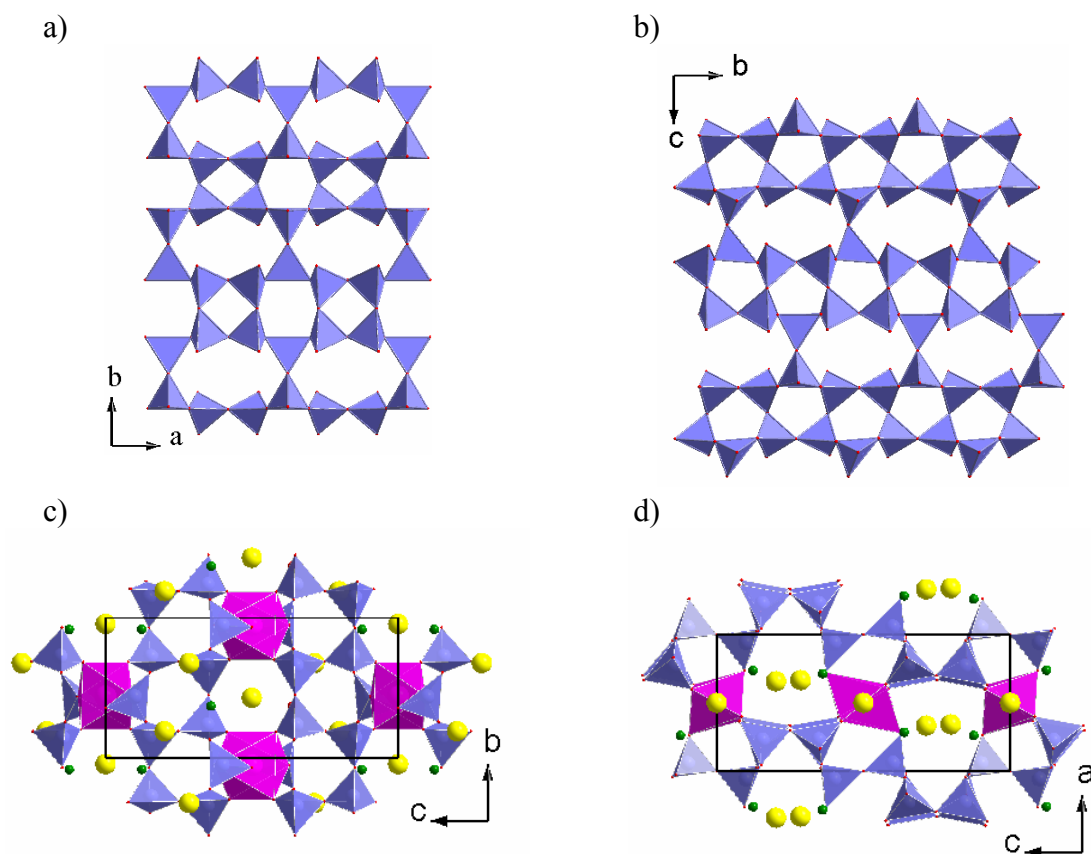


Figure 1.4 – a,b) $[\text{Si}_2\text{O}_5^{2-}]_n$ layers present in a) mineral sazhinite and in the α and β forms of $\text{K}_3(\text{NdSi}_6\text{O}_{15}) \cdot x(\text{H}_2\text{O})$; b) AV-21 and $\text{Na}_{4.8}\text{Ce}_2\text{Si}_{12}\text{O}_{30} \cdot 4\text{H}_2\text{O}$; c,d) polyhedral representation of the structure of AV-21. Polyhedra: purple LnO_6 , blue SiO_4 ; spheres: yellow K^+ , green H_2O , red O.

Another example of microporous lanthanide silicates exhibiting photoluminescence is AV-20 or $\text{Na}_{1.08}\text{K}_{0.5}\text{Ln}_{1.14}\text{Si}_3\text{O}_{8.5} \cdot 1.78\text{H}_2\text{O}$, $\text{Ln}=\text{Eu}, \text{Tb}, \text{Sm}, \text{Ce}$ [45], based on the structure of hydrated calcium silicate minerals, known as tobermorites [46]. The structural flexibility of these materials allows fine-tuning of photoluminescence properties, by introducing a second type of lanthanide ion in the framework [45]. A common feature of the tobermorite family is the layer built up by seven-coordinated (mono-capped trigonal prisms) calcium cations (Figure 1.5b). In AV-20 the substitution $2\text{Ca}^{2+} \leftrightarrow \text{Eu}^{3+} + \text{Na}^+$ occurs, with Eu^{3+} and Na^+ being seven-coordinated. In addition, some (*c.a.* 10%) Eu^{3+} ions are disordered over the Na^+ sites. Columns of $\text{Eu}^{3+}/\text{Na}^+$ polyhedra run along the [110] direction and neighboring columns in each layer present the capping ligands (water molecules and oxygen atoms) on their opposite surfaces. In mixed lanthanide samples, these columns host, at least, two different ions, such as Eu^{3+} and Tb^{3+} or Gd^{3+} and Tb^{3+} .

The silicate chains in tobermorites are of the wollastonite type and run along the [110] direction. The cavities of Eu-AV-20 contain Na^+ and K^+ ions. K^+ is seven-coordinated to four framework oxygen atoms and three water molecules, whereas Na^+ is six-coordinated to three framework oxygen atoms and three water molecules (Figure 1.5c).

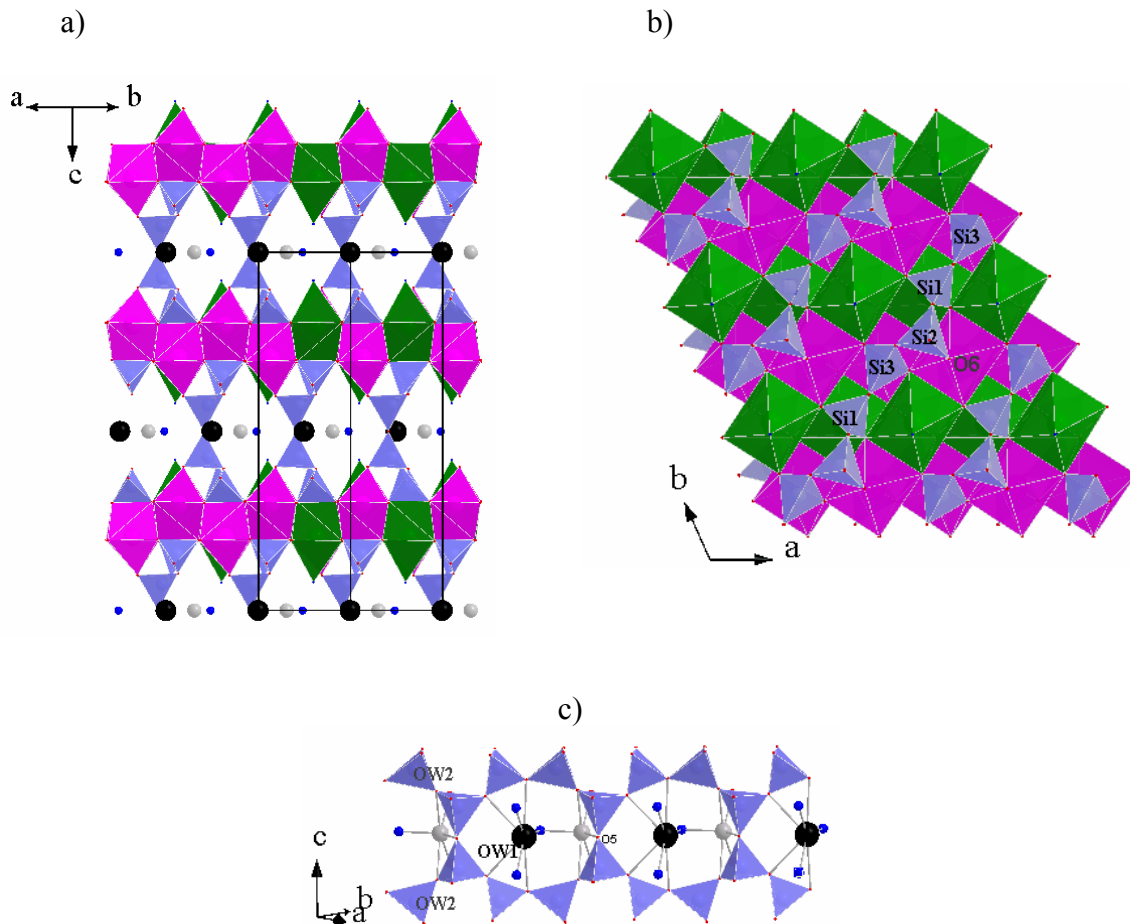


Figure 1.5 – a) Crystal structure of Eu-AV-20; b) Connection of silicate chains to the layer of EuO_7 and NaO_7 polyhedra; c) Schematic representation of the K^+ and Na^+ ions residing in the pores of Eu-AV-20. Polyhedra: purple EuO_7 , green NaO_7 , blue SiO_4 ; spheres: black $\text{KO}_4(\text{H}_2\text{O})_3$, light gray $\text{NaO}_3(\text{H}_2\text{O})_3$, dark blue H_2O red O (OW are water coordinated to the $\text{Eu}^{3+}/\text{Na}^+$ polyhedra).

The minerals gerenite $(\text{Ca},\text{Na})_2(\text{Y},\text{RE})_3\text{Si}_6\text{O}_{18}\cdot 4\text{H}_2\text{O}$, $\text{RE}=\text{La}, \text{Ce}, \text{Pr}, \text{Nd}, \text{Sm}$, [47] and kainosite $\text{Ca}_2(\text{Y},\text{Ce})_2\text{Si}_4\text{O}_{12}(\text{CO}_3)\cdot \text{H}_2\text{O}$ [48] also possess three-dimensional microporous structures defined by pores of 6-membered rings. The minerals sazykinaite-(Y), $\text{Na}_5\text{YZrSi}_6\text{O}_{18}\cdot 6\text{H}_2\text{O}$, and pyatenkoite-(Y) $\text{Na}_5(\text{Y},\text{Dy},\text{Gd})\text{TiSi}_6\text{O}_{18}\cdot 6(\text{H}_2\text{O})$ (structural

analogue where Zr^{4+} is substituted by Ti^{4+}) are microporous structures build up of rare-earth elements and transition metals both in octahedral coordination [49].

In the 1970s started the study of various new rare-earth silicates, without mineral analogues, with the aim to understand the distribution and the mobility of the rare-earth elements in natural systems [50]. Due to the unique physical properties of the rare-earth elements the field was extensively developed. Here we will illustrate some new photoluminescent microporous rare-earth silicates with no mineral analogues.

One such example is the $K_{8-x}[Yb_3Si_{12}O_{32}](OH)_{1-x} \cdot xH_2O$ (where x is approximately 2/3) silicate structure firstly reported by Pushcharovskii and co-workers [51]. Nearly twenty years later, Haile *et al.* [52], in a follow-up paper analyzed in detail the structure of $K_8[Nd_3Si_{12}O_{32}](OH)$, concluding that the K^+ deficiency described by Pushcharovskii was not a feature of their particular Nd^{3+} material [53]. In this dissertation (Chapter 6) I will report yet another $K_7[Ln_3Si_{12}O_{32}] \cdot 3H_2O$ structure [54] belonging to this family of compounds and representing very interesting photoluminescence features.

Recently a new member of open-framework lanthanide silicates $Cs_3EuSi_6O_{15}$ was reported [55]. This silicate contains stoichiometric amounts of lanthanide ions. The crystal structure and photoluminescence properties of high-temperature, high-pressure hydrothermally grown crystals of $Cs_3EuSi_6O_{15}$ were presented. The structure consists of loop-branched vierer double chains of silicate with four-, six-, and eight-membered rings, which are connected via 10-membered rings at their interfaces to form a 3-D silicate framework. AV-21 [$Na_3(EuSi_6O_{15}) \cdot 2H_2O$] [40] has the same framework stoichiometry but different structure.

Recently, Ananias *at al.* reported a new rare-earth silicate system $Na_3[(Y,Ln)Si_3O_9] \cdot 3H_2O$ ($Ln=Eu, Tb, Er, Ce$), which is an unprecedented chiral, photoluminescent system [56]. At the same time Wang and co-workers reported independently on the synthesis and photoluminescence of an isomorphous terbium silicate $Na_3TbSi_3O_9 \cdot 3H_2O$ (denoted TbSiO-CJ1) [57]. The crystal structure of $Na_3[(Y,Ln)Si_3O_9] \cdot 3H_2O$ materials displays $(Si_3O_9)_\infty$ chiral spirals interconnected by $\{(Y,Ln)O_6\}$ octahedra, and it exhibits a statistical excess of one enantiomer over the other. For the first time, Eu^{3+} photoluminescence spectroscopy with excitation by unpolarized light in the absence of an external magnetic field was used to identify, and possibly quantify, enantiomeric domains in chiral frameworks.

1.3 Layered materials

The term layered compounds encompasses clays and other classes of materials exhibiting the ability to pillar, or establish permanent intra-crystalline porosity within layers [5].

1.3.1 Clays

Clays are two-dimensionally polymerized aluminosilicate minerals [58,59]. Besides having layer polysilicate or polyaluminosilicate ions, clays are characterized by having parallel layers of octahedrally-coordinated Al^{3+} or Mg^{3+} ions and tetrahedrally-coordinated Si^{4+} ions. The bridging of the layers is achieved by OH^- ions, OH^- and /or O^{2-} ions connecting the adjacent tetrahedral layers such as ${}_{\infty}^2[\text{Si}_4\text{O}_{10}^{4-}]$ and octahedral layers such as ${}_{\infty}^2[\text{Al}_4(\text{OH})_8^{4+}]$. The simplest clay kaolinite ${}_{\infty}^2\{[\text{Al}_4(\text{OH})_8][\text{Si}_4\text{O}_{10}]\}$ (Figure 1.6a) has only two layers; the bi-layer “sandwiches” are bound to neighboring sandwiches only by comparatively weak hydrogen bonds.

Other important clays involve three layers, two of which are anionic tetrahedral polysilicate or polyaluminosilicate layers sandwiching a central cationic octahedral aluminum hydroxide or magnesium aluminum hydroxide layer. In pyrophyllite ${}_{\infty}^2\{[\text{Al}_4(\text{OH})_8][\text{Si}_4\text{O}_{10}]_2\}$ (Figure 1.6b) the central ${}_{\infty}^2[\text{Al}_4(\text{OH})_8^{8+}]$ layer exactly neutralizes the two outer layers; only hydrogen bonds link one triple layer to another, so that cleavage into sheets is very easy.

In muscovite (mica) ${}_{\infty}^2\{\text{K}_2[\text{Al}_4(\text{OH})_4][\text{AlSi}_3\text{O}_{10}]_2\}$ (Figure 1.6d), the two outer layers are each -5 charged aluminosilicate layers, so their total charge exceeds that of the central octahedral layer. Charge balance thus requires a fourth layer of cations such as K^+ . Two other clays, montmorillonite ${}_{\infty}^2\{\text{Mg}_{\delta}[\text{Mg}_{\delta}\text{Al}_{(4-\delta)}(\text{OH})_4][\text{Si}_4\text{O}_{10}]_2\}$ (on the figure $\delta=2$) (Figure 1.6c) and vermiculite ${}_{\infty}^2\{(\text{Ca}, \text{Mg})[\text{Al}_2\text{Mg}_2(\text{OH})_4][\text{AlSi}_3\text{O}_{10}]_2\}$ (Figure 1.6e) are

derived from the structure of muscovite by different isomorphous substitution process of the second kind.

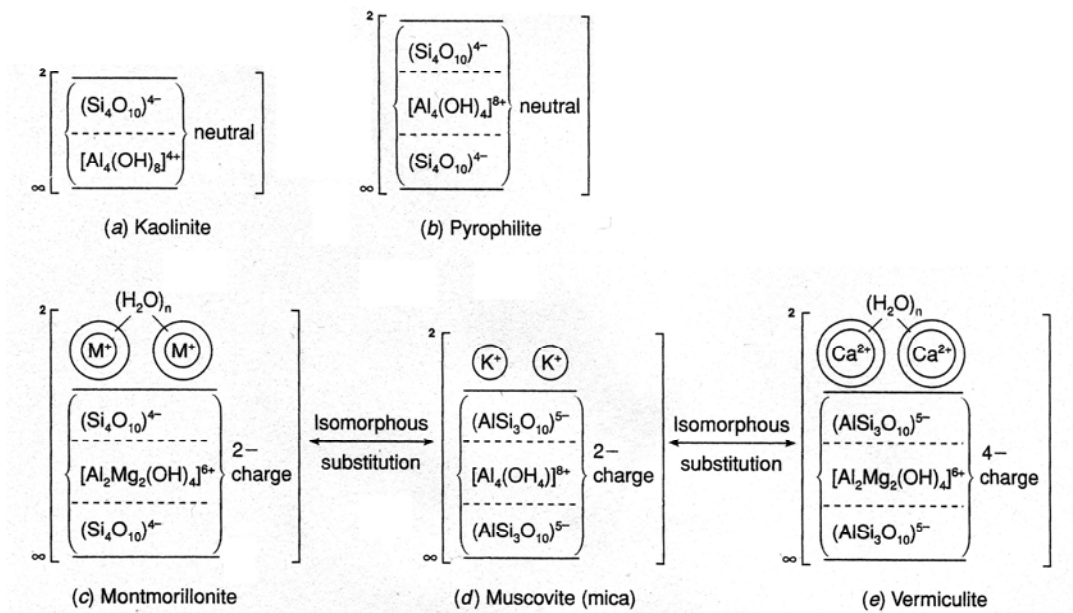


Figure 1.6 – Layered structures of selected clays and their interrelationships via isomorphous or non-isomorphous substitution. a) Kaolinite; b) Pyrophyllite; c) Montmorillonite; d) Muscovite (mica); e) Vermiculite [58].

The cations absorbed on the surface of the charged clays (muscovite, vermiculite and montmorillonite) are of low acidity, and are easily exchanged with ions from solution. Enormous quantities of hydrated cations can be held on the negatively charged surfaces of clays, including Ca^{2+} , Mg^{2+} , K^+ and Na^+ .

Clays have a variety of uses: in ceramics as acid catalysts for organic reaction, in intercalation chemistry *etc.* Most clays have water molecules intercalated between the framework sheets. Interactions between the layers are weak, and water molecules readily penetrate the interlayer space causing the lattice to expand. In some, such as vermiculite, the water may rapidly and dramatically be evacuated by heating. The result is the familiar expanded vermiculite used as a packing material and as a potting soil conditioner.

Other layered structures are: zirconium phosphates and phosphonates, double hydroxides, manganese oxides, metal chalcogenides, crystalline silicic acids and alkali silicates [5]. Here we will focus on silicates.

1.3.2 Layered titanosilicates

When attempting to prepare novel microporous framework titanosilicates several groups have obtained layered materials like AM-1 and AM-4.

AM-1 was first reported in 1995 [18] as low-level impurity contaminating ETS-10, ETS-4, and synthetic nenadkevichite. In 1996 a paper on the synthesis and characterization of JDF-L1 was published [60] and in the same year the structure was solved by *ab initio* methods [61]. Lin *et al.* have shown that JDF-L1 and AM-1 possess the same structure [62]. This is an unusual noncentrosymmetric tetragonal layered solid ($\text{Na}_4\text{Ti}_2\text{Si}_8\text{O}_{22}\cdot 4\text{H}_2\text{O}$), which contains five-coordinated Ti ions in the form of TiO_5 square pyramids in which each of the vertices of the base is linked to SiO_4 tetrahedra [$\text{TiO}\cdot\text{O}_4(\text{SiO}_3)_4$] to form continuous sheets (Figure 1.7). The interlamellar Na^+ ions are exchangeable. Interestingly AM-1 contains no Ti-O-Ti linkages and hence differs in a fundamental way from many titanosilicates, which contain infinite Ti-O-Ti chains.

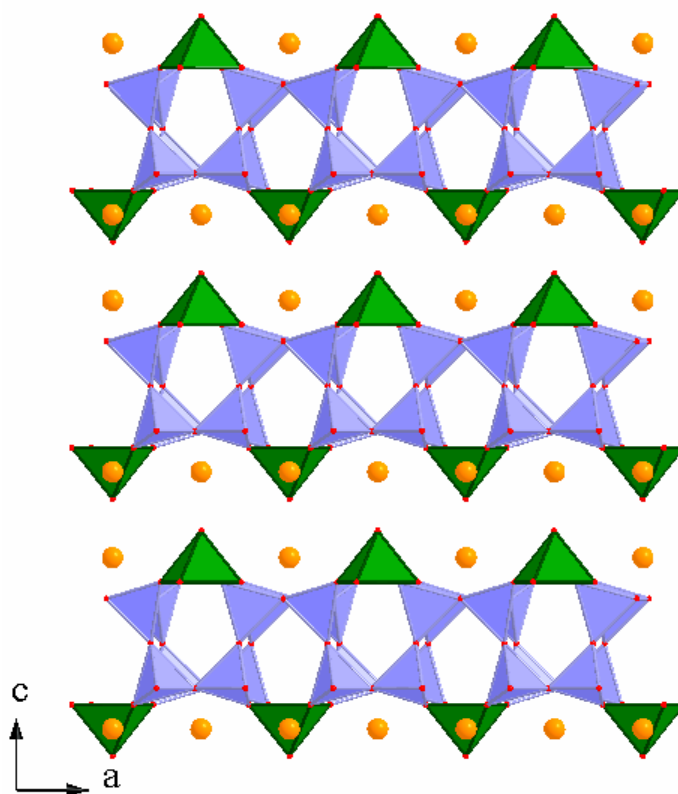


Figure 1.7 – Polyhedral representation of the layered structure of JDF-L1 and AM-1. For clarity, the H_2O molecules are not shown. Polyhedra: green TiO_5 , blue SiO_4 ; spheres: orange Na^+ , red O.

In 1997 the synthesis and powder XRD pattern of a new layered material called AM-4 were published [62] and in the same year the *ab initio* structure was reported [63].

The crystal structure of AM-4 or $\text{Na}_3(\text{Na,H})\text{Ti}_2\text{O}_2[\text{Si}_2\text{O}_6]_2 \cdot 2\text{H}_2\text{O}$ is built from TiO_6 octahedra and SiO_4 tetrahedra, which form layers perpendicular to [001]. Each layer consists of a five-tier sandwich of $\text{Si}_T : \text{Ti}_O : \text{Si}_T : \text{Ti}_O : \text{Si}_T$ (O = octahedral, T = tetrahedral) and this can be seen in Figure 1.8. Between the layers are Na^+ cations and water molecules. Sodium cations also exist in small cages within the layers. The major features of the structure are zigzag chains of edge-sharing TiO_6 octahedra running along [100] which are connected together by corner sharing pyroxene type SiO_4 tetrahedra.

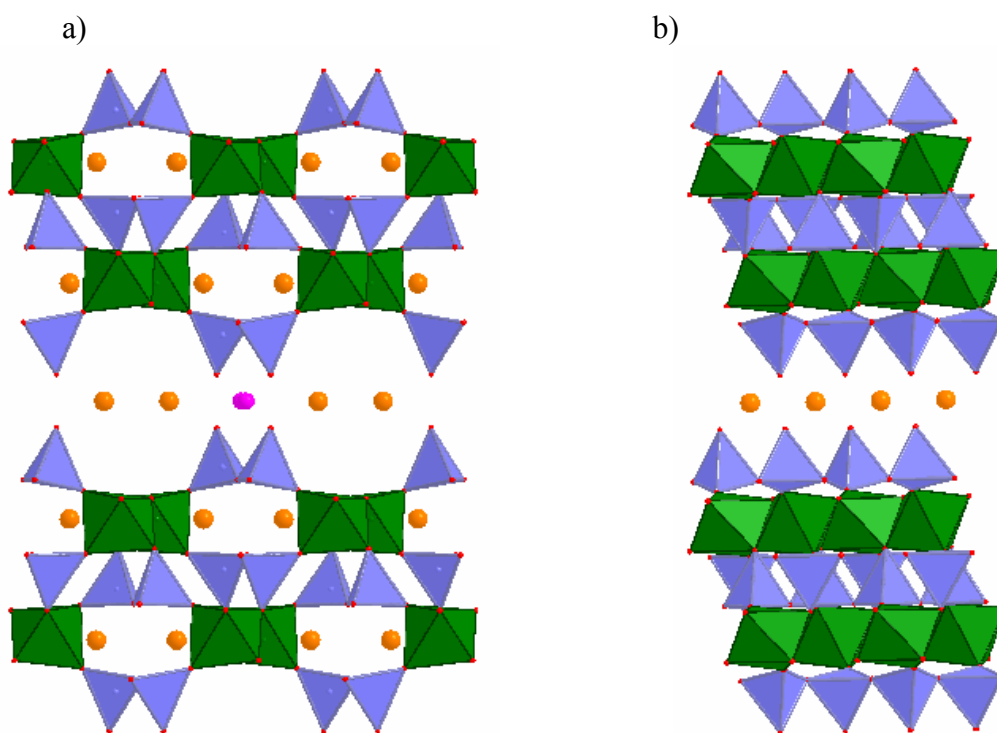


Figure 1.8 – Polyhedral representation of the layered structure of AM-4: a) viewed down a axis showing the small cages containing Na^+ cations within the titanosilicate layers and further Na^+ cations between the layers; b) viewed down b axis. Polyhedra: green TiO_6 , blue SiO_4 ; spheres: orange Na^+ , purple H_2O , red O.

Krivovichev and Armbruster [64] have recently reported the first example of a titanosilicate mineral (jonesite) with porous double layers (Figure 1.9). The structure of jonesite, $\text{Ba}_2(\text{K,Na})[\text{Ti}_2(\text{Si}_5\text{Al})\text{O}_{18}(\text{H}_2\text{O})](\text{H}_2\text{O})_n$, from the Benitoite Gem Mine, San Benito

County, California, is based upon porous double layers of distorted $\text{Ti}\Phi_6$ octahedra ($\Phi = \text{O}, \text{H}_2\text{O}$) and TO_4 tetrahedra ($\text{T} = \text{Si}, \text{Al}$) parallel to $[010]$. The layers consist of two sheets of corner-sharing $\text{Ti}\Phi_6$ octahedra and Si_2O_7 groups each. The two adjacent sheets are linked along b axis by T_4O_{12} tetrahedral rings that are disordered over two positions. The double layer has an open structure characterized by 8-membered tetrahedral rings. K^+ and water molecules reside in the pores of the double layers. Ba^{2+} cations are located between the double layers and provide their linkage into a three-dimensional structure.

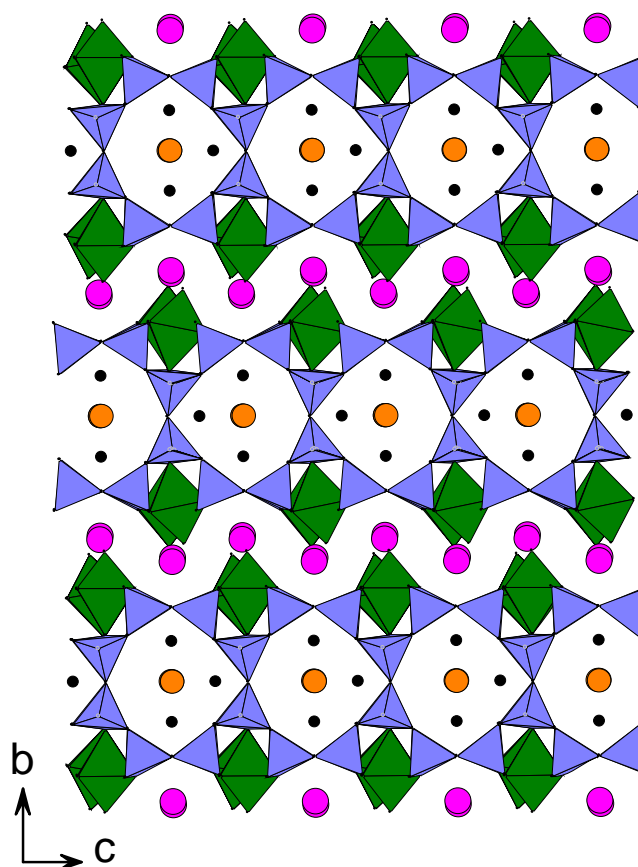


Figure 1.9 – Polyhedral representation of the layered structure of jonesite: projection along the a axis showing the titanosilicate layers parallel to $[010]$ with pores filled with (K, Na) and water molecules, linked by Ba . Polyhedra: green $\text{Ti}\Phi_6$, blue SiO_4 ; spheres: pink Ba^{2+} , orange K^+ , black H_2O .

An interesting future development is the synthesis of layered materials possessing microporous layers. These solids are of fundamental interest in exploring the connection between layered and framework silicates. One example is provided by Jeong *et al.* [65]

with a layered silicate known as AMH-3 ($\text{Na}_8\text{Sr}_8\text{Si}_{32}\text{O}_{76}\cdot 16\text{H}_2\text{O}$), which is composed of silicate layers containing eight-membered rings in all three principal crystal directions, and spaced by strontium cations, sodium cations and water molecules (Figure 1.10).

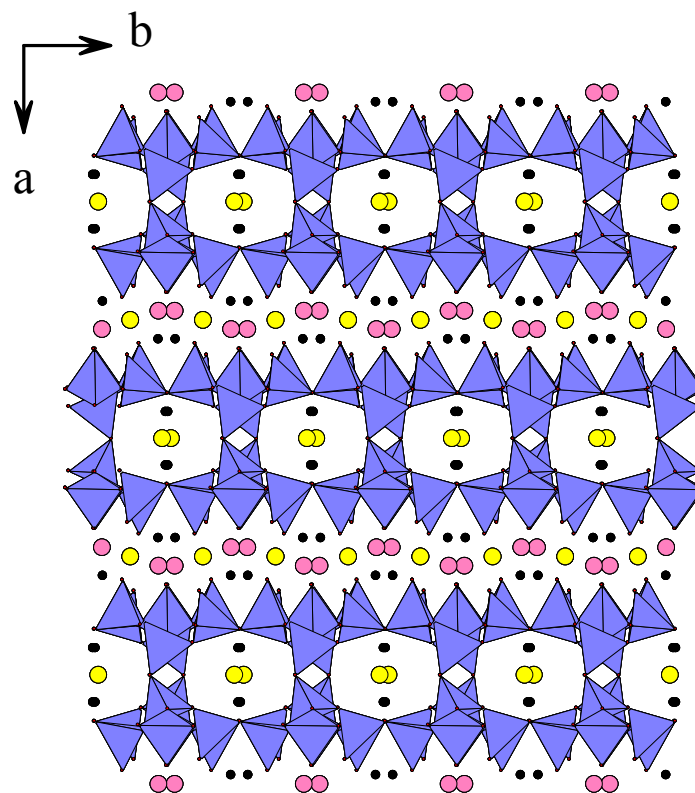


Figure 1.10 – Polyhedral representation of the layered structure of AMH-3: projection along the c axis. Polyhedra: blue SiO_4 ; spheres: pink Sr^{2+} , yellow Na^+ , black H_2O , red O.

1.3.3 Layered rare-earth silicates

In chapter 4 I will describe in detail layered rare-earth silicates ($\text{K}_3[\text{M}_{1-a}\text{Ln}_a\text{Si}_3\text{O}_8(\text{OH})_2]$, $\text{M}^{3+}=\text{Y}^{3+}$, Tb^{3+} ; $\text{Ln}^{3+}=\text{Eu}^{3+}$, Er^{3+} , Tb^{3+} , Gd^{3+} and Ce^{3+}), $1 \geq a > 0$ [38,66-68]. The structure of these materials allows the inclusion of a second (or even a third) type of rare-earth ion in the layers, micropores and interlayer spaces and, therefore, a fine-tuning of the photoluminescence properties. Upon calcination at 650°C , layered materials undergo a phase transformation to a small-pore framework system $\text{K}_3[\text{RESi}_3\text{O}_9]$, $\text{RE}^{3+}=\text{Y}^{3+}$, Er^{3+} , Eu^{3+} and Tb^{3+} [69] which I will illustrate in chapter 5.

1.4 References

- [1] D.W. Breck, Zeolite molecular sieves structure, chemistry, and use, Krieger, Malabar (FL), 1984.
- [2] R.M. Barrer, Hydrothermal chemistry of zeolites, Academic Press, London, 1982.
- [3] R. Szostak, Molecular sieves principles of synthesis and identification, Van Nostrand Reinhold, New York, 1989.
- [4] A. Dyer, An introduction to zeolite molecular sieves, John Wiley, Chichester, 1988.
- [5] S.M. Auerbach, K.A. Carrado, P.K. Dutta, Handbook of layered materials M. Dekker, New York 2004.
- [6] A.F. Cronstedt, Akad. Handl, Stockholm, 1756.
- [7] W. Loewenstein, Am. Mineral. 39 (1954) 92.
- [8] <http://www.iza-structure.org/databases/>.
- [9] J.W. McBain, The sorption of gases and vapors by solids, Rutledge and Sons, London, 1932.
- [10] J. Rocha, M.W. Anderson, Eur. J. Inorg. Chem. (2000) 801.
- [11] M. Anderson, J. Rocha, in Handbook of porous solids, Vol. 2, edited by F. Schuth, K. S. W. Sing, and J. Weitkamp, John Wiley & Sons, New York, 2002.
- [12] J. Rocha, Z. Lin, in Reviews in Mineralogy & Geochemistry Vol.57, (Eds.: G. Ferraris, S. Merlino), Mineralogical Society of America, Geochemical Society, chap. 6, 2005, p. 173.
- [13] S.M. Kuznicki, US Patent 4 853 202 (1989).
- [14] S.M. Kuznicki, US Patent 4 938 939 (1990).
- [15] D.M. Chapman, A.L. Roe, Zeolites 10 (1990) 730.
- [16] D.M. Chapman, US Patent 5 015 453 (1990).
- [17] M.W. Anderson, O. Terasaki, T. Ohsuna, A. Philippou, S.P. Mackay, A. Ferreira, J. Rocha, S. Lidin, Nature 367 (1994) 347.
- [18] M.W. Anderson, O. Terasaki, T. Ohsuna, P.J.O. Malley, A. Philippou, S.P. Mackay, A. Ferreira, J. Rocha, S. Lidin, Philos. Mag. B 71 (1995) 813.
- [19] X.Q. Wang, A.J. Jacobson, Chem. Commun. (1999) 973.

-
- [20] A.N. Merkov, I.V. Bussen, E.A. Goiko, E.A. Kulchitskaya, Y.P. Menshikov, A.P. Nedorezova, *Zap. Vses. Mineralog. Obs.* 102 (1973) 54.
- [21] S. Nair, H.K. Jeong, A. Chandrasekaran, C.M. Braunbarth, M. Tsapatsis, S.M. Kuznicki, *Chem. Mat.* 13 (2001) 4247.
- [22] J. Rocha, L.D. Carlos, *Curr. Opin. Solid State & Mat. Science* 7 (2003) 199.
- [23] T. Arakawa, T. Takata, G.Y. Adachi, J. Shiokawa, *J. Lumin.* 20 (1979) 325.
- [24] S.L. Suib, R.P. Zerger, G.D. Stucky, T.I. Morrison, G.K. Shenoy, *J. Chem. Phys.* 80 (1984) 2203.
- [25] M.D. Baker, M.M. Olken, G.A. Ozin, *J. Am. Chem. Soc.* 110 (1988) 5709.
- [26] M. Bredol, U. Kynast, C. Ronda, *Adv. Mat.* 3 (1991) 361.
- [27] O.A. Serra, E.J. Nassar, G. Zapparolli, I.L.V. Rosa, *J. Alloys Comp.* 225 (1995) 63.
- [28] J.P. Rainho, L.D. Carlos, J. Rocha, *J. Lumin.* 87-9 (2000) 1083.
- [29] J. Rocha, L.D. Carlos, J.P. Rainho, Z. Lin, P. Ferreira, R.M. Almeida, *J. Mat. Chem.* 10 (2000) 1371.
- [30] C. Borgmann, J. Sauer, T. Justel, U. Kynast, F. Schuth, *Adv. Mat.* 11 (1999) 45.
- [31] J. Rocha, P. Ferreira, Z. Lin, P. Brandao, A. Ferreira, J.D.P. de Jesus, *Chem. Commun.* (1997) 2103.
- [32] J. Rocha, P. Ferreira, Z. Lin, P. Brandao, A. Ferreira, J.D.P. de Jesus, *J. Phys. Chem. B* 102 (1998) 4739.
- [33] G.Y. Chao, *Can. Mineral.* 16 (1978) 561.
- [34] S. Ghose, P.K. Sengupta, C.F. Campana, *Am. Mineral.* 72 (1987) 365.
- [35] J. Rocha, P. Ferreira, L.D. Carlos, A. Ferreira, *Angew. Chem. Int. Ed.* 39 (2000) 3276.
- [36] D. Ananias, A. Ferreira, J. Rocha, P. Ferreira, J.P. Rainho, C. Morais, L.D. Carlos, *J. Am. Chem. Soc.* 123 (2001) 5735.
- [37] D. Ananias, J.P. Rainho, A. Ferreira, J. Rocha, L.D. Carlos, *J. Alloys Comp.* 374 (2004) 219.
- [38] J. Rocha, L.D. Carlos, A. Ferreira, J. Rainho, D. Ananias, Z. Lin, *Adv. Mat. Forum II* 455-456 (2004) 527.
- [39] N.G. Shumyatskaya, A.A. Voronkov, Y.A. Pyatenko, *Kristallografiya* 25 (1980) 728.

- [40] J. Rocha, L.D. Carlos, F.A.A. Paz, D. Ananias, J. Klinowski, in *Recent Advances in the Science and Technology of Zeolites and Related Materials, Studies in Surface Science and Catalysis*, Vol.154 (A,B,C), Elsevier, Amsterdam, 2004, p. 3028.
- [41] H.K. Jeong, A. Chandrasekaran, M. Tsapatsis, *Chem. Commun.* (2002) 2398.
- [42] S.M. Haile, B.J. Wuensch, *Acta Crystal. Sec. B* 56 (2000) 335.
- [43] S.M. Haile, B.J. Wuensch, *Acta Crystal. Sec. B* 56 (2000) 349.
- [44] S.M. Haile, B.J. Wuensch, R.A. Laudise, J. Maier, *Acta Crystal. Sec. B* 53 (1997) 7.
- [45] A. Ferreira, D. Ananias, L.D. Carlos, C.M. Morais, J. Rocha, *J. Am. Chem. Soc.* 125 (2003) 14573.
- [46] S. Merlino, E. Bonaccorsi, T. Armbruster, *Eur. J. Mineral.* 13 (2001) 577.
- [47] L.A. Groat, *Can. Mineral.* 36 (1998) 801.
- [48] I.M. Rumanova, G.F. Volodina, N.V. Belov, *Sov. Phys. Crystal.* 11 (1967) 485.
- [49] N.V. Chukanov, I.V. Pekov, R.K. Rastsvetaeva, *Usp. Khim.* 73 (2004) 227.
- [50] K. Byrappa, M. Yoshimura, *Handbook of hydrothermal technology*, N.Y. William Andrew Pub., Park Ridge, 2001.
- [51] D.I. Pushcharovskii, A.M. Dago, E.A. Pobedimskaia, N.V. Belov, *Dokl. Akad. Nauk SSSR* 258 (1981) 1111.
- [52] S.M. Haile, B.J. Wuensch, T. Siegrist, R.A. Laudise, *Solid State Ion.* 53-6 (1992) 1292.
- [53] S.M. Haile, B.J. Wuensch, T. Siegrist, *J. Solid State Chem.* 148 (1999) 406.
- [54] M.H. Kostova, D. Ananias, F.A.A. Paz, L.D. Carlos, J. Rocha, (2007) in prepar.
- [55] M.Y. Huang, Y.H. Chen, B.C. Chang, K.H. Lii, *Chem. Mat.* 17 (2005) 5743.
- [56] D. Ananias, F.A.A. Paz, L.D. Carlos, C. Geraldes, J. Rocha, *Angew. Chem. Int. Ed.* 45 (2006) 7938.
- [57] G.M. Wang, J.Y. Li, J.H. Yu, P. Chen, Q.H. Pan, H.W. Song, R.R. Xu, *Chem. Mat.* 18 (2006) 5637.
- [58] G. Wulfsberg, *Inorganic chemistry*, University Science Books, Sausalito (CA), 2000.
- [59] W.E. Worrall, *Clays and ceramic raw materials*, Applied Science, London, 1975.
- [60] H.B. Du, J.S. Chen, W.Q. Pang, *J. Mat. Chem.* 6 (1996) 1827.

-
- [61] M.A. Roberts, G. Sankar, J.M. Thomas, R.H. Jones, H. Du, J. Chen, W. Pang, R. Xu, *Nature* 381 (1996) 401.
- [62] Z. Lin, J. Rocha, P. Brandao, A. Ferreira, A.P. Esculcas, J.D.P. de Jesus, A. Philippou, M.W. Anderson, *J. Phys. Chem. B* 101 (1997) 7114.
- [63] M.S. Dadachov, A. LeBail, *Eur. J. Solid State and Inorg. Chem.* 34 (1997) 381.
- [64] S.V. Krivovichev, T. Armbruster, *Am. Mineral.* 89 (2004) 314.
- [65] H.K. Jeong, S. Nair, T. Vogt, L.C. Dickinson, M. Tsapatsis, *Nat. Mat.* 2 (2003) 53.
- [66] D. Ananias, M. Kostova, F.A.A. Paz, A. Ferreira, L.D. Carlos, J. Klinowski, J. Rocha, *J. Am. Chem. Soc.* 126 (2004) 10410.
- [67] M.H. Kostova, R.A.S. Ferreira, D. Ananias, L.D. Carlos, J. Rocha, *J. Phys. Chem. B* 110 (2006) 15312.
- [68] M.H. Kostova, D. Ananias, L.D. Carlos, J. Rocha, *J. Alloys Comp.* (2007) in press.
- [69] M.H. Kostova, D. Ananias, F.A.A. Paz, A. Ferreira, J. Rocha, L.D. Carlos, *J. Phys. Chem. B* 111 (2007) 3574.

2 Lanthanide ions

Index

2.1	Introduction	26
2.2	Electronic configurations.....	28
2.3	The Hamiltonian for the free ion	31
2.4	The ions in a chemical environment.....	32
2.5	$4f^n \rightarrow 4f^n$ transitions	36
2.6	$4f^n \rightarrow 4f^{n-1}5d$ (fd) transitions	38
2.7	Lifetimes.....	40
2.8	Energy transfer	42
2.9	Applications.....	47
2.10	References	52

2.1 Introduction

According to the IUPAC (International Union of Pure and Applied Chemistry) nomenclature the rare-earth series comprises elements 21 (Sc), 39 (Y), 57 (La) and the lanthanide series from 58 (Ce) to 71 (Lu). The first of these to be discovered was yttrium. The history of the rare-earth elements began in 1787 when the Swedish army officer, Carl Alex Arrhenius discovered a new heavy black mineral, which he named ytterbite after the adjacent village of Ytterby [1]. From this mineral in 1794 the Finish chemist Johan Gadolin isolated a new "earth" which we now know to be yttria - Y_2O_3 [1]. Although yttrium was not obtained in pure elemental form, Gadolin's 1794 isolation is taken to represent the discovery of the first rare-earth element [1].

Gadolin's isolation of yttria represented the first of a number of rare-earths that were extracted from the ytterbite, which later was renamed by Ekeberg to gadolinite in honor of Gadolin. As indicated in Figure 2.1, chemical analysis of gadolinite was responsible for the discovery of nine members of the rare-earths series [1]. These are sometimes referred as the "yttric" group, which encompasses the heavy lanthanides (from terbium to lutetium). The discovery of the remaining ones (except element 61) was due to direct or indirect extraction from the mineral cerite (Figure 2.1) [1]. These elements are sometimes referred to as "ceric" group and they constitute the light lanthanides (from lanthanum to gadolinium). More than one century was necessary to identify all rare-earth elements. Problems of purification were compounded by the lack of good methods for identifying elements and their purity, as well as complete ignorance of the number of different rare-earths that actually existed. During their discovery, several mistakes happened due to the great chemical similarity. Inefficient and laborious techniques, such as fractional precipitation and crystallization, were used to separate rare-earths. Technology and theory aided progress because of the advantages in ion-exchange chromatography in the 20th century.

In 1913 Mosely found that the atomic number of an element could be determined from its X-ray spectrum. Calculations based on that base quickly revealed that all possible rare-earth elements had already been discovered, except one, element 61 [1].

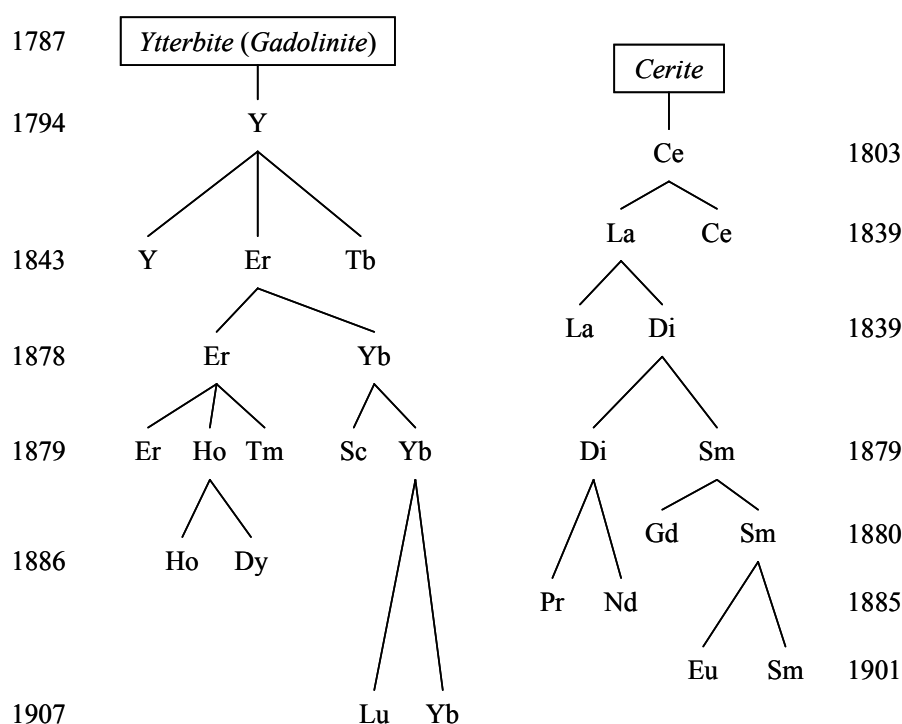


Figure 2.1 – Chronology and dendrology of the isolation of rare-earth elements [1].

The discovery of the last rare-earth element was delayed by the fact that it is an unstable radioactive element that exists naturally on earth in only minutes of quantities. The last element, 61 promethium (Pm) does not occur in nature except in vanishingly small traces as a spontaneous fragment of uranium in uranium ores [2]. It was isolated from the fission products only in 1947 by Marinsky and collaborators [3]. Eleven isotopes ^{141}Pm to ^{151}Pm have now been identified. ^{147}Pm is the longest-lived (2.64 years), and milligram quantities of the pink $^{141}\text{Pm}^{3+}$ salts have been isolated [2].

The lanthanide elements were originally known as “rare-earth” elements from their occurrence in oxides or in old usage earth mixtures. Actually, they are not particularly rare elements. The least abundant, thulium, is as common as bismuth and more common than arsenic, mercury, cadmium or selenium, none of which is usually considered rare [2]. The most abundant, cerium, neodymium and lanthanum, are more common than lead [4]. Along the series, it is observed that the elements with odd atomic numbers (Z) (less stable nuclei) are significantly less abundant and that the “heavy” lanthanides are less abundant than the “light” lanthanides. The abundance of the even Z lanthanides decreases regularly

from Ce to Yb, while the abundance of the odd Z members decreases in parallel fashion from La to Lu.

The aim of this chapter is to represent the basic concepts, crucial to understand the photoluminescence of the lanthanide ions, incorporated in silicates, which will be described in the next chapters.

2.2 Electronic configurations

The lanthanides are strictly the fourteen elements following lanthanum in which the fourteen $4f$ electrons are being consecutively added to the lanthanum configuration. Table 2.1 gives some principal characteristics of the lanthanide atoms and ions.

All neutral lanthanides possess the xenon electronic structure $[\text{Xe}] 1s^2 2s^2 2p^6 3s^2 3p^6 3d^{10} 4s^2 4p^6 4d^{10} 5s^2 5p^6$, with two or three outer electrons ($6s^2$ or $5d6s^2$), and present in the fundamental state the electronic configuration $[\text{Xe}] 4f^{n-1} 5d^1 6s^2$ for Ce, Gd and Lu atoms and $[\text{Xe}] 4f^n 6s^2$ for the rest of elements from the series, where n represents the electrons on the f orbital.

The lanthanides may be ionized by the successive removal of electrons. The first stage of ionization (Ln^+), except for lutetium, results from the removal of a $6s$ -electron. In the second stage of ionization (Ln^{2+}), the removal of a further $6s$ -electron occurs. In the third stage (Ln^{3+}) the two $6s$ -electrons, $5d$ - or $4f$ -electron, have been removed to leave, apart from the xenon structure, a $4f^N$ configuration, where $N=1$ for cerium and increases regularly to $N=14$ for lutetium (Table 2.1). The valence electrons of the lanthanide ions are situated on the $4f$ orbitals, the main difference to the other metal ions [5].

All of the lanthanides form Ln^{3+} ions. Oxidation states other than +3 are known for several lanthanides, although these are always less stable than the characteristic group valence. The existence of the oxidation states +2 and +4 can be correlated with the electronic structures, if we assume that there is a special stability associated with an empty, half-filled or filled f shell. Thus cerium and terbium occur in the +4 state having stable configurations $4f^0$ and $4f^7$ respectively, and europium and ytterbium occur in the +2 state with stable configurations. Although the special stability of $4f^0$, $4f^7$ and $4f^{14}$ may be one factor, there are other thermodynamic and kinetic factors, which are of equal or greater importance in determining the stability of oxidation states.

Table 2.1 – Normal electronic configuration of the neutral lanthanides, the first three stages of ionization and the Ln^{3+} radii.

At. N°	Ln	Ln^0	Ln^+	Ln^{2+}	Ln^{3+}	Radii Ln^{3+}
58	Ce	$4f^1 5d^1 6s^2$ (1G_4)	$4f^1 5d^1 6s^1$ ($^2G_{7/2}$)	$4f^2$ (3H_4)	$4f^1$ ($^2F_{5/2}$)	1.034
59	Pr	$4f^3 6s^2$ ($^4I_{9/2}$)	$4f^3 6s^1$ (5I_4)	$4f^3$ ($^4I_{9/2}$)	$4f^2$ (3H_4)	1.013
60	Nd	$4f^4 6s^2$ (5I_4)	$4f^4 6s^1$ ($^6I_{7/2}$)	$4f^4$ (5I_4)	$4f^3$ ($^4I_{9/2}$)	0.995
61	Pm	$4f^5 6s^2$ ($^6H_{5/2}$)	$4f^5 6s^1$ (7H_2)	$4f^5$ ($^6H_{5/2}$)	$4f^4$ (5I_4)	0.979
62	Sm	$4f^6 6s^2$ (7F_0)	$4f^6 6s^1$ ($^7F_{1/2}$)	$4f^6$ (7F_0)	$4f^5$ ($^6H_{5/2}$)	0.964
63	Eu	$4f^7 6s^2$ ($^8S_{7/2}$)	$4f^7 6s^1$ (9S_4)	$4f^7$ ($^8S_{7/2}$)	$4f^6$ (7F_0)	0.950
64	Gd	$4f^7 5d^1 6s^2$ (9D_2)	$4f^7 5d^1 6s^1$ ($^{10}D_{5/2}$)	$4f^7 5d^1$ (9D_2)	$4f^7$ ($^8S_{7/2}$)	0.938
65	Tb	$4f^9 6s^2$ ($^6H_{15/2}$)	$4f^9 6s^1$ (7H_8)	$4f^9$ ($^6H_{15/2}$)	$4f^8$ (7F_6)	0.923
66	Dy	$4f^{10} 6s^2$ (5I_8)	$4f^{10} 6s^1$ ($^5I_{17/2}$)	$4f^{10}$ (5I_8)	$4f^9$ ($^6H_{15/2}$)	0.908
67	Ho	$4f^{11} 6s^2$ ($^4I_{15/2}$)	$4f^{11} 6s^1$ (5I_8)	$4f^{11}$ ($^6I_{15/2}$)	$4f^{10}$ (5I_8)	0.894
68	Er	$4f^{12} 6s^2$ (3H_6)	$4f^{12} 6s^1$ ($^4H_{13/2}$)	$4f^{12}$ (3H_6)	$4f^{11}$ ($^4I_{15/2}$)	0.881
69	Tm	$4f^{13} 6s^2$ ($^2F_{7/2}$)	$4f^{13} 6s^1$ (3F_4)	$4f^{13}$ ($^2F_{7/2}$)	$4f^{12}$ (3H_6)	0.869
70	Yb	$4f^{14} 6s^2$ (1S_0)	$4f^{14} 6s^1$ ($^2S_{1/2}$)	$4f^{14}$ (1S_0)	$4f^{13}$ ($^2F_{7/2}$)	0.858
71	Lu	$4f^{14} 5d^1 6s^2$ ($^2D_{3/2}$)	$4f^{14} 6s^2$ (1S_0)	$4f^{14} 6s^1$ ($^1S_{1/2}$)	$4f^{14}$ (1S_0)	0.848

The lanthanide contraction consists of a significant and steady decrease in the size of the atoms and ions increasing the atomic number (Table 2.1). The cause of this contraction is the imperfect shielding of one electron by another in the same subshell [6]. The shielding of one $4f$ electron by another is quite imperfect owing to the shapes of the orbitals.

An absorption spectrum of a lanthanide ion in a solid or in a solution reveals fine lines of the respective inter- $4f$ transitions. These appear due to the $4f$ -shell, which is deeply imbedded inside the external $5s$ and $5p$ shells and is relatively unaffected by the $6s$ -electrons as shown in Figure 2.2. The example is for Gd^{3+} , which has two $6s$ electrons added to the trivalent ion. The figure applies, with only small changes, to all the rare-earth ions and indicates that the $4f$ orbitals are indeed inner orbits. In contrast with the fine $4f^n \rightarrow 4f^n$ transition lines the experimental measurements on $4f^n \rightarrow 4f^{n-1} 5d$ transitions of the lanthanides usually result in wide bands.

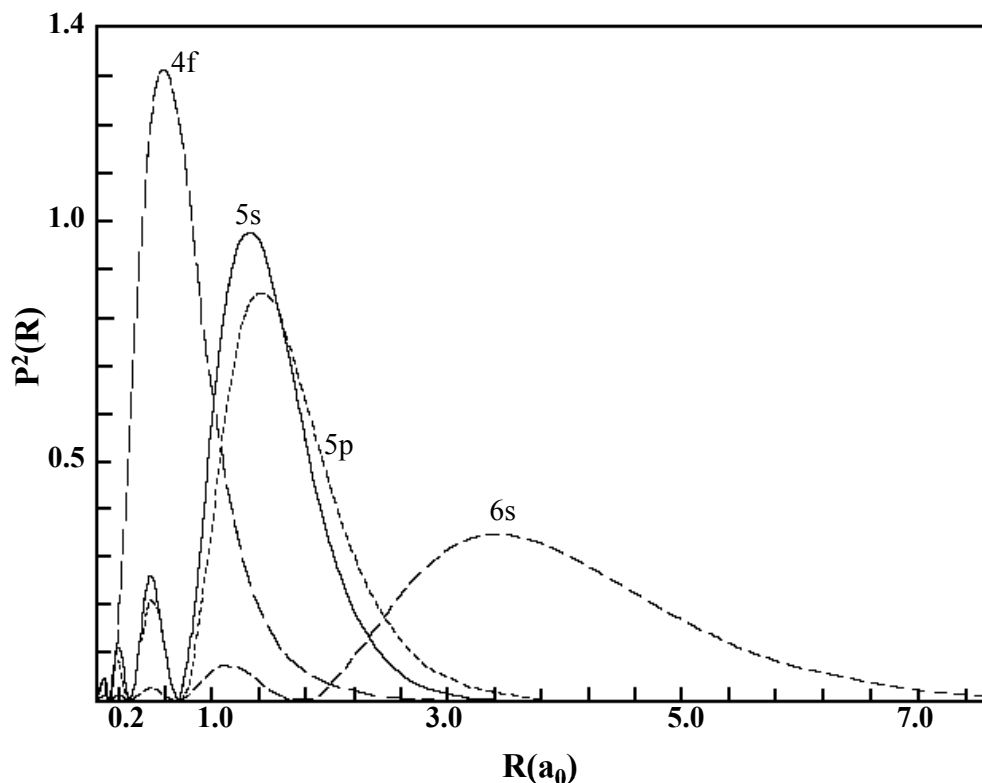


Figure 2.2 – Radial charge distribution $P^2(R)$ as a function of R for the $4f$, $5s$, $5p$, and $6s$ orbitals of Gd^+ [7].

The degeneracy of a configuration may be thought of as the number of different ways to arrange the N electrons in the orbitals, taking the spin into account. If the ions are perfectly isolated from any interaction, the degeneracy of the electronic configuration is given by:

$$\frac{(4l+2)!}{N!(4l+2-N)!} \quad (2.1)$$

where l is the quantum number associated with the angular momentum of each electron and N the number of electrons in the subshell. In this way, for $Eu^{3+} 4f^6$ ($l=3$, $N=6$) configuration the degeneracy of the ground electronic configuration amounts to 3003 and for $Er^{3+} 4f^{11}$ ($l=3$, $N=11$) equals 364.

2.3 The Hamiltonian for the free ion

The Hamiltonian for the rare-earth free ion H_{FI} is composed by one part due to the central field, H_O , and several other interactions which are in general treated as perturbations. Among these interactions the interelectronic repulsion, H_C , and the spin-orbit interaction, H_{SO} , are the most relevant [8].

$$H_{FI} = H_O + H_C + H_{SO} \quad (2.2)$$

The magnitudes of these interactions follow the order $H_O > H_C > H_{SO}$.

In the diagonalization procedure of the Hamiltonian H_{FI} the spin-spin, spin-orbit and orbit-orbit interactions are in general of much less importance. Thus, in a first step, the eigenfunctions of H_{FI} may be constructed from the eigenfunctions of the angular momentum operators L^2 , S^2 and J^2 where:

L = total orbital angular momentum

S = total spin angular momentum

J = total angular momentum

J_z = the z component of J

with $L = \sum_i \ell_i$ and $S = \sum_i s_i$, ℓ and s being mono-electronic orbital and spin angular momentum, respectively. The quantum number J must satisfy the condition $|L - S| \leq J \leq L + S$.

It is shown that L , S , J and M_J quantum numbers are not enough to classify each eigenstate of energy individually and to obtain several multiplets described with the same values of L and S . For rare-earth ions an adequate scheme to represent the basis of eigenfunctions is the well-known L - S coupling scheme $| (4f^N) \alpha SLJM_J \rangle$. This notation implies that these eigenstates are pure $4f^N$ states, or, in other words, no configuration interaction (CI) via H_{FI} is taken into account. It is justified the introduction of additional quantum numbers, represented as α which allow to classify each eigenstate individually [9].

The usual form of H_{FI} is:

$$H_{FI} = E_b(4f^N) + \sum_{k=0,1,2,3} E^k e_k + \zeta_{4f} \sum_i \vec{\ell}_i \cdot \vec{s}_i + CI \quad (2.3)$$

where E_b is the energy of the baricenter of the $4f^N$ configuration (eigenvalue of the central field Hamiltonian). The second and third terms on the right-hand-side of this expression correspond to the interelectronic repulsion and spin-orbit interaction, respectively. The last term contains configuration interaction effects.

The term H_C does not act on the spin, because it has origin in an electrostatic interaction and it splits the configurations in $(2S+1)(2L+1)$ spectroscopic terms ^{2S+1}L . The spin-orbit interaction (H_{SO}) further splits these terms into $^{2S+1}L_J$ in spectroscopic levels, with $|L - S| \leq J \leq L + S$. The ground states are given by the Hund's rules:

- 1) The term with highest spin multiplicity ($2S_{max} + 1$) is the lowest in energy.
- 2) If there are several terms with the same ($2S_{max} + 1$) multiplicity, that of higher degeneracy (L_{max}) is lowest in energy.
- 3) The level lowest in energy has the lowest J -value, if the sub-shell is less than half filled, and the highest J -value if the sub-shell is more than half-filled.

For a free atom or ion, spherical symmetry exists, and each level is $(2J+1)$ fold degenerated. On placing the ion in a crystal, the spherical symmetry is destroyed and each level splits under the influence of the electric field produced by the local environment.

2.4 The ions in a chemical environment

Even though weak, the interaction between $4f$ electrons and the chemical environment is responsible for the most interesting spectroscopic features of rare-earth ions. The non-spherical even parity part of this interaction, responsible for the Stark splitting of $4f$ levels, is commonly written as

$$H_{LF} = \sum_{k,q,i} B_q^k C_q^{(k)}(i) \quad (2.4)$$

where the B_q^k 's ($k = 2, 4$ and 6) are the so-called ligand field parameters of even rank and $C^{(k)}$ is a Racah tensor operator of rank k . The values of k are restricted by parity and triangularity rules for f orbitals [5]. The allowed values of q depend on the symmetry of the ligand field around the rare-earth ion, and in this expression the index i runs over the $4f$ electrons. B_q^k 's are phenomenological parameters. The total Hamiltonian to be diagonalized is

$$H = H_{FI} + H_{LF} \quad (2.5)$$

The ligand field interaction is also of fundamental importance in the case of $4f - 4f$ transition intensities. These transitions are in principle electric dipole forbidden by Laporte's rule (states with the same parity). However, provided the site occupied by the rare-earth ion does not present a center of inversion, Laporte's rule is relaxed due to odd parity terms in the ligand field Hamiltonian. The more general form of H_{LF} is

$$H_{LF} = H_{LF}(\text{even}) + H_{LF}(\text{odd}) \quad (2.6)$$

It is important to note that if the diagonalization of the total Hamiltonian H in equation (2.5) is restricted to a basis formed by the states $| (4f^N) \alpha SLJM_J \rangle$, due to parity selection rules the component $H_{LF}(\text{odd})$ will have no effect on the final results. This odd component is in general expressed as

$$H_{LF}(\text{odd}) = \sum_{t,p,i} \gamma_p^t r_i^t C_p^{(t)}(i) \quad (2.7)$$

where r_i is the radial coordinate of the i -th electron and the γ_p^t 's ($t = 1, 3, 5$ and 7) are the so-called odd-rank ligand-field parameters. The values of t are restricted by parity and triangularity rules involving f , d and g orbitals. The index i , in principle, runs over all electrons of the rare-earth ion. As for the values of q in equation (2.4), the allowed values of p depend on the symmetry around the rare-earth ion. It follows that transitions between $4f$ levels become partially electric-dipole allowed.

The maximum number of observed energy levels or Stark sublevels due to the local field effect, depend on the point group of symmetry of the ion in the host, as it can be seen in the Table 2.2 [5,9,10]. Analyzing this table it is verified that the number of split components increases with the decrease of the degree of symmetry of the ion in the host.

Table 2.2 – The number of energy J -sublevels for the 32 point symmetry groups^a versus the quantum number J (J integer or semi-integer).

Crystallographic System	J									
	0	1	2	3	4	5	6	7	8	
(J integer)										
Cubic	1	1	2	3	4	4	6	6	7	
Hexagonal and Trigonal	1	2	3	5	6	7	9	10	11	
Tetragonal	1	2	4	5	7	8	10	11	13	
Triclinic, Monoclinic and Orthorhombic	1	3	5	7	9	11	13	15	17	

(J semi-integer)	1/2	3/2	5/2	7/2	9/2	11/2	13/2	15/2
Cubic	1	1	2	3	3	4	5	5
All other symmetries	1	2	3	4	5	6	7	8

^a Cubic System: O_h , O , T_d , T_h , and T ; Hexagonal System: D_{6h} , D_6 , C_{6v} , C_{6h} , C_6 , D_{3h} and C_{3h} ; Tetragonal System: D_{4h} , D_4 , C_{4v} , C_{4h} , C_4 , D_{2d} and S_4 ; Trigonal System: D_{3d} , D_3 , C_{3v} , S_6 and C_3 ; Orthorhombic System: D_{2h} , D_2 and C_{2v} ; Monoclinic System: C_{2h} , C_2 and C_s (or C_{1h}) and Triclinic System: S_2 (or C_i) and C_1 .

Figure 2.3 presents an illustrative outline of the order of magnitude of the energies involved in the splitting of a given configuration, in this case $4f^6$ of the Eu^{3+} ion.

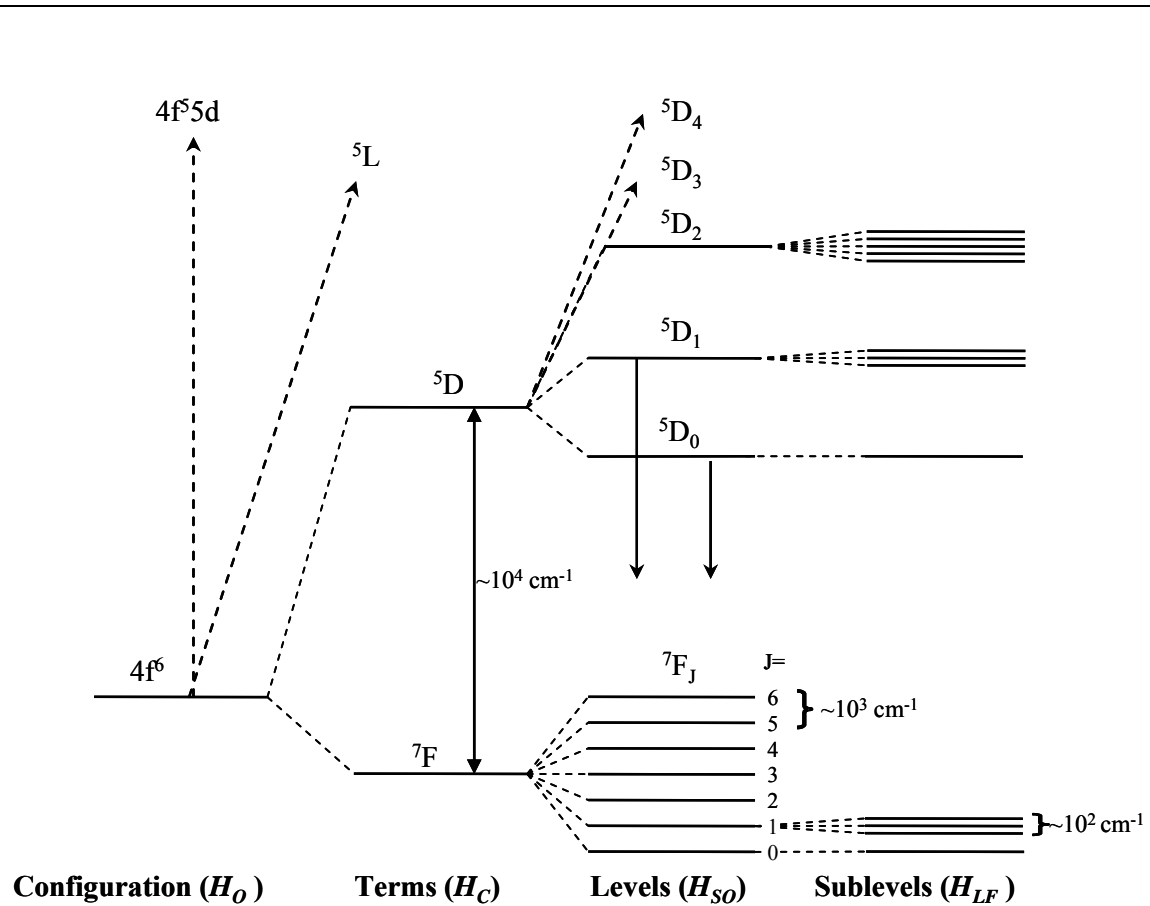


Figure 2.3 – Partial energy diagram for Eu^{3+} ion, presenting the approximate values of the energies associated to different Hamiltonians, which influences the $4f^6$ configuration. Downward arrow indicates the most luminescent excited state [11].

The rare-earth ions are characterized by an incomplete filled $4f$ shell. The $4f$ orbital lies inside the ion and is shielded from the surroundings by the filled $5s^2$ and $5p^6$ orbitals. Therefore, the influence of the host lattice on the optical transitions within the $4f^n$ configuration is small (but essential). Figure 2.4 represents a substantial part of the energy levels originating from the $4f^n$ configuration as a function of n for the trivalent lanthanide ions when they are in crystal network in this case LnF_3 [12].

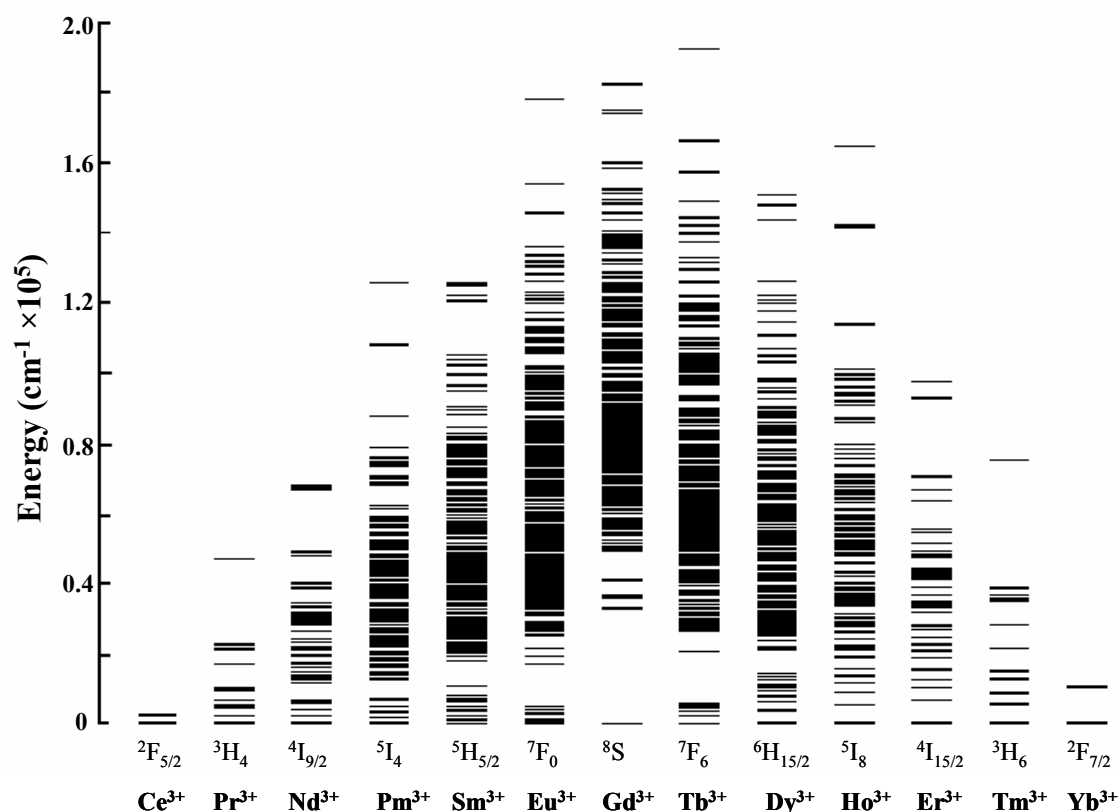


Figure 2.4 – Energy levels of the $4f^n$ configurations of the trivalent lanthanide ions in crystals of LnF_3 , representing the fundamental level of each ion [12].

2.5 $4f^n \rightarrow 4f^n$ transitions

The intra- $4f^n$ ($4f^n \rightarrow 4f^n$) transitions may be electric dipole (ED) or magnetic dipole (MD) by nature. The electric dipole transitions are forbidden among states of the same configuration and, thus, can only occur among states with opposite parity (Laporte's selection rule) [9]. That selection rule forbids transitions among orbitals having the same symmetry properties towards an inversion center (parity); thus p - p , d - d , and f - f are not allowed. In spite of that, the electric-dipole transitions dominate the spectra of the lanthanide ions.

In 1937 Van Vleck explained the predominant observation of dipolar electric transitions in the lanthanide ions. He verified that the odd parity part of the field can mix $4f$ states, making possible these type of transitions [13]. The interaction with the ligand-field

or with vibrational states mixes electronic states of different parity into the $4f$ wavefunctions. Moreover, the interaction with the ligand-field tensor operator mixes electronic states with different J but same S and L . This is the so-called J -mixing [14]. This admixture makes the transitions possible and explains the low intensity of the f - f transitions. The transitions between these modified states are called forced (or induced) electric dipole transitions.

The intensity of a spectral line associated to a certain transition between two levels depends on the transition probability between those levels. That probability is proportional to the square of the matrix element $\langle \alpha SLJM_J | \vec{\theta} | \alpha' SLM'_J \rangle$, where $\vec{\theta}$ may be \vec{P}_{ED} (dipolar electric) or \vec{P}_{MD} (dipolar magnetic) operator. \vec{P}_{ED} is defined as

$$\vec{P}_{ED} = -e \sum_i \vec{r}_i \quad (2.8)$$

where e it is the charge of the electron and \vec{r}_i represents the vector position of the $4f$ electrons.

The operator \vec{P}_{ED} has odd parity

$$\vec{P}_{ED} = -e \sum_i \vec{r}_i = e \sum_i (-\vec{r}_i) \quad (2.9)$$

which implies that the transition probability among states is not null only if they have opposite parity. If the functions that characterize the states have the same parity, the resultant product is a function of even parity, which associated to the parity of the electric dipolar operator, originates a function of odd parity. As the integral, extended to all space, of an odd function is null, the transitions have only non-null probability, if the states between which the transitions occur have opposite parity. Only in this case the resultant product is a function of even parity, which makes the probability non-null for the respective transition. In this way, the dipolar electric transitions may not happen among states with the same configuration.

The selection rules for the forced dipolar electric transitions [15] are different from the ones applicable to the free ion and they can be expressed in the following way: $\Delta l = \pm 1$;

$\Delta S=0$ is not applicable because of the spin-orbit interaction; $\Delta L \leq 6$ is valid until J is a "good" quantum number (until unequivocally distinguish all of the states) and $\Delta J \leq 6$ with the transition $J=0 \rightarrow J'=0$ forbidden and $\Delta J=2, 4, 6$ if one level has $J=0$, e.g. the ${}^5D_0 \rightarrow {}^7F_J$ transitions in Eu^{3+} [15].

Some transitions have an intensity which is more sensitive to the chemical environment than normal $f \rightarrow f$ transitions. They are referred to as hypersensitive transitions and, with possible exceptions they follow the selection rules $\Delta J \leq 2$, $\Delta L \leq 2$, and some $\Delta S=0$. Typical examples are ${}^5D_2 \rightarrow {}^7F_0$ and ${}^5D_0 \rightarrow {}^7F_2$ for Eu^{3+} [15].

The magnetic dipole transitions are allowed by the parity rule. They can occur among states with the same parity, because the magnetic dipole operator has even parity [5,9,10,15].

$$\vec{P}_{MD} = -\left(\frac{e\hbar}{2mc}\right)(\vec{L} + 2\vec{S}) \quad (2.10)$$

The magnetic-dipole transitions have extremely low oscillator strength in the range 10^{-9} to 10^{-7} . The selection rules for these transitions are: $\Delta l=0$, $\Delta S=0$ and $\Delta L \leq 0$, valid until J is considered as a "good" quantum number and $\Delta J \leq 0, \pm 1$ with $J=0 \rightarrow J'=0$ forbidden.

The intensity of a magnetic-dipole transition is relatively insensitive to the environment of the Ln^{3+} ion, so that it may be used as internal standard to avoid the difficult experimental measurement of absolute emission intensities. A typical example of such a transition is ${}^5D_0 \rightarrow {}^7F_1$ (or ${}^5D_1 \rightarrow {}^7F_0$) in Eu^{3+} compounds [15]. The difference between electric and magnetic transitions is not always obvious. Due to the mixing of wavefunctions, some transitions exhibit both characteristics. Experimentally, it is possible to distinguish between electric and magnetic-dipole transitions by performing experiments on single crystals in absence and in the presence of a magnetic field, and taking polarization into account [9].

2.6 $4f^n \rightarrow 4f^{n-1}5d$ (fd) transitions

The lack of research on fd transitions is partly caused by the fact that they lie generally in the UV and vacuum ultraviolet (VUV) regions, making them experimentally

less accessible. In addition, since the lanthanide $5d$ orbitals are much more extended than the $4f$ orbitals, most of the intensity is in vibronic bands, making the spectra more difficult to analyze.

The transitions $4f^n \rightarrow 4f^{n-1}5d$ (fd) are inter-configurational and thus, they are parity-allowed [16]. These transitions are observed at relatively low energies for the divalent lanthanide ions (Sm^{2+} , Eu^{2+} and Yb^{2+}) and for some of the trivalent lanthanide ions (Ce^{3+} and Tb^{3+}). For the remaining Ln^{3+} ions the fd transitions are located generally in the vacuum ultraviolet spectral region VUV (wavelengths lower than 200 nm) [16]. Because the $5d$ and $4f$ orbitals are not protected, the local environment effect of the ion, such as the nature of the ligands, is substantial and has a strong influence on the position of the lower energy fd band. For the heavy lanthanide ions ($4f^n$, $n > 7$), fd spin-forbidden bands were observed on the emission and excitation spectra, besides the fd spin-allowed bands, which are observable for all lanthanides [17]. The occurrence of both types of transitions, spin-allowed and spin-forbidden, for heavy lanthanide ions is schematically explained in Figure 2.5 illustrated by Tb^{3+} ($4f^8$). In the ground state (GS) of the configuration $4f^8$, the maximum number of unpaired electrons is 6, which results in a total spin quantum number $S=3$ and therefore, a spin multiplicity $2S+1=7$. When an electron is promoted from $4f$ to the $5d$ shell two possibilities exist: a) The electron can orientate his spin antiparallel with the 7 remaining $4f$ electrons; this creates an excited state of low-spin (LS) $4f^75d$, with total spin and spin multiplicity the same as for the ground state ($S=3$ and $2S+1=7$) and illustrates a spin-allowed transition; b) If the electron orientates his spin parallel with the 7 remaining $4f$ electrons this gives rise to a high-spin state (HS) with $S=4$ and a spin multiplicity $2S+1=9$ and illustrates spin-forbidden transition. The fd transitions of high- and low-spin are more easily detected in the excitation spectra. According to Hund's rule, the high-spin state will be lower in energy. As a consequence of that rule the transition from the ground state to the lowest $4f^75d$ will be spin-forbidden ($\Delta S \neq 0$) and relatively weak compared to the high-energy $f-d$ excitations, which are spin-allowed.

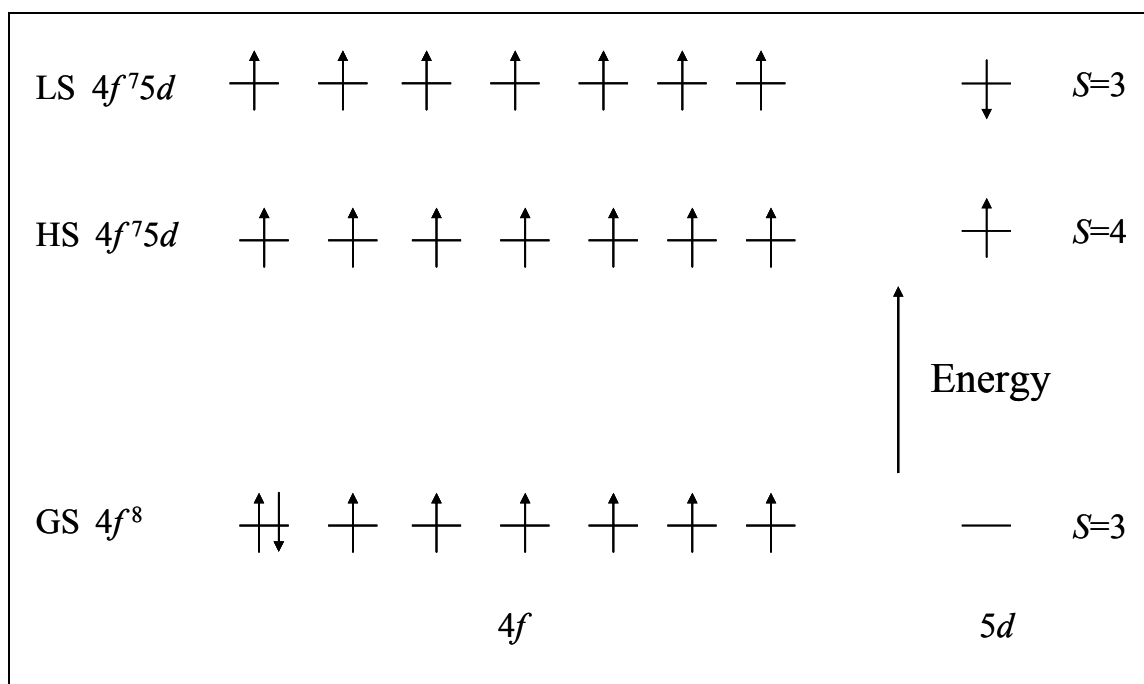


Figure 2.5 – Schematic representation of the electronic configuration for the ground state, the lowest-energetic high-spin $4f^7 5d$ state and the higher-energetic low-spin $4f^7 5d$ state for Tb^{3+} . Adapted from [18].

Besides the transitions discussed previously it is still possible to observe, quadrupolar electric and energy transfer transitions. The charge-transfer bands occur, for instance, in systems where the lanthanide ions are in oxidation state +2 (Sm^{2+} , Eu^{2+} , Tm^{2+} and Yb^{2+}) or +4 (Ce^{4+}) and the ligands are easily oxidized [5,9,11].

2.7 Lifetimes

The relaxation of an excited state may occur by radiative or nonradiative processes. The radiative decay processes occur as direct electronic transition from a higher energy level to a lower energy level by emission of photon. On the other hand, the nonradiative decay processes occur, mainly, through vibrational transitions or multiphonon processes. If the excited ion is in solution, it loses vibrational energy in collision with the molecules of the solvent. If it is in a solid, the vibrational energy is lost by exchange with the vibrational modes of the host. The emission is an exponential decay of the excited state population,

$$N(t) = N_0 e^{-\frac{t}{\tau}} \quad (2.11)$$

N_0 represents the number of excited ions in $t = 0$ and τ the lifetime of the excited state (the time to reduce the intensity to $1/e$). In luminescence experiments we do not observe the number of excited ions, but rather luminescence intensity, which is proportional to $N(t)$. The time dependent luminescence intensity $I(t)$, associated to the decay of N ions situated in the excited state to the fundamental state for a single exponential decay, is

$$I(t) = I_0 e^{-\frac{t}{\tau}} \quad (2.12)$$

where I_0 is the intensity at time $t = 0$. If only radiative and nonradiative mechanisms are considered in the depopulation of the state, the lifetime τ is the inverse of the total decay rate,

$$\tau = (k_r + k_{nr})^{-1} \quad (2.13)$$

where k_r and k_{nr} are, respectively, the radiative and nonradiative probabilities.

The time dependent intensity is measured following the excitation pulse, and the decay time τ is calculated from the slope of a plot of $\log I(t)$ versus t , or from the time at which the intensity decreases to $1/e$ of the intensity at $t = 0$. This expression is only valid if the excited state has been populated for a period of time much smaller than the decay time [19].

In time-resolved spectroscopy, excitation occurs via a pulsed lamp (or laser) and a time delay is applied before measurement. In this way, the short lived background luminescence is allowed to fade off before measuring the long-lived metal-centered luminescence, which ensures a better signal-to noise ratio (Figure 2.6). Very high sensitivity within a few minutes can be achieved.

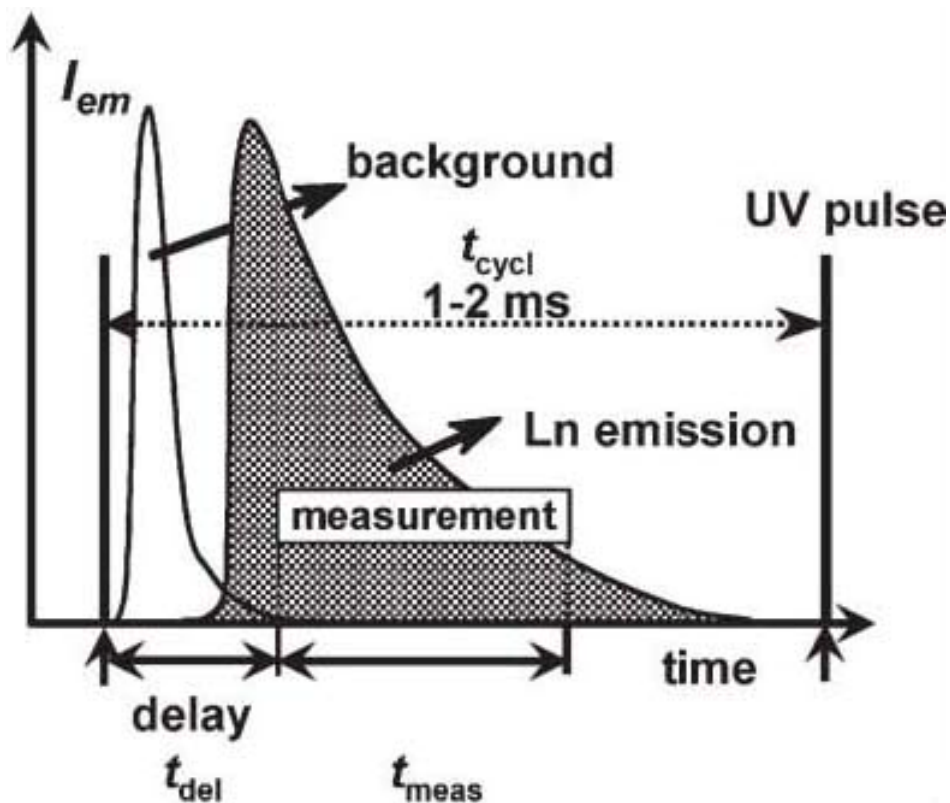


Figure 2.6 – Principles of time-resolved spectroscopy [20].

The quantum efficiency η of a certain energy state can be defined as

$$\eta = \frac{k_r}{k_r + k_{nr}} \quad (2.14)$$

2.8 Energy transfer

One of the possible ways for an ion or molecule in the excited state to return to the ground state is to transfer the excess of energy to neighboring ions or molecules in a radiative or nonradiative way. Another possibility to return to the ground state is by transfer of the excitation energy from the excited centre (D^*) to another centre (A). We denote D as donor (sensitizer) and A as acceptor (activator). $D^* + A \rightarrow D + A^*$ (Figure 2.7).

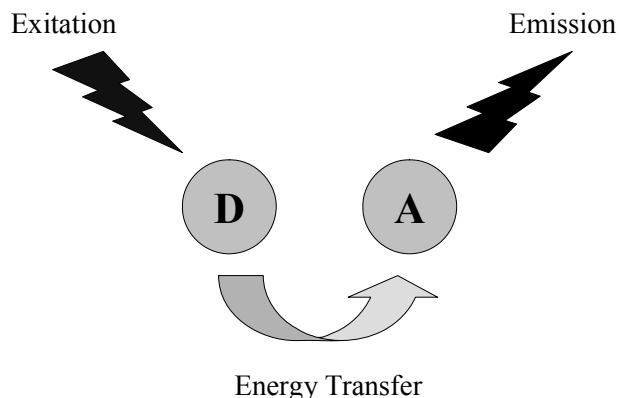


Figure 2.7 – Energy transfer from a donor to an acceptor.

The energy level schemes are also given in Figure 2.8. An asterisk indicates the excited state. The donor and acceptor are separated by a distance R . If D is in the excited state and A in the ground state, the relaxed excited state of D may transfer its energy to A. Energy transfer can only occur if the energy differences between the ground- and excited states of D and A are equal (resonance condition) and if a suitable interaction H_{DA} between both centers exists. The interaction between luminescence centers may be: a) between two different centers, or b) between identical centers (concentration quenching) [21].

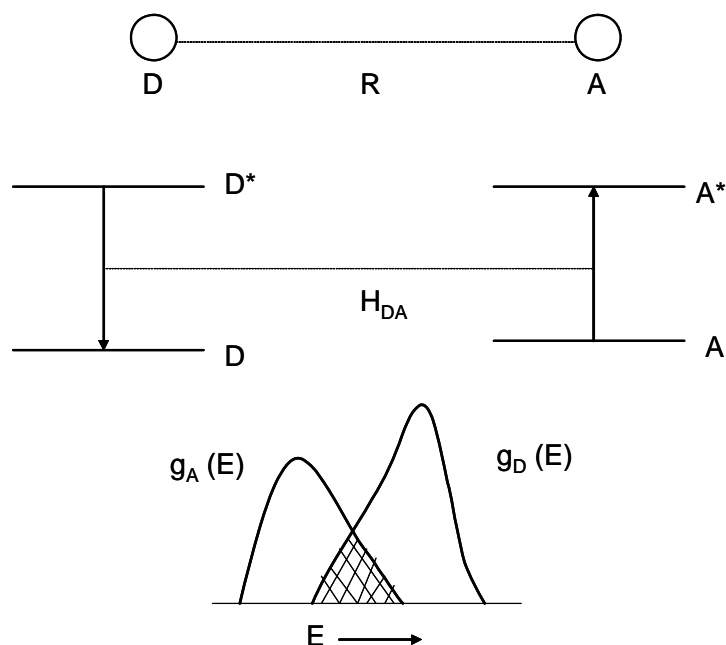


Figure 2.8 – Energy transfer between centers D and A. The two centers are at a distance R (top). The energy level schemes and the interaction H_{DA} are given in the middle. The spectral overlap is illustrated at the bottom (hatched part) [21].

The transfer between the donor and the acceptor may be radiative or nonradiative [22-24]. Radiative energy transfer is indicated by the dips in the emission peak of the donor corresponding to the f - f absorption lines of the acceptor. In most cases, the radiative energy transfer mechanism is unimportant, especially for rare-earth ions, which typically have very low absorption coefficients (<10).

Two models: Förster's [25,26] and Dexter's [27] describe the nonradiative energy transfers that occur between a donor and an acceptor. The interaction between the donor and acceptor may be: a) an electron exchange interaction and b) a direct through-space multipolar interaction (dipole-dipole, dipole-quadrupole or quadrupole-quadrupole). In practice, the resonance condition can be tested by considering the spectral overlap of the D emission and the A absorption spectra (Figure 2.8). Förster first developed an approach based on electric dipole-dipole interaction [25,26], which was later extended by Dexter [27] to include higher-order multipolar and exchange interactions.

The Dexter transfer was firstly described in inorganic solids where a resonant transfer can be obtained between an allowed transition in the donor and a forbidden transition in the acceptor. In such cases, an acceptor which does not normally respond to a given pumping radiation spectrum can be made to luminescence after energy transfer from the donor. A double electron transfer occurs between the donor and the acceptor.

According to the theory of energy transfer developed by Dexter [22,23,27], the energy transfer process through multipolar interaction depends on the extent of overlap of the emission spectrum of the donor with the absorption spectrum of the acceptor, the relative orientation of interacting dipoles and the distance between the donor and the acceptor. Considering the dipole-dipole interaction, the energy transfer probability P_{DA} (in s^{-1}) from a donor to an acceptor is given by the following formula:

$$P_{DA}(dd) = \frac{3.024 \times 10^{12} f_a}{R^6 \tau_D} \int \frac{f_D(E) F_A(E)}{E^4} dE, \quad (2.15)$$

Here f_a is the oscillator strength of the involved absorption transition of the acceptor, τ_D is the radiative decay time of the donor (in s), R is the donor-acceptor average distance (in Å), $f_D(E)$ represents the normalized emission line shape function of the donor and $F_A(E)$

the normalized absorption line shape function of the acceptor, and E is the energy involved in the transfer (in eV).

The critical distance (R_C) of energy transfer from the donor to the acceptor is defined as the distance for which the probability of transfer equals the probability of radiative emission of the donor, *i.e.* the distance for which $P_{DA}\tau_D = 1$. Therefore, R_C can be obtained from

$$R_C^6 = 3.024 \times 10^{12} f_a \int \frac{f_D(E)F_A(E)}{E^4} dE, \quad (2.16)$$

The main difference between the Dexter's and Förster's models is the distance over which these interactions can occur [28] (Figure 2.9). The Dexter mechanism operates efficiently over very short distances ($<10 \text{ \AA}$) - since orbital overlap is needed-, whereas in the Förster mechanism the transfer has been reported to occur over much longer distances and is strongly dependent on the spectral overlap of the emission spectrum of the donor and the absorption spectrum of the acceptor. In Dexter's model, the interaction strength decreases exponentially $\exp(-2R/L)$ as a function of distance (L is the van der Waals or Bohr radii and depends on the system under consideration), whereas in Förster's model, it decreases as R^{-n} ($n=6, 8, \dots$) (n is the order of interaction). This means that energy transfer rate for the electron-exchange mechanism drops to negligibly small values (relative to the donor lifetime) as the distance R between the donor and the acceptor increases, which makes the Dexter energy transfer insignificant beyond $R=10 \text{ \AA}$ between the donor and the acceptor.

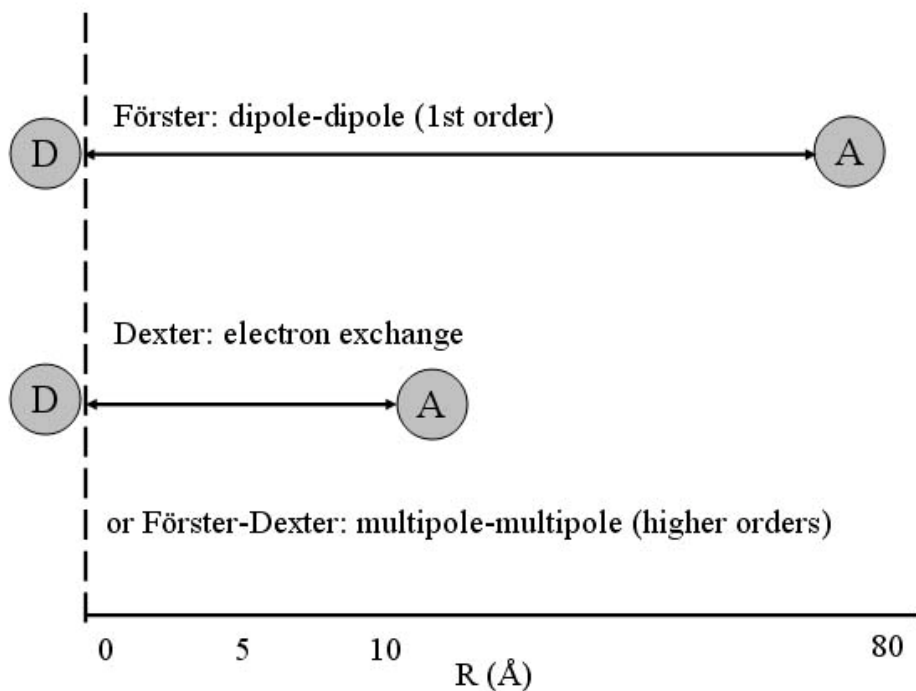


Figure 2.9 – Ranges of interaction in Förster's and Dexter's models [28].

Only for some specific cases the interaction type is known. The intensity of the optical transitions determines the strength of the electric multipolar interaction. High transfer rates can only be expected if the optical transitions involved are allowed electric-dipole transitions. If the absorption strength vanishes, the transfer rate for electric-multipolar interaction vanishes too. However, the overall transfer rate does not necessarily vanish, because there may be contributions by exchange interaction. The transfer rate due to exchange interaction depends on wave function overlap (and of course, spectral overlap), but not on the spectral properties of the transitions involved [21].

If the optical transitions of D and A are allowed electric-dipole transitions with a considerable spectral overlap, R_C may be some 30 Å. If these transitions are forbidden, we need exchange interaction for the transfer to occur. This restricts the value of R_C to some 5 - 8 Å [21].

A simple operational definition of the energy transfer probability between the donor and the acceptor ($P_{d \rightarrow a}$), in terms of lifetimes, is given by [22,24]:

$$P_{d \rightarrow a} = \frac{1}{\tau} - \frac{1}{\tau_0} \quad (2.17)$$

where τ and τ_0 represent the lifetimes of the donor in the presence and absence of acceptor, respectively. The energy transfer efficiency ($E_{d \rightarrow a}$) is defined as [22,24]:

$$E_{d \rightarrow a} = 1 - \frac{\tau}{\tau_0} \quad (2.18)$$

2.9 Applications

The industrial application of the lanthanides began in 1891 with the use of the incandescent mantle, composed by 99 % thorium and 1 % cerium, developed by Carl Auer von Welsbach [29]. Since then, thanks to the separation industry, it is possible to obtain the lanthanides with high purity and controlled morphology and reactivity, which further develops several industrial applications. In these technologically advanced applications the chemical and physical properties of lanthanides are used.

In quantitative terms the main lanthanide applications are in the ceramic and glass industry, metallurgy, heterogeneous catalysis and in magnetic devices. These applications together are more than 90 % of the total amount of lanthanide consumption, mainly in the form of mixtures of oxides or alloys composed of several lanthanides. The lanthanides are used in the traditional glass and ceramics industry as polishing, discoloring, and coloring agents for glass and as coloring agents for glasses for ceramics and in the preparation of glasses and optical lenses [29]. In the chemical industry the use is as drying agents in paints, as auxiliaries in synthetic ammonia, synthetic rubber and plastics, and as catalyst for exhaust gas purification.

One of the most important applications of lanthanides in the high-technology field is in lightning and displays [21]. Ln-containing materials emit over the entire spectral range: near infrared (Nd^{3+} , Er^{3+}), red (Eu^{3+} , Pr^{3+} , Sm^{3+}), green (Er^{3+} , Tb^{3+}), and blue (Tm^{3+} , Ce^{3+}) [30]. Lanthanide-doped materials are of great interest for a wide range of devices, such as fluorescent lamps, cathode ray tubes, projection televisions, fluorescent tubes and X-ray detectors, tunable (UV and visible) lasers, light-emitting diodes, low-energy scintillators, amplifiers for optical communications, and optical storage [21,30].

Low- pressure mercury discharge lamps, also known as luminescent, fluorescent or energy-saving lamps have penetrated the market to an impressive degree [21,30]. A luminescent lamp is filled with a noble gas at a pressure of 400 Pa, containing a small amount of mercury (ca. 0.8 Pa). In the discharge the mercury atoms are excited (indicated as Hg^* in Figure 2.10). Returning to the ground state, they emit (mainly) ultraviolet radiation. About 85 % of the emitted radiation is at 254 nm and 12 % at 185 nm. The remaining 3 % is found in the longer wavelength ultraviolet and visible region (365, 405, 436 and 546nm). The lamp phosphor (luminescent powder) is composed of narrow band emitters and converts the 254 and 185 nm radiation into visible light (Figure 2.11). The white light emission in these lamps is based on the tricolor concept with emission at 450, 550 and 610 nm which is achieved by narrow band emitters like Eu^{2+} , Tb^{3+} and Eu^{3+} .

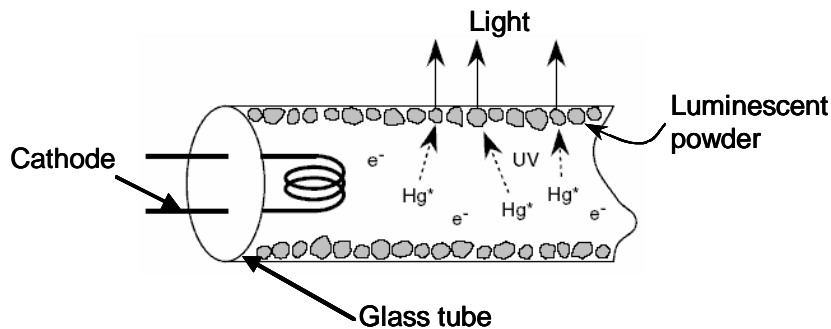


Figure 2.10 – Schematic diagram of a fluorescent lamp illustrating the light generation process [21].

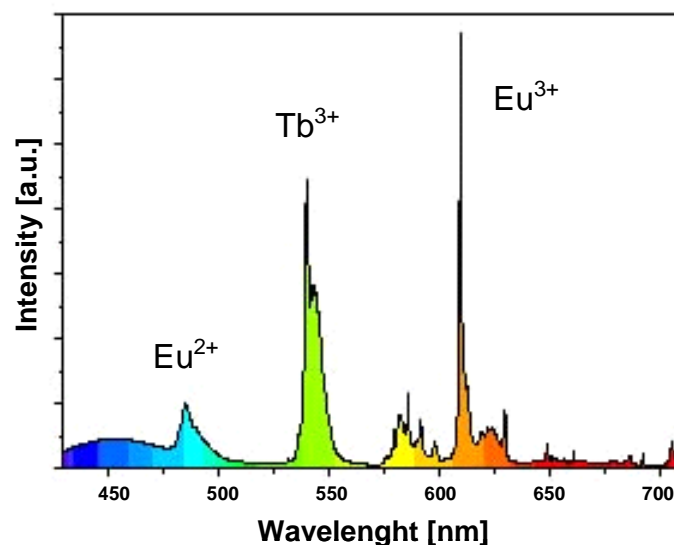


Figure 2.11 – Emission spectrum of a tricolor fluorescent lamp (CHINT®) excited at 254 nm [31].

Another field where lanthanides are applied is in integrated-optic waveguide amplifiers. The silica-on silicon format for integrated optics is favored for a variety of functions in optical communication systems. Fabrication technologies based on flame hydrolysis deposition (FHD) [32] and plasma-enhanced chemical vapor deposition (PECVD) [33] are now highly developed. Different fabrication routes, such as radio-frequency (RF) sputtering and sol-gel techniques, are also reported [34-36]. Another application is in fiber amplifiers for wavelength division multiplexing (WDM) network systems. Since silica-based transmission fibers have a wide window from 1.4 to 1.7 μm , amplification of all these ranges is essential for a broad WDM network. Currently, a gain band of 1530–1600 nm is realized by development of an erbium doped fiber amplifier [37,38]. Thulium doped optical fiber amplifiers, taking advantage of its $^3\text{H}_4 \rightarrow ^3\text{H}_6$ transition at 1460 nm have also been made [39,40].

An organic medium incorporating Ln^{3+} complexes is expected to facilitate the development of photonic devices such as luminescent polymers, electro-luminescence devices, and plastic thin-film lasers [41]. Amplified spontaneous emission of Nd^{3+} using their ideal 4 level $f-f$ transition can lead to the development of amplification of signals in plastic fibers and high-power laser materials. In particular, the Nd^{3+} -doped luminescent polymer systems are expected to open up some new optical fields, especially, telecommunication networks and novel laser materials. However, the organic Nd^{3+} systems are not suitable for plastic optical fibers (POF) in near-IR telecommunications, since conventional organic compounds have strong absorption in the near-IR range.

Lanthanide complexes show characteristic luminescence with narrow emission bands and long emission lifetimes, which allow them to be suited to sensing devices: physical and biological sensors [41].

Another very important application of lanthanides is in biomedical analysis, medical diagnosis and cell imaging [20]. Rare-earth β -diketonates are among the most investigated Ln^{3+} coordination compounds, useful in a wealth of applications, ranging from complexation agents in solvent-solvent extraction processes, to NMR shift reagents, luminescent probes for time-resolved immunoassays, and electroluminescent materials [20].

The use of lanthanide complexes to simplify unresolved proton resonances in low-field NMR spectra is the lanthanide induced shift, method applied in various NMR

problems: qualitative spectral simplification, proof of molecular stereochemistry, quantitative analysis of dynamic solution structures, perfused tissues and organs. The bases for these applications are three fundamental properties of the lanthanide cations: a) Lewis acid character; b) unpaired f electrons; c) tendency to form complexes with primary sphere coordination numbers between 8 and 10.

When a Lewis base interacts with lanthanide ion, any NMR – active nucleus within that base is influenced by the presence of the unpaired f electrons, leading to its paramagnetic relaxation and broadening of its resonance and in some cases to a shift to a different NMR frequency. Gd^{3+} has 7 unpaired electrons and can not produce NMR dipolar shift. The shift that Gd^{3+} produces is called contact shift and is used to test for contact shift contributions to a measured lanthanide induced shift [42].

There are available pharmaceuticals called contrast agents [43] which, when introduced into body cavities are easily detected in an image. The presence or absence and the kinetic behavior of the agents in the tissues is used by physicians to determine the status of normal and diseased tissues. There are three currently types of medical imaging where lanthanides might be used as contrast agents: Nuclear Imaging, X-ray Imaging and Nuclear Magnetic Resonance Imaging (MRI).

To date Gd^{3+} based contrast agents are commonly used in Magnetic Resonance Imaging. It is necessary to use ligands that form very stable chelates with the lanthanide ion, because the metal administration as a free ion is strongly toxic. There are several approved Gd based contrast agents [44,45]. There has been an increase in the number of reports published on paramagnetic contrast agents utilizing other lanthanide ions with chelating ligands. This is due to the potential use of Eu^{2+} as a redox responsive contrast agent, and Dy^{3+} as a high field contrast agent [45].

The shift properties of paramagnetic Ln^{3+} complexes ($Ln \neq Gd$) have been exploited for designing a novel class of contrast agents based on the transfer of saturated magnetization to the bulk water signal from exchangeable protons on the contrast agent molecules (chemical exchange saturation transfer (CEST) agents) or from water molecules interacting with a lanthanide shift reagent [44].

The intrinsic advantages of luminescent lanthanide ions, have led to the development of time-resolved luminescent immunoassays [20]. Different spectral ranges

can be covered by the emission of Sm^{3+} , Eu^{3+} , Tb^{3+} , and Dy^{3+} , which permit the development of multiple immunoassays.

Immunoassays rely on a biochemical reaction between an antigen (the analyte) and a specific antibody. In luminescent immunoassays, the latter is labeled with a lanthanide chelate. Initially, the proposed method called for a heterogeneous, two-step procedure (Figure 2.12a). After completion of the biochemical reaction (step 1), the solution pH is lowered which resulted in the dissociation of the Ln^{3+} . Then in step 2, an enhancement solution is added containing a second chelating agent, tri-octyl phosphine oxide to complete the Ln^{3+} coordination sphere and Triton1 X-100 to form protective micelles around the new chelate for optimum luminescence efficiency. In this way, quantum yields of Eu^{3+} -containing systems easily reached 70 %. A simpler method was subsequently proposed (Figure 2.12b) in which the initial chelate is an efficient donor for sensitizing emission of an acceptor chromophore. The biochemical reaction brings the two entities close enough so that directional nonradiative resonant energy transfer occurs upon UV excitation of the chelate.

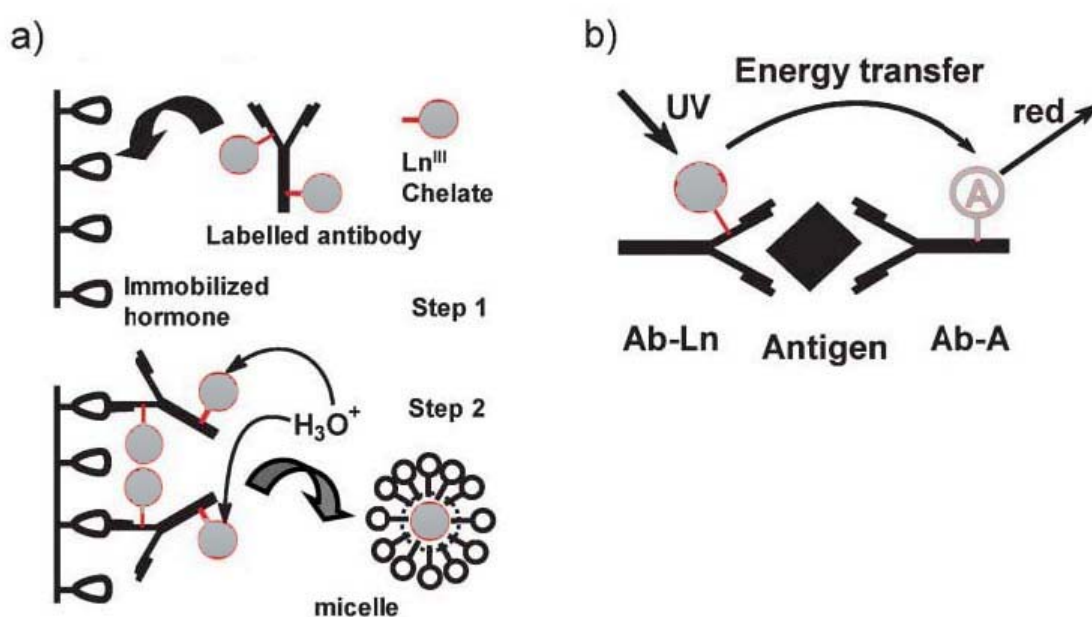


Figure 2.12 – Principles of a) heterogeneous immunoassays and b) homogeneous immunoassays [20].

2.10 References

- [1] C.H. Evans, in *Episodes from the history of the rare earth elements*, edited by C.H. Evans, Kluwer, Dordrecht, 1996.
- [2] F.A. Cotton, *Advanced inorganic chemistry*, John Wiley, New York, 1999.
- [3] J.A. Marinsky, in *Episodes from the history of the rare earth elements*, edited by C.H. Evans, Kluwer, Dordrecht, 1996.
- [4] *A Lanthanide lanthology, Part I (A-L)*, Molycorp Inc., Mountain Pass, 1997.
- [5] B.G. Wybourne, *Spectroscopic Properties of Rare Earths*, Interscience Publishers, John Wiley & Sons, New York, 1965.
- [6] C.K. Jorgensen, *Journal of Inorganic & Nuclear Chemistry* 1 (1955) 301.
- [7] A.J. Freeman, R.E. Watson, *Phys. Rev.* 127 (1962) 2058.
- [8] O.L. Malta, L.D. Carlos, *Quimica Nova* 26 (2003) 889.
- [9] S. Hufner, *Optical spectra of transparent rare-earth compounds*, Academic Press, New York, 1978.
- [10] G.H. Dieke, *Spectra and Energy Levels of Rare Earth Ions in Crystals*, Interscience Publishers, John Wiley & Sons, New York, 1968.
- [11] J.-C.G. Bunzli, in *Lanthanide probes in life, chemical and earth science theory and practices*, edited by J.-C. G. Bunzli and G. R. Choppin, Elsevier, Amsterdam, 1989.
- [12] W.T. Carnall, G.L. Goodman, K. Rajnak, R.S. Rana, *Journal of Chemical Physics* 90 (1989) 3443.
- [13] J.H. van Vleck, *J. Phys. Chem.* 41 (1937) 67.
- [14] P. Porcher, P. Caro, *J. Lumin.* 21 (1980) 207.
- [15] I.I. Sobel'man, *Atomic spectra and radiative transitions*, Springer, Berlin, 1996.
- [16] L. van Pieterse, PhD thesis, Utrecht University, Utrecht 2001.
- [17] R.T. Wegh, H. Donker, A. Meijerink, *Phys. Rev. B* 57 (1998) R2025.
- [18] R.T. Wegh, A. Meijerink, *Phys. Rev. B* 60 (1999) 10820.
- [19] J.R. Lakowicz, *Principles of fluorescence spectroscopy*, Springer, New York (NY), 2006.
- [20] J.C.G. Bunzli, C. Piguet, *Chem. Soc. Rev.* 34 (2005) 1048.
- [21] G. Blasse, B.C. Grabmaier, *Luminescent materials*, Springer, Berlin, 1994.

-
- [22] H.Y.D. Ke, E.R. Birnbaum, *J. Lumin.* 63 (1995) 9.
- [23] H.P. You, X.Y. Wu, H.T. Cui, G.Y. Hong, *J. Lumin.* 104 (2003) 223.
- [24] R. Reisfeld, C. K.Jørgenson, in *Handbook on the physics and chemistry of rare earths*, edited by K.A. Gschneidner, Jr., L. R. Eyring, North-Holland Physics Publishing, Amsterdam, 1979.
- [25] T. Forster, *Annalen Der Physik* 2 (1948) 55.
- [26] T. Forster, *Comparative Effects of Radiation*, Wiley, New York, 1960.
- [27] D.L. Dexter, *J. Chem. Phys.* 21 (1953) 836.
- [28] F. Lucarz, MSc thesis, University College London, London, 2003.
- [29] P. Maestro, *Rare Earths*, Editorial Complutense, Madrid, 1998.
- [30] T. Justel, H. Nikol, C. Ronda, *Angew. Chem. Int. Ed.* 37 (1998) 3085.
- [31] CHINT is a product of the Chint Group Corporation (<http://www.chint.com>), PRC.
- [32] M. Kawachi, *Iee Proceedings-Optoelectronics* 143 (1996) 257.
- [33] Y.P. Li, C.H. Henry, *Iee Proceedings-Optoelectronics* 143 (1996) 263.
- [34] E.M. Yeatman, M.M. Ahmad, O. McCarthy, A. Vannucci, P. Gastaldo, D. Barbier, D. Mongardien, C. Moronvalle, *Opt. Commun.* 164 (1999) 19.
- [35] C. Tosello, F. Rossi, S. Ronchin, R. Rolli, G.C. Righini, F. Pozzi, S. Pelli, M. Fossi, E. Moser, M. Montagna, M. Ferrari, C. Duverger, A. Chiappini, C. De Bernardi, *J. Non-Crys. Sol.* 284 (2001) 230.
- [36] G. Ehrhart, M. Bouazaoui, B. Capoen, V. Ferreiro, R. Mahiou, O. Robbe, S. Turrell, *Opt. Mat.* doi:10.1016/j.optmat.2006.09.006 (2006).
- [37] J. Kani, K. Hattori, M. Jinno, S. Aisawa, T. Sakamoto, K. Oguchi, *Electr. Lett.* 35 (1999) 321.
- [38] S. Tanabe, N. Sugimoto, S. Ito, T. Hanada, *J. Lumin.* 87-9 (2000) 670.
- [39] T. Kasamatsu, Y. Yano, T. Ono, *IEEE Photonics Tech. Lett.* 13 (2001) 433.
- [40] Y.Q. Wang, A.J. Steckl, *Appl. Phys. Lett.* 82 (2003) 502.
- [41] Y. Hasegawa, Y. Wada, S. Yanagida, *J. Photochem. Photobiol. C* 5 (2004) 183.
- [42] A.D. Cherry, C.F.G.C. Geraldes, in *Lanthanide probes in life, chemical and earth science theory and practices*, edited by J.-C. G. Bunzli and G. R. Choppin, Elsevier, Amsterdam, 1989.
- [43] M.F. Tweedle, in *Lanthanide probes in life, chemical and earth science theory and practices*, edited by J.-C. G. Bunzli and G. R. Choppin, Elsevier, Amsterdam, 1989.

- [44] S. Aime, S.G. Crich, E. Gianolio, G.B. Giovenzana, L. Tei, E. Terreno, *Coord. Chem. Rev.* 250 (2006) 1562.
- [45] M. Bottrill, L.K. Nicholas, N.J. Long, *Chem. Soc. Rev.* 35 (2006) 557.

3 Experimental techniques

Index

3.1	Introduction	56
3.2	Luminescence	56
3.2.1	Excitation sources.....	57
3.2.2	Light dispersing elements.....	60
3.2.3	Detectors.....	64
3.2.4	Experimental conditions.....	68
3.3	Other techniques.....	72
3.3.1	Single-crystal X-ray diffraction.....	72
3.3.2	Powder X-ray diffraction.....	72
3.3.3	Solid-state nuclear magnetic resonance (NMR).....	72
3.3.4	Raman spectroscopy.....	73
3.3.5	Scanning electron microscopy / Energy dispersive spectrometry.....	73
3.3.6	Elemental analysis.....	73
3.3.7	Thermal analyses.....	74
3.4	References	75

3.1 Introduction

This chapter presents in a brief way the experimental conditions of the techniques used in this thesis, namely, photoluminescence spectroscopy, single –crystal and powder X-ray diffraction, solid-state nuclear magnetic resonance, Raman spectroscopy, scanning electron microscopy /energy dispersive spectrometry, thermal analysis and elemental analysis. The photoluminescence spectroscopy is presented in detail because it is the core technique of this thesis.

When relevant, the details of the experimental conditions are presented together with the obtained results.

3.2 Luminescence

The term “luminescence” (the literal translation from Latin is “*weak glow*”) was introduced into the literature by Wiedemann (1888). He defined luminescence as the excess emission over and above the thermal emission background. This definition was not entirely accurate, because it does not distinguish luminescence from other types of glow that are also excess emission over and above the thermal emission background [1]. More precisely, luminescence may be defined as nonequilibrium radiation that is an excess over and above the thermal radiation background and arises in the presence of intermediate processes of energy transformation between absorption and emission [1]. For this emission of radiation from luminescent material to take place it is necessary, absorption of a certain amount of energy from a suitable source. The different designations of that luminescence are based on the type of energy involved in the excitation process of the material. Table 3.1 presents the more significant luminescence types [2].

Table 3.1 – Different luminescence types [2].

Designation	Description
Bioluminescence	Emission of light by living animals and plants.
Candoluminescence	Emission of light by mixed oxides in a gas or hydrogen flame.
Cathodoluminescence	Emission of light resulting from bombardment by electrons.
Chemiluminescence	Luminescence occurring during chemical reaction.
Electroluminescence	Light accompanying an electric discharge of an applied voltage.
Fluorescence	Emission of electromagnetic radiation upon exposure to the same type of radiation, having either the same energy (resonance) or a larger energy.
Photoluminescence	Emission of light resulting of excitation by photons.
Radioluminescence	Emission of light resulting from bombardment by ionizing particles such as electrons, α particles or X-rays and γ -rays.
Thermoluminescence	Emission of light by heating substances.
Triboluminescence	Emission of light resulting after mechanical reaction on solids.

Two classes of luminescence spectra can be distinguished: excitation and emission. The excitation spectrum gives information concerning the positions of the excited states, while the emission spectrum supplies information of the spectral distribution of light, emitted by the sample. To collect luminescence spectra three basic elements are necessary: light source, light-dispersing element and light detector.

3.2.1 Excitation sources

The light source must generate a beam of radiation with sufficient power in the desired region for easy detection and measurement. Its output power should be stable and reproducible. There are two types of spectroscopic sources: continuum sources (lamps), which emit radiation that changes in intensity only slowly as a function of wavelength and line sources (lasers), which emit a limited number of lines or bands of radiation each of which spans a limited range of wavelengths [3-5].

There are two types of lamps: incandescent and arc [3-5]. The most common incandescent lamp is the tungsten filament. The energy distribution of this source

approximates that of a black-body and is temperature dependent (Figure 3.1). In most absorption instruments, the operating filament temperature is 2870 K; the bulk of the energy is thus emitted in the infrared region. A tungsten filament lamp is useful for the wavelength region between 350 and 2500 nm [4]. The highest temperature (3300 K) is reached by using a tungsten filament in combination with halogen in the bulb to regenerate the slowly evaporating tungsten wire. Incandescent lamps are used as excitation sources in the visible and infrared regions. The highest efficiencies that can be obtained are 5-30 lumens/W [3]. These lamps practically do not emit in the ultraviolet range and arc lamps are used to bridge this gap. Arc lamps create radiation by discharging energy through ionized gases. In low-pressure discharge lamps the characteristic lines of the atoms in the discharge are emitted (for low-pressure mercury discharge at 185, 254 and 365 nm) [3].

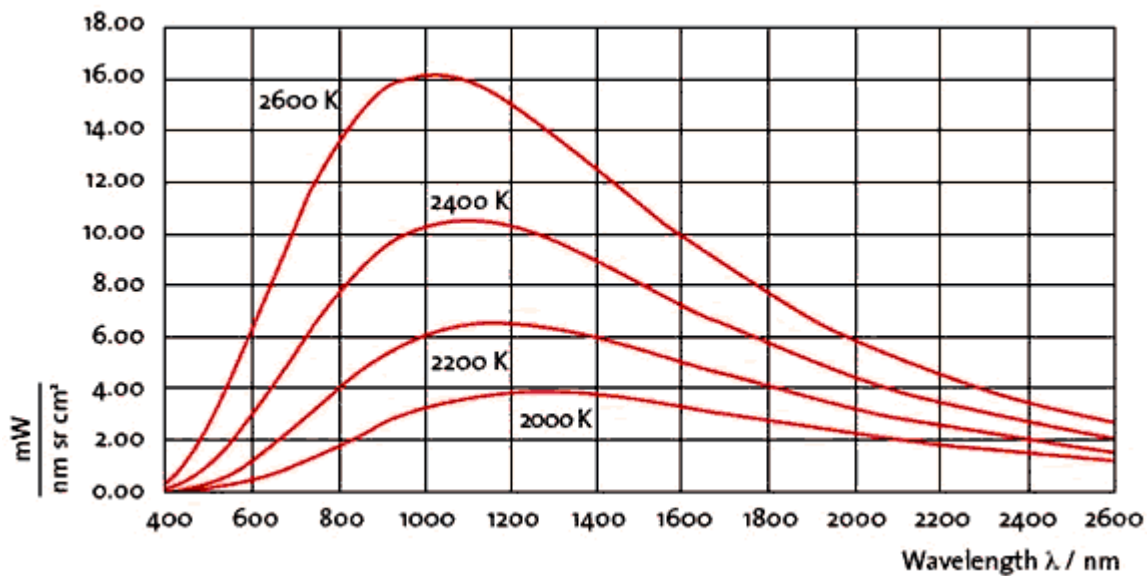


Figure 3.1 – Spectral distribution of tungsten filament lamp at different temperatures [6].

At high pressure and temperature a continuous background comes up owing to broadening of the spectral lines. The most widely used arc lamps are those of high-pressure xenon, mercury, and deuterium (Figure 3.2). Xenon and mercury lamps give a continuous background between 220 and 2000 nm [3]. On top of the background, the line spectrum is still visible, which is undesirable for a continuous excitation source. For mercury lamps the spectral lines are more pronounced and this is the reason why xenon lamps are more

widely used in spectrofluorometers as a continuous excitation source. Deuterium lamps are not as bright as those of xenon and mercury, but they produce a good continuous spectrum at short wavelengths and are used for measurements below 240 nm [3].

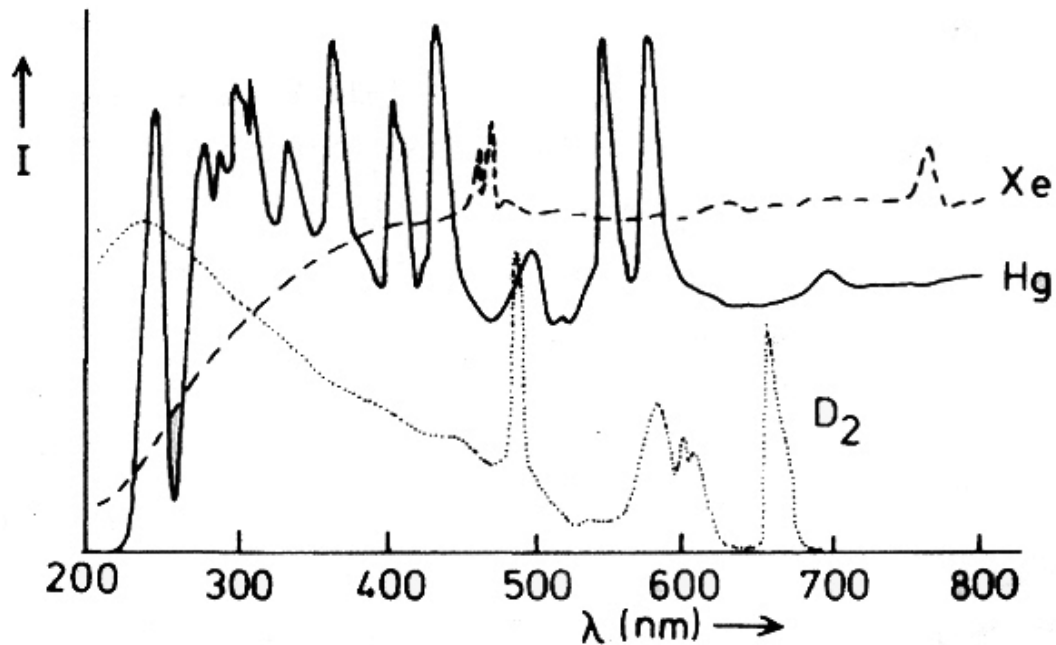


Figure 3.2 – Spectral distribution of high-pressure xenon, mercury and deuterium lamps [3].

A laser is a monochromatic light source and has a radiative power at a given frequency several orders of magnitude larger than other light sources. The term laser is an acronym for Light Amplification by Stimulated Emission of Radiation and lasers have all the characteristics of a perfect excitation source: high power, small divergence, coherence, monochromatism and the capability of very short pulses. As a result of their light-amplifying characteristics, lasers produce spatially narrow and extremely intense beams of radiation. The process of stimulated emission produces a beam of highly monochromatic and remarkably coherent radiation. Because of these unique properties, lasers have become important sources for use in the ultraviolet, visible and infrared regions of the spectrum [4].

The main component of a laser device is the lasing medium which could be a solid crystal (*e.g.* ruby), a semiconductor (*e.g.* gallium arsenide), a solution of organic dye (*e.g.* Rhodamine B) or a gas (*e.g.* krypton or argon). The activation of the lasing material is often achieved by radiation from an external source. A few photons of proper energy trigger

the formation of a cascade of photons of the same energy. This process is called pumping and could be also accomplished by an electrical current or by an electrical discharge [4].

Of all available types of lasers developed from the discovery of the well known ruby laser, built by Maiman in 1960, the most frequently used in luminescence spectroscopy are the solid-state (Nd^{3+} :YAG and Ti^{4+} :sapphire) and the gaseous ones (He-Ne, Ar^+ and He-Cd) [3,4].

3.2.2 Light dispersing elements

The light dispersing elements are used to produce monochromatic light from a source of continuous light and to analyze the distribution of the emitted light. Several types of light dispersing elements exist, such as monochromators, based on diffraction gratings or prisms and interferometers [1,4].

The most commonly used light-dispersing element in luminescence spectroscopy is the grating monochromator. Of the various designs for monochromators with flat gratings (Ebert, Czerny-Turner and Littrow) or curved gratings (Rowland, Passchen-Runge, and Wadsworth) the most popular design is the Czerny-Turner configuration, shown in Figure 3.3. The monochromator consists of narrow entrance and exit slits, a grating and focusing mirror. The entrance slit provides a rectangular optical image. The collimating lens or mirror produces a parallel beam of radiation. The prism or a grating disperses the radiation in its component wavelengths. The focusing element reforms the image on the entrance slit and focuses it on a planar surface called *AB* focal plane and the exit slit in the focal plane isolates the desired spectral band. Nearly all commercial monochromators are based upon reflection gratings because they are cheap to fabricate, disperse radiation linearly along the focal plane, and provide better wavelength separation for the same size dispersing element [4].

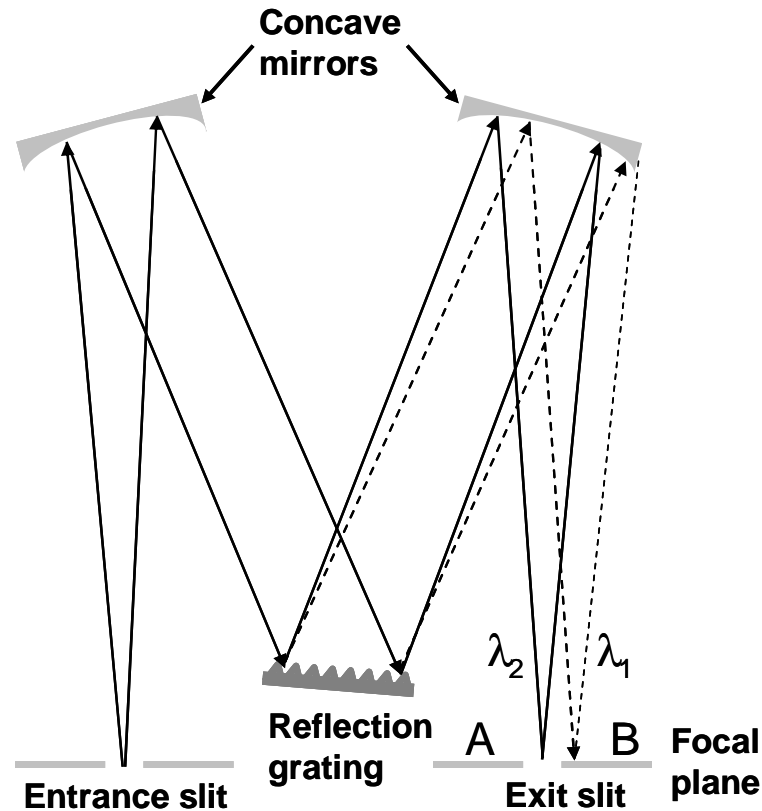


Figure 3.3 – Czerny-Turner configuration of a grating monochromator ($\lambda_1 > \lambda_2$) [4].

A grating for the ultraviolet and visible regions will typically contain from 300 to 2000 grooves/mm, while for the infrared region 10 to 200 grooves/mm are encountered [4]. Figure 3.4 presents the diffraction mechanism of an echellette-type grating with a saw-tooth shape. The parallel beams of monochromatic radiation 1 and 2 are shown striking the grating at an incident angle i to the grating normal. Maximum constructive interference is shown as occurring at the reflection angle r . It is evident that beam 2 travels a larger distance than beam 1 and the difference in the paths is equal to $(\overline{CB} + \overline{BD})$. To occur constructive interference this difference must equal $n\lambda$. That is,

$$n\lambda = (\overline{CB} + \overline{BD}) \quad (3.1)$$

where n , a small whole number is called the diffraction order. Note that angle CAB is equal to angle i and that the angle DAB is identical to the angle r . From simple trigonometry, we obtain the following equation for the condition for constructive interference:

$$n\lambda = d(\sin i + \sin r), \text{ with } n = 0, \pm 1, \pm 2, \dots, \quad (3.2)$$

where d is the spacing between the reflecting surfaces.

Equation (3.2) suggests that several values of λ exist for a given diffraction angle r . Thus, if a first-order line ($n = 1$) of 800 nm is found at r , second-order (400 nm) and third-order (200 nm) lines also appear at this angle. The higher-order lines can be removed by filters.

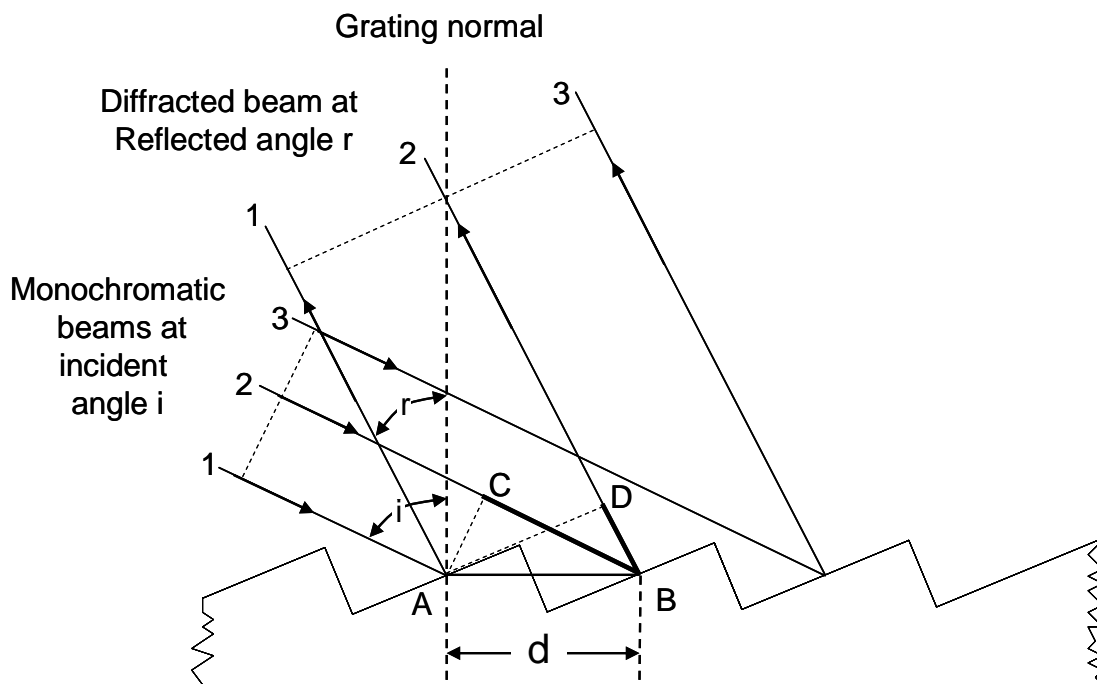


Figure 3.4 – Mechanisms of diffraction from an echellette-type grating [4].

The angular dispersion of a grating can be obtained by differentiating equation (3.2) keeping i constant:

$$\frac{dr}{d\lambda} = \frac{n}{d \cos r} \text{ (rad/nm)} \quad (3.3)$$

The ability to separate two closely spaced spectral lines is expressed in terms of a linear dispersion (D) in equation (3.4). D refers to the variation of the wavelength as a function of y , the distance along the line AB of the focal planes as shown in Figure 3.4. If F

is the focal length of the monochromator, the linear dispersion can be related to the angular dispersion by the relationship [3,4]:

$$D = \frac{dy}{d\lambda} = \frac{Fdr}{d\lambda} \text{ (nm/mm)} \quad (3.4)$$

The resolution or resolving power of monochromator R is the ability to distinguish as separate entities adjacent spectral features (absorption bands or emission lines). The definition for resolution is:

$$R = \frac{\lambda}{d\lambda} = nN \quad (3.5)$$

where λ is the wavelength under study, $d\lambda$ the wavelength difference measured between line (or peak) centers, determined by the value $\Delta\lambda$ for which exists constructive interference at λ and destructive interference at $\lambda + \Delta\lambda$, n is the diffraction order and N the total number of diffracting grooves of the grating.

To have high resolution (0.1 nm) on a grating with 1800 gr/mm the dispersion of the monochromator must be low (1 nm/mm) and slits must be 100 μm opened. If the dispersion is larger, to keep the same resolution, the slits must be closed, (smaller aperture) which means that not enough light will enter.

In order to enhance the efficiency of monochromator in a selected wavelength range, gratings are ruled with the grooves at a specific angle with the grating surface known as the blazed angle β . The wavelength for which the reflection and diffraction angles are equal is defined as blazed wavelength λ_β . Admitting that the incidence angle is equal to the diffraction angle, the equation can be written in the following way [3-5,7].

$$\lambda_\beta = 2d \sin \beta \quad (3.6)$$

3.2.3 Detectors

A detector converts electromagnetic radiation into electrons, subsequently flowing into the readout circuit. There are single-element detectors, such as photovoltaic cells, solid-state photodiodes, photoemissive tubes, and photomultiplier tubes, and multiple-element detectors such as solid-state array detectors. The success of luminescence spectroscopy frequently depends on the capacity to detect low intensity signals. The most used single-element detectors are the photomultiplier tubes and the solid-state photodiodes [3-5,7].

The photomultiplier tube consists of a photoemissive layer cathode (photocathode), focusing electrodes, an electron multiplier and an electron collector (anode). All these devices are sealed in a vacuum tube (Figure 3.5). Incident radiation ejects photoelectrons from the cathode. The emitted electrons are focused by an electrostatic field and accelerated toward a curved electrode, the first dynode that ejects several electrons. Repeating this electron multiplying process over successive dynodes maintained at higher voltages produces a current avalanche that finally impinges on the anode [5]. Internal current amplification, or gain, is thereby achieved. Typically, the overall gain is $10^5 - 10^8$. The electrons that are collected at the anode give the output signal, a small current in the picoampere to microampere range [3].

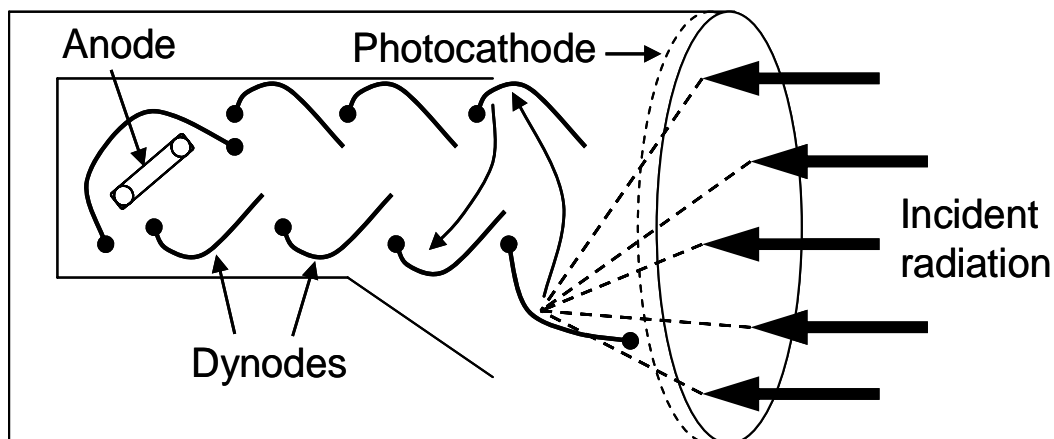


Figure 3.5 – Schematic representation of photomultiplier tube [5].

Beyond 900 nm the sensitivity of photomultiplier tubes is low. In this region photodiodes, which are photovoltaic detectors are used. The detection of light is achieved

by photoexcitation of electron-hole pairs near a junction. Absorption of photons with energy larger than the band gap leads to the formation of electron-hole pairs. Small potential difference across the junction is created separating the electron and the hole.

For p - n junction in semiconductors, a region depleted of mobile charge carriers with a high internal electric field across it exists between the p - and n -type materials. This region is known as the depletion region. When light irradiates the depletion region, electron-hole pairs are generated through the absorption of photons and the internal field causes the electrons and holes to separate. This accumulated charge can be detected by measuring the electric potential between the p and n regions while the device is open-circuit (the photovoltaic mode of operation). The charge can also be detected by measuring the current flow between the p and n regions by applying a reverse bias (the photoconductive mode of operation).

Representative solid-state photodiode is the silicon diode. A typical structure is shown in Figure 3.6. It should be noted that electrical contact to the semiconductor material is always made via a metal- n^+ (or $-p^+$) junction [7].

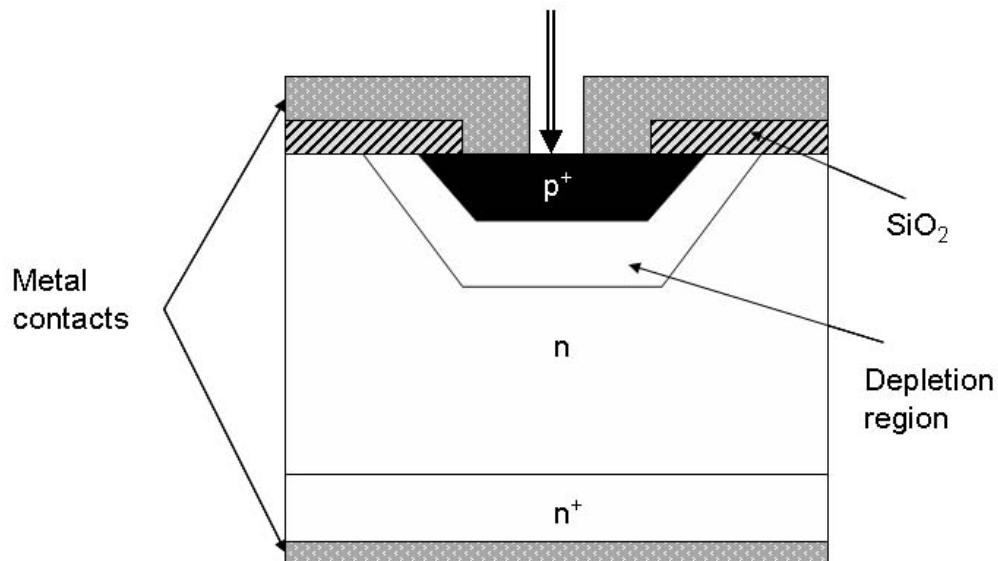


Figure 3.6 – Schematic representation of a silicon photodiode [7].

The most used photodiodes are made of silicon (200-1100 nm) or germanium (400-1800 nm) [3]. They are more sensitive than vacuum phototubes but less sensitive than photomultiplier tubes [4]. Cooling to 77 K by liquid nitrogen reduces the number of thermally generated free charge carriers, and the sensitivity is increased [3].

Other detectors often used not only for scientific purposes but also applied in consumer products, such as fax machines and cameras, are the charge-coupled devices (CCD) due to improved performance. Figure 3.7 presents a schematic representation of charge-coupled devices. A CCD consists of arrays of metal-oxide-semiconductor (MOS) capacitors, which are made from *p*-type silicon grown on an insulating layer of SiO₂. On top of the SiO₂ layer a thin metal structure (called the gate) is deposited. Electric contacts are made on the gates and the Si substrate. Applying positive voltage to the gate leads to pushing the holes away from it. Illumination of the MOS capacitor creates free electrons and holes. The electrons are collected at the Si-SiO₂ interface under the gate as long as the potential is applied (the integration time). The number of electrons trapped under the gate is proportional to the number of incident photons [7].

Each pixel in a CCD consists of three gates. During illumination a voltage is applied to the middle gate G_1 via voltage line V_1 and electrons are collected under all the middle gates G_1 . After illumination the image on the CCD plate has to be read out. This is done by transferring the charge collected in each pixel to the detector, point by point and array by array. The transfer of the electrons takes place over long distances without the loss of electrons and is controlled by applying voltages to G_1 , G_2 , and G_3 of each pixel in the sequence shown in Figure 3.7. Applying a voltage V_2 equal to V_1 leads to shifting and smearing out of accumulated electrons over the area under gates G_1 and G_2 . Reducing the voltage V_1 leads to movement of all electrons to gate G_2 . The same voltage sequence is repeated to gates G_2 and G_3 to move the electrons to gate G_3 . This voltage sequence is repeated many times under the control of CCD clock. The number of stored electrons is measured for every pixel. The sensitivity of a CCD is very high. Thermal electrons are the main source of noise and by cooling the CCD to 77K this noise can be reduced [3].

The spectral response of a CCD is determined by the light absorption in the Si substrate and this is similar to that of the silicon photodiode (200-1100 nm). For many applications in luminescence spectroscopy a linear (1D) CCD array is sufficient to record a spectrum. The CCD array can measure a complete spectrum instantaneously without the need to scan a monochromator. In this case a CCD array is placed at the exit slit where the light that is diffracted from the grating is focused. The dispersed light is incident on the CCD and every pixel on the array will detect light of a slightly different wavelength. The wavelength resolution is determined by the number of pixels on the CCD array and the

linear dispersion of the monochromator at the position of the array 2D CCDs having 256 x 256 up to 4096 x 4096 pixels are also available. For larger number of pixels the long read out time becomes a problem [3].

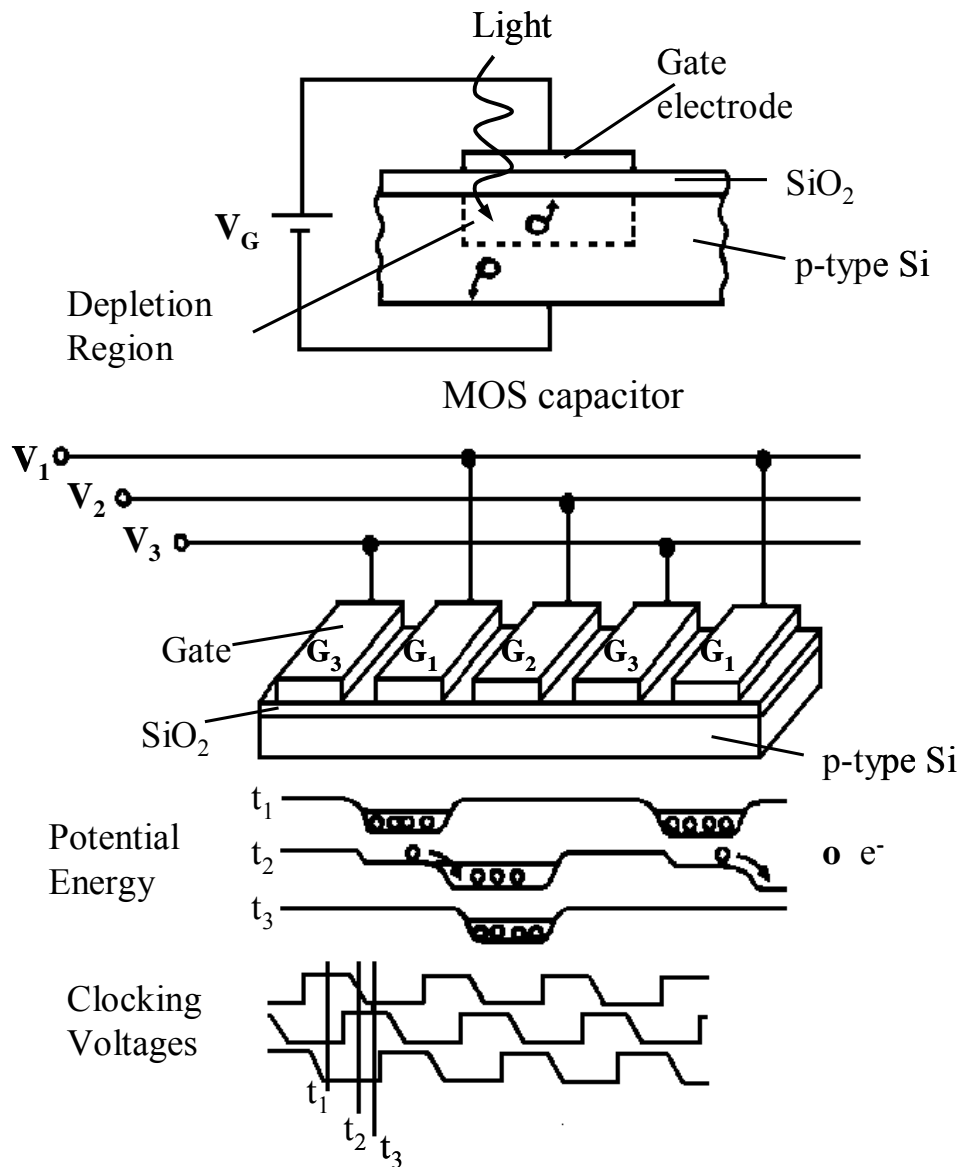


Figure 3.7 – Schematic representation of the operation of a CCD [3].

The great advantage of a CCD array is that all wavelengths in a spectrum can be recorded at the same time. The high sensitivity of a CCD camera can be used to measure very weak signals, using long integration times [3].

3.2.4 Experimental conditions

The emission spectrum represents the variation of the luminescence intensity as a function of given and fixed excitation wavelength (normally the excitation monochromator is fixed at the wavelength, corresponding to the most intensive transition on the excitation spectra), respectively the excitation spectrum shows the luminescence intensity for fixed emission wavelength (the emission monochromator is fixed on the most intensive emission transition) [8].

The emission and excitation photoluminescence spectra were measured in the temperature range between 10 and 300 K. The temperature of 10 K was reached using a He closed-cycle cryostat from APD Cryogenics-HC2. The resistance connected to the cold end of the cryostat allows variation of the temperature, which is controlled, with a precision of 0.1 °C, by temperature controller APDE 3700, coupled with Chrome-Gold thermocouple. A vacuum system composed by rotary vacuum pump and diffusion vacuum pump Edwards were used to obtain pressure inside the cryostat with 10^{-5} - 10^{-6} Torr in order to guarantee a good thermal isolation of the system.

Figure 3.8 presents a scheme of the configuration used in the acquisition of the photoluminescence spectra. In this work, in general, the photoluminescence measurements were recorded on a Fluorolog®-3 Model FL3-2T with double excitation monochromator and single-emission monochromator (Triax-320) with different gratings for UV-VIS and NIR range. The used excitation sources were a 450 W Xe arc lamp and a pulsed Xe-Hg lamp (6 μ s pulse, 20-30 μ s tail) for the steady-state and time-resolved measurements, respectively. The double excitation monochromator has a Czerny-Turner mounting, fitted with a ruled grating 1200 grooves/mm, blazed wavelength 330 nm, dispersion 2.1 nm/mm and three slits: from 0 to 7 mm). The single-emission monochromator (Triax-320) for UV-VIS range has a Czerny-Turner mounting, grating fitted with 1200 grooves/mm, blazed at 500 nm, dispersion 2.6 nm/mm, band pass from 0 to 18.5 nm and for NIR range a Czerny-Turner mounting, fitted with a grating with 600 grooves/mm, blazed at 1 μ m, dispersion 5.2 nm/mm, band pass from 0 to 37 nm. The excitation spectra were corrected from 240 to 600 nm for the spectral distribution of the lamp intensity using a silicon photodiode reference detector. Two emission detectors were used depending on the spectral range. For UV-VIS range up to (850-900 nm) PMT R928 and for NIR range (950-1700 nm) PMT

H9170-75 detectors were coupled. Emission and excitation spectra were also corrected for the spectral response of the monochromators and the detector, using typical correction spectra provided by the manufacturer. The time-resolved measurements were carried out using a 1934D3 phosphorimeter coupled to the Fluorolog-3.

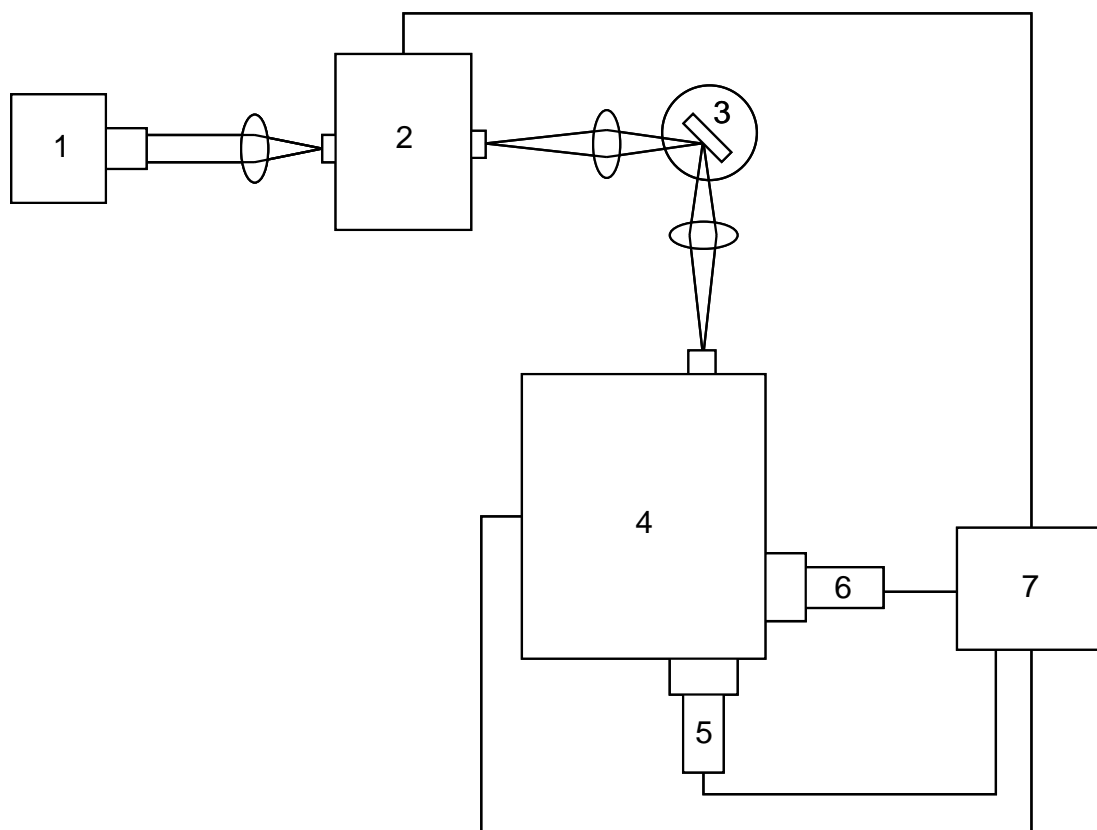


Figure 3.8 – Schematic representation of the configuration used for steady-state measurements 1) Xe arc lamp; 2) double excitation monochromator; 3) He closed-cycle cryostat and sample; 4) emission monochromator; 5) UV-VIS detector; 6) NIR detector ; 7) computer and data scan [9].

Figure 3.9 presents a scheme of the configuration used for time-resolved measurements. The main difference between steady state and time-resolved (life time) measurements is the applied excitation source: continuous lamp and pulsed lamp, respectively. The phosphorimeter allows to measure with a certain delay depending on the pulses of the lamp. The important experimental parameters are: initial delay, sample window, time per flashes and number of flashes. ID - "*Initial Delay*" or "*Delay after Flash*" (0.01 - 10000 ms, increment 0.001 ms) is the time between the start of the lamp flash and the beginning of data acquisition (opening of the sample window). ID should be

long enough to allow the fluorescence emission and lamp decay to occur. Usually $ID=0.05$ ms. SW - "*Sample Window*" (0.01 - 10000 ms) sets the duration of signal acquisition. The SW opens when the ID ends. When the SW is open, the signals that enter the phosphorimeter control module is counted and integrated for subsequent output to the software. After the preset time, the SW closes and any signal arriving after this point is ignored. TPF - "*Time per Flashes*" (0.04 - 60 s) dictates the repetition rate of the xenon pulse lamp. The ($TPF \geq 40$ ms) must be slow enough to allow the SW to close before another flash. $TPF \geq ID+MD+SW+20ms$ (MD - "*Maximum Delay*"). NF - "*Number of Flashes*" (1 - 999) sets the number of flashes or lamp pulses and contributes to each data point. These parameters were adjusted for each experiment to have good intensities and base lines [10,11].

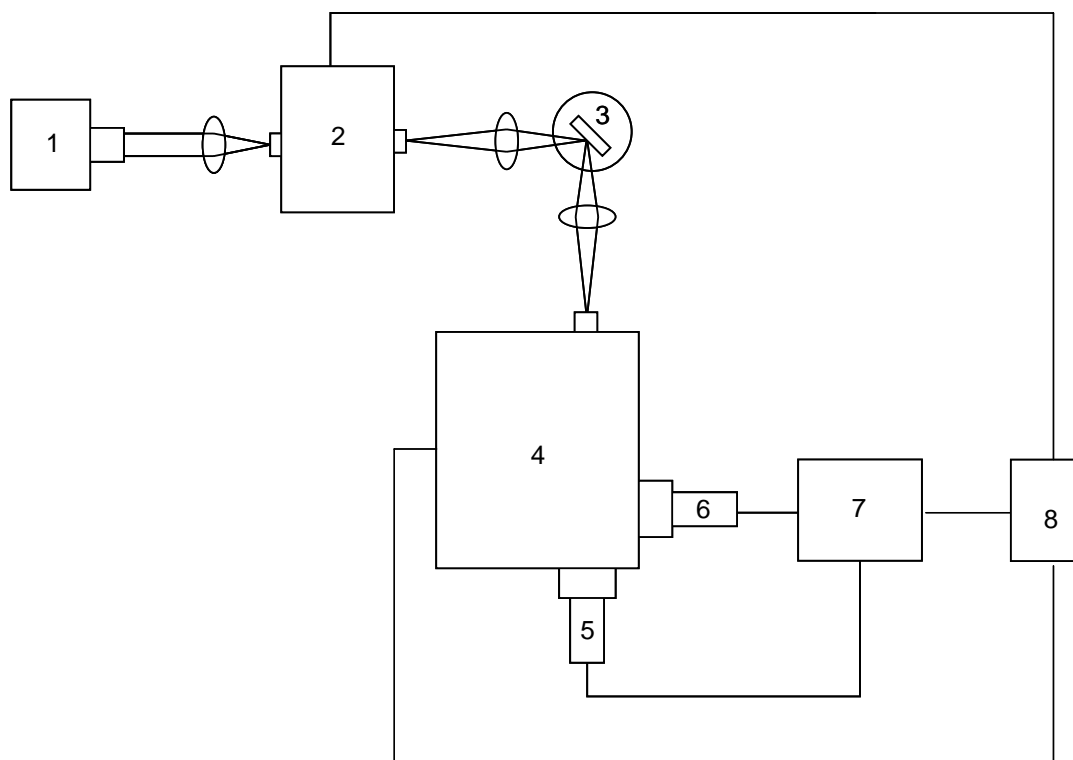


Figure 3.9 – Schematic representation of the configuration used for time-resolved measurements 1) Xe pulsed lamp; 2) double excitation monochromator; 3) He closed-cycle cryostat and sample; 4) emission monochromator; 5) UV-VIS detector; 6) NIR detector; 7) phosphorimeter; 8) computer and data scan [9].

When different samples were compared, the spectra were measured keeping the experimental set-up fixed (slits width, irradiated area and optics geometry). In this case, the sample pellets were prepared at the same pressure.

Radiance is a quantity, specifying the amount of energy radiated in a given direction from a surface. Mostly used with non-ionizing, electromagnetic radiation in the visible spectrum (light), ultra-violet or infrared. More precisely, it is defined as radiated power over solid angle and area, the SI unit being [W/(m² sr)].

Radiance is defined by

$$L = \frac{d^2\Phi}{dA d\Omega \cos \theta} = \frac{\Phi}{A \Omega \cos \theta} \quad (3.6)$$

where the approximation holds for small A and Ω , L is the radiance [W/(m² sr)], Φ is the radiant flux or power (W), θ is the angle between the surface normal and the specified direction, A is the area of the source (m²), and Ω is the solid angle (sr).

The radiance measurements and the CIE (Commission Internationale d'Eclairage) (x,y) emission color coordinates were performed using a telescope optical probe (TOP 100 DTS140-111, Instrument Systems). The excitation source was a Xe arc lamp (150 W) coupled to a Jobin Yvon-Spex monochromator (TRIAX 180). The width of the rectangular excitation spot was 2 mm and the diameter used to collect the emission intensity 0.5 mm, ensuring that the entire sample was illuminated. The experimental conditions (excitation and detection optical alignment) were kept constant to enable the quantitative comparison between the measurements. Moreover, because radiance depends on the surface density of the emitting centers, care was also taken in the samples preparation: pellets with controlled thickness, containing the same amount and compaction degree were made. The radiance values were corrected for the spectral distribution of the lamp intensity. The experimental error is within 5%.

3.3 Other techniques

3.3.1 Single-crystal X-ray diffraction

The single-crystal X-ray diffraction data were measured on different equipments. The details of the experimental conditions are presented together with the obtained results in each chapter. The structures were solved by Doctor Filipe Almeida Paz.

3.3.2 Powder X-ray diffraction [12]

Powder X-ray diffraction data were collected on a Philips X'Pert MPD diffractometer using $\text{CuK}\alpha$ ($\lambda=1.54180 \text{ \AA}$) radiation with a curved graphite monochromator, a fixed divergence slit of $1/4^\circ$ and proportional detector. A flat plate sample holder in a Bragg-Brentano parafocusing optics configuration was used. PXRD was performed for all the samples between 3 e 40° (2θ) using a step size of 0.02° , a scan step of $0.3^\circ/\text{min}$ and time 55 s . Silicon powder was used as internal standard when the aim was to compare the diffractograms of different samples.

The diffractograms necessary for solving the structure or for Rietveld refinement were performed in an extended range of 2θ (typically 3 - 140°) and with a step (*ca.* 10 s per point). The Rietveld refinement was performed using FULLPROF with the collaboration of Doctor Artur Ferreira from Escola Superior de Tecnologia e Gest3o de 3gueda.

3.3.3 Solid-state nuclear magnetic resonance (NMR) [12,13]

The solid-state nuclear magnetic resonance spectra were obtained on a Bruker Advance 400 spectrometer at 9.4 T .

^{29}Si magic angle spinning (MAS) NMR spectra were recorded at 79.5 MHz with 40° pulses; recycle delay from 5 to 60 s and spinning rate of 5 kHz . The chemical shifts are quoted in ppm from tetramethylsilane (TMS).

3.3.4 Raman spectroscopy [12,14]

Raman emission spectra were recorded on a FT-Raman Bruker spectrometer, model RSF 100, at room temperature. The excitation source was a YAG:Nd laser ($\lambda_{Exc.}=1064$ nm) (varying excitation power 15-200 mW). The energy values from Raman shift (cm^{-1}), E_R , were converted into emission energy (cm^{-1}), E_E , using the expression: $E_E = E_{Laser} - E_R$, where $E_{Laser} = 9398.5 \text{ cm}^{-1}$.

3.3.5 Scanning electron microscopy / Energy dispersive spectrometry [15]

The morphology was analyzed using scanning electron microscopy (SEM) on a Hitachi S-4100 Field Emission Gun tungsten filament operating in a voltage of 25 kV. Energy dispersive spectrometry (EDS) was carried out using an EDS Römteck system with polymeric window attached to the scanning electron microscope, allowing measurement of the chemical composition of crystals or parts of them. The samples were affixed to the aluminum holder using adhesive tape. A conductive carbon coating was applied to the samples to avoid charge accumulation with consequent deflection of the incident beam, leading to image distortion and significantly changing the emission of secondary electrons and to improve the quality of the obtained images.

3.3.6 Elemental analysis

Chemical analyses by ICP-AES were done at C.A.C.T.I. - Laboratorio Análisis Instrumental, University of Vigo, Spain and L.C.A. - Laboratório Central de Análise, University of Aveiro, Portugal. Before analyzing, the samples were fused with lithium metaborate and the melts dissolved in nitric acid 0.8 M.

3.3.7 Thermal analyses [16]

TG analyses between 25 and 900 °C were carried out in a Shimadzu TGA-50 instrument with a 5 °C/min scanning rate and in a Labsys TG-DTA1600°Crod, from TA Instruments, in an atmosphere of nitrogen with a 10 °C/min heating rate.

3.4 References

- [1] V.P. Gribkovskii, in *Luminescence of solids*, edited by D. R. Vij, Plenum, New York, 1998.
- [2] J.-C.G. Bunzli, in *Lanthanide probes in life, chemical and earth science theory and practices*, edited by J.-C. G. Bunzli and G. R. Choppin, Elsevier, Amsterdam, 1989.
- [3] A. Meijerink, in *Luminescence of solids*, edited by D. R. Vij, Plenum, New York, 1998.
- [4] D.A. Skoog, F.J. Holler, T.A. Nieman, *Principles of instrumental analysis*, Saunders College Publishing, Philadelphia, 1998.
- [5] H.H. Wilard, *Instrumental methods of analysis*, Wadsworth, Belmont, 1981.
- [6] <http://www.visualpathways.com/assets/tech/trueColor/fig2b.gif>.
- [7] S. Shionoya, W.M. Yen, *Phosphor handbook*, CRC Press, Boca Raton (FL), 1999.
- [8] J.R. Lakowicz, *Principles of fluorescence spectroscopy*, Springer, New York (NY), 2006.
- [9] FL3-2 Triax 320 Installation, HORIBA Jobin Yvon, University of Aveiro, 2004.
- [10] D.A. Marques, Ph.D. thesis, Aveiro University, Aveiro, 2004.
- [11] J.P.J. Rainho, Ph.D. thesis, Aveiro University, Aveiro, 2002.
- [12] A.K. Cheetham, P. Day, *Solid state chemistry techniques*, Clarendon Press, Oxford, 1995.
- [13] G. Engelhardt, D. Michel, *High-resolution solid-state NMR of silicates and zeolites*, John Wiley, Chichester, 1987.
- [14] N. Nakamoto, *Infrared and Raman spectra of inorganic and coordination compounds*, John Wiley, New York, 1986.
- [15] J.C.H. Spencer, *Experimental high-resolution electron microscopy*, University Press, Oxford, 1988.
- [16] D.N. Todor, *Thermal analysis of minerals*, Abacus, Tunbridge Wells, 1976.

4 Layered rare-earth silicates ($K_3[M_{1-a}Ln_aSi_3O_8(OH)_2]$, $M^{3+}=Y^{3+}, Tb^{3+}$; $Ln^{3+}=Eu^{3+}, Er^{3+}, Tb^{3+}, Gd^{3+}$ and Ce^{3+}), $1 \geq a > 0$

Index

4.1	Introduction	78
4.2	Synthesis	78
4.3	Structural characterization	80
4.4	Photoluminescence spectroscopy	92
4.5	Conclusions	113
4.6	References	115

4.1 Introduction

As a result of a systematic study with intention of incorporating optically active lanthanide centres in the structure of silicates, layered rare-earth silicates ($K_3[M_{1-a}Ln_aSi_3O_8(OH)_2]$, $M^{3+}=Y^{3+}, Tb^{3+}$; $Ln^{3+}=Eu^{3+}, Er^{3+}, Tb^{3+}, Gd^{3+}$ and Ce^{3+}), $1 \geq a > 0$ [1-3] were obtained. These solids were named AV-22 materials (Aveiro material number 22), and they are related to layered $K_3[RE]Si_3O_8(OH)_2$, $RE^{3+}= Ho^{3+}, Y^{3+}$ and Yb^{3+} materials [4-6] on which structural work had been done previously. Layered rare-earth silicates are host-guest systems suitable for engineering multifunctional materials with tuneable properties. The Tb- and Eu-AV-22 samples are visible emitters (green and red, respectively) with output radiance comparable to those of standards used in commercial lamps, while Er-AV-22 is a room temperature infrared phosphor. The structure of these materials allows the inclusion of a second (or even a third) type of RE^{3+} ion in the framework and, therefore, the fine-tuning of their photoluminescence properties. For the mixed Tb^{3+}/Eu^{3+} [1] and Tb^{3+}/Ce^{3+} [2] materials evidence has been found of the inclusion of Eu^{3+} and Ce^{3+} ions in the interlayer space by replacing K^+ ions, further allowing the activation of energy transfer mechanisms.

In this chapter, I present the hydrothermal synthesis and the structural characterization of layered rare-earth silicates. Single-crystal (180 K) and powder X-ray diffraction studies were done in cooperation with Dr. Filipe Paz and Dr. Artur Ferreira. Chemical analysis, thermogravimetry, scanning electron microscopy and ^{29}Si MAS NMR were also applied. Photoluminescence spectroscopy in the visible and infrared region was used to study the optical properties of these solids.

4.2 Synthesis

The synthesis of AV-22 materials was described in [1]. Figure 4.1 outlines the steps involved in the preparation of these layered silicates. The synthesis was carried out in Teflon-lined autoclaves (volume 37 cm³, filling rate 0.62), at mild temperature (230 °C) and autogeneous pressure conditions, contrasting with previous work, where 500 °C and

1000-1500 atm were routinely used. In all the syntheses, the autoclaves were removed and quenched in cold water after an appropriate time. The obtained microcrystalline powders were filtered, washed at room temperature with distilled water, and dried at 100 °C. Crystals suitable for single-crystal X-ray diffraction could only be obtained for $K_3[TbSi_3O_8(OH)_2]$ and $K_3[Tb_{0.9}Eu_{0.1}Si_3O_8(OH)_2]$.

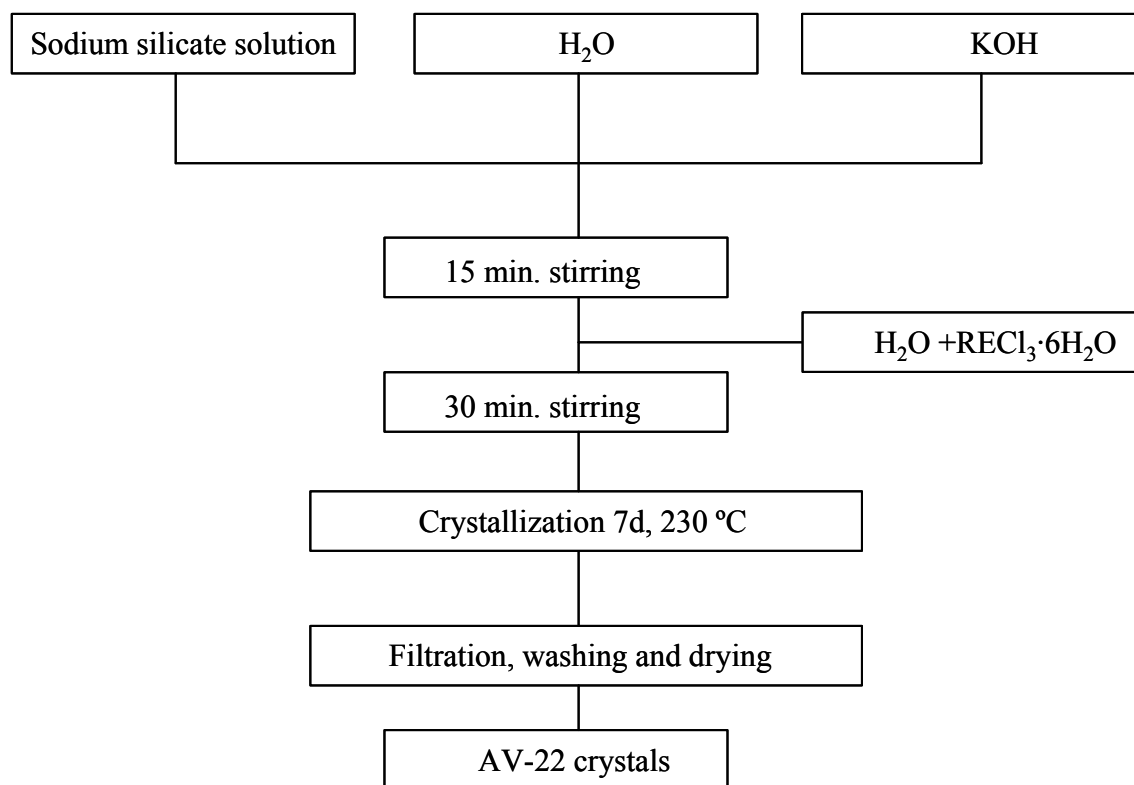


Figure 4.1 – Schematic representation of the synthesis of AV-22 materials.

Typical $K_3YSi_3O_8(OH)_2$, $K_3ErSi_3O_8(OH)_2$ and $K_3EuSi_3O_8(OH)_2$ synthesis. An alkaline solution was made by mixing 4.45 g sodium silicate solution, 15.97 g H_2O , 7.69 g KOH. An amount of 1.69 g of $YCl_3 \cdot 6H_2O$ was added to this solution, and the mixture was stirred thoroughly. The gel, with composition 0.28 Na_2O :3.42 K_2O :1.0 SiO_2 :0.14 Y_2O_3 :44 H_2O was autoclaved under autogeneous pressure for 7 days at 230 °C. Er and Eu layered silicates were synthesized with substitution of $YCl_3 \cdot 6H_2O$ by $LnCl_3 \cdot 6H_2O$, $Ln^{3+}=Er^{3+}$ or Eu^{3+} . Mixed $K_3[Y_{1-a}Er_aSi_3O_8(OH)_2]$ ($a=0.005-1$) samples were prepared by introducing the desired Y^{3+} and Er^{3+} contents in the initial gel. Y/Ce mixed samples were made by introducing in the parent gel 5 % Ce.

Typical $K_3TbSi_3O_8(OH)_2$ synthesis. An alkaline solution was made by mixing 1.24 g precipitate SiO_2 , 20.32 g H_2O and 9.12 g KOH. An amount of 0.82 g of $TbCl_3 \cdot 6H_2O$ was added to this solution, and the mixture was stirred thoroughly. The gel, with composition 4.23 K_2O :1.0 SiO_2 :0.06 Tb_2O_3 :58 H_2O was autoclaved under autogeneous pressure for 7 days at 230 °C. The inclusion of a second (or third) type of RE^{3+} ion in the framework has been done by introducing the desired lanthanide contents in the initial gel. Tb/Ce mixed samples were made by introducing in the parent gel 5 % Ce.

The characteristics of the used reagents are shown in Table 4.1.

Table 4.1 – Characteristics of the used reagents.

Reagent	Composition, Purity	Brand
Sodium silicate solution	27 % m/m SiO_2 , 8 % m/m Na_2O	Merck
precipitate SiO_2	93 % m/m SiO_2 ,	Riedel-de Haën
KOH	Pro-analyze	Merck
$RECl_3 \cdot 6H_2O$ (Ln=Eu, Ce, Er, Y, Gd, Tb)	99.9 %	Aldrich

4.3 Structural characterization

X-ray diffraction analysis was performed on suitable single crystals of $K_3[TbSi_3O_8(OH)_2]$ and $K_3[Tb_{0.9}Eu_{0.1}Si_3O_8(OH)_2]$. However, as almost similar sets of data were collected for the two compounds, we only report on the former material. Crystals were mounted on a glass fiber using perfluoropolyether oil [7]. Data were collected at 180(2) K on a Nonius Kappa charge coupled device (CCD) area-detector diffractometer (MoK α graphite-monochromated radiation, $\lambda = 0.7107 \text{ \AA}$), equipped with an Oxford Cryosystems cryostream and controlled by the Collect software package [8]. Images were processed by Denzo and Scalepack [9], and the data were corrected for absorption by using the empirical method employed in Sortav [10,11]. Structures were solved by the direct methods of SHELXS-97 [12], and refined by full-matrix least squares on F^2 using

SHELXL-97 [13]. All atoms were directly located from difference Fourier maps and refined with anisotropic displacement parameters, except for H(1) which was refined with an isotropic thermal displacement parameter (U_{iso}) fixed at 1.5 times U_{eq} of the parent atom [O(3)]. The O–H bond distance was also restrained to 0.95(1) Å. This was intended to provide best hydrogen-bonding fit for the X-ray data, but it does not reflect the true position of the hydrogen nucleus. The last difference Fourier map synthesis for $K_3[TbSi_3O_8(OH)_2]$ (Tb-AV-22) showed a residual electron density with the highest peak (1.703 eÅ⁻³) located at 1.38 Å from O(6), and the deepest hole (-1.935 eÅ⁻³) located at 1.01 Å from Tb(1).

The crystal structure of Tb-AV-22 was determined by single-crystal XRD and was found to be identical to the analogous compounds containing Ho³⁺ and Y³⁺ previously reported by Ponomarev *et al.* [4] and Maksimov *et al.* [5], respectively. Phase purity and homogeneity of the bulk sample were further confirmed using powder XRD.

Appendix I collects information concerning crystallographic data collection and structure refinement of Tb-AV-22. Atomic coordinates, isotropic displacement parameters, main bond lengths and angles are given in tables.

Tb-AV-22 contains a single crystallographically unique Tb³⁺ centre, TbO₆, coordinated to six SiO₄ tetrahedra (Figure 4.2), with a geometry best described as a slightly distorted octahedron [Tb–O bond lengths and angles in the 2.225(6)-2.33(4) Å and 83.78(13)-176.42(12)° ranges, respectively]. The two crystallographically independent silicon tetrahedra have distinct structural functions: SiO₄H [Si(2)] establish corner-sharing bridges between adjacent TbO₆ octahedra, leading to the formation of one-dimensional arrays running along the *c* direction [Tb(1)⋯Tb(1)ⁱ 5.9072(12) Å; symmetry code: (i) *x, y, z+1*]; SiO₄ units [Si(1)] share corners with two SiO₄H tetrahedra and two TbO₆ octahedra [through O(1) and O(6) atoms; Figure 4.2], establishing links between adjacent one-dimensional arrays [Tb(1)⋯Tb(1)ⁱⁱ 6.8872(13) Å; symmetry code: (ii) *x-1/2, y, 1/2-z*] and leading to the formation of a two-dimensional [TbSi₃O₈(OH)₂]³⁻ anionic perforated plane net perpendicular to the *b* direction (Figures 4.2, 4.3).

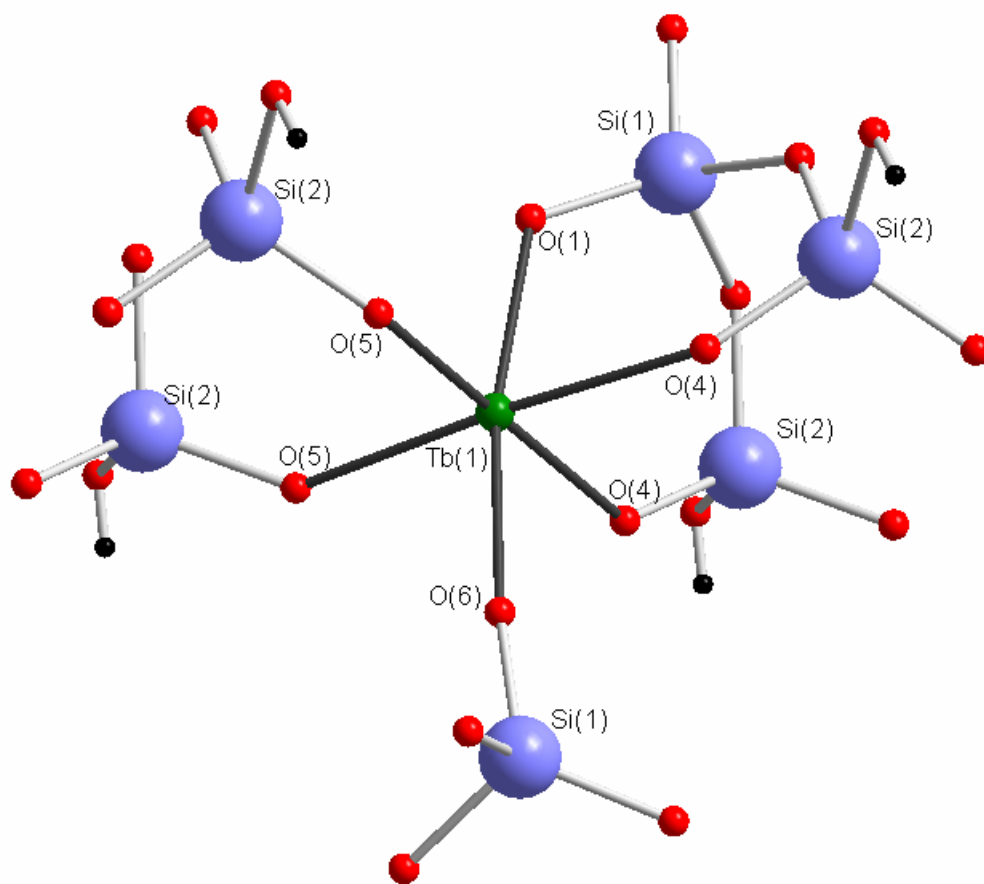


Figure 4.2 – Perspective view of a portion of the $[\text{TbSi}_3\text{O}_8(\text{OH})_2]^{3-}$ anionic layer of Tb-AV-22.

The crystal structure of Tb-AV-22 can be described as the parallel packing in a [ABAB \cdots] fashion along the *b* direction of $[\text{TbSi}_3\text{O}_8(\text{OH})_2]^{3-}$ anionic layers (two per *b* axis), which are further interconnected through classical strong O–H \cdots O hydrogen bonds between neighboring Si–OH groups [O(3)–H(1) \cdots O(4)ⁱⁱⁱ; $d(\text{D–H}) = 0.947(10)$ Å; $d(\text{H}\cdots\text{A}) = 1.73(2)$ Å; $d(\text{D}\cdots\text{A}) = 2.666(5)$ Å; $\angle(\text{DHA}) = 167(7)^\circ$; symmetry code (iii) $-x, 1-y, 1-z$] (Figure 4.3).

Two crystallographically unique charge-balancing K^+ cations are located within the channels of the hydrogen-bonded $[\text{TbSi}_3\text{O}_8(\text{OH})_2]^{3n-}$ anionic framework, with the minimum K(1) \cdots K(2)^{iv} distance being 3.7373(16) Å [symmetry code: (iv) $x, y, z+1$]. K(1) is located within the pores of the $[\text{TbSi}_3\text{O}_8(\text{OH})_2]^{3-}$ layers (Figure 4.3), and is surrounded by nine O-atoms with the K \cdots O distances 2.638(5)–3.248(4) Å. K(2) occupies instead the interlayer space interacting with eight neighboring O-atoms [K \cdots O distances

2.716(4)-3.293(2) Å]. The minimum Tb(1)⋯K(1)ⁱⁱ and Tb(1)⋯K(2)^v distances are 3.6752(18) Å and 3.8261(14) Å, respectively [symmetry codes: (v) 1/2-x, 1-y, -1/2+z].

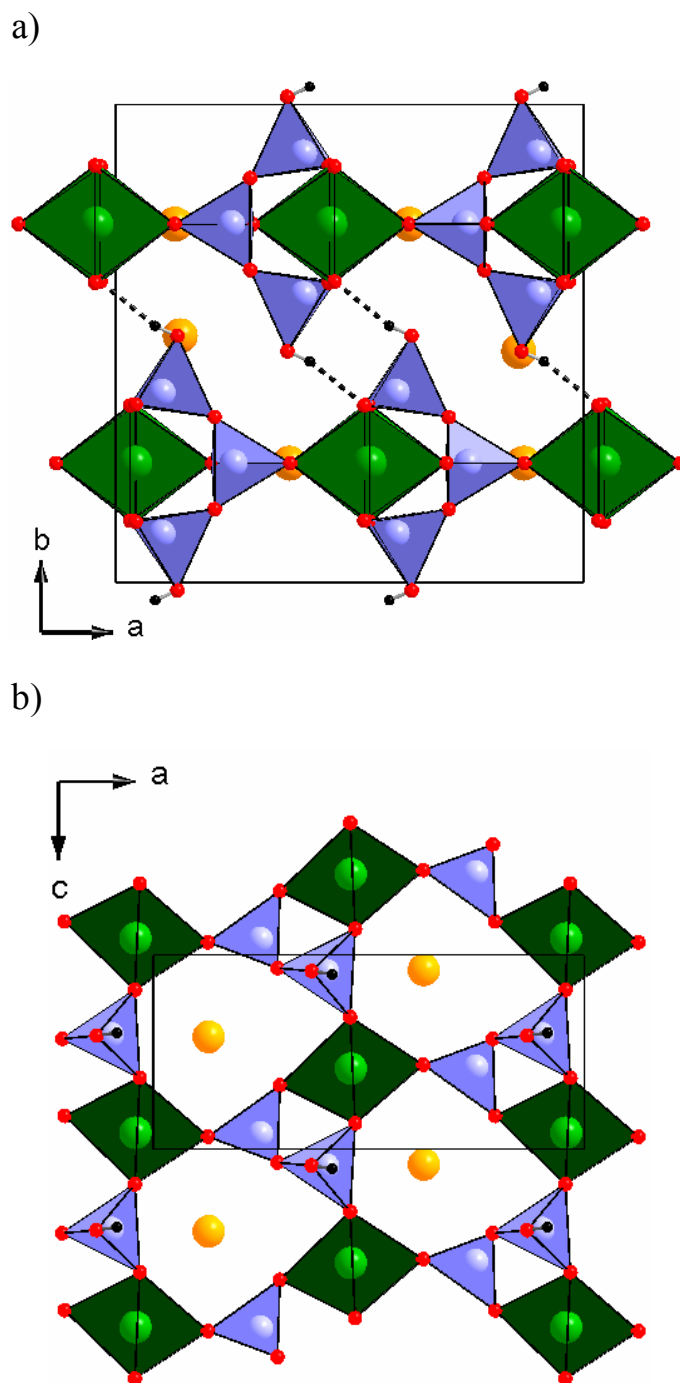


Figure 4.3 – a) Polyhedral representation of the unit cell contents of Tb-AV-22 viewed along the *c* axis. O–H⋯O hydrogen bonds are drawn as black dashed lines and K⁺ ions as orange circles. b) Perforated, single [TbSi₃O₈(OH)₂]³⁻ layer showing K(1) ions. Polyhedra: green TbO₆, blue SiO₄H and SiO₄; spheres: orange K⁺, black H, red O.

The powder XRD patterns of Er-AV-22 and Eu-AV-22 are similar to the pattern of Tb-AV-22 and were indexed with the PowderX package [14] using the first 24 well-resolved lines. An orthorhombic unit cell with $a = 13.5264$, $b = 13.1564$, $c = 5.8663$ Å for Er-AV-22, and $a = 13.5928$, $b = 13.2292$, $c = 5.9284$ Å for Eu-AV-22 was indicated by the TREOR90 indexing program [15] with high figures of merit, $M_{24} = 66$ and 69 , respectively.

The coordinates of atoms of Tb-AV-22 (single-crystal data) were used as the starting point in the Rietveld refinement of the structures of Er- and Eu-AV-22 samples by the FULLPROF program [16]. The final profile analysis refinement was carried out in the range $12.00 - 129.99^\circ 2\theta$ for the occurring 997 “independent” reflections and involved the following: structural parameters – 31 fractional atomic coordinates; 4 isotropic temperature factors; two parameters for the preferred orientation function (March's function), profile parameters – one scale factor, one parameter (η) for the pseudo-Voigt peak shape function, three parameters (U , V , W) to describe the angular dependence of the peak full-width-at-half-maximum (FWHM), three unit cell parameters, two peak asymmetry parameters; global parameters – one zero-point shift, six coefficients of polynomial background. Soft constraints to some of the bond distances were applied. The final conventional R -factors were $R_p = 9.04$, $R_{wp} = 11.7$, $R_{exp} = 7.05$, $\chi^2 = 2.76$ and $R_B = 5.74$ for Er-AV-22, and $R_p = 14.4$, $R_{wp} = 17.6$, $R_{exp} = 6.80$, $\chi^2 = 6.70$ and $R_B = 9.52$ for Eu-AV-22. The final profile fit for Er and Eu-AV-22 are shown in Figure 4.4 and Figure 4.5, respectively. Final lattice parameters are summarized in Table 4.2 and compared with related data for similar materials.

Table 4.2 – Unit cell parameters of AV-22 materials.

RE	a (Å)	b (Å)	c (Å)	Volume (Å ³)	Space Group
Y [5]	13.536(5)	13.17(1)	5.867(2)	1045.91(95)	<i>Pmnb</i>
Ho [4]	13.534(5)	13.175(5)	5.880(4)	1048.5	<i>Pmnb</i>
Yb [6]	13.088(3)	13.505(3)	5.843(1)	1032.8(4)	<i>Pnma</i>
Eu	13.2462(2)	13.6103(3)	5.9436(2)	1071.54(5)	<i>Pnma</i>
Er	13.1526(3)	13.5228(3)	5.8676(2)	1043.61(5)	<i>Pnma</i>

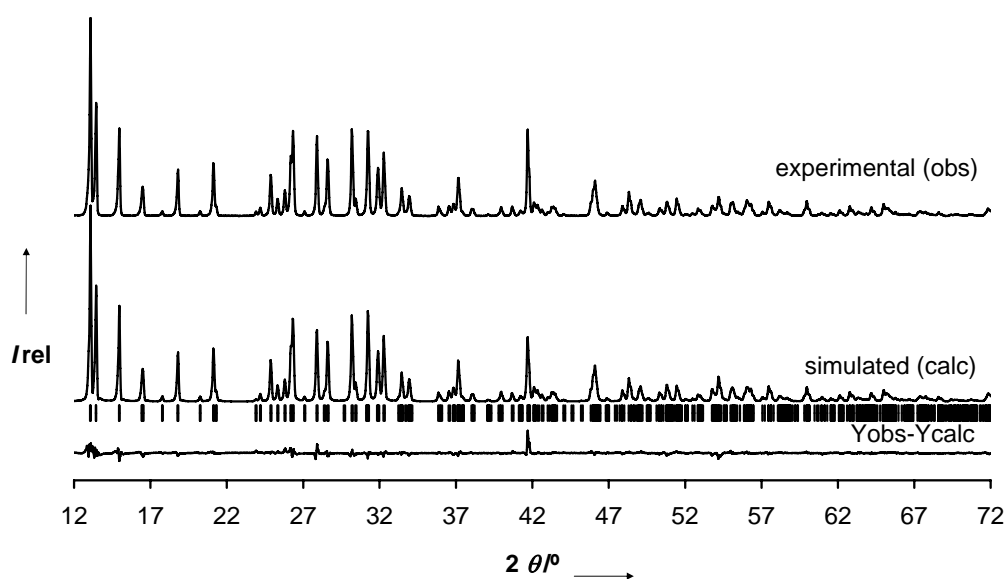


Figure 4.4 – Experimental and simulated powder XRD patterns of Er-AV-22.

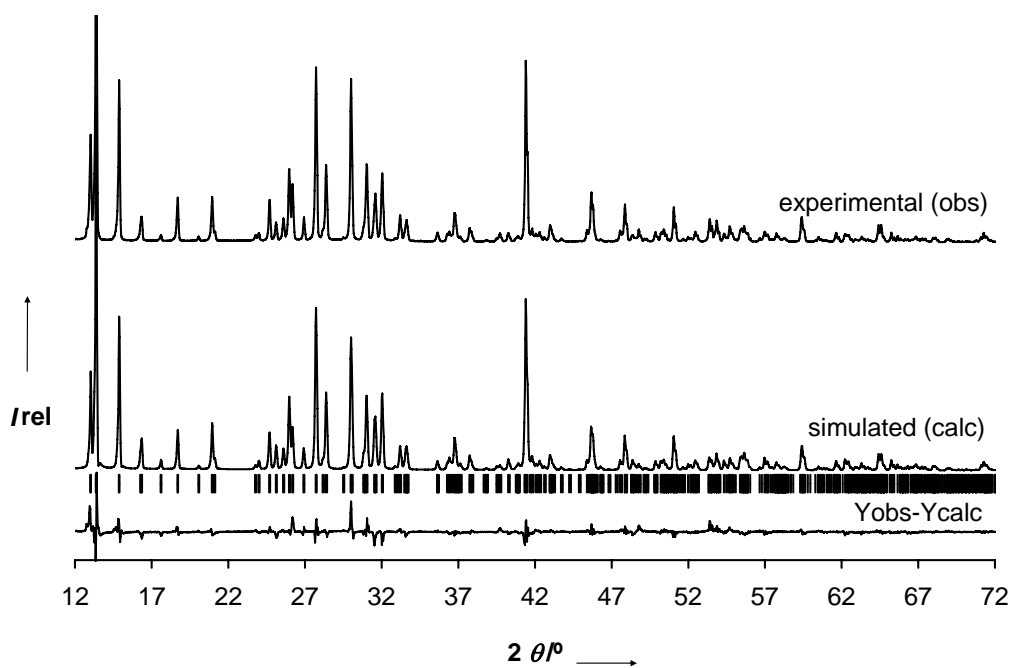


Figure 4.5 – Experimental and simulated powder XRD patterns of Eu-AV-22.

All studied $(K_3[M_{1-a}Ln_aSi_3O_8(OH)_2])$, $M=Y^{3+}, Tb^{3+}$; $Ln=Eu^{3+}, Er^{3+}, Tb^{3+}, Gd^{3+}$ and Ce^{3+} , $1 \geq a > 0$ materials display powder XRD patterns characteristic of AV-22 (Figure 4.6 and Figure 4.7) and no evidence was found for the presence of any impurity phases.

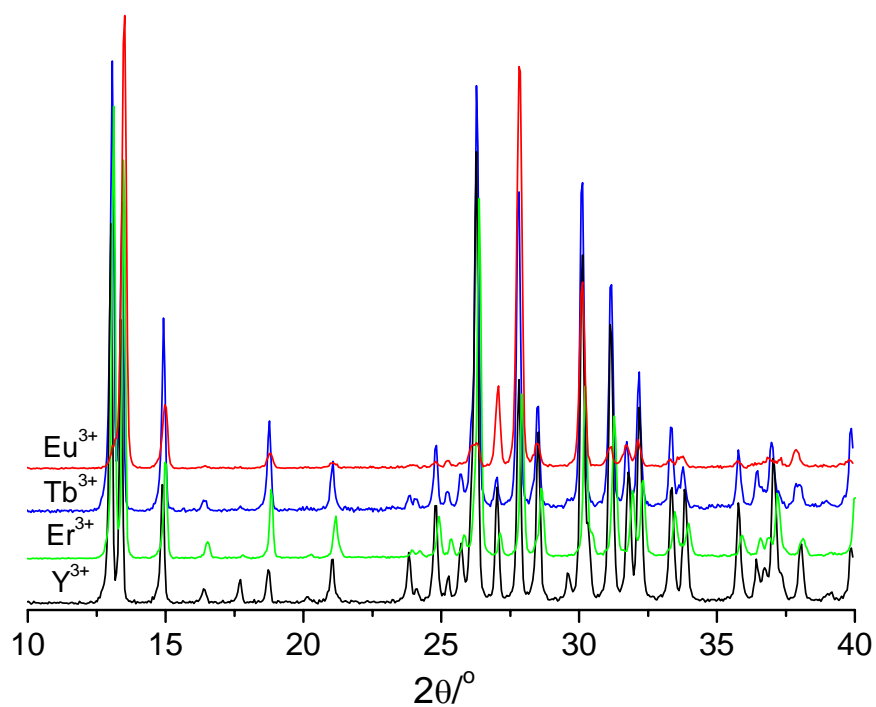


Figure 4.6 – Experimental powder XRD patterns of pure AV-22 samples.

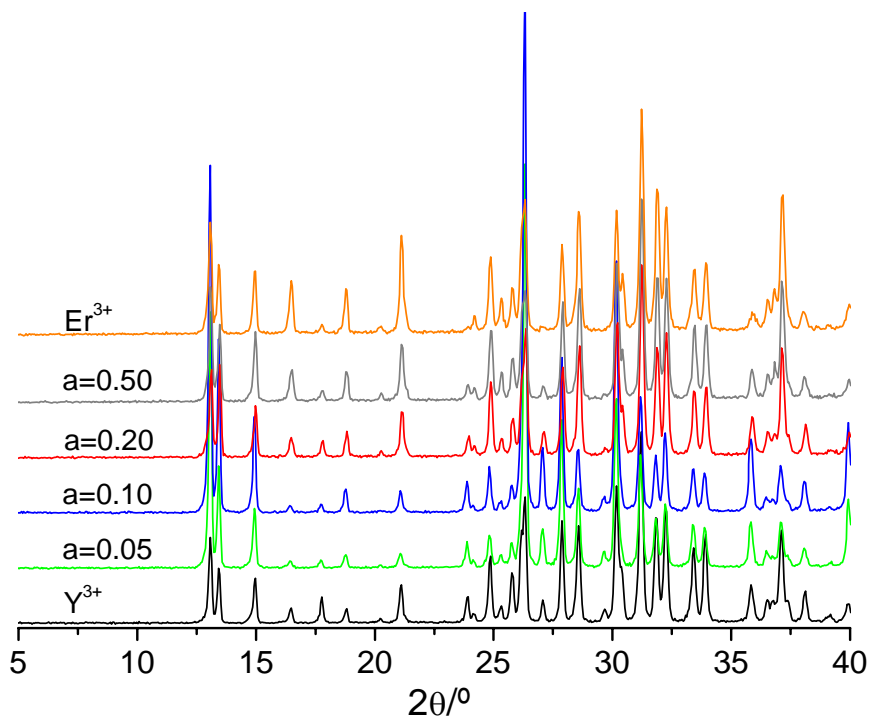


Figure 4.7 – Experimental powder XRD patterns of mixed Y/Er-AV-22 samples (a indicates the Er^{3+} content)

Figure 4.8 displays the scanning electron microscopy images of RE-AV-22 materials (RE=Y, Er, Tb and mixed Y/Er, Tb/Eu and Tb/Ce).

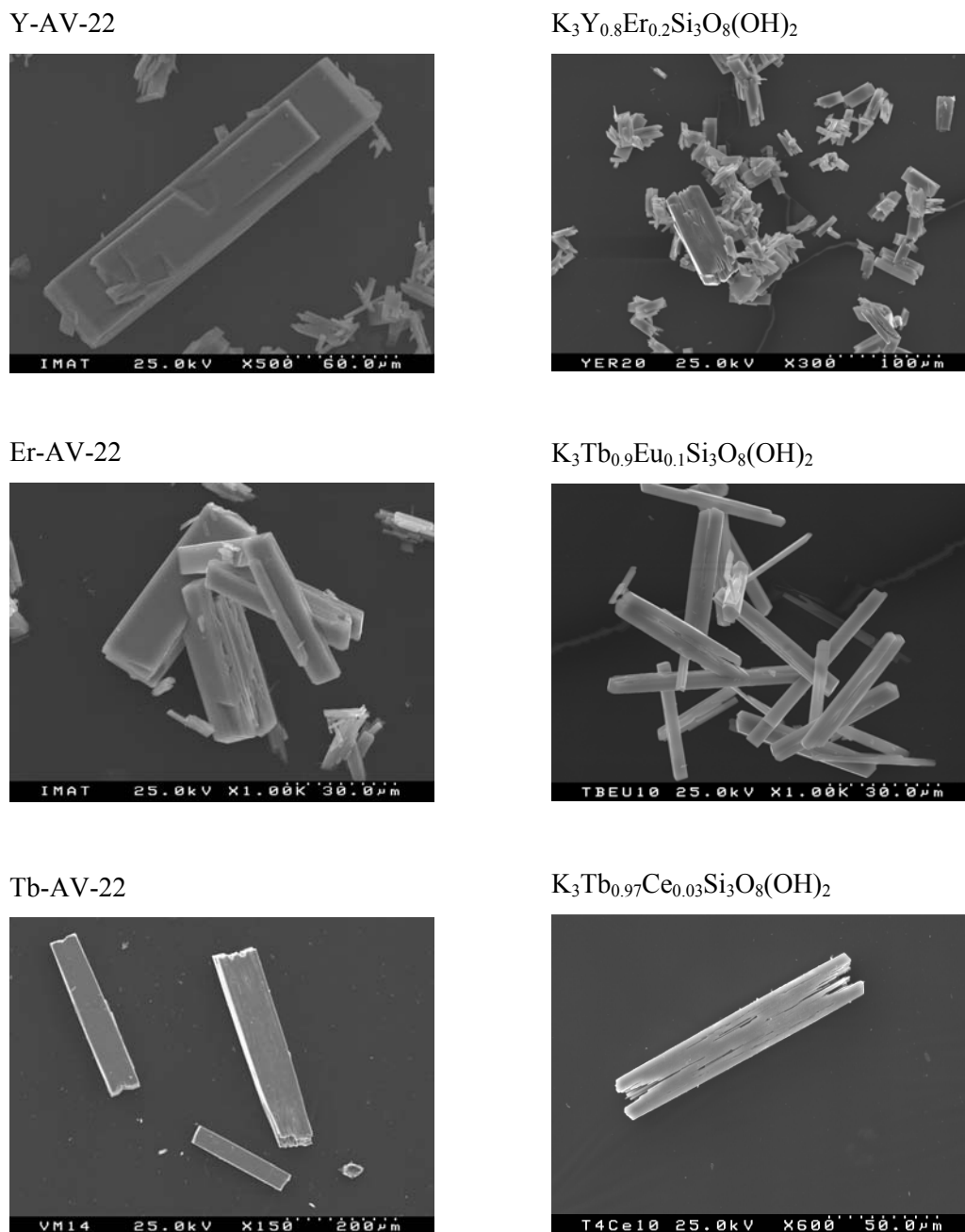


Figure 4.8 – Scanning electron micrographs of pure and mixed AV-22 compositions.

Within experimental error, chemical analysis by EDS confirmed the Si:Ln:K molar ratios obtained by powder XRD, *ca.* 3:1:3. Mixed samples $K_3[M_{1-a}Ln_aSi_3O_8(OH)_2]$,

$M^{3+}=Y^{3+}, Tb^{3+}; Ln^{3+}=Eu^{3+}, Ce^{3+}$ $1 \geq a > 0$ contained a small excess of RE^{3+} ions [(K/M+RE) molar ratio 2.8-2.9]. For mixed RE^{3+} samples, no crystals rich in an individual rare-earth were found. All results indicated that rare-earths are randomly distributed within the crystals. ICP-AES chemical analysis yielded *ca.* 3.2 and 2.1 mol % Ce for, respectively, the Tb/Ce and Y/Ce samples, despite the fact that larger Ce amounts (5 mol % Ce) were present in the parent synthesis gel.

Table 4.3 – Molar ratios obtained by EDS (normalized to the RE content).

Sample	Si	M or (M+Ln)	K
Y-AV-22	3.0	1.0	3.0
Tb/Eu-AV-22	3.0	1.0	2.8
Y/Ce-AV-22	3.0	1.0	2.9
Tb/Ce-AV-22	3.0	1.0	2.9

TGA curves were measured under nitrogen atmosphere using a 10 °C/min heating rate. They reveal a weight loss step at 600-650 °C. Figure 4.9 shows the TG and DTA curves for Er-AV-22. The total weight loss between 26 and 700 °C was 3.91, 3.53, 3.45 and 3.33 % for, respectively, Y-, Eu-, Tb- and Er-AV-22 materials, corresponding to *ca.* 1 water molecule.

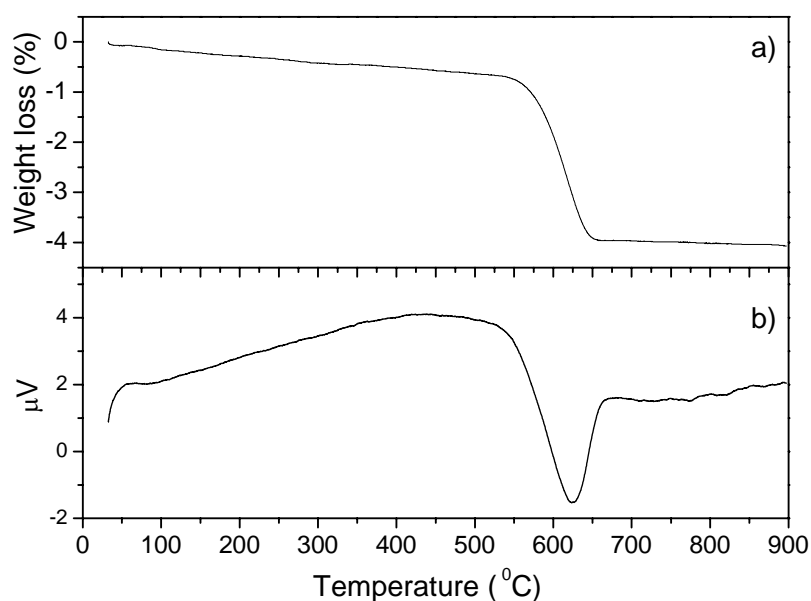


Figure 4.9 – a) TG and b) DTA curves for Er-AV-22.

The ^{29}Si MAS NMR spectrum of Y-AV-22 (Figure 4.10) displays two resonances at -75.4 and -85.4 ppm in a 2:1 area ratio, in accord with the crystal structure which calls for the presence of two Si local environments with 2:1 populations.

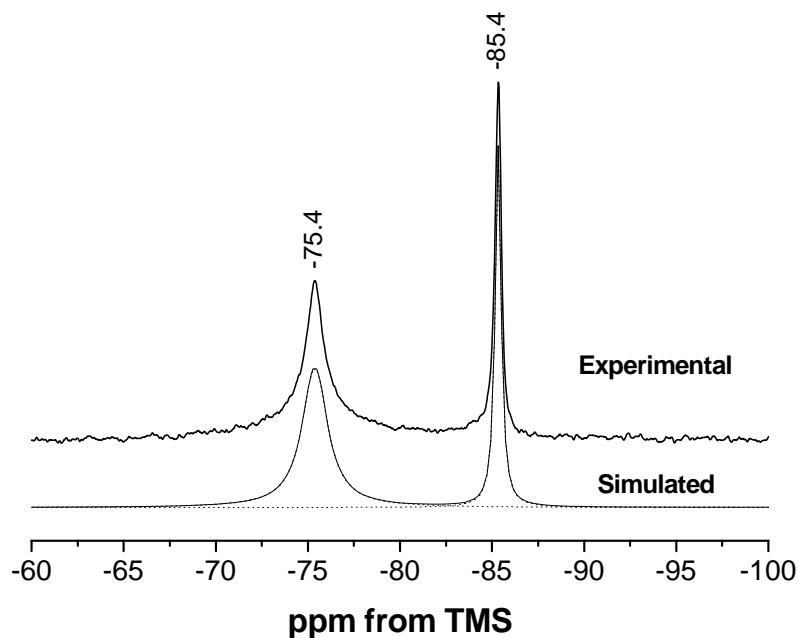


Figure 4.10 – Experimental and simulated ^{29}Si MAS NMR spectra of Y-AV-22.

Figure 4.11 represents the two different Si local environments according to the crystal structure. Si(1) is of the type Q^2 $\text{Si}[2\text{Si}; 2\text{Y}]$ and should represent resonances at higher isotropic chemical shift compared to Si(2), which type is Q^1 $\text{Si}[1\text{Si}; 2\text{Y}, \text{K}]$.

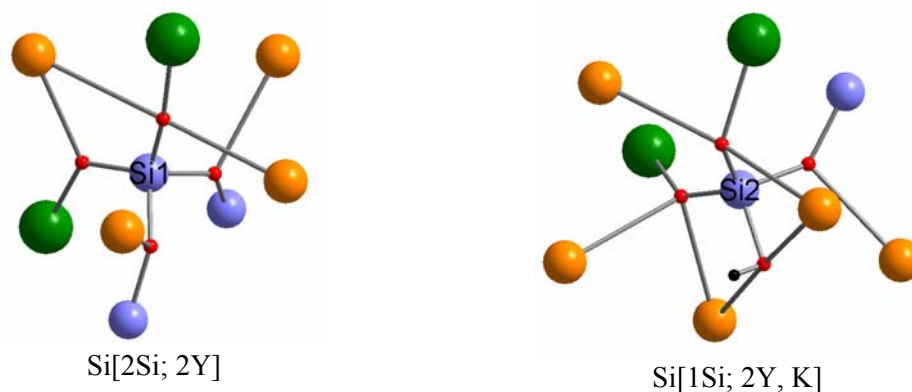


Figure 4.11 – Si local environments in the structure of Y-AV-22. Green - Y^{3+} , blue - Si^{4+} , red - O^{2-} , orange - K^+ , black - H^+ .

The FWHM of the former peak narrows from 132 to 53 Hz when the spinning rate increases from 5 to 15 kHz. A similar resolution improvement is observed with high-power ^1H decoupling at 5 kHz MAS (Figure 4.12). Moreover, upon ^1H - ^{29}Si cross-polarization the intensity of the -75.4 ppm peak increases relatively to the intensity of the -85.4 ppm resonance. These effects confirm that the -75.4 ppm peak is attributed to Si(2) which, being connected to a hydroxyl group, has a significant dipolar interaction with ^1H .

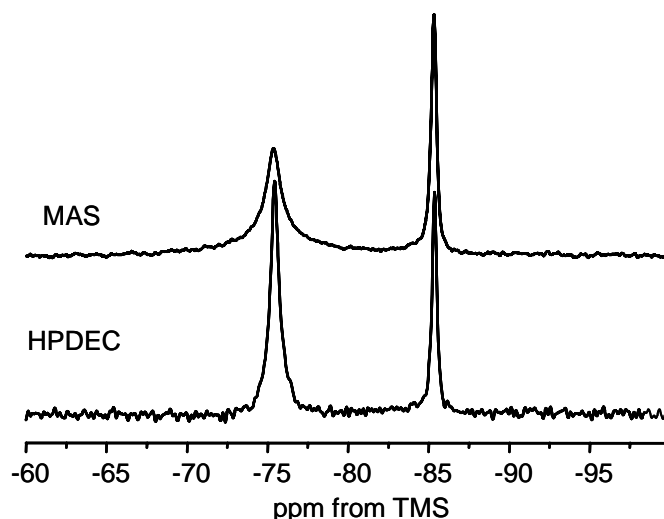


Figure 4.12 – ^{29}Si MAS and high-power ^1H decoupling (HPDEC) MAS NMR spectra of Y-AV-22 recorded with a 5 kHz spinning rate and 60 s recycle delay.

Due to the paramagnetism of Eu^{3+} , Tb^{3+} and Er^{3+} lanthanide ions, it was not possible to obtain ^{29}Si MAS NMR spectra with acceptable quality for the pure Eu^{3+} -, Tb^{3+} - and Er^{3+} -AV-22 samples. However, by using fast (15 kHz) MAS rates and short (1 s) recycle delays we were able to record spectra of some mixed Y/Er-AV-22 samples (a indicates the Er content). For $a=0.05$ the spectrum gives two ^{29}Si MAS NMR peaks in a 2:1 area ratio at, respectively, -75.4 and -85.4 ppm (Figure 4.13). For $a=0.20$ only one resonance is observed at -78.7 ppm, together with several spinning sidebands, while sample $a=0.50$ gives a broad peak at -86.7 ppm and very intense spinning sidebands. No spectra could be recorded at higher Er contents. The broadening of the NMR resonances and the strong spinning sideband patterns observed are caused by the interaction between the Ln^{3+} unpaired electrons and the ^{29}Si nuclei (a through-space dipolar interaction, when the pseudo-contact shift is dominant). This clearly shows that Er^{3+} (or other Ln^{3+} ion) is being inserted in the lattice of AV-22, in accord with EDS microanalysis which indicates

that (i) the crystallites contain both Y^{3+} and Er^{3+} , and (ii) no significant amount of any separated Er^{3+} -rich phase is present.

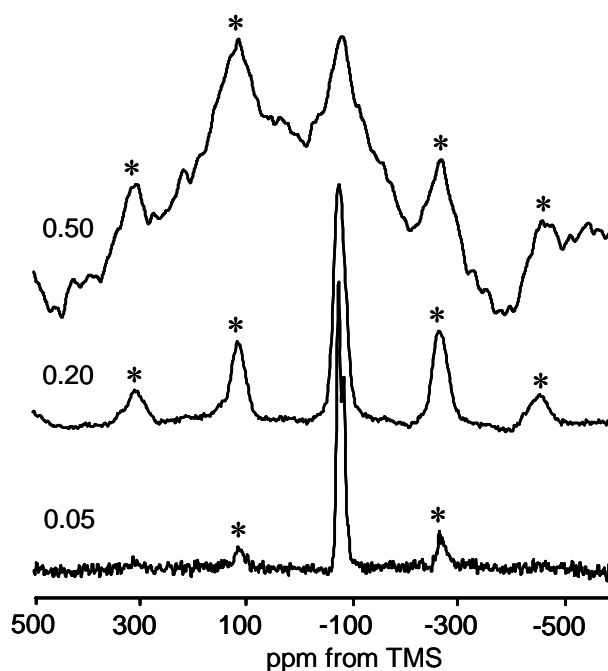


Figure 4.13 – ^{29}Si MAS NMR spectra of $\text{K}_3[\text{Y}_{1-a}\text{Er}_a\text{Si}_3\text{O}_8(\text{OH})_2]$ (a is indicated) recorded with a 15 kHz spinning rate and 60 s recycle delay. Asterisks depict spinning sidebands.

The Raman spectrum of Tb-AV-22 (Figure 4.14) shows several sharp bands between 100 and 1200 cm^{-1} . Numerous bands in the low-, medium-, and high-wavenumber range were recorded. Symmetric Si–O stretching vibrations of SiO_4 groups with one, two, three, or four nonbridging oxygens emerge in alkali silicates with different contents of metal oxides in the high-wavenumber range (800–1200 cm^{-1}) [17–19]. Bands in the intermediate-wavenumber range (400–800 cm^{-1}) result from symmetric bending vibrations of the Si–O–Si bridging oxygens between adjacent SiO_4 tetrahedra. Compared to the Raman shifts observed in silicate glasses and melts, the Raman bands in the range between 400 and 600 cm^{-1} and below 400 cm^{-1} can be assigned to the presence of Si–O–Si symmetric stretching vibrations and the bending of the Si–O–Si linkages, respectively [20]. In yttrium orthosilicate crystals, vibration bands in the 500–700 cm^{-1} range are generally characteristic of the YO_6 octahedra [21] and thus the band at 668 cm^{-1} is attributed to Tb–O stretching vibrations of TbO_6 octahedra. Below 400 cm^{-1} bands are mainly caused by lattice vibrations of the framework or skeleton and cation-oxygen bonding [17]. Typical

values for Ln-O stretching vibrations are around 300 cm^{-1} , located in the region of lattice vibrations thus the band at 332 cm^{-1} is attributed to Tb-O stretching vibrations [22].

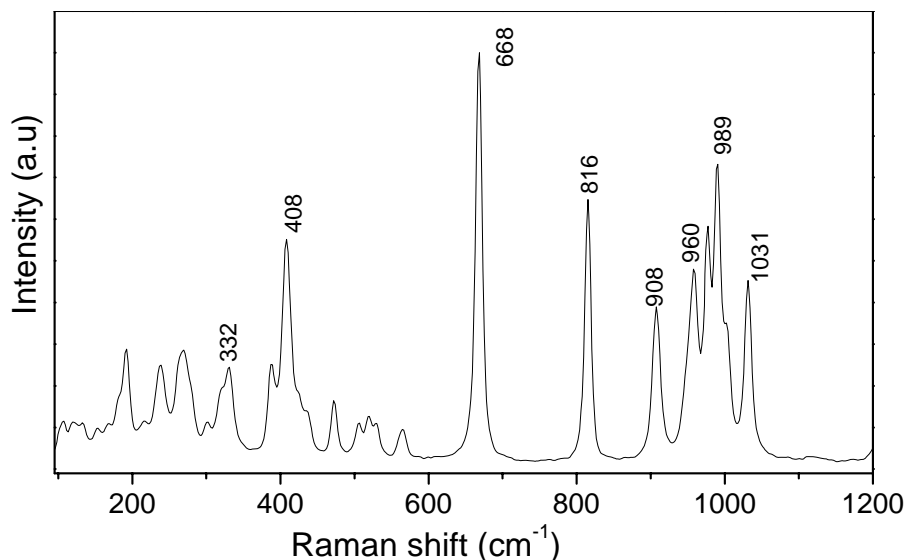


Figure 4.14 – Raman spectrum of Tb-AV-22.

4.4 Photoluminescence spectroscopy

Figure 4.15 shows the UV/Vis excitation spectra of $\text{K}_3[\text{Y}_{1-a}\text{Tb}_a\text{Si}_3\text{O}_8(\text{OH})_2]$ for $a=0.1$ and 1 (pure Tb^{3+} sample) at room temperature (RT), monitored at the Tb^{3+} $^5\text{D}_4 \rightarrow ^7\text{F}_5$ transition (540.5 nm). To allow a quantitative comparison, spectra were consecutively recorded keeping the experimental set-up fixed (slits width, irradiated area, optics geometry), and using powders of similar grain size packed in quartz cells. The sharp lines between 300 and 500 nm are assigned to $^7\text{F}_6 \rightarrow ^5\text{D}_{4-0}$, $^5\text{L}_{10}$ and $^5\text{G}_{6-3}$ intra-configurational forbidden $4f^8 \rightarrow 4f^8$ transitions of Tb^{3+} . The broad band between 250 and 300 nm is ascribed to the spin-forbidden (high-spin, HS) inter-configurational $4f^8 \rightarrow 4f^7 5d^1$ transition of Tb^{3+} [23-25]. At low temperature (10 K), the HS band distinctly shows three components at *ca.* 35510, 37510 and 38110 cm^{-1} due to the crystal field splitting of the $5d$ configuration (inset in Figure 4.15). This type of spin-forbidden fd band may be observed for (heavy) lanthanide ions with more than seven $4f$ electrons at an energy lower than the energy of spin-allowed (low-spin, LS) fd transitions [24,25]. The broad band at *ca.* 234 nm (inset in Figure 4.15) is assigned to the spin-allowed (LS) inter-

configurational fd transition of Tb^{3+} and the energy separation between the LS and HS fd transitions is *ca.* 7200 cm^{-1} . This is very similar to the energy separation between the LS and HS fd bands reported for the $YPO_4:Tb$ (1%), $CaF_2:Tb$ (0.1%), and $LiYF_4:Tb$ (1%) crystals (7370 , 7920 , and 7995 cm^{-1} , respectively) [24]. We note that the excitation spectra intensity has not been corrected for wavelengths lower than 240 nm and, therefore, the relative intensity of the LS band is not directly comparable.

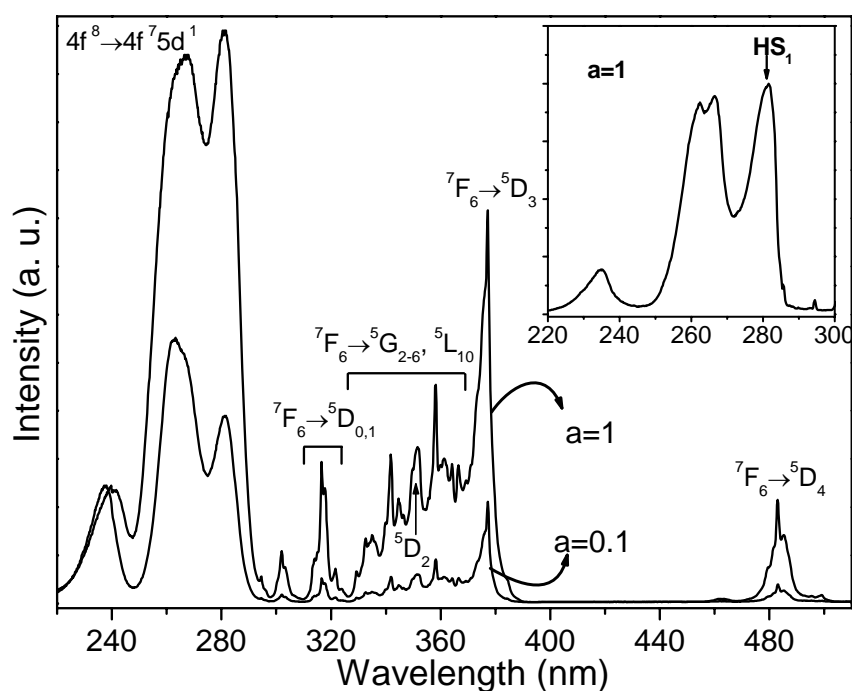


Figure 4.15 – Excitation spectra of $K_3[Y_{1-a}Tb_aSi_3O_8(OH)_2]$ ($a=1, 0.1$) monitored at the 7F_5 manifold (540.5 nm) at room temperature. The inset shows the excitation spectrum of a pure Tb^{3+} sample ($a=1$) monitored at the 7F_5 manifold (540.5 nm) at 10 K , showing the region in which the transition to the high-spin and low-spin fd states are observed.

Figure 4.16 shows the RT emission spectrum of $K_3[TbSi_3O_8(OH)_2]$ excited at 254 nm , which was selected because it corresponds to the highest excitation line of commercial mercury lamps. The emission lines are assigned to the ${}^5D_4 \rightarrow {}^7F_{2-6}$ transitions of Tb^{3+} . Luminescence from the higher (*e.g.* 5D_3) excited states is not detected, even for the samples with the lowest Tb^{3+} content, indicating very efficient non-radiative relaxation to the 5D_4 level. The same emission is obtained either with excitation at the maximum of the HS fd band or at the intra 5D_3 (377 nm) line. Mixed Y^{3+}/Tb^{3+} samples also display the same

emission spectrum. To evaluate the potential use of this phosphor in commercial save-energy lamps, the emission efficiency was qualitatively compared to that characteristic of the power of a standard commercial lamp. The standard used is 18W CHINT® [26] and its emission spectrum is displayed in Figure 2.11. The two spectra were measured keeping the experimental set-up fixed (slits width, irradiated area, and optics geometry). The two powders have different grain size and thus different cross-absorption. The integrated intensity of the $^5D_4 \rightarrow ^7F_5$ transition of the pure Tb^{3+} sample is about 0.87 of the integrated intensity of the mixture of lanthanide ions used in the commercial save-energy lamp.

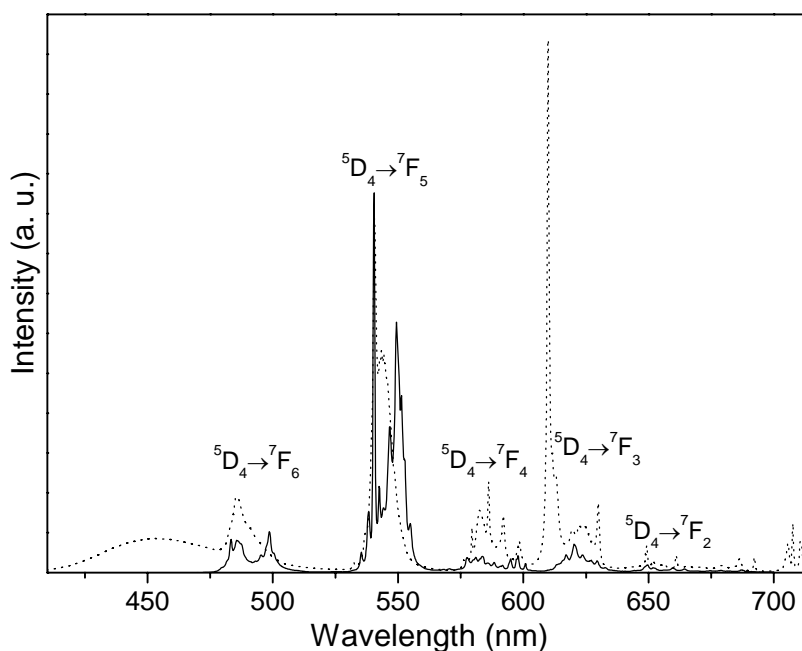


Figure 4.16 – Room temperature emission spectra of Tb-AV-22 (solid line) and a commercial save-energy 18W CHINT® lamp (dashed line) excited at 254 nm. The assignment of the emission lines is for Tb-AV-22.

Figure 4.17 shows the RT lifetimes for the 5D_4 level of Tb^{3+} in $K_3[Y_{1-a}Tb_aSi_3O_8(OH)_2]$, $a=0.05-1$. The lifetime curves of all samples are well fitted by a single exponential, indicating the presence of a single Tb^{3+} environment, in accord with the crystal structure. The room temperature decay curve for pure Tb-AV-22 sample is illustrated on Figure 4.18. Different excitation wavelengths (namely 280 nm, within the $4f^75d^1$) give similar 5D_4 lifetime values which remain essentially constant at *ca.* 4.74 ± 0.02 ms up to $a=0.2$ when it decreases linearly down to *ca.* 4.45 ± 0.02 ms.

Therefore, the 5D_4 lifetime only decreases by about 7%, indicating that the energy migration between Tb^{3+} ions is negligible.

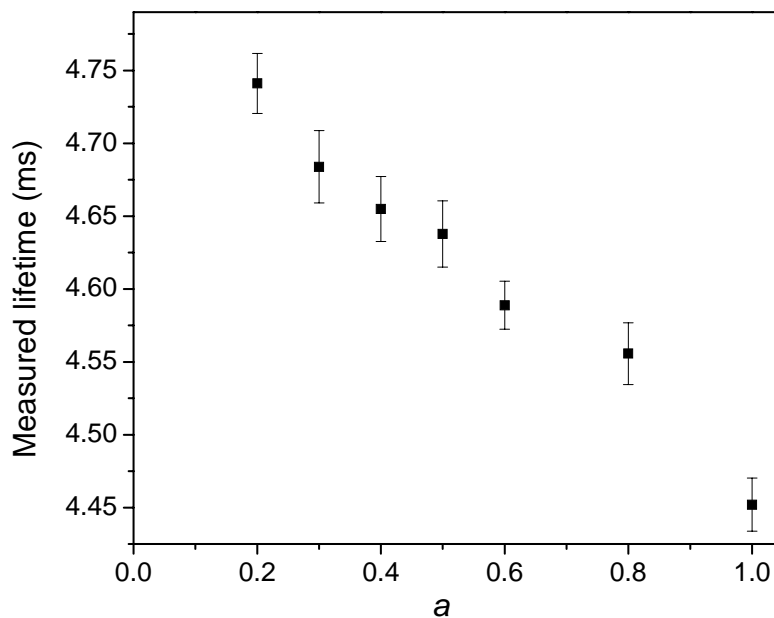


Figure 4.17 – Lifetime of the 5D_4 level of Tb^{3+} detected at the strongest 7F_5 manifold and excited at 377 nm, as a function of Tb^{3+} content in $K_3[Y_{1-a}Tb_aSi_3O_8(OH)_2]$, $a=0.05-1$.

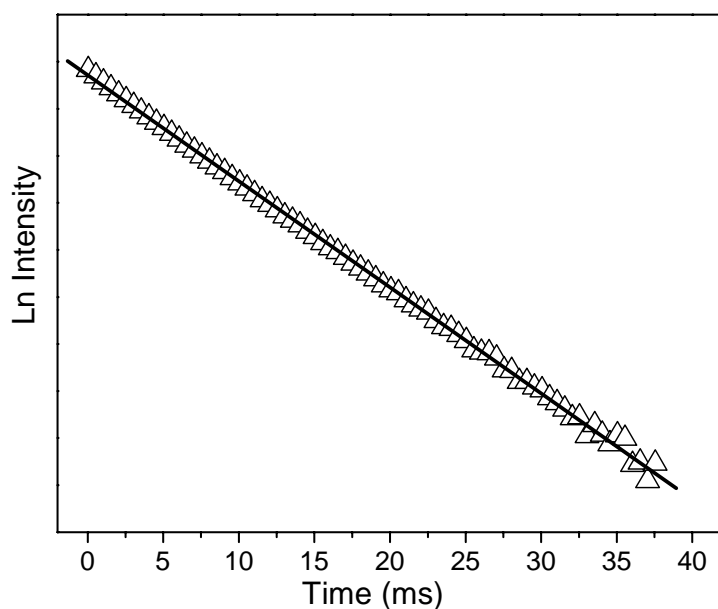


Figure 4.18 – Room temperature 5D_4 decay curve of Tb-AV-22 monitored at 540.5 nm under 377 nm excitation. The straight line is the best fit ($r^2 > 0.99$) to the data considering a single exponential behavior.

Non-radiative energy transfer from sensitizers to activators may occur via exchange interaction (requiring orbital overlap) and direct, through-space, multipolar interactions [27-29]. Because in AV-22 the TbO₆ octahedra are isolated from each other by six SiO₄ tetrahedra and the shortest Tb-Tb distance is almost 6.9 Å, a direct overlap of orbitals on different Tb³⁺ ions is difficult and, thus, the occurrence of exchange interaction mechanisms is unlikely [27,28]. Furthermore, the relatively small concentration quenching effect observed indicates that multipolar interactions between Tb³⁺ ions are unlikely.

Assuming that only non-radiative and radiative processes are essentially involved in the depopulation of the ⁵D₄ state, the efficiency, q may be defined as:

$$q = \tau_{exp} / \tau_r \quad (4.1)$$

where the experimental lifetime, τ_{exp} , is directly related to the radiative (k_r) and nonradiative (k_{nr}) probabilities of Tb³⁺

$$\tau = (k_r + k_{nr})^{-1} \quad (4.2)$$

and τ_r is the inverse of the radiative probability (lifetime in absence of quenching). Taking τ_r as the lifetime at 10 K (5.15 ± 0.02 ms) of $a=0.05$ sample (no measurable quenching concentration) and considering the RT lifetime (4.78 ± 0.02 ms), the efficiency of the ⁵D₄ → ⁷F₅ emission is estimated to be 0.92.

The excitation spectrum of K₃[EuSi₃O₈(OH)₂] monitored at the Eu³⁺ ⁵D₀ → ⁷F₂ (610.5 nm) transition (Figure 4.19) displays a series of sharp lines assigned to the ⁷F₀₋₁ → ⁵D₄₋₀, ⁵L₆, ⁵G₂₋₆, ⁵H₃₋₇ and ⁵F₁₋₅ Eu³⁺ intra $4f^6 \rightarrow 4f^6$ transitions. The faint broad (LS) band at high energy is probably the beginning of the spin-allowed, inter-configurational fd , Eu³⁺ transition band, which normally appears at an energy higher than the equivalent Tb³⁺ band.

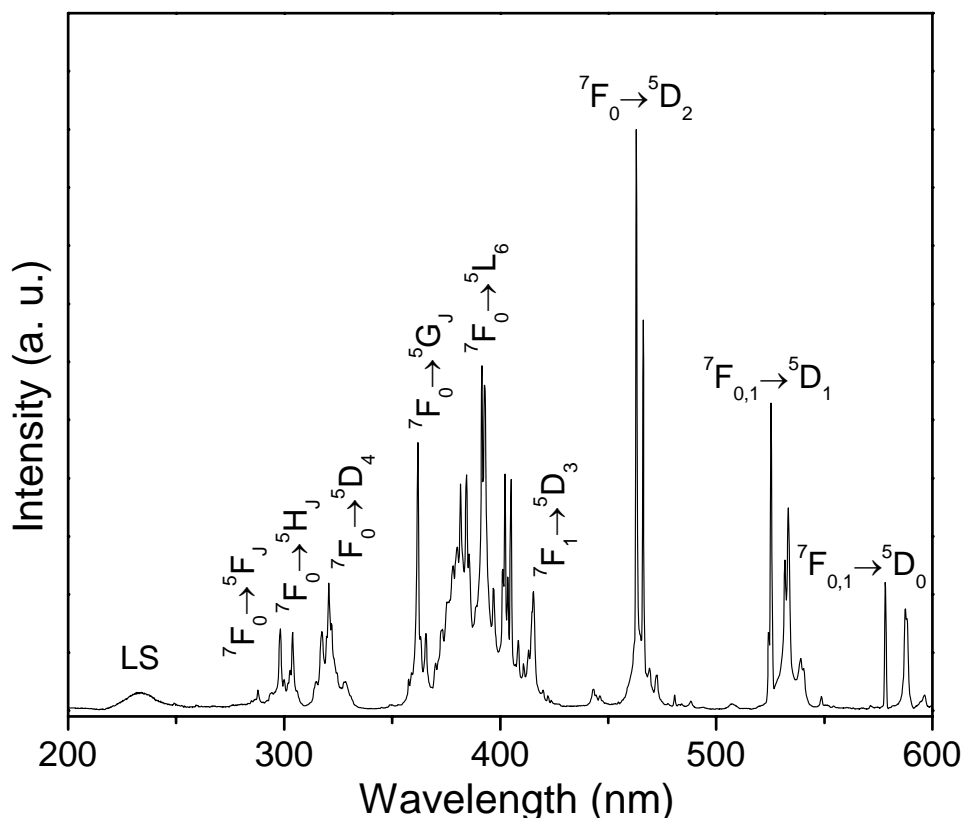


Figure 4.19 – Room temperature excitation spectrum of Eu-AV-22 monitored at the 7F_2 manifold (610.5 nm).

The room temperature emission spectrum of Eu-AV-22 (excited at 394 nm) is shown in Figure 4.20. The sharp emission lines are assigned to transitions between the first excited non-degenerate 5D_0 state and the ${}^7F_{0-4}$ levels of the fundamental Eu^{3+} septet. Eu^{3+} luminescence from higher excited states, such as 5D_1 , is not detected, indicating very efficient non-radiative relaxation to the 5D_0 level. The local-field splitting of the ${}^5D_0 \rightarrow {}^7F_1$ transition measured at 10K in five Stark components (inset in Figure 4.20) clearly shows the presence of two distinct Eu^{3+} environments. According to the XRD structure, both the Eu^{3+} ions residing in the layers and the K(1) ions (on the plane of the layers) are located on a mirror plane of the $Pnma$ (D_{2h}^{16}) space group, whereas K(2) ions in the interlayer space are in a generic crystallographic position (Figure 4.3). Thus, since the group-theoretical selection rules of the D_{2h} space group do not allow the occurrence of ${}^5D_0 \rightarrow {}^7F_0$ line and ${}^5D_0 \rightarrow {}^7F_2$ electric-dipole transitions with intensities greater than the ${}^5D_0 \rightarrow {}^7F_1$ magnetic-dipole lines [30] some Eu^{3+} ions must inevitably occupy the K(2) positions. This is

supported by EDS chemical analysis which revealed a K/Eu molar ratio of *ca.* 2.9 slightly smaller than 3.

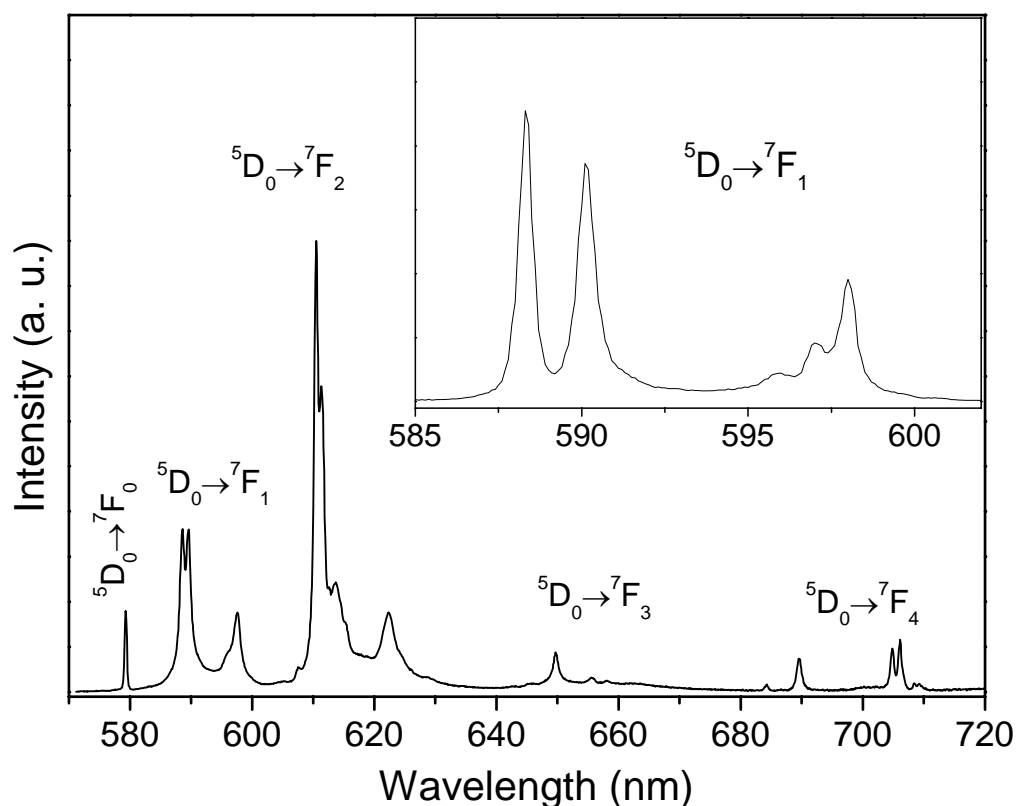


Figure 4.20 – Room temperature emission spectrum of Eu-AV-22 excited at 5L_6 manifold (394 nm). The inset shows an expansion of the $\text{Eu}^{3+} \ ^5D_0 \rightarrow \ ^7F_1$ transition collected at 10 K.

Lifetime measurements (Figure 4.21) confirm the presence of two local Eu^{3+} environments in $\text{K}_3[\text{EuSi}_3\text{O}_8(\text{OH})_2]$. The 5D_0 decay curve detected at 595.5 nm and excited at 394 nm is well fitted by a bi-exponential function yielding lifetimes of *ca.* 2.02 ± 0.02 and 0.58 ± 0.02 ms. When compared with the curve measured at 579.3 nm, the contribution of the shorter lifetime to the 5D_0 decays decreases for detection within the $^5D_0 \rightarrow \ ^7F_0$ (579.3 nm) and $^5D_0 \rightarrow \ ^7F_2$ (610.5 nm) transitions. Moreover, lifetime measurements of $\text{K}_3[\text{Y}_{1-a}\text{Eu}_a\text{Si}_3\text{O}_8(\text{OH})_2]$ ($a=0.1, 0.2, 0.4$ and 0.5) samples indicate that the short lifetime is present only for $a>0.2$. Indeed, the decay curves of $a=0.1$ and 0.2 samples are well fitted by an exponential, yielding lifetimes of *ca.* 2.46 ± 0.01 and 2.41 ± 0.01 ms, respectively. The longer lifetimes of samples $a=0.4$ and 0.5 are 2.36 ± 0.01 and 2.32 ± 0.01 ms, respectively. Hence, the 5D_0 lifetime decreases about 17%. Although the concentration quenching effects are more important than observed for

$K_3[Y_{1-a}Tb_aSi_3O_8(OH)_2]$ samples, the energy migration between Eu^{3+} ions still play a minor role. The structural similarity of Eu-AV-22 and Tb-AV-22 implies that energy transfer between active optical Eu^{3+} centers located in the layers is unlikely. Thus, the energy migration should occur between Eu^{3+} centers in the layers and in the interlayer space in K(2) positions (probably both by exchange and multipolar interactions mechanisms) [27-29].

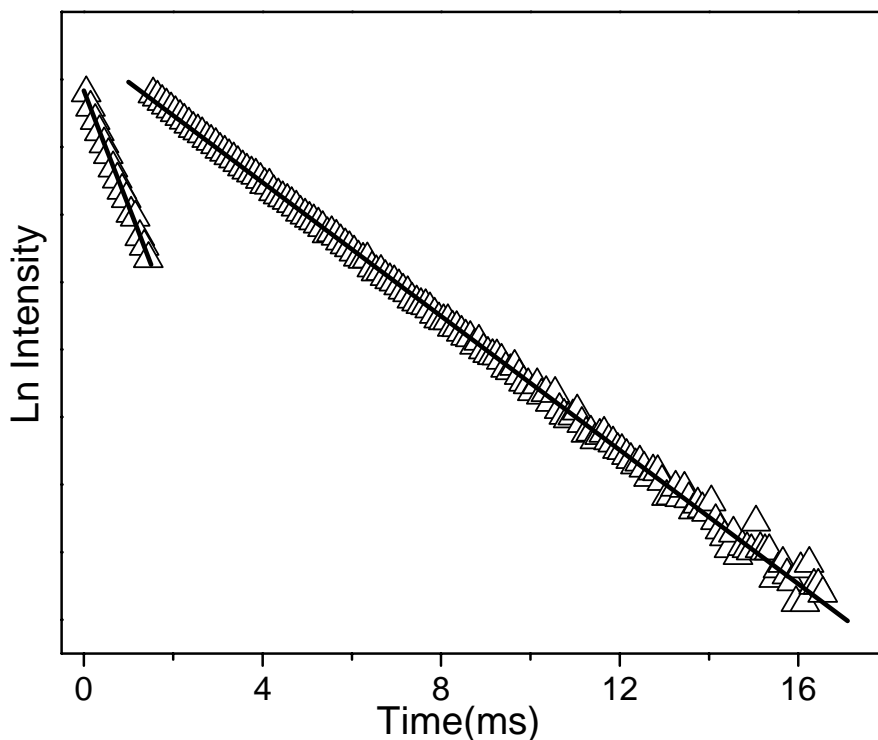


Figure 4.21 – Room temperature 5D_0 decay curve of Eu-AV-22 monitored at 610.5 nm under 394 nm excitation. The straight lines are the best fits ($r^2 > 0.99$) to the data considering a bi-exponential behavior.

The excitation spectra of $K_3[Tb_{0.95}Eu_{0.05}Si_3O_8(OH)_2]$ and $K_3[EuSi_3O_8(OH)_2]$, monitored at the main ${}^5D_0 \rightarrow {}^7F_2$ line (610.5 nm), display the same Eu^{3+} lines (Figure 4.22) and, in addition, the characteristic excitation spectrum of $K_3[TbSi_3O_8(OH)_2]$ (Figure 4.15). This is clear evidence for efficient Tb^{3+} -to- Eu^{3+} energy transfer. Furthermore, the Tb^{3+} -to- Eu^{3+} energy transfer is also detected in the emission of the $K_3[Tb_{0.95}Eu_{0.05}Si_3O_8(OH)_2]$ samples, (Figure 4.23).

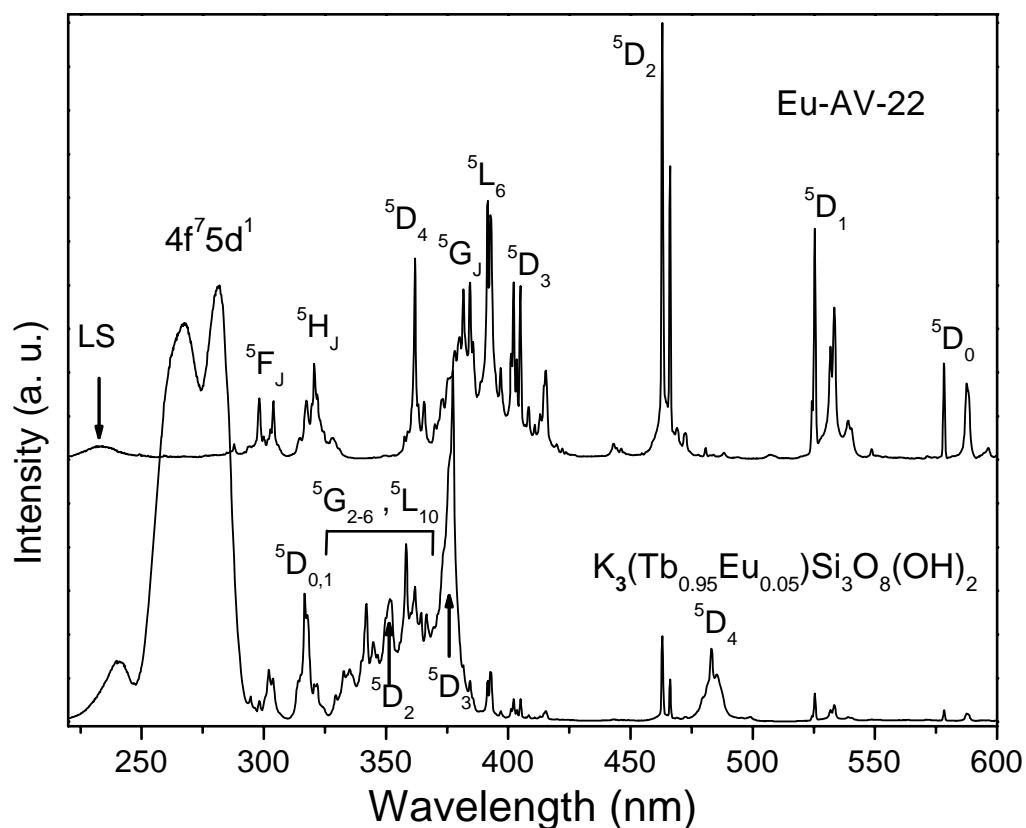


Figure 4.22 – Room temperature excitation spectra of Eu-AV-22 and $K_3[Tb_{0.95}Eu_{0.05}Si_3O_8(OH)_2]$, monitored at the 7F_2 manifold (610.5 nm).

Figure 4.23 illustrates the emission spectrum of $K_3[Tb_{0.95}Eu_{0.05}Si_3O_8(OH)_2]$ excited in the Tb^{3+} (377 nm) levels shows the typical Eu^{3+} lines (present in the spectrum of the pure Eu^{3+} sample) and ${}^5D_4 \rightarrow {}^7F_{5,6}$ transitions of the pure Tb^{3+} sample. Similar spectra were recorded with excitation within other Tb^{3+} levels (485 nm, 5D_4 and 280 nm, HS *fd*), not overlapping with Eu^{3+} states. For a sample with higher ($a=0.1$) Eu^{3+} content, the intensity of the ${}^5D_4 \rightarrow {}^7F_{5,6}$ Tb^{3+} transitions decreases 40 %, relatively to the sample with $a=0.05$. This further supports the above mentioned energy transfer between Tb^{3+} and Eu^{3+} .

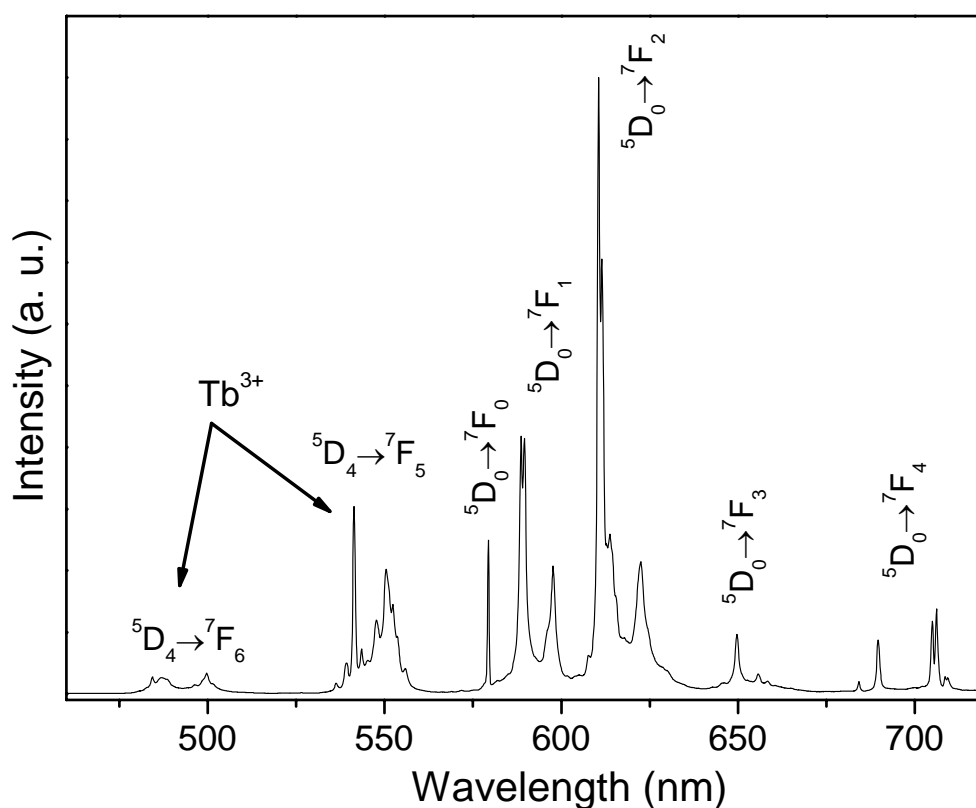


Figure 4.23 – Room temperature emission spectrum of $K_3[Tb_{0.95}Eu_{0.05}Si_3O_8(OH)_2]$ excited at 5D_3 manifold (377 nm).

Lifetime measurements of mixed Tb^{3+}/Eu^{3+} AV-22 samples (Figure 4.24) show the presence of two local Eu^{3+} (Tb^{3+}) environments. The Tb^{3+} 5D_4 decay curve of $K_3[Tb_{0.95}Eu_{0.05}Si_3O_8(OH)_2]$ is well fitted by a bi-exponential function, giving lifetimes of *ca.* 1.19 ± 0.02 and 0.68 ± 0.02 ms. The incorporation of a small amount of Eu^{3+} into the Tb-AV-22 structure reduces drastically the 5D_4 lifetime measured under direct Tb^{3+} excitation (377 nm), increasing its dependence with non-radiative effects. This suggests that the replacement of Tb^{3+} by Eu^{3+} ions into the layers, leads to the formation of localized defects which act as preferential non-radiative recombination regions. However, the existence of two distinct Tb^{3+} and Eu^{3+} local environments implies that the Eu^{3+} ions will also replace K^+ cations residing within the pores of the layers, K(1), and/or interlayer space, K(2).

Considering the measured 5D_4 lifetimes for pure Tb-AV-22 and for the mixed $K_3[Tb_{0.95}Eu_{0.05}Si_3O_8(OH)_2]$ samples, and given the small amount of Eu^{3+} present in the mixed sample, we consider that the longer lifetime is attributed to Tb^{3+} ions in regular

crystallographic positions in the layers (site I with lifetime τ_I). Whereas the shorter one is ascribed to Tb^{3+} ions whose coordination sphere was affected by the replacement of K^+ residing in the pores of the layers and/or in the interlayer space by Eu^{3+} ions (site II with lifetime τ_{II}).

Comparing two samples with Eu^{3+} contents ($a=0.05$ and 0.1) we observe that for $a=0.05$ the two Tb^{3+} lifetimes are 1.19 ± 0.02 and 0.68 ± 0.02 ms and at higher ($a=0.1$) Eu^{3+} content, the two Tb^{3+} lifetimes decrease to 0.70 ± 0.02 and 0.40 ± 0.02 ms, respectively, due to Tb^{3+} -to- Eu^{3+} energy transfer. A simple operational definition of Tb^{3+} -to- Eu^{3+} energy transfer probability $P_{Tb \rightarrow Eu}$ in terms of lifetimes is:

$$P_{Tb \rightarrow Eu} = (1/\tau) - (1/\tau_0) \quad (4.3)$$

where τ and τ_0 are the Tb^{3+} donor lifetimes in the presence and absence of the Eu^{3+} acceptor respectively [27,29,31]. For the longer lifetime, the values of P are 0.62 ($a=0.05$) and 1.20 ms^{-1} ($a=0.1$). The corresponding energy transfer efficiency $E_{Tb \rightarrow Eu}$ [27,29,31] is:

$$E_{Tb \rightarrow Eu} = (1 - \tau / \tau_0) \quad (4.4)$$

The Tb^{3+} -to- Eu^{3+} energy transfer efficiency for these samples with Eu^{3+} contents ($a=0.05$ and 0.1) is very high, 0.73 and 0.84 , respectively.

For times up to *ca.* 4 ms, the $K_3[Tb_{0.95}Eu_{0.05}Si_3O_8(OH)_2]$ decay curve, excited at 377 nm and detected at 610.5 nm, exhibits a non-exponential behavior. Subtracting the 5D_0 single-exponential component (lifetime of *ca.* 2.56 ± 0.01 ms) from the measured intensity in the time range 0-4 ms, a “grow-in” behavior is observed (inset in Figure 4.24), which indicates that the decay curves have a contribution from a Tb^{3+} -to- Eu^{3+} energy transfer pathway.

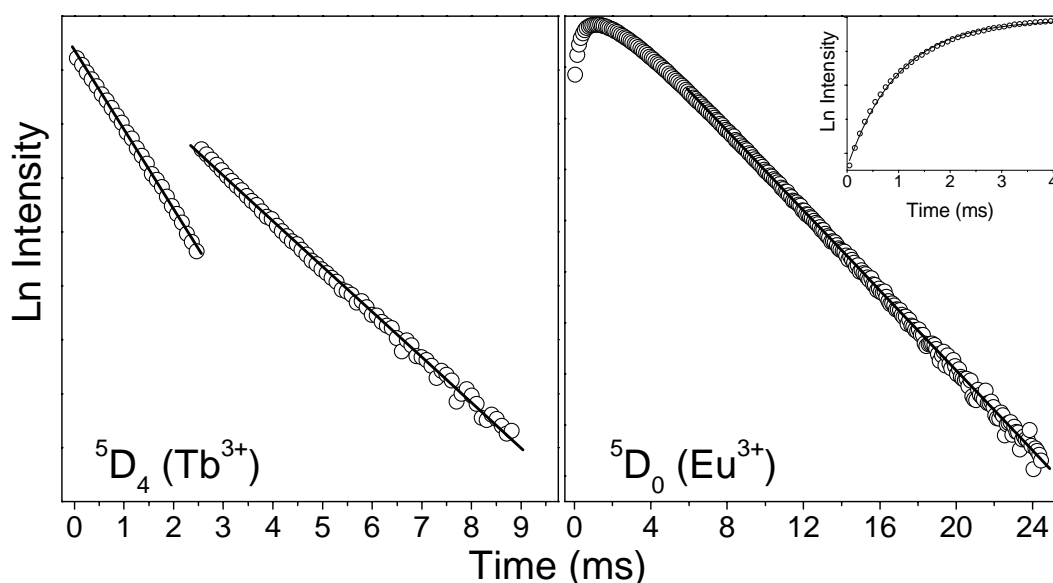


Figure 4.24 – Room temperature 5D_4 and 5D_0 decay curves of $K_3[Tb_{0.95}Eu_{0.05}Si_3O_8(OH)_2]$ detected at 540.5 nm (Tb^{3+}) and 610.5 nm (Eu^{3+}). Tb^{3+} and Eu^{3+} were excited at 377 nm. The solid lines are the best data linear fit ($r^2 > 0.99$). The inset shows the “grow-in” component of the $K_3[Tb_{0.95}Eu_{0.05}Si_3O_8(OH)_2]$ luminescence emission profile. The solid line is a fit to the data ($r^2 > 0.99$) considering an exponential growth function.

The XRD structure of AV-22 materials calls for the presence of a single Ln^{3+} environment, while PL spectroscopy shows the presence of two Eu^{3+} and Tb^{3+} sites in $K_3[EuSi_3O_8(OH)_2]$, $K_3[Y_{1-a}Eu_aSi_3O_8(OH)_2]$ ($a \geq 0.5$) and $K_3[Tb_{1-a}Eu_aSi_3O_8(OH)_2]$ ($a = 0.05, 0.1$). PL data indicate that the Ln^{3+} ion may reside in the layers or in the interlayer space. To further investigate this possibility, the crystal structures of $K_3[TbSi_3O_8(OH)_2]$ and the mixed sample $K_3[Tb_{0.9}Eu_{0.1}Si_3O_8(OH)_2]$ were re-assessed but no clear evidence for the presence of interlayer Tb^{3+} (or Eu^{3+}) ions was found. Moreover, the figures of merit of the powder XRD Rietveld refinement of $K_3[EuSi_3O_8(OH)_2]$ did not improve when some Eu^{3+} replaced K^+ ions. We must conclude that photoluminescence is a particularly well-suited technique to detect the presence of relatively small amounts of Eu^{3+} in the interlayer space.

Efficient Gd^{3+} -to- Tb^{3+} and Tb^{3+} -to- Eu^{3+} energy transfer is also observed in the excitation and emission spectra of AV-22 samples containing a third type of Ln^{3+} ion. This effect clearly shows the remarkable ability to tune the AV-22 system and is illustrated here with the sample $K_3[Gd_{0.67}Tb_{0.28}Eu_{0.05}Si_3O_8(OH)_2]$ (Figure 4.25).

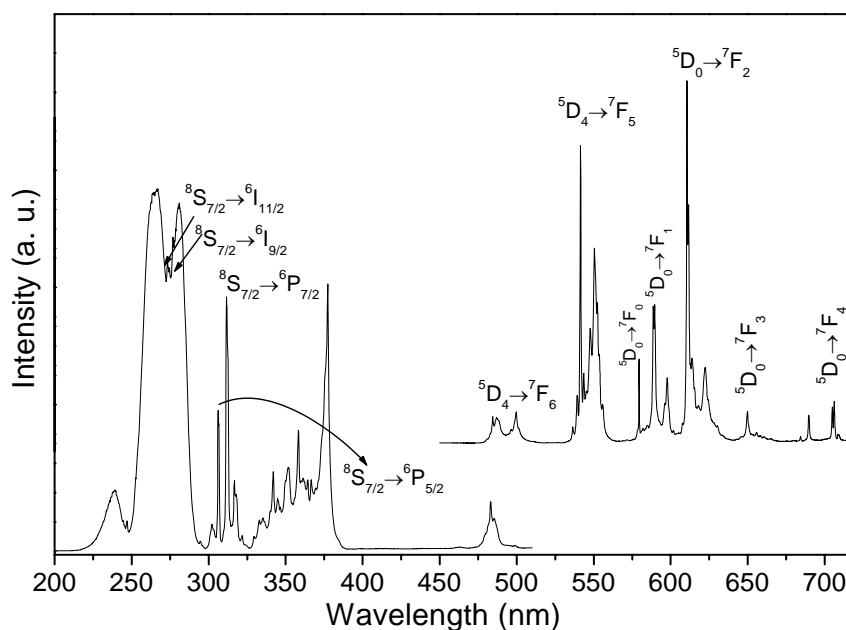


Figure 4.25 – Room temperature excitation and emission spectra of $K_3[Gd_{0.67}Tb_{0.28}Eu_{0.05}Si_3O_8(OH)_2]$. The excitation was performed at 377 nm, while emission was monitored at 540.5 nm (Tb^{3+} levels). An analogous emission spectrum is obtained for excitation within the ${}^6P_{7/2,5/2}$ Gd levels.

The room temperature excitation spectra of Tb/Ce-AV-22 materials (Figure 4.26a) display a series of sharp Tb^{3+} lines, ascribed to the intra $4f^8$ transitions between the 7F_6 and ${}^5G_{4-6}$, ${}^5L_{9,10}$, ${}^5D_{2-4}$ levels, superimposed on a broad band in the range 300-360 nm, also observed in the spectra of Y/Ce materials, and ascribed to the $Ce^{3+} 4f^1 \rightarrow 5d^1$ transition. The two broad bands at 236 and 250-290 nm are assigned to, respectively, the spin-allowed (low-spin, LS) and spin-forbidden (high-spin, HS) interconfigurational $Tb^{3+} fd$ transitions [23,24,32]. Figure 4.26b shows the 14 K excitation spectra of Tb/Ce-AV-22, monitored at the ${}^5D_4 \rightarrow {}^7F_5$ transition (543 nm) and at 420 nm. Although the room temperature and 14 K excitation spectra of Tb/Ce-AV-22 are similar, the intensity of the $Ce^{3+} 4f^1 \rightarrow 5d^1$ transition increases relatively to the sharp Tb^{3+} lines and the ${}^7F_6 \rightarrow {}^5G_{5,6}$, ${}^5L_{10}$ transitions are better seen. The spectrum monitored at 420 nm displays only the broad $Ce^{3+} 4f^1 \rightarrow 5d^1$ band. Again, this transition is clearly present in the 14 K excitation spectrum of the Y/Ce sample. This band displays three components at *ca.* 345, 323 and 313 nm originated from transitions from the ${}^2F_{5/2}$ level of the ground state to the crystal field split $5d$ level components (see energy scheme in Figure 4.26b). The HS band shows three components at

ca. 282, 267 and 262 nm due to the crystal field splitting of the $5d$ configuration and the energy separation between the LS and HS fd transitions (ca. 7320 cm^{-1}) is very similar to the energy separation reported before for Tb-AV-22. The presence of the $\text{Ce}^{3+} 4f^1 \rightarrow 5d^1$ transition monitoring within the $\text{Tb}^{3+} 4f^8$ lines indicates that the Ce^{3+} -to- Tb^{3+} energy transfer channel is active in the range 14-300 K, being more efficient at low temperature. The Ce^{3+} to Tb^{3+} energy transfer is also evidenced by the decrease of the relative intensity of the $\text{Tb}^{3+} 4f^8 \rightarrow 4f^7 5d^1$ lines compared to the lines of Tb-AV-22. This observation has been previously reported [32] and suggests that the excitation of Tb^{3+} occurs mainly through the excitation of Ce^{3+} . Due to the strong interaction between Ce^{3+} and Tb^{3+} (i.e. Ce^{3+} -to- Tb^{3+} energy transfer) Tb^{3+} is more easily excited by Ce^{3+} than Tb^{3+} itself.

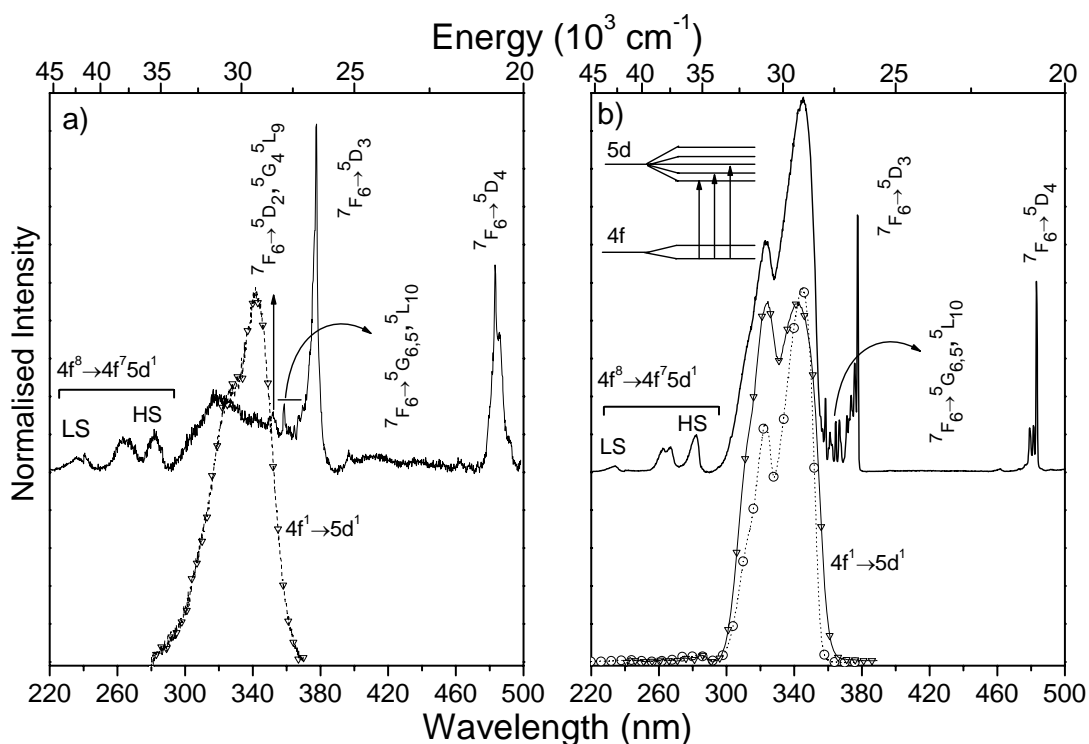


Figure 4.26 – a) Room temperature excitation spectra of Tb/Ce-AV-22 (monitored at 543 nm, solid line) and Y/Ce-AV-22 (monitored at 420 nm, triangles); b) 14 K excitation spectra of Tb/Ce-AV-22 monitored at 543 nm (solid line) and 420 nm (circles), and Y/Ce monitored at 420 nm (triangles).

The room temperature emission spectrum of Tb/Ce-AV-22 excited in the $\text{Ce}^{3+} 4f^1 \rightarrow 5d^1$ transition (Figure 4.27a) exhibits a series of sharp lines assigned to the

$^5D_4 \rightarrow ^7F_{2-6}$ transitions of Tb^{3+} and luminescence from the higher excited states (e.g. 5D_3) is not observed, indicating very efficient non-radiative relaxation to the 5D_4 level. The spectrum also displays a broad band (370-525 nm) attributed to the allowed Ce^{3+} $5d^1 \rightarrow 4f^1$ transition. This assignment is based on the Y/Ce emission spectrum (recorded using the same excitation conditions), which also displays the 370-525 nm band, inset of Figure 4.27a. The deconvolution of this broad band shows the spin-orbit splitting of the Ce^{3+} ground state in the $^2F_{5/2}$ and $^2F_{7/2}$ levels (separated by *ca.* 2000 cm^{-1}). Lowering the temperature to 14 K, the intensity of the $5d^1 \rightarrow 4f^1$ transition decreases nine fold, in accord with the increase in the Ce^{3+} -to- Tb^{3+} energy transfer, as the excitation spectra in Figure 4.26 suggest. The analysis of the intensity of this Ce^{3+} band relatively to the Tb^{3+} lines makes this point very clear. Upon excitation of the Ce^{3+} absorption band, the spectra in Figure 4.27 exhibit Ce^{3+} and Tb^{3+} emissions with relative intensities $I_{Ce}:I_{Tb}=2.89$ and 1.39, at room temperature and 14 K, respectively. This implies that the Ce^{3+} -to- Tb^{3+} energy transfer is not complete at the present Ce^{3+}/Tb^{3+} concentrations and is more efficient at 14 K.

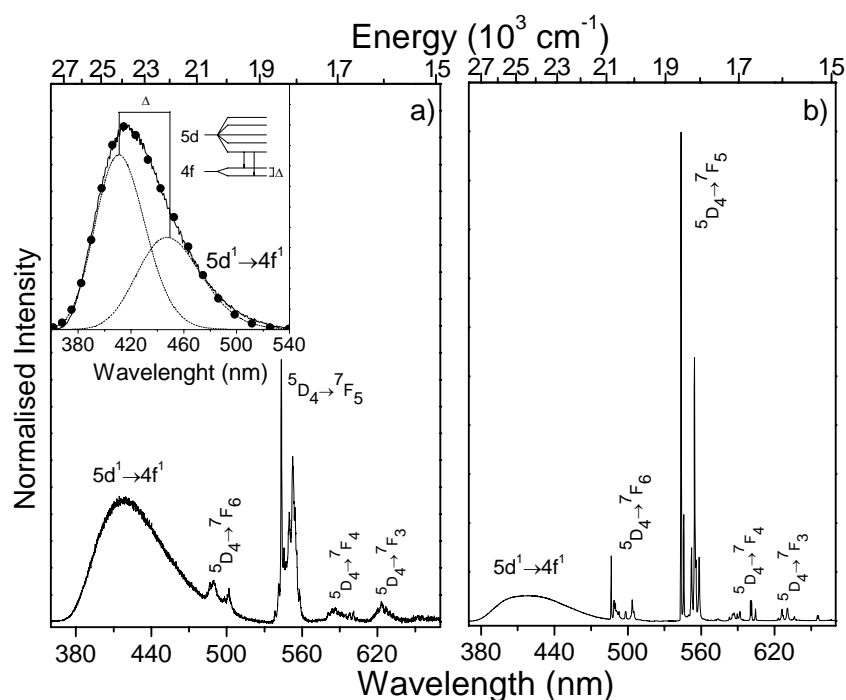


Figure 4.27 – a) Room temperature and b) 14 K emission spectra of Tb/Ce-AV-22 excited at 342 nm. The inset shows the Y/Ce-AV-22 room temperature emission spectrum recorded at 342 nm. Δ *ca.* 2000 cm^{-1} represents the spin-orbit splitting of the Ce^{3+} ground state in the $^2F_{5/2}$ and $^2F_{7/2}$ components.

The Ce³⁺-to-Tb³⁺ energy transfer may take place via radiative transfer, exchange interaction and electric multipole interaction. The absence in the Ce³⁺ emission of *f-f* Tb³⁺ absorption lines (Figure 4.27) shows, that radiative energy transfer between the donor and the acceptor may be neglected. While Ce³⁺ and Tb³⁺ ions are reducing ions, the exchange interaction would require very high energy and, thus, the energy transfer in Tb/Ce-AV-22 should take place, essentially, via electric multipole (dipole-dipole) interaction [25,28]. According to the Dexter theory of energy transfer [25,28,33] the critical radius for energy transfer by dipole-dipole interaction is defined as the distance for which the probability of transfer equals the probability of radiative emission of the sensitizer and can be obtained by:

$$R_C^6 = 3.024 \times 10^{12} f_a \int \frac{f_D(E) F_A(E)}{E^4} dE, \quad (4.5)$$

where f_a *ca.* 10^{-6} is the oscillator strength of the Tb³⁺ transitions involved in the energy transfer [28], E the energy at maximum spectral overlap, f_D the normalized emission line shape function of Ce³⁺ (calculated from the inset of Figure 4.27) and F_A the normalized absorption line shape function of Tb³⁺ (calculated from the excitation spectrum of Y/Tb-AV-22, Figure 4.15). The critical distance obtained is *ca.* 2.71 Å, reflecting the low overlap integral between the emission spectrum of Ce³⁺ and the excitation one of Tb³⁺.

The ⁵D₄ Tb³⁺ lifetimes were monitored as a function of the excitation wavelength and temperature. Figure 4.28 shows the room temperature and 14 K ⁵D₄ decay curves of Tb/Ce-AV-22 excited on the Tb³⁺ levels (377 nm) and on the broad band (342 nm). All ⁵D₄ decay curves are bi-exponential, in perfect agreement with the presence of two distinct local Tb³⁺ environments. The corresponding lifetimes are gathered in Table 4.4. We have previously shown that whereas Tb-AV-22 sample displays only one local Tb³⁺ site, mixed Tb/Eu-AV-22 samples exhibit two distinct Eu³⁺ and Tb³⁺ local environments. For comparison, the corresponding ⁵D₀ and ⁵D₄ lifetimes are also listed in Table 4.4 (the concentration of Eu³⁺ in Tb/Eu-AV-22 is similar to that of Ce³⁺ in Tb/Ce-AV-22). Comparable to the incorporation of a small amount of Eu³⁺ into the Tb-AV-22 structure, inserting Ce³⁺ also reduces drastically the ⁵D₄ lifetime measured under direct Tb³⁺

excitation (377 nm), increasing its dependence with non-radiative effects. Analogous to mixed Tb/Eu-AV-22 samples, the replacement of Tb^{3+} by Ce^{3+} ions into the layers leads to the formation of localized defects which act as preferential non-radiative recombination regions. However, the existence of two distinct Tb^{3+} local environments implies that the Ce^{3+} ions will also replace K^+ cations residing within the pores of the layers, K(1), and/or interlayer space, K(2). It is not easy to distinguish between these two types of Ce^{3+} insertion because they induce similar changes in the nearest Tb^{3+} coordination sphere, due to the similar Tb^{3+} -K(1) and Tb^{3+} -K(2) distances (3.68 and 3.83 Å, respectively). Accordingly to the critical distance estimated, the efficiency of the Ce^{3+} -to- Tb^{3+} energy transfer through dipole-dipole interaction ranges from 11-15% (for Ce^{3+} replacing K(1) and K(2) sites) and *ca.* 1% (for Ce^{3+} replacing Tb^{3+} ions located in the layers, average distance of 5.91 Å).

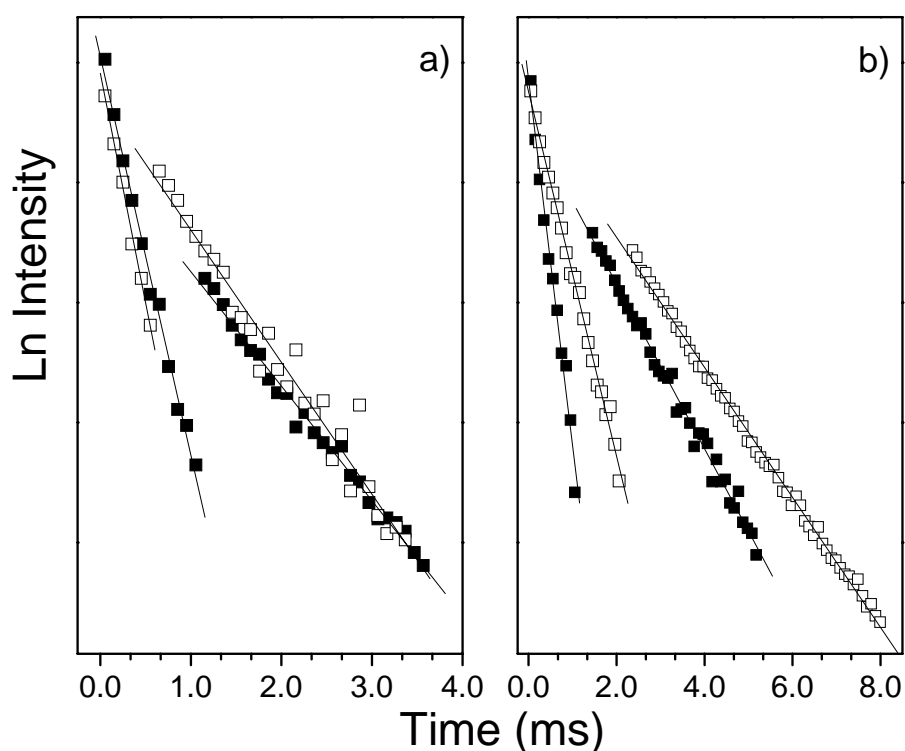


Figure 4.28 – a) Room temperature and b) 14 K $^5\text{D}_4$ decay curves of as-prepared Tb/Ce-AV-22, monitored at 543 nm under (■) 377 nm and (□) 342 nm excitation. The solid lines are the best data linear fit ($r^2 > 0.99$).

Analogous to the previous attribution of the 5D_4 lifetimes measured for pure Tb-AV-22 and for the mixed Tb/Eu-AV-22, for the mixed Tb/Ce-AV-22 sample with small amount of Ce^{3+} , we assign the longer lifetime to Tb^{3+} ions in the layers (site I with lifetime τ_I), whereas the shorter one is ascribed to Tb^{3+} ions replacing K^+ cations residing in the pores of the layers and/or in the interlayer space (site II with lifetime τ_{II}). All the data are summarized in (Table 4.4).

Table 4.4 – 5D_4 lifetimes (ms) of Tb/Ce-, Tb/Eu- and Tb-AV-22 monitored at 543 nm; measured for different excitation wavelengths λ (342 and 377 nm) at 14 and 300 K.

	Tb/Ce-AV-22				Tb/Eu-AV-22	Tb-AV-22
	300 K		14 K		300 K	300 K
λ	342 nm	377 nm	342 nm	377 nm	377 nm	377 nm
τ_I	1.28±0.02	0.92±0.02	1.63±0.02	1.31±0.01	1.19±0.02	4.45±0.02
τ_{II}	0.34±0.01	0.22±0.01	0.48±0.01	0.21±0.01	0.68±0.01	

Excitation on the Ce^{3+} levels (342 nm) increases the 5D_4 lifetimes of both Tb^{3+} sites relatively to the direct intra- $4f^8$ excitation (377 nm), which indicates that the Ce^{3+} -to- Tb^{3+} energy transfer is slower than the 5D_4 emission rate. The 5D_4 lifetimes decrease as the temperature increases from 14 to 300 K and this effect depends on the Tb^{3+} local environment and excitation wavelength (Table 4.4). On direct intra- $4f$ excitation (377 nm) τ_{II} remains essentially constant and τ_I decreases *ca.* 30 %, while upon excitation on the Ce^{3+} levels (342 nm) τ_I and τ_{II} decrease 20-30 %. The larger increase in τ_I for direct intra- $4f$ excitation (377 nm) might be explained by the non-radiative components of the two Tb^{3+} coordination spheres. The contribution of the phonons of the $[LnSi_3O_8(OH)_2]^{3-}$ layers for the Tb^{3+} non-radiative deactivation should be larger for site I than for site II. Furthermore, the larger thermal activated non-radiative channels for τ_{II} excited into the Ce^{3+} levels should not be associated with the 5D_4 level (attending to the distinct decrease rates as the excitation wavelength changes) and, therefore, should be ascribed to the Ce^{3+} -to- Tb^{3+} energy transfer mechanisms. The preferential Tb^{3+} levels (5L_9 , 5G_4 , 5D_2) involved in the Ce^{3+} -to- Tb^{3+} energy transfer are approximately 400-700 cm^{-1} bellow the lower energy side of the $4f^1 \rightarrow 5d^1$ transition, whereas the 5D_1 level is located *ca.* 200 cm^{-1} bellow the higher

energy side of the same Ce^{3+} transition. As the temperature increases from 14 to 300 K and for an excitation on the Ce^{3+} levels (342 nm), the Tb^{3+} -to- Ce^{3+} back-transfer rate may increase, due to phonon-assisted thermally activated mechanisms, in complete agreement with the reported increase in the intensity of the $5d^1 \rightarrow 4f^1$ transition (Figure 4.27a).

The radiances of the $Gd_2O_2S:Tb$ standard green phosphor, Tb-AV-22 and mixed Tb/Ce-AV-22 samples were measured and compared for different excitation wavelengths (Table 4.5). At 270 nm excitation, the quantum yield of $Gd_2O_2S:Tb$ is *ca.* 95 %. The radiance of Tb-AV-22, excited at 377 nm, and $Gd_2O_2S:Tb$ are of the same order, the former being *ca.* 25% smaller.

Table 4.5 – Room temperature radiance ($\mu W/cm^2$) and (x,y) CIE color coordinates for the standard green phosphor $Gd_2O_2S:Tb$, Tb-AV-22 and Tb/Ce-AV-22 measured for different excitation wavelengths λ .

	Tb/Ce-AV-22		Tb-AV-22	$Gd_2O_2S:Tb$
λ	377 nm	342 nm	377 nm	270 nm
(x,y)	(0.308, 0.565)	(0.239, 0.236)	(0.336, 0.606)	(0.369, 0.579)
Radiance	0.177	0.329	1.804	2.462

Under direct Tb^{3+} excitation (377 nm), the Tb/Ce-AV-22 radiance is smaller than the radiance of Tb-AV-22. Since the Tb contents of both materials are similar, the lower radiance is due to more effective non-radiative channels, as already suggested. Upon 342 nm excitation, the Tb/Ce-AV-22 radiance is about two times larger than the radiance measured under direct Tb^{3+} excitation. This supports the existence of an effective room temperature Ce^{3+} to Tb^{3+} energy transfer.

The (x,y) emission color coordinates were measured according to the Commission Internationale d'Eclairage (CIE) for the same excitation wavelengths used in the radiance measurements (Table 4.5). For convenience, the color coordinates of AV-22 materials and the green standard are plotted in the CIE (1931) diagram (Figure 4.29). Clearly, the Tb-AV-22 and $Gd_2O_2S:Tb$ color coordinates are similar. The Ce/Tb-AV-22 color coordinates are shifted to the blue, reflecting the Ce^{3+} blue-band contribution to the overall emission. Although the Ce/Tb-AV-22 radiance is smaller than the pure Tb-AV-22

radiance, the incorporation of Ce^{3+} allows the tuning of the emission color coordinate from the green to the blue spectral region.

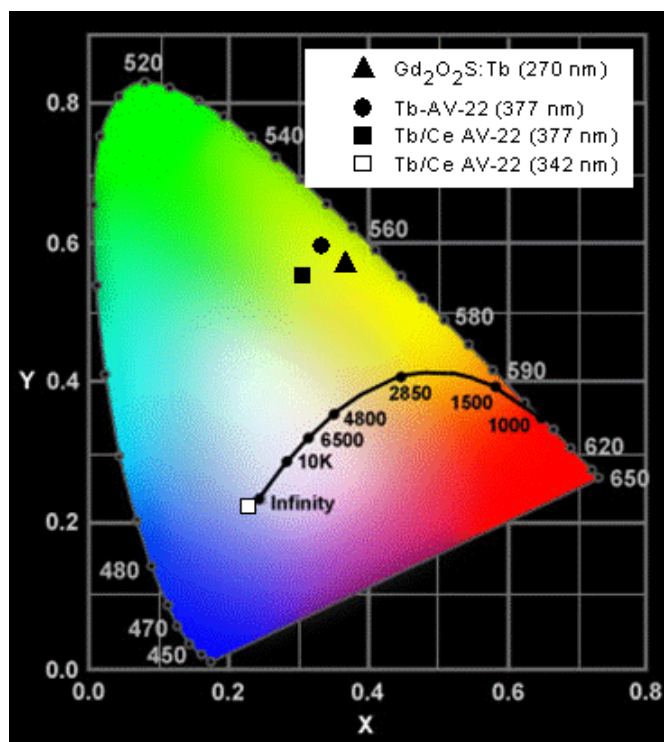


Figure 4.29 – CIE chromaticity diagram showing the room-temperature (x,y) color coordinates, measured at the excitation wavelengths depicted (see also Table 4.5).

FT-Raman spectra were recorded in order to quantitatively study the photoluminescence intensity as a function of the Er^{3+} content in the Y/Er-AV-22 system $\text{K}_3[\text{Y}_{1-a}\text{Er}_a\text{Si}_3\text{O}_8(\text{OH})_2]$, $a=0.005-1$, (Figure 4.30). As expected, the vibronic transitions appear in the Raman shift range $50-1200\text{ cm}^{-1}$, while the intra $4f^{11}$ electronic transitions are detected at $3500-2500\text{ cm}^{-1}$. The emission lines are assigned to the intra $4f^{11}$ transitions between the ${}^4\text{I}_{13/2}$ and ${}^4\text{I}_{15/2}$ levels of the ground multiplet of Er^{3+} . Provided the intensities of the vibrational spectra of the different samples in the series are similar, the variation of the photoluminescence intensity as a function of the Er^{3+} content may be estimated directly from the intensity of the strongest electronic line ($1.54\text{ }\mu\text{m}$) in the $3500-2500\text{ cm}^{-1}$ (insets in Figure 4.30). In Y/Er-AV-22 the ${}^4\text{I}_{13/2} \rightarrow {}^4\text{I}_{15/2}$ emission integrated area increases with increasing Er^{3+} content, due to the larger number of optically-active centers. The photoluminescence is essentially quenched by the presence of OH vibrations [3].

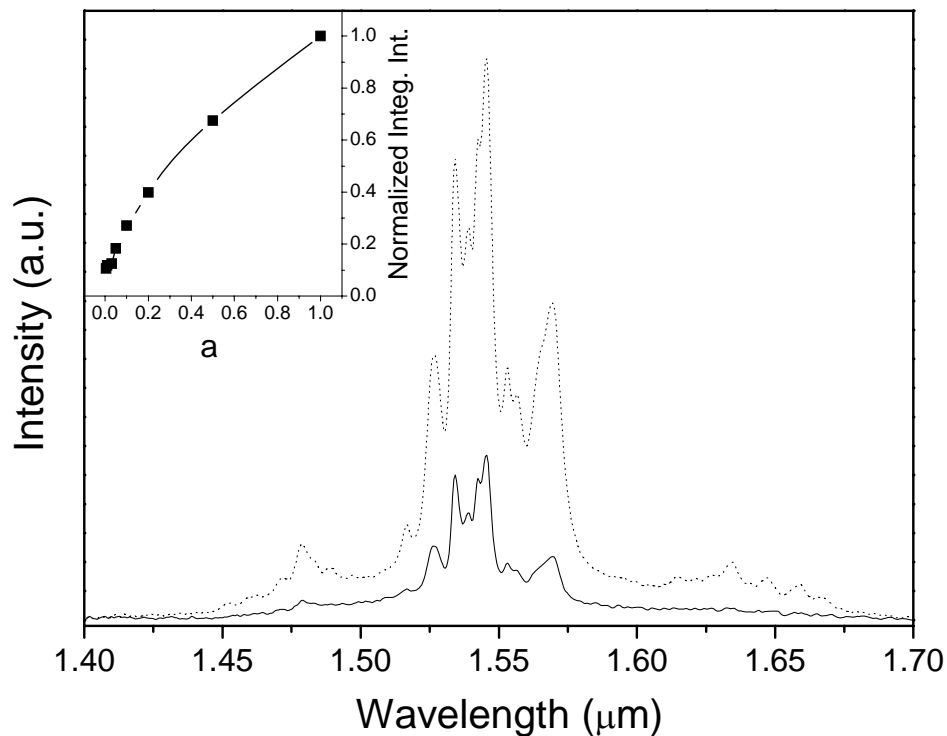


Figure 4.30 – FT-Raman spectra of $K_3[Y_{1-a}Er_aSi_3O_8(OH)_2]$ $a=0.1$ (solid line) and $a=1.0$ (dotted line). The insets depict the normalized integrated intensity of the 1.54 μm photoluminescence as a function of the Er^{3+} content for the samples with a in the range 0.005 to 1.

Figure 4.31 shows the 75 K and room temperature infrared photoluminescence spectra of $K_3[\text{ErSi}_3\text{O}_8(\text{OH})_2]$. The emission lines are assigned to the intra $4f^{11}$ transitions between the $^4I_{13/2}$ and $^4I_{15/2}$ levels of the Er^{3+} ground multiplet. Raising the temperature from 75 to 300 K increases the $^4I_{13/2} \rightarrow ^4I_{15/2}$ integrated intensity for Er-AV-22 by a factor of *ca.* 2.7, an effect which is particularly important above *ca.* 225 K (inset in Figure 4.31). This is the reverse of the trend usually observed for other siliceous materials, such as Er^{3+} -doped crystalline [34,35] and porous silicon [36]. Recent work on Er^{3+} -doped crystalline silicon reported a similar behavior for 1.54 μm electroluminescence, which was explained in terms of Auger recombinations [37]. For $\text{Na}_3\text{ErSi}_3\text{O}_9$ and Er-AV-9, we have suggested that, as the temperature rises, the redistribution of population between the Stark levels of the fundamental multiplet is probably relevant for understanding this unusual temperature dependence [38,39].

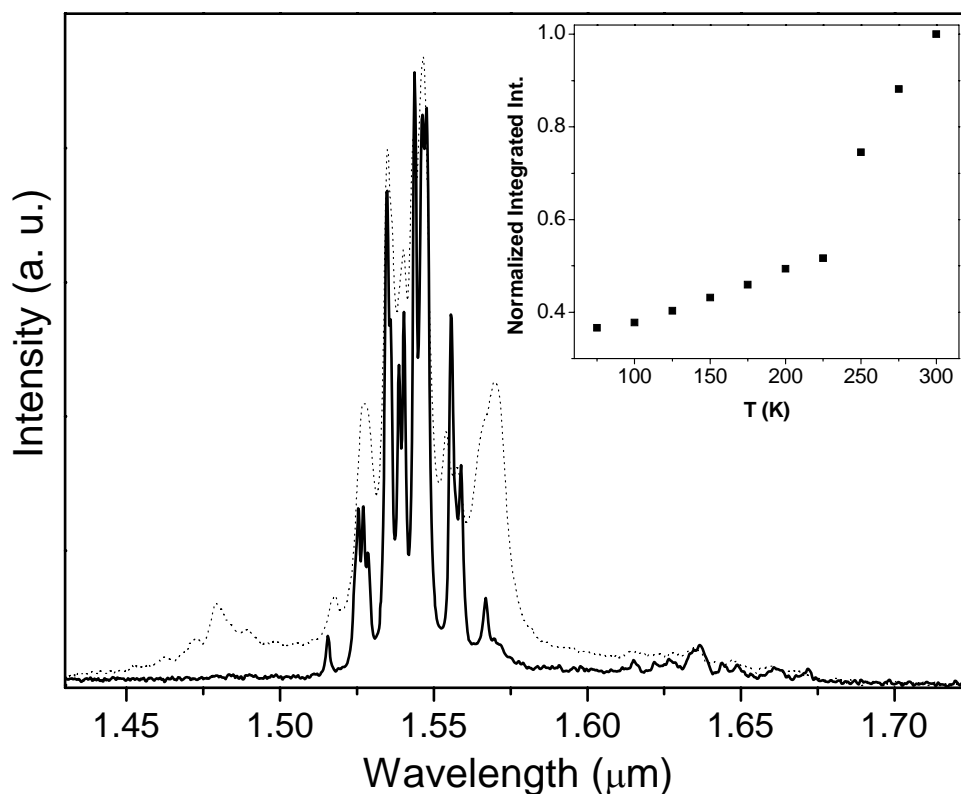


Figure 4.31 – Infrared emission spectra of Er-AV-22 excited at 514.5 nm, recorded at 75 (solid line) and 300 K (dotted line). The inset shows the normalized integrated intensity of the 1.54 μm PL as a function of temperature. The excitation power was 200 mW.

4.5 Conclusions

The synthesis and structural characterization of new layered rare-earth silicates ($\text{K}_3[\text{M}_{1-a}\text{Ln}_a\text{Si}_3\text{O}_8(\text{OH})_2]$, $\text{M}^{3+}=\text{Y}^{3+}$, Tb^{3+} ; $\text{Ln}^{3+}=\text{Eu}^{3+}$, Er^{3+} , Tb^{3+} , Gd^{3+} and Ce^{3+}), $1 \geq a > 0$ named AV-22 materials have been reported.

For the mixed samples, although it was not possible to calculate exactly the Tb \cdots Eu (Ce) distances by XRD analysis, indicative values may be obtained from the XRD data of pure Tb-AV-22: Tb \cdots Tb and Tb \cdots K(2) distances are, respectively, *ca.* 5.9 and 3.8 Å. Thus, Tb $^{3+}$ -to-Eu $^{3+}$ energy transfer is likely to occur (both via exchange and multipolar, dipole-dipole, interactions) between optical centers in the layers and in the interlayer space [K(1) and [K(2) sites]. Energy transfer between Tb $^{3+}$ and Eu $^{3+}$ ions present in the layers is unlikely because the Tb \cdots Eu estimated distance, *ca.* 5.91 Å, is

comparatively large. In addition, Tb³⁺-to-Eu³⁺ energy transfer between optical centers in the interlayer space is also unlikely because the few Ln³⁺ ions present will be far apart.

In mixed Tb/Ce-AV-22 energy transfer occurs from the large Ce³⁺ 4*f*¹ → 5*d*¹ broad band to the sharp Tb³⁺ 4*f*⁸ lines with an efficiency of *ca.* 15 %, estimated assuming the dipole-dipole interaction is the dominant transfer mechanism. Although low, this value enables the fine-tuning of the color emission in the blue-green region of the chromaticity diagram.

The layered rare-earth silicate system exhibits remarkable photoluminescence properties which may be tuned by judicious choice of the rare-earth ions and the occupancy of the layer and interlayer metal sites. This has been illustrated for K₃[M_{1-a}Ln_aSi₃O₈(OH)₂], M³⁺=Y³⁺, Tb³⁺; Ln³⁺=Eu³⁺, Er³⁺, Tb³⁺, Gd³⁺ and Ce³⁺ and it may be extended to other lanthanides ions in the future.

4.6 References

- [1] D. Ananias, M. Kostova, F.A.A. Paz, A. Ferreira, L.D. Carlos, J. Klinowski, J. Rocha, *J. Am. Chem. Soc.* 126 (2004) 10410.
- [2] M.H. Kostova, R.A.S. Ferreira, D. Ananias, L.D. Carlos, J. Rocha, *J. Phys. Chem. B* 110 (2006) 15312.
- [3] M.H. Kostova, D. Ananias, L.D. Carlos, J. Rocha, *J. Alloys Comp.* (2007) in press.
- [4] V.I. Ponomarev, O.S. Filipenko, L.O. Atovmyan, *Kristallografiya* 33 (1988) 98.
- [5] B.A. Maksimov, V.V. Ilyukhin, N.V. Belov, *Sov. Phys. Dokl.* 13 (1969) 638.
- [6] O.S. Filipenko, G.V. Shilov, L.S. Leonova, N.S. Tkacheva, O.V. Dimitrova, V.I. Ponomarev, *Russ. J. Coord. Chem.* 25 (1999) 877.
- [7] T. Kottke, D. Stalke, *J. App. Crystallogr.* 26 (1993) 615.
- [8] R. Hooft, B.V. Nonius, Delft, The Netherlands (1998).
- [9] Z. Otwinowski, W. Minor, in *Macromolecular Crystallography*, Pt A, 1997, p. 307.
- [10] R.H. Blessing, *Acta Cryst. A* 51 (1995) 33.
- [11] R.H. Blessing, *J. Appl. Crystallogr.* 30 (1997) 421.
- [12] Sheldrick, G. M. SHELXS-97, Program for Crystal Structure Solution, University of Göttingen, 1997.
- [13] Sheldrick, G. M. SHELXL-97, Program for Crystal Structure Refinement, University of Göttingen 1997.
- [14] C. Dong, *J. Appl. Crystallogr.* 32 (1999) 838.
- [15] P.E. Werner, L. Eriksson, M. Westdahl, *J. Appl. Crystallogr.* 18 (1985) 367.
- [16] J. Rodriguez-Carvajal, FULLPROF - A Program for Rietveld Refinement and Pattern Matching Analysis, Abstract of the Satellite Meeting on Powder Diffraction of the XV Congress of the IUCR, Toulouse, France, 1990, p.127.
- [17] J.L. You, G.C. Jiang, H.Y. Hou, H. Chen, Y.Q. Wu, K.D. Xu, *J. Raman Spec.* 36 (2005) 237.
- [18] M. Akaogi, N.L. Ross, P. McMillan, A. Navrotsky, *Am. Mineral.* 69 (1984) 499.
- [19] D.M. Tobbens, V. Kahlenberg, R. Kaindl, *Inorg. Chem.* 44 (2005) 9554.
- [20] P. McMillan, *Am. Mineral.* 69 (1984) 622.

- [21] S. Campos, A. Denoyer, S. Jandl, B. Viana, D. Vivien, P. Loiseau, B. Ferrand, J. Phys. Cond. Matter 16 (2004) 4579.
- [22] H. Assaaoudi, A. Ennaciri, A. Rulmont, Vibr. Spec. 25 (2001) 81.
- [23] M. Laroche, J.L. Doualan, S. Girard, J. Margerie, R. Moncorge, J. Opt. Soc. Am. B 17 (2000) 1291.
- [24] L. van Pieterse, M.F. Reid, G.W. Burdick, A. Meijerink, Phys. Rev. B 65 (2002) 45114.
- [25] M.F. Hazenkamp, G. Blasse, Chem. Mat. 2 (1990) 105.
- [26] CHINT is a product of the Chint Group Corporation (<http://www.chint.com>), PRC.
- [27] H.Y.D. Ke, E.R. Birnbaum, J. Lumin. 63 (1995) 9.
- [28] H.P. You, X.Y. Wu, H.T. Cui, G.Y. Hong, J. Lumin. 104 (2003) 223.
- [29] R. Reisfeld, C. K.Jørgenson, in Handbook on the physics and chemistry of rare earths, edited by K.A. Gschneidner, Jr., L. R. Eyring, North-Holland Physics Publishing, Amsterdam, 1979.
- [30] L.D. Carlos, A.L.L. Videira, Phys. Rev. B 49 (1994) 11721.
- [31] D. Sendor, M. Hilder, T. Juestel, P.C. Junk, U.H. Kynast, New J. Chem. 27 (2003) 1070.
- [32] J. Lin, Q. Su, J. Mat. Chem. 5 (1995) 1151.
- [33] D.L. Dexter, J. Chem. Phys. 21 (1953) 836.
- [34] H. Przybylinska, W. Jantsch, Y. SuprunBelevitch, M. Stepikhova, L. Palmetshofer, G. Hendorfer, A. Kozanecki, R.J. Wilson, B.J. Sealy, Phys. Rev. B 54 (1996) 2532.
- [35] A. Polman, J. Appl. Phys. 82 (1997) 1.
- [36] J.H. Shin, G.N. Vandenhoven, A. Polman, Appl. Phys. Lett. 66 (1995) 2379.
- [37] M.S. Bresler, O.B. Gusev, P.E. Pak, N.A. Sobolev, I.N. Yassievich, J. Lumin. 80 (1998) 375.
- [38] D. Ananias, J.P. Rainho, A. Ferreira, M. Lopes, C.M. Morais, J. Rocha, L.D. Carlos, Chem. Mat. 14 (2002) 1767.
- [39] D. Ananias, J.P. Rainho, A. Ferreira, J. Rocha, L.D. Carlos, J. Alloys Comp. 374 (2004) 219.

5 Small-pore rare-earth silicates ($K_3RESi_3O_9$, $RE^{3+} = Tb^{3+}$, Eu^{3+} , Y^{3+} and Er^{3+})

Index

5.1	Introduction	118
5.2	Synthesis.....	118
5.3	Structural characterization.....	119
5.4	Transformation of AV-22 to AV-23.....	123
5.5	Photoluminescence spectroscopy	129
5.6	Conclusions	138
5.7	References	139

5.1 Introduction

In order to gain further insight into the evolution of photoluminescence in rare-earth silicates across dimensionality it is interesting to bridge between the fields of layered rare-earth silicates and microporous rare-earth materials. In chapter 4 we have reported on the layered system $K_3[RESi_3O_8(OH)_2]$, named AV-22. Upon calcination at 650 °C, AV-22 materials undergo a phase transformation to a small-pore framework system $K_3[RESi_3O_9]$, RE=Y, Er, Eu and Tb [1,2], named here AV-23 (Aveiro material number 23), whose structure bears some similarity with the structure of the Ho^{3+} silicate, first reported by Ponamarev *et al.* [3]. The crystal structure of AV-23 materials calls for the presence of a single independent RE^{3+} environment. Despite this, detailed photoluminescence studies showed the presence of two or three RE^{3+} sites, which may be ascribed to metal centers in regular framework positions, defect regions, and micropores, replacing K^+ [1]. The radiance value of the Tb-AV-23 sample is of the same order of magnitude of that of standard Tb^{3+} green phosphors [1]. The calcination process increases the intensity of the Er^{3+} emission (essentially due to the removing of OH groups) and the importance of the Er^{3+} - Er^{3+} interactions as a quenching emission channel [2].

In this chapter, I present the preparation and the structural characterization of small-pore rare-earth silicates AV-23 (RE=Tb, Eu, Y and Er). Single-crystal X-ray diffraction was done in cooperation with Dr. Filipe Paz and Dr. Artur Ferreira. Chemical analysis, thermogravimetry, scanning electron microscopy and ^{29}Si MAS NMR were applied. Photoluminescence spectroscopy was used to study the optical properties of these solids.

5.2 Synthesis

The synthesis of RE-AV-22 (RE=Y, Er, Eu and Tb) and mixed Y/Er-AV-22 materials was performed using a procedure described in Chapter 4. Figure 5.1 outlines the steps involved in the preparation of small-pore AV-23 silicates.

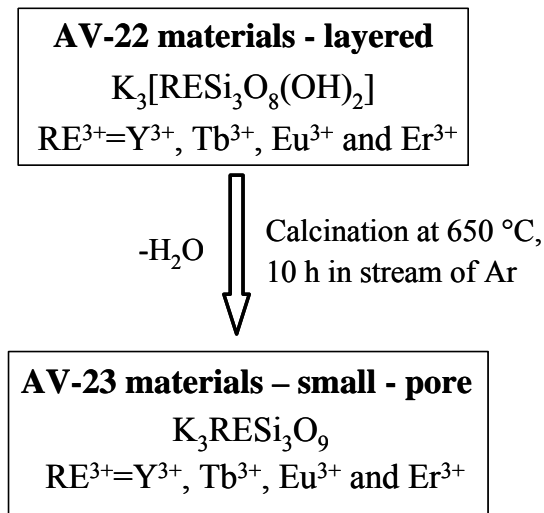


Figure 5.1 – Schematic representation of the synthesis of AV-23 materials.

Because TGA reveals that the thermal transition from the layered to small-pore materials occurs in the range 600-650 °C, AV-22 samples were calcined at 650 °C in a stream of argon for 10 h (after the temperature had been raised at a heating rate of 5 °C/min).

5.3 Structural characterization

Several $K_3[TbSi_3O_9]$ (Tb-AV-23) single-crystals (from different batches), all exhibiting a poorly defined morphology, were mounted on a glass fiber using perfluoropolyether oil [4], and data were collected at 100(2) K (Unidade de Raios-X, RIAIDT, University of Santiago de Compostela, Spain, on a Bruker SMART 1000 charge-coupled device (CCD) area-detector diffractometer equipped with $MoK\alpha$ graphite-monochromated radiation ($\lambda = 0.7107 \text{ \AA}$) and controlled by the SMART software package [5]. Images were processed using the SAINTPlus software package [6], and data were corrected for absorption by using the semiempirical method of SADABS [7]. A considerable internal disorder of all crystals was immediately indicated by the overall poor diffraction and very high mosaicities (typically around 5° per reflection). Even so, a possible crystal solution for this material was attempted by solving the reduced data with

SHELXS-97 [8], and refining the model by full-matrix least squares on F^2 using SHELXL-97 [9].

The XPREP interface was used to analyze the data symmetry, with the systematic absences suggesting two possible space groups for the crystal data, $Pmn2_1$ and $Pm\bar{m}n$, both characterized by relatively low figures of merit. Considering the experimental problems in the data collection and reduction, the structure was solved and refined in both space groups. Even though the calculated mean $|E^2 - 1|$ value strongly indicated a centrosymmetric $Pm\bar{m}n$ space group, this did not lead to the most sensible crystal model. The final selection of the $Pmn2_1$ space group was also motivated by the previous work of Ponomarev *et al.* reporting on a similar material, containing Ho^{3+} [3].

The location of Tb^{3+} was straightforward from Patterson synthesis, with the remaining atoms being located from difference Fourier maps calculated from successive least-squares refinement cycles. The structure was refined with a geometry heavily restrained for the $\{\text{SiO}_4\}$ tetrahedra, with all the Si–O bond lengths and tetrahedral internal O··O distances restrained to common values, which converged to 1.60(2) and 2.61(2) Å, respectively. The refined anionic $[\text{TbSi}_3\text{O}_9]_n^{3n-}$ small-pore framework showed the presence of several Q peaks inside the tunnels, assigned to highly disordered charge-balancing K^+ cations. Ten crystallographic distinct K^+ sites were refined with variable occupancy, adding up to a fixed charge of +3. The quality of the crystal data was not suitable for anisotropic refinement of each atom, and common refinable isotropic displacement parameters were used instead (one per atom type). To allow a sensible (and more stable) refinement of the structure, the Tb^{3+} center was refined using anisotropic displacement parameters to better account for the electron density around its crystallographic position. However, the atom refined as a nonpositive definite, as a consequence of the low quality of the crystal data. Toward the end of the refinement, racemic twinning of the crystals was taken into consideration and the TWIN law (-1 0 0, 0 -1 0, 0 0 -1) was implemented along with one BASF parameter which refined to *ca.* 0.50. The last difference Fourier map synthesis showed a residual electron density with the strongest peak ($4.855 \text{ e}\text{\AA}^{-3}$) at 1.18 Å from K(4), and the deepest hole ($-4.695 \text{ e}\text{\AA}^{-3}$) at 0.94 Å from Tb(1).

Crystals of Tb-AV-23 which were placed in an atmosphere saturated with water were also studied. The very high mosaicity of these samples (*ca.* 10° per reflection) precluded the solution and refinement of a valid structural model. However, it was possible

to successfully index the material [$a = 14.203(3) \text{ \AA}$, $b = 5.8910(12) \text{ \AA}$, $c = 13.089(3) \text{ \AA}$, volume = $1095.2(4) \text{ \AA}^3$] in space group $Pmn2_1$ ($R_{int} = 0.0580$).

Y-AV-23 samples also exhibited poor crystal morphology and a very high mosaicity. A poorly diffracting crystal of Y-AV-23, saturated with water (plate prismatic $0.12 \times 0.07 \times 0.03 \text{ mm}$ crystal), was mounted on a Bruker KAPPA CCD-2000 charge coupled device (CCD) area-detector diffractometer (Unidade de Raios-X, RIAIDT, University of Santiago de Compostela, Spain), equipped with $\text{CuK}\alpha$ radiation ($\lambda = 1.54180 \text{ \AA}$) from a rotating anode source (operated at 100 mA and 45 kV). Although the crystal diffracted only until *ca.* 1.2 \AA a primitive (P) unit cell could be determined: $a = 5.889 \text{ \AA}$, $b = 13.053 \text{ \AA}$, $c = 14.163 \text{ \AA}$, $\alpha = \beta = \gamma = 90^\circ$.

The calcination of layered $\text{K}_3[\text{LnSi}_3\text{O}_8(\text{OH})_2]$ ($\text{Ln}^{3+} = \text{Tb}^{3+}$ and Y^{3+}), AV-22, yields mixed tetrahedral-octahedral frameworks, $\text{K}_3[\text{LnSi}_3\text{O}_9]$ or AV-23 materials (Figure 5.2a), which were characterized by powder and single-crystal X-ray diffraction. Because it was only possible to refine a structure for Tb-AV-23 (Y-AV-23 was confirmed by single-crystal XRD to be isostructural), here we shall focus on this material.

The structure of Tb-AV-23 (Figure 5.2) contains a single crystallographically independent Tb^{3+} metal center coordinated to six $\{\text{SiO}_4\}$ tetrahedra in a distorted octahedral geometry ($\{\text{TbO}_6\}$, Figure 5.2b): the Tb–O bond distances are in the range $2.263(14)$ – $2.346(14) \text{ \AA}$, while the *cis* and *trans* octahedral angles are $82.5(6)$ – $96.3(6)^\circ$ and $171.6(6)$ – $175.6(6)^\circ$, respectively (see Appendix II). Individual $\{\text{TbO}_6\}$ octahedra are isolated from each other by wollastonite-type siliceous chains, $(\text{Si}_6\text{O}_{17})_n^{10n-}$, running parallel to the *a*-axis of the unit cell (Figure 5.2c). The shortest $\text{Tb}\cdots\text{Tb}^{\text{i}}$ internuclear distance is $5.909(1) \text{ \AA}$ [symmetry code: (i) $x, 1+y, z$], a value which is retained from the parent AV-22 distance for the individual anionic $[\text{TbSi}_3\text{O}_8(\text{OH})_2]_n^{3n-}$ layers. When these layers fuse upon calcination (see the discussion below concerning the likely condensation mechanism), the individual triple siliceous units are joined together leading to the formation of wollastonite-type silica chains and imposing a new $\text{Tb}\cdots\text{Tb}^{\text{iii}}$ separation of $7.206(1) \text{ \AA}$ [symmetry code: (iii) $-x, y, z$].

The anionic $[\text{TbSi}_3\text{O}_9]_n^{3n-}$ framework is characterized by a three-dimensional channel system, filled with highly disordered K^+ cations, with the main tunnels running parallel to the $[100]$ and $[010]$ directions. The former are reminiscent of the distorted seven-membered pores of the anionic $[\text{TbSi}_3\text{O}_8(\text{OH})_2]_n^{3n-}$ (Tb-AV-22) layers which, upon

layer condensation, align with the a -axis forming channels. The latter, more regular channels are formed by eight-membered elliptical rings with a cross-section of ca. $2.0 \times 4.0 \text{ \AA}$ (Figure 5.2a). The adjacent channels along $[100]$ and $[001]$ are mutually rotated by 90° , leading to a typical basketweave-type distribution (Figure 5.2a).

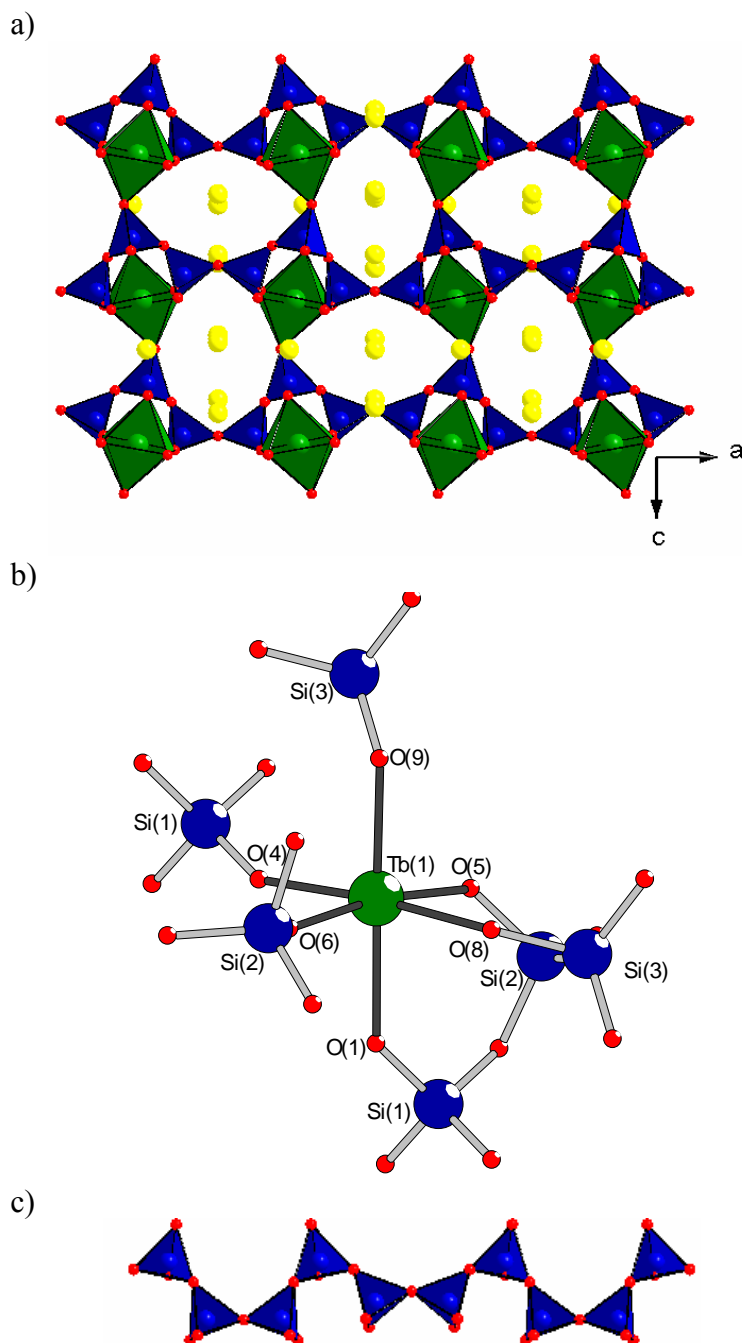


Figure 5.2 – a) Polyhedral representation of the crystal packing in Tb-AV-23, viewed along the b axis b) Distorted octahedral $\{\text{TbO}_6\}$ coordination environment. c) $(\text{Si}_6\text{O}_{17})_n^{10n-}$ wollastonite-type silicate chain, running along a . Polyhedra: green TbO_6 , blue SiO_4 ; spheres: yellow K^+ red O.

Appendix II collects information concerning crystallographic data collection and structure refinement of Tb-AV-23. Atomic coordinates, isotropic displacement parameters, main bond lengths and angles are given in tables.

5.4 Transformation of AV-22 to AV-23

We now try to rationalize the transformation of layered AV-22 into small-pore AV-23. The former is built up of perforated anionic $[\text{RESi}_3\text{O}_8(\text{OH})_2]_n^{3n-}$ layers in the *ac* plane, which pack along the [010] direction in an [ABAB...] fashion (Figure 5.3, top left). The three-dimensional anionic $[\text{RESi}_3\text{O}_9]_n^{3n-}$ (AV-23) framework could, in principle, be generated by rotating half of the AV-22 layers by 180°, all in the same direction, thus removing the inversion symmetry relating adjacent layers. This process seems very unlikely. Alternatively, all AV-22 layers may rotate only by 90° (A- and B-type layers rotating in opposite directions, Figure 5.3, top right), bringing closer the Si–OH groups from adjacent layers. Condensation at high temperatures, with the corresponding release of one water molecule per formed Si–O–Si bridge, yields the anionic $[\text{MSi}_3\text{O}_9]_n^{3n-}$ (AV-23) framework. This condensation also produces a linear chain of corner-sharing silicate tetrahedra (Figure 5.2c), making the final material an inosilicate of the pyroxenoid family (the wollastonite-type chain exhibits a repeating unit with more than two tetrahedral units) [10]. The condensation will only take place in an ordered way if the rotation of the layers is exactly 90°. However, at the relatively high temperature the materials are prepared, the kinetics of layer condensation is probably fast, and the mutual rotation of the layers may not always be complete (<90°). As a result, defect regions may form in the crystal, explaining the high mosaicity of the AV-23 crystals studied.

In summary, the AV-22 dehydration causes the disordered condensation of adjacent two-dimensional $[\text{RESi}_3\text{O}_8(\text{OH})_2]_n^{3n-}$ nets, yielding AV-23, a material characterized by multiple crystal lattices. Thus, the AV-23 crystal structure described above is only a spatial average of all microdomains, explaining the high *R*-factors obtained (Table 1 in Appendix II) and problems encountered while refining the model. This issue will be further addressed in the photoluminescence studies section.

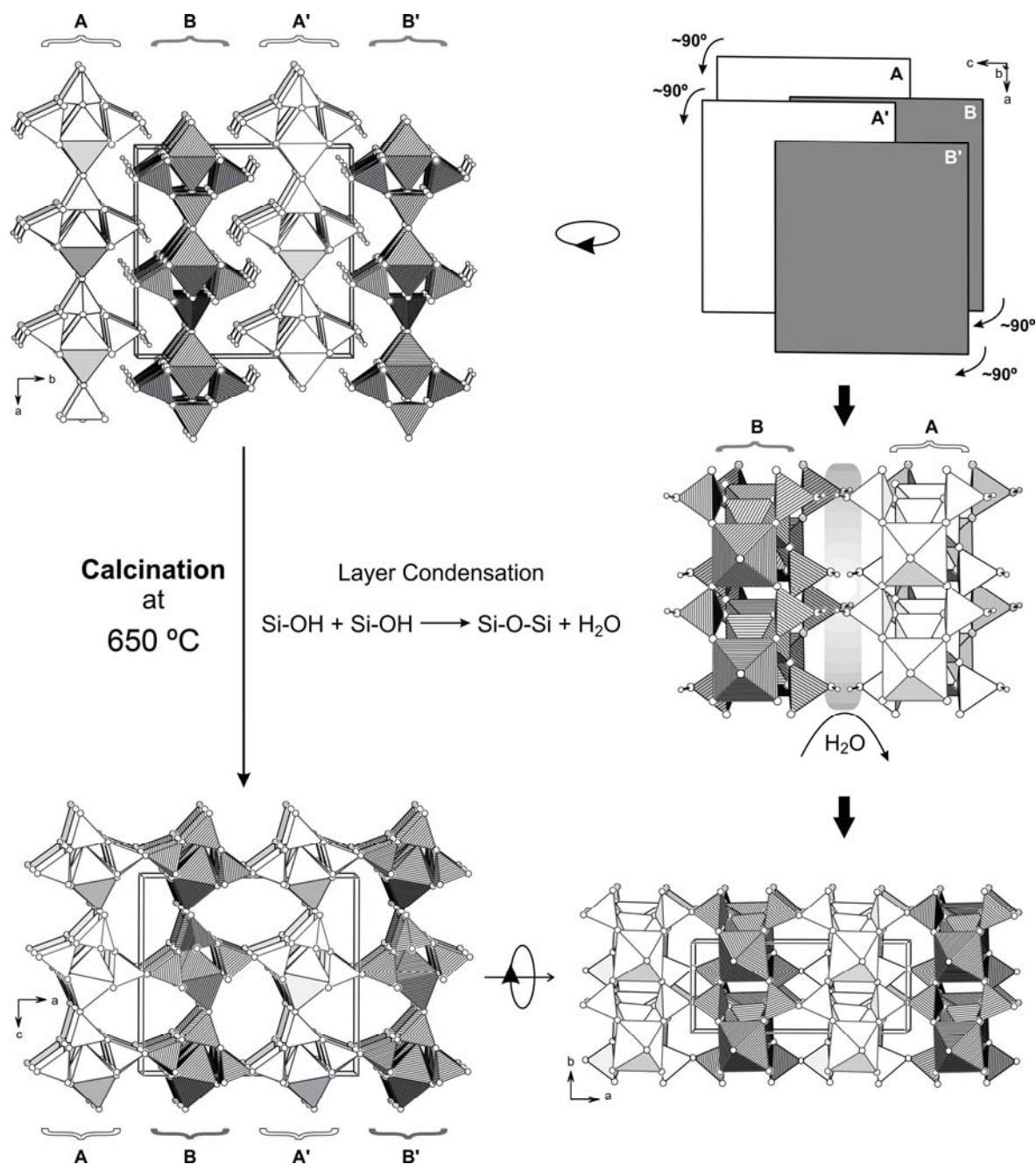


Figure 5.3 – Schematic representation of the condensation ($\text{Si-OH} + \text{Si-OH} \rightarrow \text{Si-O-Si} + \text{H}_2\text{O}$) of adjacent anionic layers of AV-22 yielding the framework of AV-23.

All studied $\text{K}_3\text{RESi}_3\text{O}_9$, $\text{RE}^{3+}=\text{Y}^{3+}$, Tb^{3+} , Eu^{3+} and Er^{3+} and mixed Y/Er materials display powder XRD patterns characteristic of AV-23 (Figure 5.4 and Figure 5.5) and no evidence was found for the presence of any impurity phases.

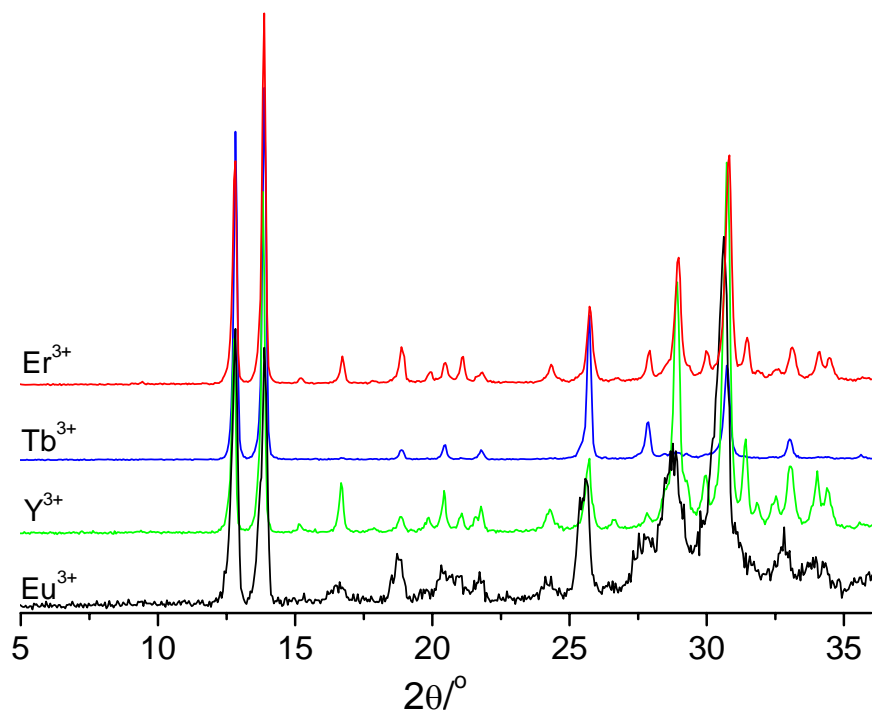


Figure 5.4 – Experimental powder XRD patterns of pure AV-23 samples.

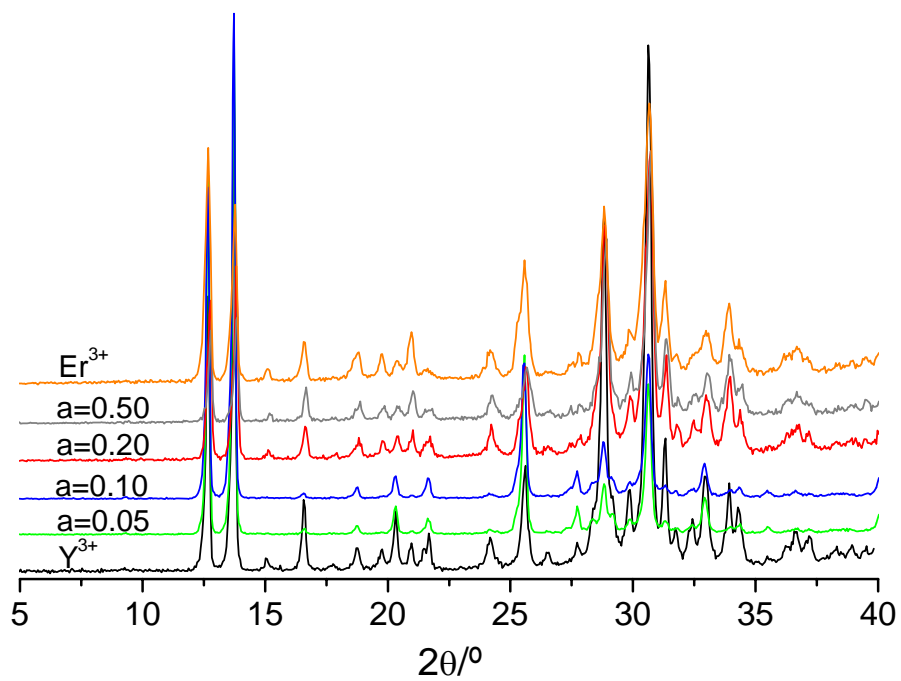


Figure 5.5 – Experimental powder XRD patterns of mixed Y/Er-AV-23 samples (a indicates the Er^{3+} content).

Figure 5.6 displays a scanning electron microscopy image of Tb-AV-23 crystals.

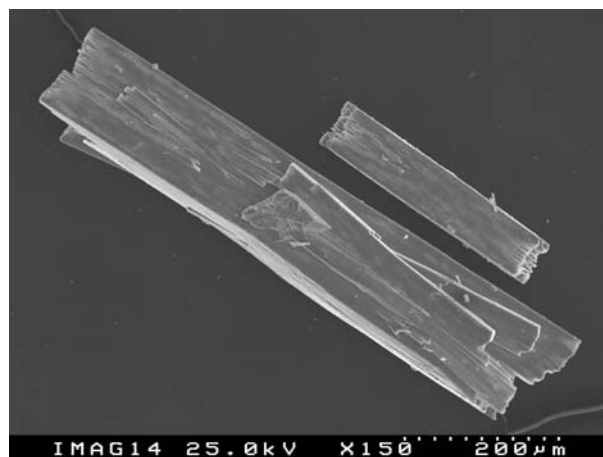


Figure 5.6 – Scanning electron micrograph of Tb-AV-23 crystals.

The ^{29}Si MAS NMR spectrum of Y-AV-23 (Figure 5.7) displays three resonances at -82.1, -83.1 and -87.7 ppm in a 1:1:1 intensity ratio, in accord with the XRD crystal structure, which calls for the presence of three Si local environments with 1:1:1 populations.

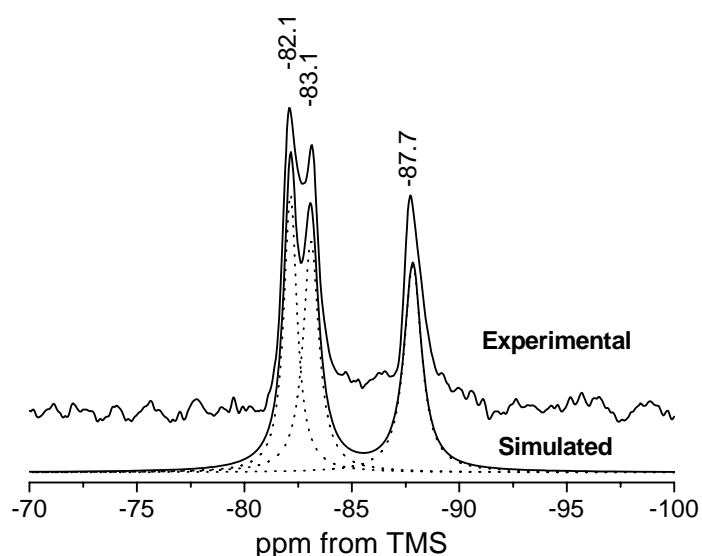


Figure 5.7 – Experimental and simulated ^{29}Si MAS NMR spectra of Y-AV-23.

All three Si sites have as second-nearest-neighbors two Si and two Y atoms. Figure 5.8 represents the three different Si local environments according to the crystal structure. Assuming the well-known correlation between the ^{29}Si isotropic chemical shift and the average Si–O–Si bond angle holds [11], the resonances are tentatively assigned as

follows: -87.7 ppm to Si(3) (average bond angle 149.7°), -83.1 ppm to Si(1) (141.0°) and -82.1 ppm to Si(2) (135.5°). Indeed, if one uses the simple correlation $\delta = -0.555\alpha - 7.462$, valid for $Q^4(4Al)$ zeolites, the calculated isotropic chemical shifts are, respectively, -90.5, -85.7 and -82.7 ppm, in good agreement with our experimental results, considering the significant differences in the Si coordination spheres of AV-23 and zeolites.

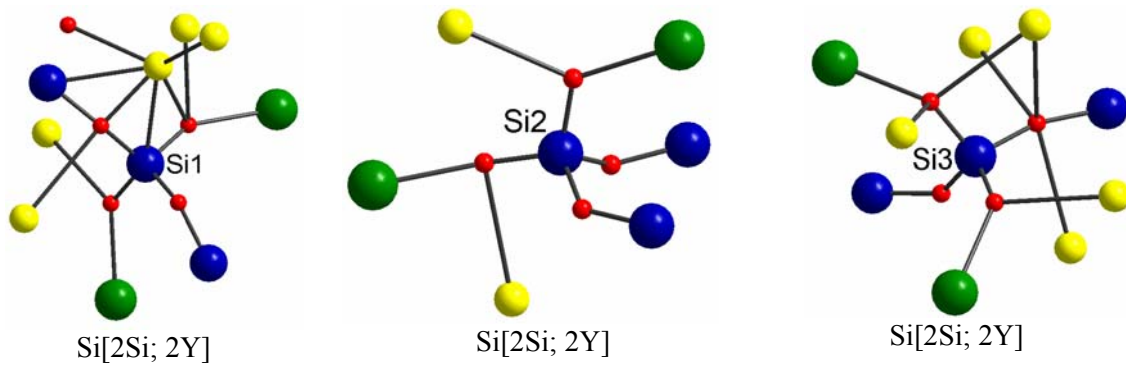


Figure 5.8 – Si local environments in the structure of Y-AV-23. Green - Y^{3+} , blue - Si^{4+} , red - O^{2-} , yellow - K^+ .

The calcined phase transforms, when kept in an atmosphere saturated with water, but not to the initial as-prepared AV-22 phase. The transformation process was monitored with powder X-ray diffraction and ^{29}Si NMR (Figure 5.9 and Figure 5.10).

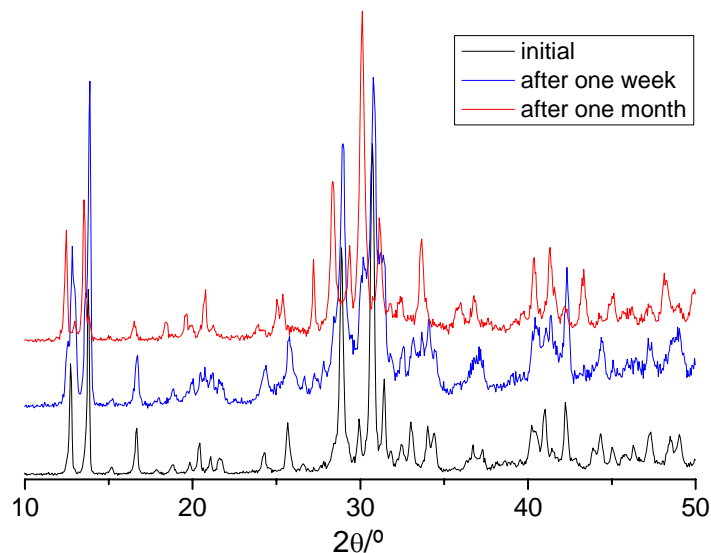


Figure 5.9 – Powder XRD spectra illustrating the changes of the structure of Y-AV-23 with the time of hydration.

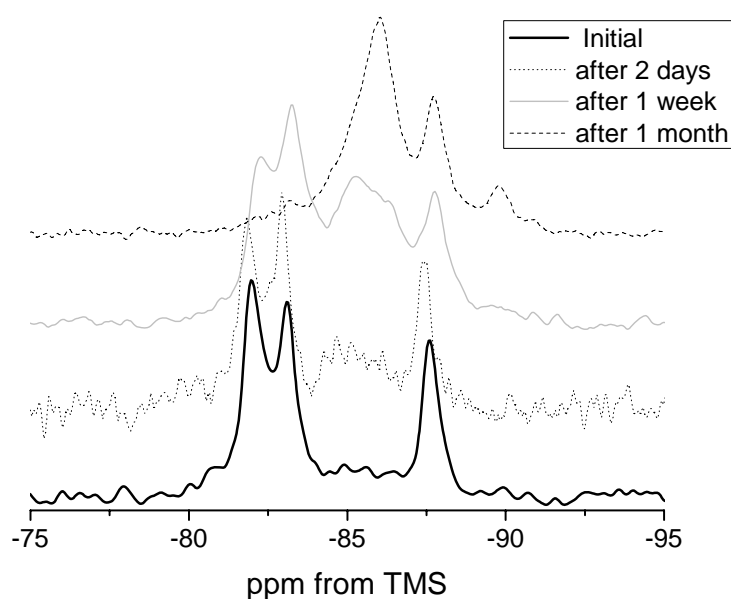


Figure 5.10 – ^{29}Si MAS NMR spectra recorded with 5 kHz MAS illustrating the changes of the structure of Y-AV-23 with the time of hydration.

The Raman spectrum of Tb-AV-23 (Figure 5.11) shows several sharp bands between 100 and 1200 cm^{-1} . Bands in the intermediate-wavenumber range (400-800 cm^{-1}) result from symmetric bending vibrations of the Si-O-Si bridging oxygens between adjacent SiO_4 tetrahedra. Compared to the Raman shifts observed in silicate glasses and melts, the Raman bands in the range between 400 and 600 cm^{-1} and below 400 cm^{-1} can be assigned to the presence of Si-O-Si symmetric stretching vibrations and the bending of the Si-O-Si linkages, respectively [12]. In yttrium orthosilicate crystals, bands in the 500-700 cm^{-1} range are generally characteristic for the YO_6 octahedra [13]. In Tb-AV-22 we ascribed the band at 668 cm^{-1} to the Tb-O stretching vibrations of TbO_6 octahedra and thus the band at 666 cm^{-1} , and the bands at 645 and 693 cm^{-1} in Tb-AV-23 can be attributed to the same Tb-O stretching vibrations. Numerous bands in the low-, medium-, and high-wavenumber range were recorded. Symmetric Si-O stretching vibrations of SiO_4 groups with one, two, three, or four nonbridging oxygens emerge in alkali silicates with different contents of metal oxides in the high-wavenumber range (800-1200 cm^{-1}) [14-16]. Below 400 cm^{-1} bands are mainly caused by lattice vibrations of the framework and cation-oxygen bonding and lattice vibrations of the skeleton or framework [14]. Typical values for Ln-O stretching vibrations are around 300 cm^{-1} , located in the region of lattice vibrations thus the band at 319 cm^{-1} is attributed to Tb-O stretching vibrations [17].

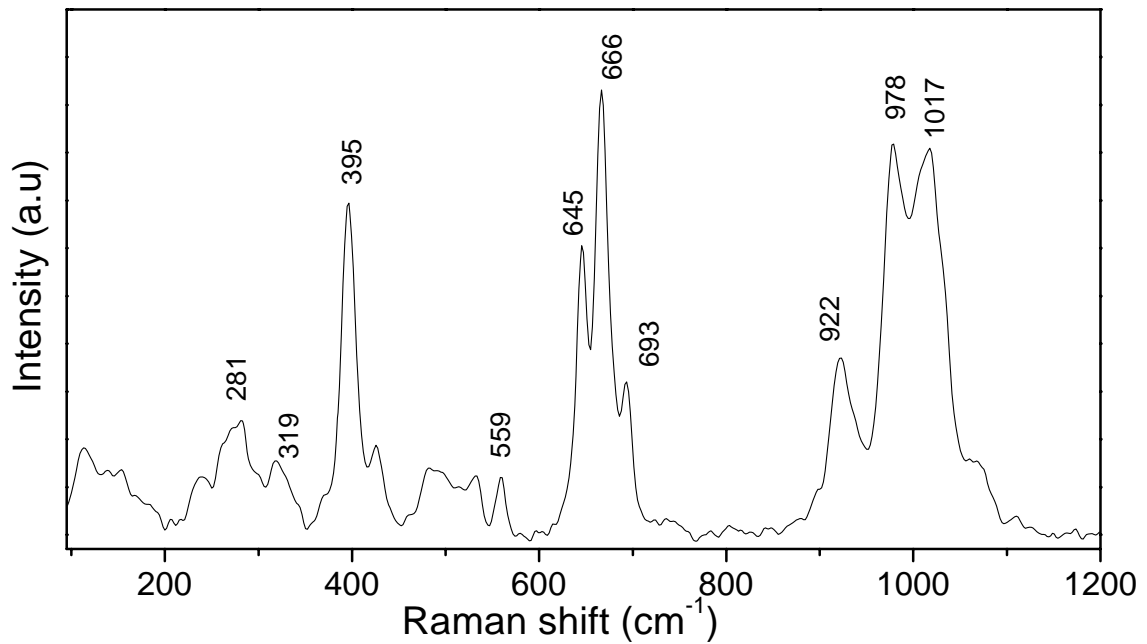


Figure 5.11 – Raman spectrum of Tb-AV-23.

5.5 Photoluminescence spectroscopy

All photoluminescent studies were performed on AV-23 samples left in air. The obtained photoluminescent spectra were reproducible, which means that the calcined phase is stable in air. The stability is also confirmed by powder XRD.

Figure 5.12 shows the excitation spectrum of Tb-AV-23, monitored at the $^5D_4 \rightarrow ^7F_5$ transition of Tb^{3+} (542 nm). The sharp lines between 300 and 500 nm are assigned to the intraconfigurational $4f^8$ transitions of Tb^{3+} between the 7F_6 ground state and the $^5D_{4-0}$, $^5L_{10}$ and $^5G_{6-3}$ excited levels. The broad bands between 250 and 300 nm are ascribed to the spin-forbidden (high-spin, HS) interconfigurational $4f^8 \rightarrow 4f^75d^1$ (fd) transition of Tb^{3+} [18,19]. These fd bands may be observed for (heavy) Ln^{3+} ions with more than seven $4f$ electrons, at an energy lower than the energy of the spin-allowed (low-spin, LS) fd transitions. The shoulder at *ca.* 240 nm is assigned to the LS interconfigurational fd transition of Tb^{3+} .

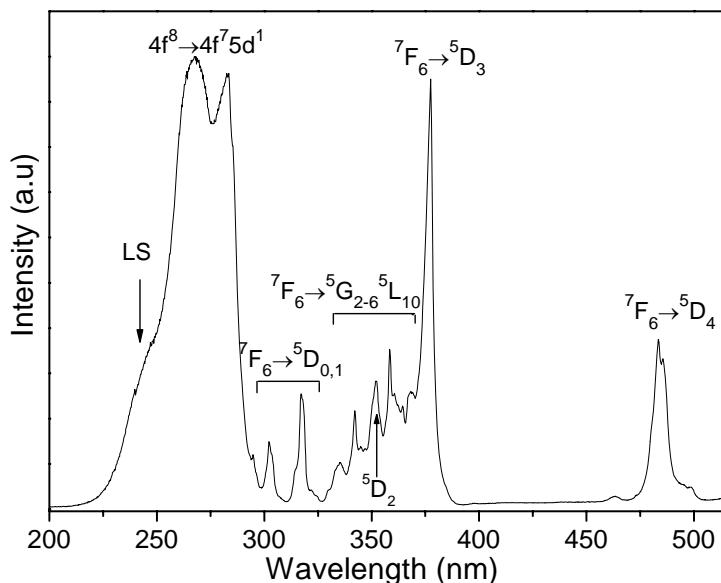


Figure 5.12 – Excitation spectrum of Tb-AV-23, monitored at the 7F_5 manifold (542 nm).

The emission lines of Tb-AV-23 (Figure 5.13) are assigned to the ${}^5D_4 \rightarrow {}^7F_{2-6}$ transitions of Tb^{3+} . Luminescence from the higher (e.g. 5D_3) excited states is not detected, indicating a very efficient nonradiative relaxation to the 5D_4 level. The deactivation of excited states by cross-relaxation between adjacent centers (concentration quenching) may also explain the absence of emission from high-energy states (e.g. 5D_3). The same emission is obtained with excitation at the maximum of the HS *fd* band.

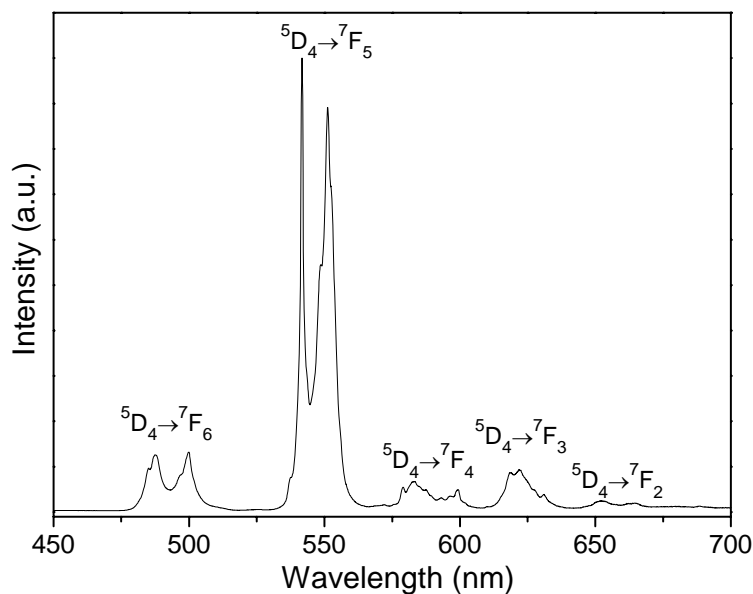


Figure 5.13 – Emission spectrum of Tb-AV-23, excited at the 5D_3 manifold (377 nm).

The presence of more than one local Tb^{3+} environment is detected in the ${}^5\text{D}_4$ decay curves (excited at 283 or 377 nm and detected at the ${}^5\text{D}_4 \rightarrow {}^7\text{F}_5$ transition). These curves (Figure 5.14) are well fitted by a bi-exponential function, yielding the two lifetimes depicted in Table 5.1. We have previously shown that as-prepared Tb-AV-22 displays only one local Tb^{3+} site with a lifetime of 4.45 ms, similar to the Tb-AV-23 τ_1 lifetime, 4.02 ms. The crystal structures of AV-22 and AV-23 materials call for the presence of a single independent RE^{3+} environment. As discussed above, the AV-23 crystals exhibit considerable internal disorder, indicated by the overall poor diffraction and high mosaicity. This suggests that the thermal transformation of AV-22 into AV-23 may generate defect crystal regions. Moreover, TGA analysis of AV-23 samples left in air for a few days reveals weight losses equivalent to ca. 0.5 water molecules, presumably associated with these defect regions. If so, the two lifetimes measured for AV-23 may be ascribed to RE^{3+} centers in regular framework positions, and in defect regions. The facts that (i) one of the lifetimes is significantly shorter (1.17 ms) than the other (4.02 ms), and (ii) τ_1 and τ_{II} decrease, respectively, 15 % and 60 % from 10 K to room temperature, support this hypothesis because in the defect regions RE^{3+} ions are probably associated with water molecules [20].

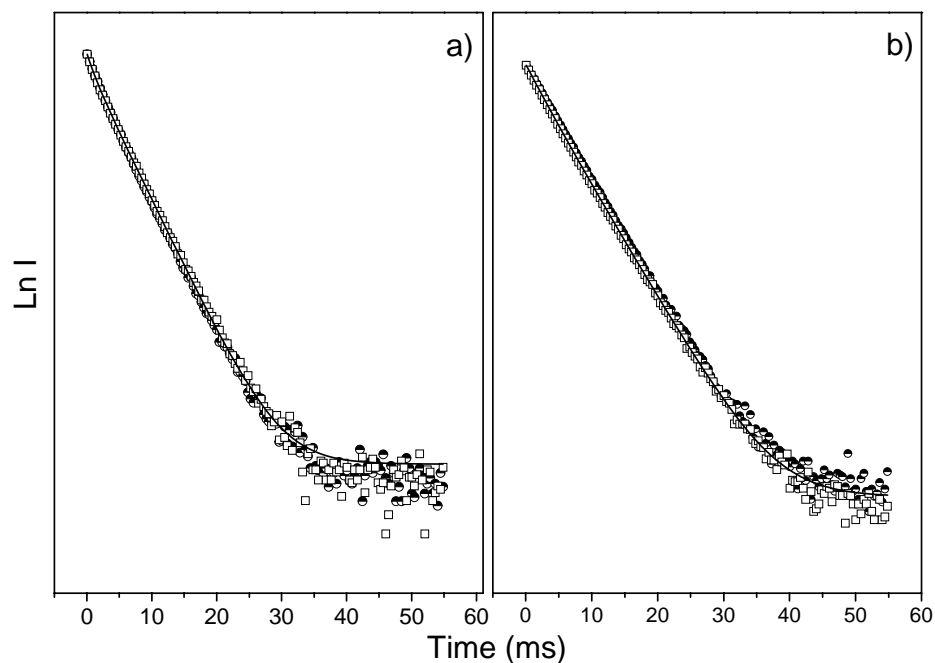
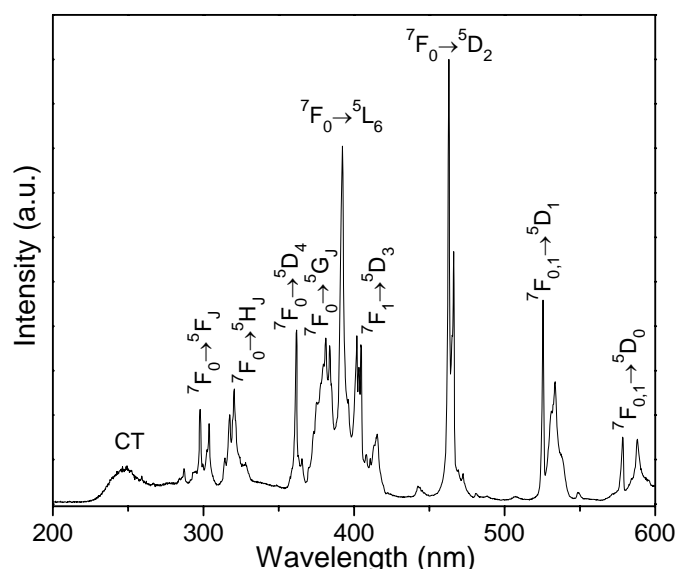


Figure 5.14 – a) Room temperature and b) 10 K ${}^5\text{D}_4$ decay curves of Tb-AV-23, monitored at 542 nm under (\bullet) 283 nm and (\square) 377 nm excitation. The black lines are the best data bi-exponential fit ($r^2 > 0.99$).

Table 5.1 – 5D_4 lifetimes of Tb-AV-22 and Tb-AV-23 measured at 300 and 10 K (excitation wavelength 377 nm).

Sample	Tb-AV-22		Tb-AV-23	
T (K)	300	300	300	10
$\lambda_{\text{Emis.}}$ (nm)	540.5	542	542	542
τ_I (ms)	4.45±0.02	4.02±0.02	4.78±0.02	4.78±0.02
τ_{II} (ms)	-	1.17±0.02	2.88±0.02	2.88±0.02

The excitation spectrum of Eu-AV-23 monitored at the $^5D_0 \rightarrow ^7F_2$ transition at 609.5 nm (Figure 5.15), displays a series of sharp lines assigned to the $^7F_{0-1} \rightarrow ^5D_{4-0}$, 5L_6 , $^5G_{2-6}$, $^5H_{3-7}$ and $^5F_{1-5}$ intra $4f^6$ transitions of Eu^{3+} . The broad band at 250 nm is assigned to a $\text{Eu} \rightarrow \text{O}$ charge-transfer transition [21].

**Figure 5.15** – Excitation spectrum of Eu-AV-23, monitored at the 7F_2 manifold (609.5 nm).

The emission spectrum of Eu-AV-23 (excited at 392 nm) is shown in Figure 5.16. The sharp emission lines are assigned to transitions between the first excited non-degenerate 5D_0 state and the $^7F_{0-4}$ levels of the fundamental Eu^{3+} septet. Except for the $^5D_0 \rightarrow ^7F_1$ lines, which have a predominant magnetic-dipole character, the observed transitions are mainly of electric-dipole nature. The $^5D_0 \rightarrow ^7F_1$ magnetic transition is weaker than the $^5D_0 \rightarrow ^7F_2$ forced electric-dipole one. The two $^5D_0 \rightarrow ^7F_0$ lines reveal the presence of, at least, two distinct Eu^{3+} environments (inset in Figure 5.16).

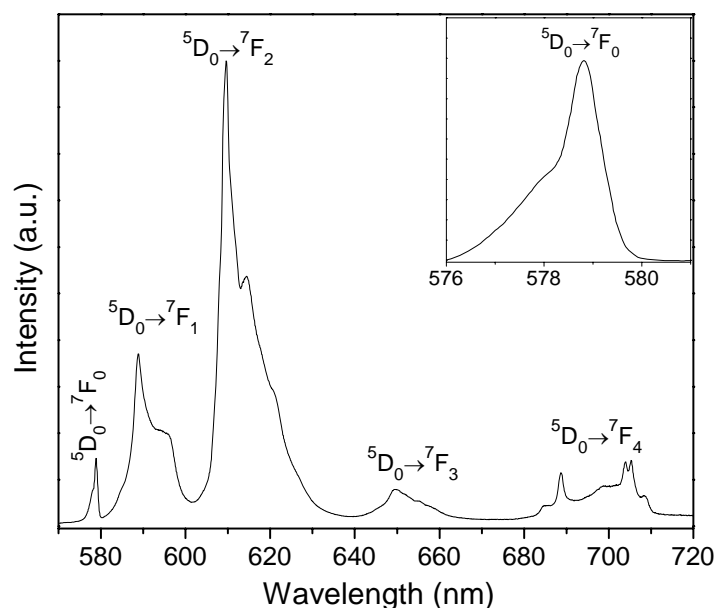


Figure 5.16 – Emission spectrum of Eu-AV-23, excited at the 5L_6 manifold (392 nm).

Eu^{3+} luminescence from higher excited states, such as 5D_1 , is not detected, indicating a very efficient nonradiative relaxation to the 5D_0 level. As mentioned before, the deactivation of excited states by cross-relaxation between adjacent centers may also explain the absence of the 5D_1 emission. This is confirmed by the similarity of the steady-state and time-resolved (delay time of 0.05 ms) spectra recorded at 14 K (Figure 5.17) in the $^5D_0 \rightarrow ^7F_1$ region ($^5D_1 \rightarrow ^7F_3$ lines are not observed).

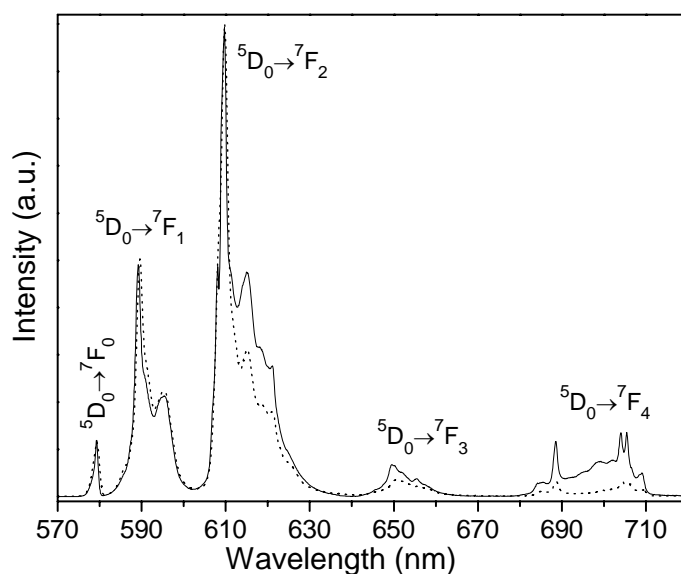


Figure 5.17 – Photoluminescence steady-state (solid line) and time-resolved (dotted line) emission spectra of Eu-AV-23 acquired at 14 K and excited at the 5L_6 manifold (392 nm).

These local environments were further investigated by recording the decay curves (Figure 5.18) on the 5D_0 levels as a function of the excitation wavelength (392 or 463 nm). The results are well fitted by (i) bi-exponential functions when monitoring at the maximum of the ${}^5D_0 \rightarrow {}^7F_{1,2}$ transitions, and (ii) three-exponential functions when monitoring both at the maximum of the ${}^5D_0 \rightarrow {}^7F_0$ transition and the low-energy side of the ${}^5D_0 \rightarrow {}^7F_2$ transition. The lifetimes of AV-22 and AV-23 are gathered in Table 5.2.

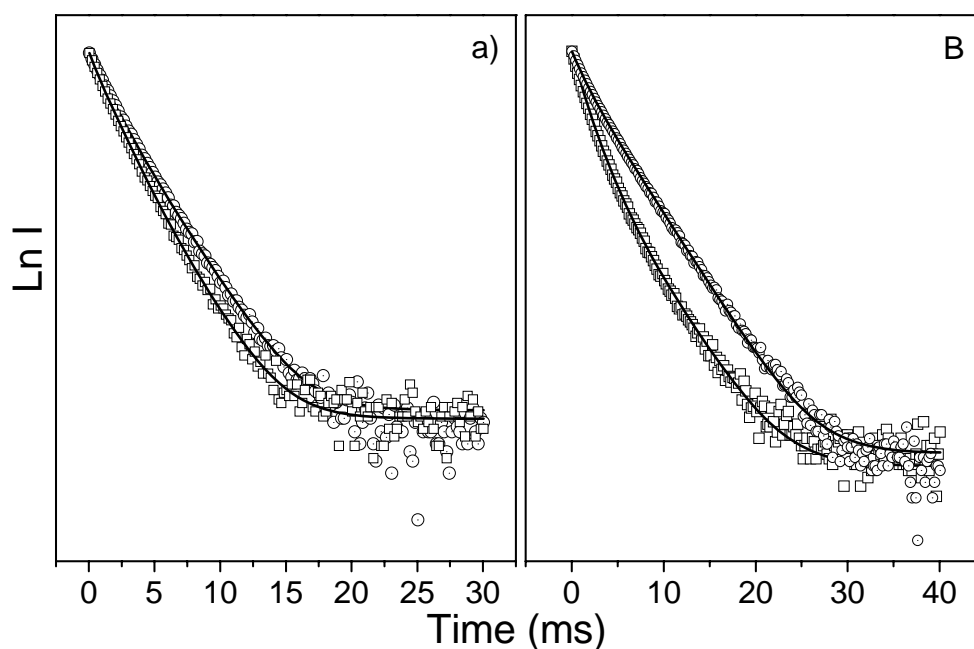


Figure 5.18 – a) Room temperature and b) 10 K 5D_0 decay curves of Eu-AV-23, monitored at 609.5 nm (\odot) and 615 nm (\square) under 392 nm excitation. The black lines are the best data bi- and three-exponential fit ($r^2 > 0.99$).

Table 5.2 – 5D_0 lifetimes of Eu-AV-22 and Eu-AV-23 measured at 300 and 10 K (excitation wavelength 392 nm).

Sample	Eu-AV-22		Eu-AV-23			
	300	10	300		10	
$\lambda_{\text{Emis.}}$ (nm)	609.5	609.5	609.5	615	609.5	615
τ_I (ms)	2.02 ± 0.02	2.49 ± 0.02	2.13 ± 0.02	2.13 ± 0.03	3.32 ± 0.02	3.27 ± 0.03
τ_{II} (ms)	0.58 ± 0.02	0.64 ± 0.02	1.25 ± 0.03	1.25 ± 0.02	1.40 ± 0.01	1.43 ± 0.02
τ_{III} (ms)				0.33 ± 0.01		0.40 ± 0.01

Detailed photoluminescence studies of AV-22 have shown that the Eu^{3+} ions may be present in regular crystallographic positions in the layers (site I with the larger lifetime τ_I), and replacing the K^+ ions residing in the pores of the layers and/or in the interlayer space (site II with smaller lifetime τ_{II}). The transformation of the layered AV-22 material to small-pore AV-23 generates three Eu^{3+} local environments. The lifetime of one of these sites is similar to that of site I in AV-22, respectively, 2.13 and 2.02 ms and, thus, is attributed to Eu^{3+} ions in the framework, which is, essentially, built up of fused AV-22 layers. The smallest AV-23 lifetime (0.33 ms) is ascribed to Eu^{3+} ions in defect regions associated with water molecules, and therefore, the AV-23 site II must be assigned to Eu^{3+} ions replacing K^+ ions in the micropores. The comparison of the low temperature (14K) emission spectra of Eu-AV-22 and Eu-AV-23 (Figure 5.19) in the ${}^5\text{D}_0 \rightarrow {}^7\text{F}_2$ region supports this assignment. Indeed, the two spectra are quite similar in the high-energy region of the ${}^5\text{D}_0 \rightarrow {}^7\text{F}_2$ transition. The ${}^5\text{D}_0$ decay curves monitored at this energy are well-fitted by two exponential functions yielding the two lifetimes depicted in Table 5.2. The lifetime of site II is larger for Eu-AV-23, in accord with the absence of OH groups due to the calcination process. The Eu^{3+} site corresponding to the regular crystallographic position shows the smallest full width at half-maximum (FWHM) (21.5 cm^{-1}). The site ascribed to Eu^{3+} substituting for K^+ exhibits larger local disorder, witnessed by the larger FWHM (26.5 cm^{-1}), while the third site ascribed to Eu^{3+} in defect crystal regions displays the largest FWHM (44.0 cm^{-1}).

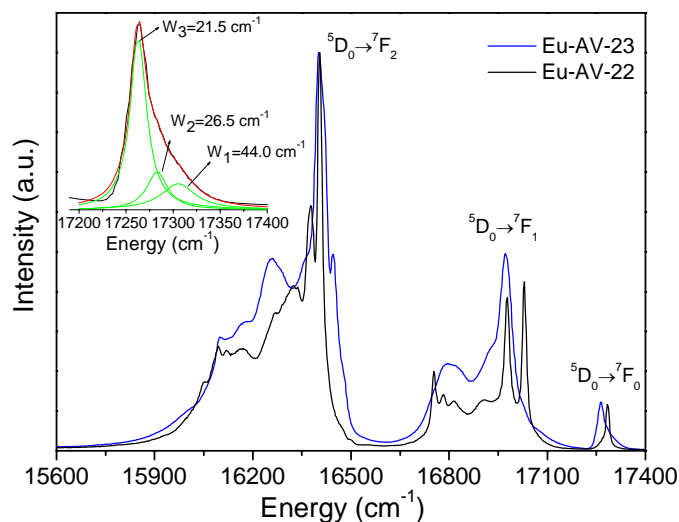


Figure 5.19 – Emission spectra of Eu-AV-22 and Eu-AV-23 acquired at 14 K and excited at the ${}^5\text{L}_6$ manifold (392 nm). The inset shows the FWHM deconvolution for the three Eu sites.

The radiances of Tb- and Eu-AV-22 and Tb- and Eu-AV-23 samples and standard Gd₂O₂S:Tb, green, and Y₂O₂:Eu, red, phosphors were measured and compared for different excitation wavelengths (Table 5.3). The Tb-AV-23 radiance at 270 nm is ca. 55 % smaller than that of Tb-AV-22, which, in turn, is ca. 60 % smaller than the radiance of Gd₂O₂S:Tb. The Eu-AV-23 radiance at 392 nm is ca. 54 % smaller than that of Eu-AV-22, which, itself, is 1 order of magnitude smaller than the Y₂O₂:Eu radiance (264 nm excitation). The lower radiance of AV-23 relatively to AV-22 is due to more effective nonradiative channels caused by the presence in the former of defect crystal regions.

Table 5.3 – Room temperature radiance for the standard green Gd₂O₂S:Tb and red Y₂O₂:Eu phosphors, Tb-and Eu-AV-22, Tb-and Eu-AV-23 measured at different excitation wavelengths (λ).

	Gd ₂ O ₂ S:Tb	Tb-AV-22	Tb-AV-23	Y ₂ O ₂ S:Eu	Eu-AV-22	Eu-AV-23
λ (nm)	270	270	270	264	392	392
Radiance ($\mu\text{W}/\text{cm}^2$)	0.924	0.351	0.193	0.299	0.052	0.028

FT-Raman spectra were recorded to quantitatively study the PL intensity as a function of the Er³⁺ content in the Y/Er-AV-23 system K₃(Y_{1-a}Er_aSi₃O₉), $a=0.005-1$, (Figure 5.20). As expected, the vibronic transitions appear in the Raman shift range 50-1200 cm⁻¹ (not shown), while the intra-4f¹¹ electronic transitions are detected at 3500-2500 cm⁻¹. The emission lines are assigned to the intra-4f¹¹ transitions between the ⁴I_{13/2} and ⁴I_{15/2} levels of the ground multiplet of Er³⁺. Provided the intensities of the vibrational spectra of the different samples in the series are similar, the variation of the PL intensity as a function of the Er³⁺ content may be estimated directly from the intensity of the strongest electronic line (1.54 μm) in the 3500-2500 cm⁻¹ region (inset in Figure 5.20). In Y/Er-AV-23 the ⁴I_{13/2} → ⁴I_{15/2} PL integrated area increases with increasing Er³⁺ content, from 0.005 to 0.05, and then decreases reaching 0.04 for $a=0.2$, and 0.02 for $a=0.5$. This suggests that PL first increases due to the increase in the number of optically active centers, but after the maximum, at ca. $a=0.05$, the PL is strongly quenched by Er³⁺-Er³⁺ interactions.

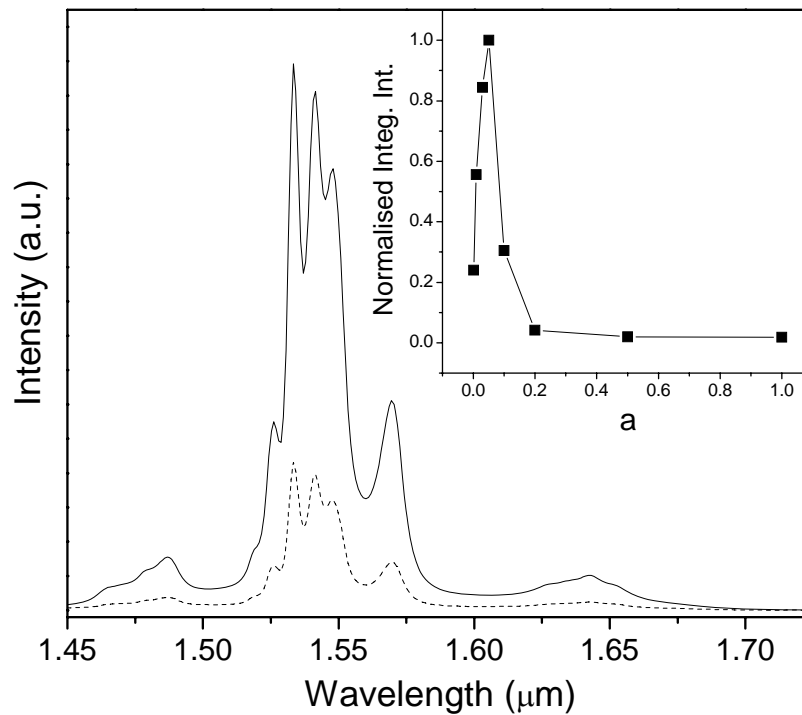


Figure 5.20 – FT-Raman spectra of $K_3(Y_{1-a}Er_aSi_3O_9)$, $a=0.05$ (solid line) and $a=0.005$ (dashed line). The inset depicts the normalized integrated intensity of the $1.54 \mu\text{m}$ photoluminescence as a function of the Er^{3+} content for the samples with a in the range 0.005 to 1.

The Er^{3+} - Er^{3+} interactions were further investigated by room temperature ${}^4I_{13/2}$ decay curves (excitation at 376 nm), which are well fitted by bi-exponential functions, indicating the presence of two Er^{3+} sites (Table 5.4). Increasing the Er^{3+} content leads to a decrease of the lifetimes, which is more significant for the larger lifetime, attributed to Er^{3+} ions in regular crystallographic positions in the layers. Quenching is observed for $a=0.05$, due to Er^{3+} - Er^{3+} interactions, suggesting that the maximum efficiency is reached at low Er^{3+} concentrations.

Table 5.4 – Room temperature ${}^4I_{13/2}$ lifetimes of $K_3(Y_{1-a}Er_aSi_3O_9)$ ($a=0.01$ - 0.20) excited at 376 nm.

a	0.01	0.05	0.10	0.20
τ_I (ms)	7.71 ± 0.20	3.90 ± 0.03	1.99 ± 0.04	0.57 ± 0.01
τ_{II} (ms)	1.11 ± 0.06	0.81 ± 0.03	0.42 ± 0.03	0.15 ± 0.01

5.6 Conclusions

The structural characterization of small-pore $K_3RESi_3O_9$, $Ln=Y, Eu, Tb$ and Er materials, named AV-23 has been reported. The dehydration process of layered rare-earth silicates AV-22 ($K_3[RESi_3O_8(OH)_2]$, $RE=Y, Eu, Tb$ and Er) into AV-23 materials has been rationalized. The crystal structure of the latter materials calls for the presence of a single independent RE^{3+} environment. Despite this, detailed PL studies showed the presence of two or three RE^{3+} sites, which may be ascribed to metal centers in regular framework positions, defect regions, and in the micropores, replacing K^+ . The lifetimes of the RE^{3+} species in the layers of AV-22 and in the framework of AV-23 are only slightly different (4.45 and 4.02 ms and 2.02 and 2.13 ms for, respectively, Tb- and Eu- containing materials). The maximum emission efficiency of $K_3(Y_{1-a}Er_aSi_3O_9)$, $a=0.005-1$, samples is observed for $0.01 \leq a \leq 0.05$. The calcination process increases the intensity of the Er^{3+} emission (essentially due to the removing of OH groups). Er^{3+} - Er^{3+} interactions quench the PL, decreasing the ${}^4I_{13/2}$ lifetime as the Er^{3+} content increases. The PL properties are, therefore adjusted by changing the dimensionality of the rare-earth silicates.

5.7 References

- [1] M.H. Kostova, D. Ananias, F.A.A. Paz, A. Ferreira, J. Rocha, L.D. Carlos, *J. Phys. Chem. B* 111 (2007) 3574.
- [2] M.H. Kostova, D. Ananias, L.D. Carlos, J. Rocha, *J. Alloys Comp.* (2007) in press.
- [3] V.I. Ponomarev, O.S. Filipenko, L.O. Atovmyan, *Kristallografiya* 33 (1988) 98.
- [4] T. Kottke, D. Stalke, *J. App. Crystallogr.* 26 (1993) 615.
- [5] SMART, Bruker Molecular Analysis Research Tool v 5.054 © Bruker AXS, Madison, Wisconsin, USA, 1997-98.
- [6] SAINTPlus, Data Reduction and Correction Program v. 6.01 © Bruker AXS, Madison, Wisconsin, USA, 1997-98.
- [7] Sheldrick, G. M. SADABS v.2.01, Bruker/Siemens Area Detector Absorption Correction Program Bruker AXS, Madison, Wisconsin, USA, 1998.
- [8] Sheldrick, G. M. SHELXS-97, Program for Crystal Structure Solution, University of Göttingen, 1997.
- [9] Sheldrick, G. M. SHELXL-97, Program for Crystal Structure Refinement, University of Göttingen 1997.
- [10] M. Henry, *Coord. Chem. Rev.* 180 (1998) 1109.
- [11] G. Engelhardt, D. Michel, *High-resolution solid-state NMR of silicates and zeolites*, John Wiley, Chichester, 1987.
- [12] P. McMillan, *Am. Mineral.* 69 (1984) 622.
- [13] S. Campos, A. Denoyer, S. Jandl, B. Viana, D. Vivien, P. Loiseau, B. Ferrand, *J. Phys. Cond. Matter* 16 (2004) 4579.
- [14] J.L. You, G.C. Jiang, H.Y. Hou, H. Chen, Y.Q. Wu, K.D. Xu, *J. Raman Spec.* 36 (2005) 237.
- [15] M. Akaogi, N.L. Ross, P. McMillan, A. Navrotsky, *Am. Mineral.* 69 (1984) 499.
- [16] D.M. Tobbens, V. Kahlenberg, R. Kaindl, *Inorg. Chem.* 44 (2005) 9554.
- [17] H. Assaoudi, A. Ennaciri, A. Rulmont, *Vibr. Spec.* 25 (2001) 81.
- [18] M. Laroche, J.L. Doualan, S. Girard, J. Margerie, R. Moncorge, *J. Opt. Soc. Am. B* 17 (2000) 1291.

- [19] L. van Pieterson, M.F. Reid, G.W. Burdick, A. Meijerink, *Phys. Rev. B* 65 (2002) 45114.
- [20] J.-C.G. Bunzli, in *Lanthanide probes in life, chemical and earth science theory and practices*, edited by J.-C. G. Bunzli and G. R. Choppin, Elsevier, Amsterdam, 1989.
- [21] D. Ananias, F.A.A. Paz, L.D. Carlos, C. Geraldes, J. Rocha, *Angew. Chem. Int. Ed.* 45 (2006) 7938.

6 Microporous lanthanide silicates ($K_7M_{3-a}Ln_aSi_{12}O_{32}\cdot 3H_2O$, $M^{3+} = Tb^{3+}$, Gd^{3+} ; $Ln^{3+} = Eu^{3+}$, Sm^{3+} , Tb^{3+} and Gd^{3+}), $3 \geq a > 0$

Index

6.1	Introduction	142
6.2	Synthesis.....	142
6.3	Structural characterization.....	144
6.4	Photoluminescence spectroscopy	154
6.5	Conclusions	167
6.6	References	169

6.1 Introduction

As a result of a systematic study with intention of incorporating optically active lanthanide centers in the structure of silicates, microporous lanthanide silicates $K_7M_{3-a}Ln_aSi_{12}O_{32}\cdot 3H_2O$, $M^{3+} = Tb^{3+}, Gd^{3+}$; $Ln^{3+} = Eu^{3+}, Sm^{3+}, Tb^{3+}$ and Gd^{3+} , $3 \geq a > 0$ [1] were obtained. These solids were named AV-24 materials (Aveiro material number 24), and they are related to a potassium-deficient structure $K_{8-x}[Yb_3Si_{12}O_{32}](OH)_{1-x}\cdot xH_2O$ (where x is approximately 2/3) [2] and $K_8[Nd_3Si_{12}O_{32}](OH)$ [3,4] materials on which structural work was done previously. AV-24 is the first reported to contain Ln-O-Ln dimmers isolated in a siliceous matrix and exhibiting a unique emission feature: the lifetime of the 5D_0 excited state is remarkably long, *ca.* 10.29 ms at 10 K. The structure allows the inclusion of a second (or even third) type of Ln^{3+} ion in the framework and, therefore, the fine-tuning of the photoluminescence properties.

In this chapter, I present the hydrothermal synthesis and the structural characterization of AV-24 microporous lanthanide silicates. Single-crystal (180 K) and powder X-ray diffraction were done in cooperation with Dr. Filipe Paz. Chemical analysis, thermogravimetry, scanning electron microscopy and ^{29}Si MAS NMR were applied. Photoluminescence spectroscopy was used to study the optical properties of these solids.

6.2 Synthesis

Figure 6.1 outlines the steps involved in the preparation of the silicates. The synthesis was carried out in Teflon-lined autoclaves (volume 37 cm³, filling rate 0.62), in mild temperature (230 °C) and (autogeneous) pressure. In all the syntheses, the autoclaves were removed and quenched in cold water after an appropriate time. The obtained microcrystalline powders were filtered, washed at room temperature with distilled water, and dried at 100 °C. Crystals suitable for single-crystal X-ray diffraction could only be obtained in the case of $K_7Sm_3Si_{12}O_{32}\cdot 3H_2O$. The unit cell parameters of $K_7Eu_3Si_{12}O_{32}\cdot 3H_2O$ and mixed $K_7Tb_{1.5}Eu_{1.5}Si_{12}O_{32}\cdot 3H_2O$ were also collected.

Typical $K_7M_{3-a}Ln_aSi_{12}O_{32}\cdot 3H_2O$, $M^{3+} = Tb^{3+}, Gd^{3+}$; $Ln^{3+} = Eu^{3+}, Sm^{3+}, Tb^{3+}$ and Gd^{3+} , $3 \geq a > 0$ synthesis. An alkaline solution was made by mixing 1.05 g precipitate SiO_2 , 20.32 g H_2O , 1.50 g KF and 2.05 g KOH . An amount of 0.50 g of $SmCl_3\cdot 6H_2O$ was added to this solution, and the mixture was stirred thoroughly. Eu , Tb and Gd silicates were synthesized with substitution of $SmCl_3\cdot 6H_2O$ by $EuCl_3\cdot 6H_2O$, $TbCl_3\cdot 6H_2O$ and $GdCl_3\cdot 6H_2O$. The gel, with composition $1.91K_2O:1.0SiO_2:0.04Sm_2O_3:69H_2O$ was autoclaved under autogeneous pressure for 7 days at $230\text{ }^\circ\text{C}$. Mixed $K_3(Tb_{3-a}Eu_a)Si_{12}O_{32}\cdot 3H_2O$ and $K_3(Gd_{3-a}Eu_a)Si_{12}O_{32}\cdot 3H_2O$ ($a=0.06-2.70$) samples were prepared by introducing the desired Tb^{3+} , Eu^{3+} and Gd^{3+} contents in the parent gel.

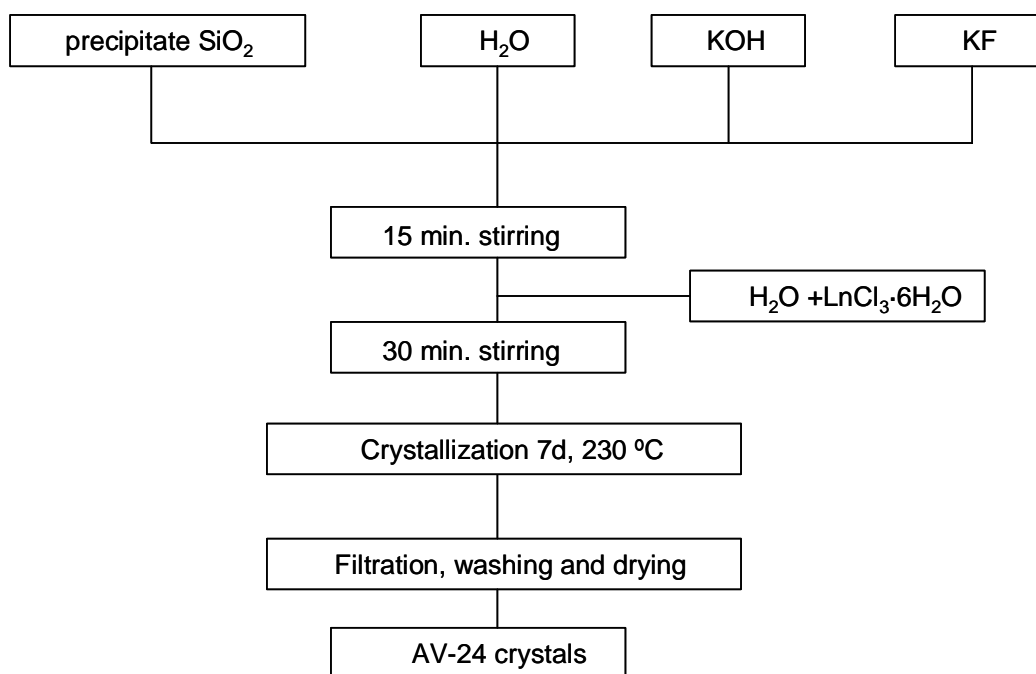


Figure 6.1 – Schematic representation of the synthesis of AV-24 materials.

The characteristics of the used reagents are shown in Table 6.1.

Table 6.1 – Characteristics of the used reagents.

Reagent	Composition, Purity	Brand
precipitate SiO_2	93 % m/m SiO_2	Riedel-de Haën
KOH	Pro-analyze	Merck
KF	Pro-analyze	Carlo ERBA
$LnCl_3\cdot 6H_2O$ ($Ln=Eu, Sm, Gd$ and Tb)	99.9 %	Aldrich

6.3 Structural characterization

Suitable single-crystals of $K_7[Sm_3Si_{12}O_{32}] \cdot 3H_2O$ (Sm-AV-24) were mounted on a glass fiber using perfluoropolyether oil [5]. Data were collected at 180(2) K on a Nonius Kappa charge coupled device (CCD) area-detector diffractometer (MoK α graphite-monochromated radiation, $\lambda = 0.7107 \text{ \AA}$), equipped with an Oxford Cryosystems cryostream and controlled by the Collect software package [6]. Images were processed using the software packages Denzo and Scalepack [7], and data were corrected for absorption by the empirical method employed in Sortav [8,9]. The structure was solved using the direct methods of SHELXS-97 [10], which allowed the direct location of the majority of the heaviest atoms (namely all the Sm and Si atoms). The remaining non-hydrogen atoms were located from difference Fourier maps, calculated from successive full-matrix least squares refinement cycles on F^2 using SHELXL-97 [11]. All atoms belonging to the three-dimensional $[Sm_3Si_{12}O_{32}]_n^{3n-}$ anionic framework were successfully refined using anisotropic displacement parameters.

The structure of $K_7[Sm_3Si_{12}O_{32}] \cdot 3H_2O$ was determined by single-crystal X-ray diffraction at 180(2) K, and found to share striking similarities with the materials formerly described by Pushcharovskii *et al.* [2] $K_{8-x}[Yb_3Si_{12}O_{32}](OH)_{1-x} \cdot xH_2O$ (where x was approximately 2/3), and Haile *et al.* [4] $K_8[Nd_3Si_{12}O_{32}](OH)$. Phase purity and homogeneity of the bulk samples were further confirmed using powder X-ray diffraction studies.

Appendix III collects information concerning crystallographic data collection and structure refinement of Sm-AV-24. Atomic coordinates, isotropic displacement parameters, main bond lengths and angles are given in tables.

The structure contains two crystallographically independent sites for the Sm^{3+} centers, Sm(1) and Sm(2), with the former being located at the inversion centre positioned in the middle of the c -axis of the unit cell. Both Sm^{3+} centers appear coordinated to six individual $\{SiO_4\}$ tetrahedra with coordination geometries resembling distorted octahedra, $\{SmO_6\}$ (Figure 6.2): for Sm(1), the calculated Sm–O bond distances are found within the 2.310(4)-2.333(4) \AA range, while the *cis* octahedral angles in the 84.34(15)-95.66(15) $^\circ$ range; instead, for Sm(2), the Sm–O bond distances are within the 2.280(4)-2.398(4) \AA

range, while the *cis* and *trans* octahedral angles in the 70.26(16)-121.66(15)° and 153.06(15)-167.79(15)° ranges, respectively.

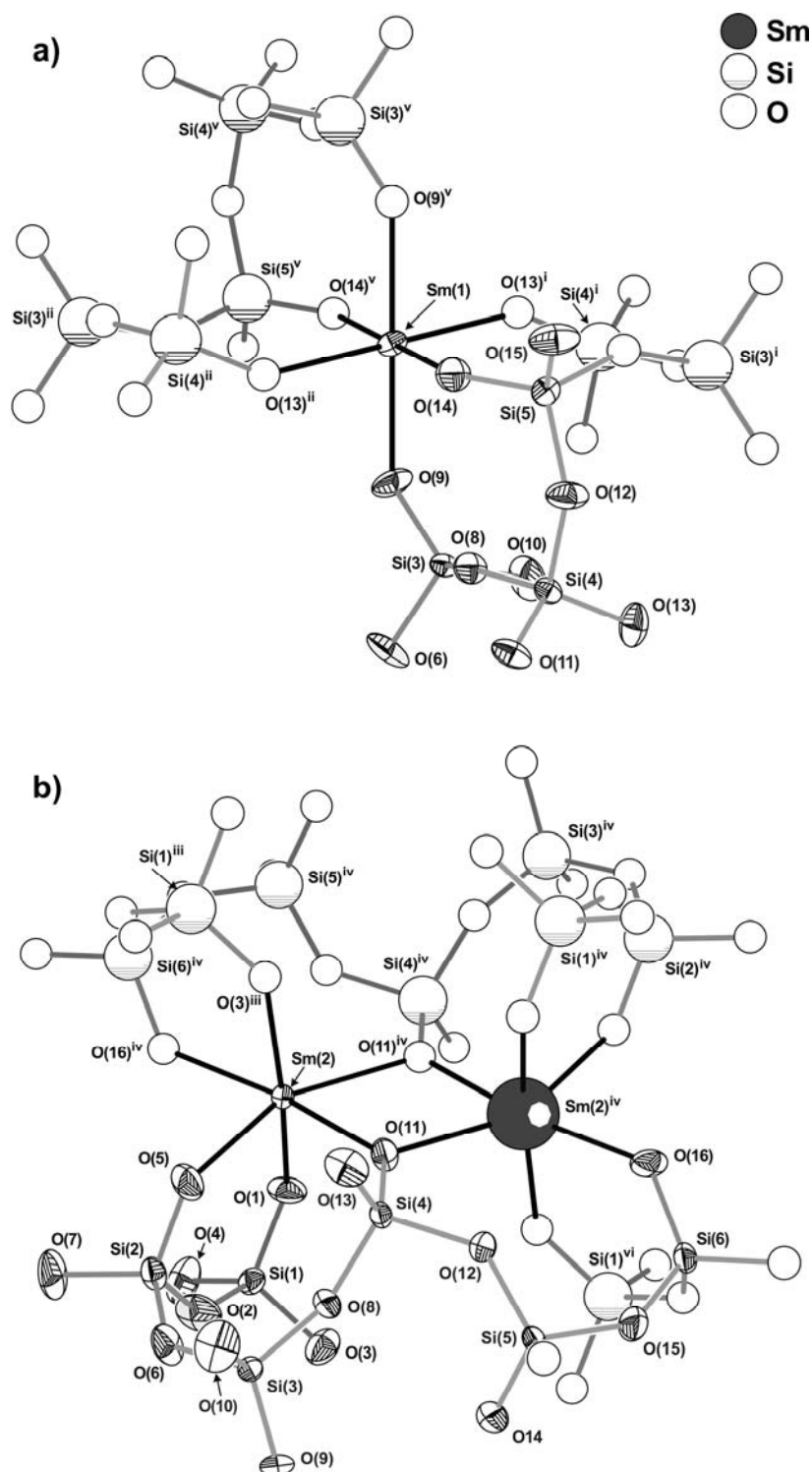


Figure 6.2 – Distorted octahedral $\{\text{SmO}_6\}$ coordination environments of a) Sm(1) and b) Sm(2) centers present in the crystal structure of Sm-AV-24. Atoms belonging to the asymmetric unit are represented as thermal ellipsoids drawn at the 90 % probability level.

To further help in the evaluation of the degree of distortion of the $\{\text{SmO}_6\}$ octahedra, we use an adaptation of a simple method proposed by Baur [12] to calculate a distortion index (DI) for bonds and angles:

$$DI_{\text{Bond}} = \frac{\sum_{i=1}^n |d(\text{Sm}-\text{O})_i - d(\text{Sm}-\text{O})_{av}|}{\sum_{i=1}^n |d(\text{Sm}-\text{O})_i|} \quad (6.1)$$

$$DI_{\text{Angle}} = \frac{\sum_{i=1}^n |\angle(\text{O}-\text{Sm}-\text{O})_i - \angle(\text{O}-\text{Sm}-\text{O})_{av}|}{\sum_{i=1}^n |\angle(\text{O}-\text{Sm}-\text{O})_i|} \quad (6.2)$$

where the subscripts i and av correspond to individual and average bond lengths and angles (see Appendix III). It is important to note that for the sake of comparative purposes, the value of DI_{Angle} should be, for an octahedron, calculated independently for the *cis* and *trans* angles.

For $\text{K}_7[\text{Sm}_3\text{Si}_{12}\text{O}_{32}] \cdot 3\text{H}_2\text{O}$, the values which arise from equations (6.1) and (6.2) are, for Sm(1), 0.004 and 0.052 (*cis*) and, for Sm(2), 0.018 and 0.095/0.037 (*cis/trans*), respectively. Hence, as empirically observed using the bond lengths and angles distribution for each metal centre, the coordination environment of Sm(2) can indeed be considered as significantly more distorted than that of Sm(1). Comparing these values for Sm(2) with those previously calculated by Haile and collaborators [4] for $\text{K}_8[\text{Nd}_3\text{Si}_{12}\text{O}_{32}](\text{OH})$ (Nd^{3+} : 0.076 and 0.100) and $\text{K}_{8-x}[\text{Yb}_3\text{Si}_{12}\text{O}_{32}](\text{OH})_{1-x} \cdot x\text{H}_2\text{O}$ (Yb^{3+} : 0.057 and 0.072) for the crystallographically analogous metallic centers, it is possible to conclude that: on the one hand, concerning bond length distributions the structure reported in this manuscript is significantly more regular; on the other hand, the octahedral angles for Sm(2) are as irregular as those found for the Nd-containing structure, with the material reported by Pushcharovskii and collaborators showing a slightly more regular site for Yb^{3+} . These findings can be rationalised according to the combined effect of the different ionic radii of the cations and their physical location in the structure of the materials.

An interesting feature of this family of materials resides in the way the siliceous fragments are connected to each individual lanthanide centre. As shown in Figure 6.2a, the Sm(1) coordination environment is formed by two Si(3↔4↔5↔3↔4) chains, which completely trap the metallic centre inside four chelate-type rings in which all oxygen-coordinating atoms are terminal. Interestingly, for Sm(2) one of the oxygen-coordinating atoms [O(11)] acts as a physical bridge, μ_2 , leading to the formation of an unprecedented binuclear optical unit which is structurally trapped by two Si(1↔6↔5↔4↔3↔2↔1) chains (Figure 6.2b). Indeed, the μ_2 -O(11) imposes a physical separation between Sm(2)⋯Sm(2)^{iv} of only 3.906(11) Å [symmetry code: (iv) $I-x, I-y, I-z$] which, to the best of our knowledge, constitutes to date the shortest distance between optical centres in stoichiometric heteropolyhedra lanthanide silicates. The shortest Sm(1)⋯Sm(1)ⁱⁱⁱ and Sm(1)⋯Sm(2) intermetallic distances are of 6.921(1) Å and 7.733(2) Å, respectively [symmetry codes: (iii) $I+x, y, z$].

The six crystallographic independent {SiO₆} tetrahedra are polymerized in such a way that two-dimensional anionic (Si₁₂O₃₂)_n¹⁶ⁿ⁻ layers are formed, ultimately rendering the K₇[Sm₃Si₁₂O₃₂]·3H₂O material as belonging to the more general phyllosilicate family. As observed for the related materials with Nd³⁺ and Yb³⁺ [2,4], these layers are created by the periodic alternation between two types of six-membered rings (R₆^{1,2}), an eight-membered ring (R₈) and a highly distorted twelve-membered ring (R₁₂) (Figure 6.3a). Physical connections between adjacent layers are assured by the Sm(1) (inside the R₆¹ rings) and the Sm(2) centres (inside the R₁₂ rings), leading to the formation of a three-dimensional [Sm₃Si₁₂O₃₂]_n⁷ⁿ⁻ anionic framework. Indeed, the R₁₂ ring (which was described by Haile as “meandering”) surrounds, and isolates from the remaining optical centers, the aforementioned Sm(2) dimmers (Figure 6.4). As the symmetry (and consequently the degree of distortion) of these (Si₁₂O₃₂)_n¹⁶ⁿ⁻ layers varies little between the three structures it is, thus, easy to understand why the smaller Yb³⁺ centers (for a coordination number of 6, the effective ionic radius is 0.87 Å) [13] show coordination geometries in the dimmers significantly more regular than those of Nd³⁺ (0.98 Å) and Sm³⁺ (0.96 Å).

The (Si₁₂O₃₂)_n¹⁶ⁿ⁻ layers stack along the [100] direction in a typical single layer sequence, leading to an alignment of all the R₈ rings along the same direction, ultimately creating a tunnel with an effective cross-section of *ca.* 3.2×3.2 Å (Figure 6.3b). This

channel contains highly disordered water molecules of crystallization, as seen by X-ray crystallography, which can be removed by heating the material at *ca.* 500 °C.

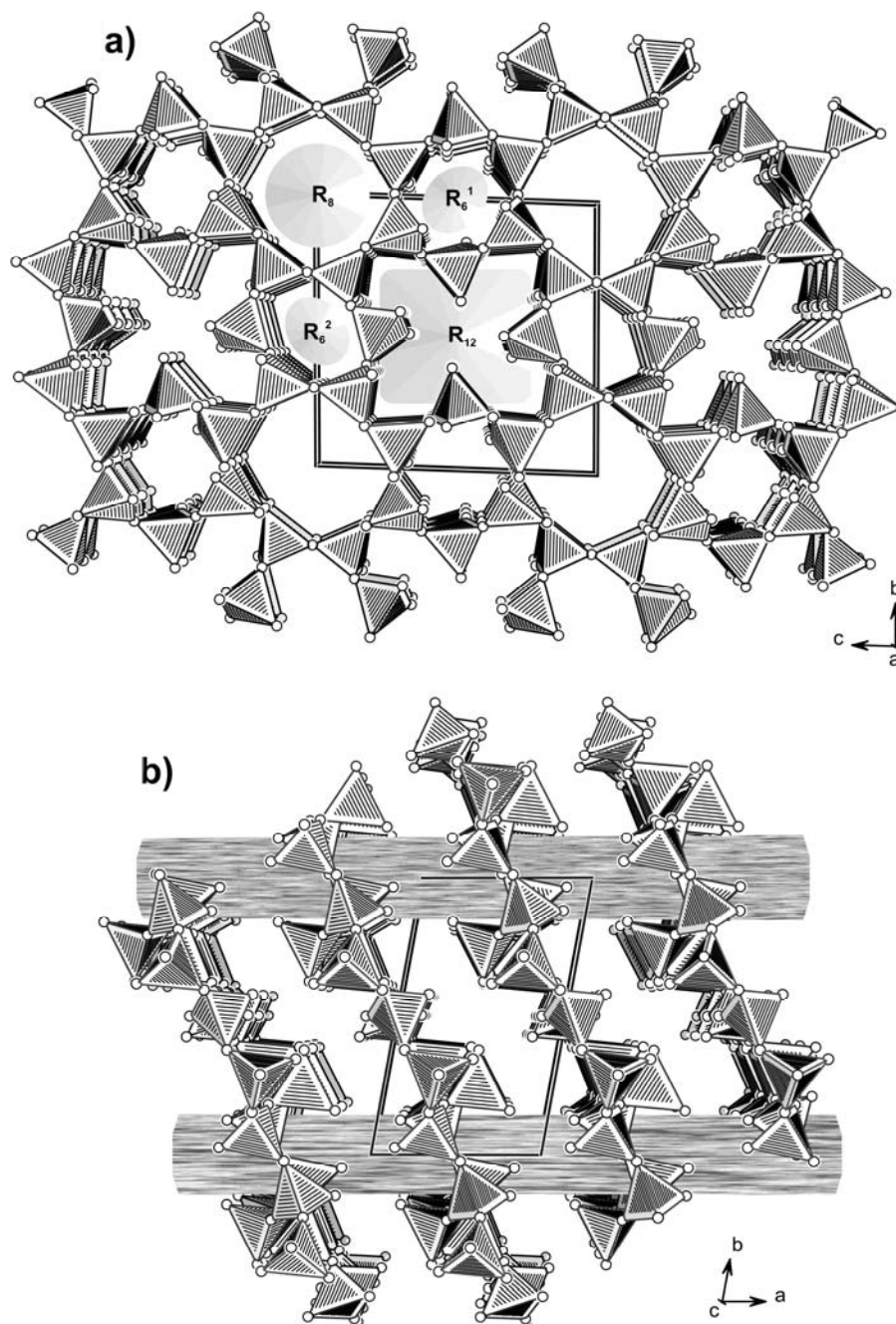


Figure 6.3 – Perspective views along the a) a axis; each layer is formed by two types of six-membered rings ($R_6^{1,2}$), an eight-membered ring (R_8) and a highly distorted twelve-membered ring (R_{12}) and b) c axis; packing of adjacent two-dimensional $(\text{Si}_{12}\text{O}_{32})_n^{16n-}$ anionic layers. The parallel packing of adjacent $(\text{Si}_{12}\text{O}_{32})_n^{16n-}$ layers leads to the formation of one-dimensional channels (running along the a axis –gray channels in the scheme) surrounded by the R_8 rings and having an effective cross-section of *ca.* 3.2×3.2 Å.

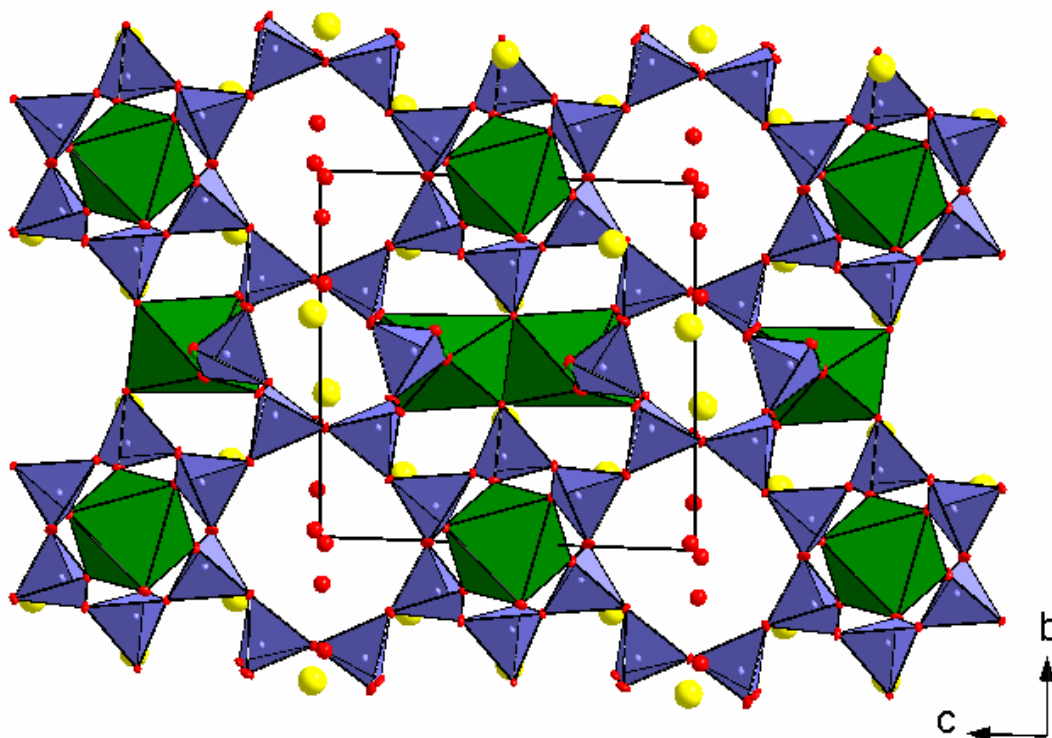


Figure 6.4 – Crystal packing of Sm-AV-24 viewed in perspective along the a axis. Polyhedra: green TbO_6 , blue SiO_4 ; spheres: yellow K^+ , red O.

Collected unit cell parameters from single-crystal analysis of $K_7Eu_3Si_{12}O_{32} \cdot 3H_2O$ and mixed $K_7Tb_{1.5}Eu_{1.5}Si_{12}O_{32} \cdot 3H_2O$ samples show that the structures are identical to that containing only Sm. Final lattice parameters are summarized in Table 6.2 and compared with related data for similar materials.

Table 6.2 – Unit cell parameters of AV-24 materials.

Ln	a (Å)	b (Å)	c (Å)	Volume (Å ³)	Space Group
Yb [2]	6.80(8)	11.43(4)	11.44(9)	891.2(2)	$P\bar{1}$
Nd [4]	6.96(6)	11.45(5)	11.66(7)	931.0(5)	$P\bar{1}$
Sm	6.92(1)	11.42(8)	11.61(2)	902.0(3)	$P\bar{1}$
Eu	6.98(5)	11.54(8)	11.68(8)	925.0 (9)	$P\bar{1}$
Mixed Eu/Tb	6.88(6)	11.40(7)	11.55(1)	891.8(6)	$P\bar{1}$

Attempts were made to refine the unit cell parameters for each member of the $K_7M_{3-a}Ln_aSi_{12}O_{32}\cdot 3H_2O$, $M^{3+}=Tb^{3+}, Gd^{3+}$; $Ln^{3+}=Eu^{3+}, Sm^{3+}, Tb^{3+}$ and Gd^{3+} family by using the software package FULLPROF [14] working in profile fitting mode using the Le Bail's extraction method [15]. However, such approach did not produce reliable results due to two main reasons: (i) the materials crystallize in the triclinic crystal system and the number of expected reflections is rather large (e.g., up to $30^\circ 2\theta$ alone there are over 700 reflections in the simulated pattern of Sm-AV-24); (ii) the collected diffraction patterns lack in resolution and also show evidence of the presence of textural effects related to the orientation of the crystallites in the X-ray beam. Therefore, sensible studies of these materials, which include indexing and Rietveld refinement, are only likely to be possible using synchrotron radiation.

All studied $K_7M_{3-a}Ln_aSi_{12}O_{32}\cdot 3H_2O$, $M^{3+}= Tb^{3+}, Gd^{3+}$; $Ln^{3+}=Eu^{3+}, Sm^{3+}, Tb^{3+}$ and Gd^{3+} materials display powder XRD patterns characteristic of AV-24 (Figure 6.5) and no evidence was found for the presence of any impurity phases.

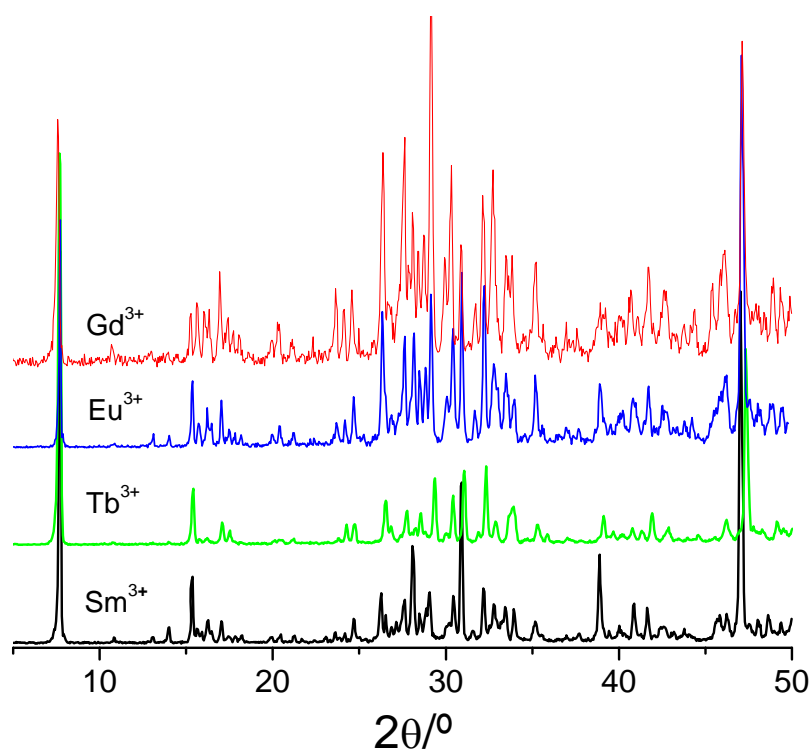
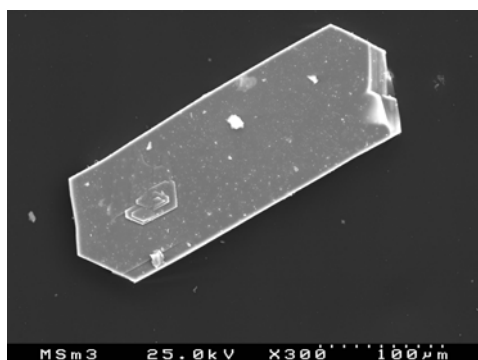
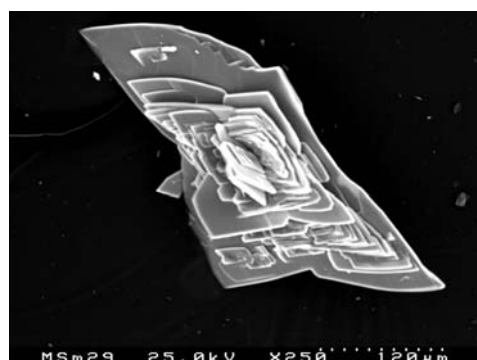


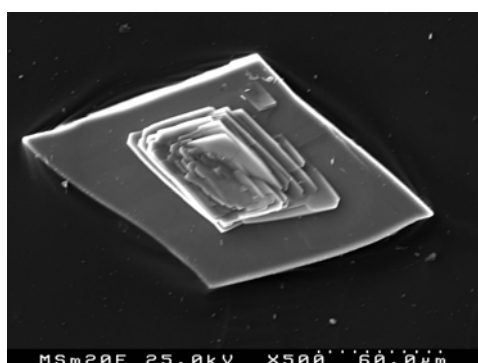
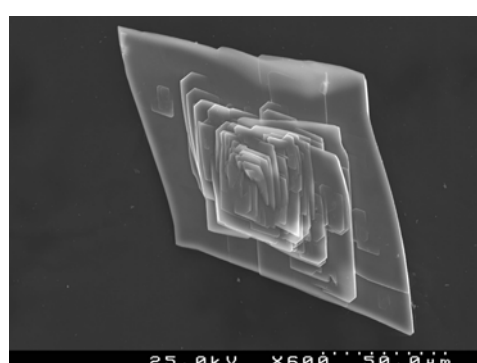
Figure 6.5 – Experimental powder XRD patterns of pure AV-24 samples.

Figure 6.6 displays the scanning electron microscopy images of Ln-AV-24 materials (Ln=Sm, Eu, Tb and mixed Tb/Eu, Eu/Tb and Gd/Tb/Eu).

Sm-AV-24

 $K_7Tb_{1.5}Eu_{1.5}Si_{12}O_{32} \cdot 3H_2O$ 

Eu-AV-24

 $K_7Eu_{2.7}Tb_{0.3}Si_{12}O_{32} \cdot 3H_2O$ 

Tb-AV-24

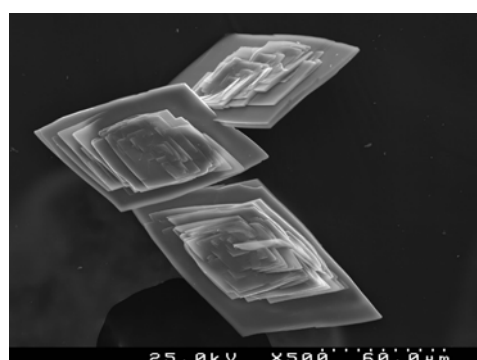
 $K_7Gd_{1.8}Tb_{0.6}Eu_{0.6}Si_{12}O_{32} \cdot 3H_2O$ 

Figure 6.6 – Scanning electron micrographs of pure and mixed AV-24 compositions.

Within experimental error, chemical analysis by EDS confirmed the K : Ln : Si molar ratios *ca.* 7 : 3 : 12. For the mixed samples $K_7M_{3-a}Ln_aSi_{12}O_{32} \cdot 3H_2O$, $M^{3+}=Tb^{3+}$, Gd^{3+} ; $Ln^{3+}=Eu^{3+}$ and Tb^{3+} where $3 \geq a > 0$ no crystals rich in an individual lanthanide were found. All results indicated that lanthanides are randomly distributed within the crystals.

Due to the paramagnetism of Eu^{3+} , Tb^{3+} and Gd^{3+} lanthanide ions, it was not possible to obtain ^{29}Si MAS NMR spectra with acceptable quality for the Eu^{3+} , Tb^{3+} and Gd^{3+} -AV-24 samples. Because Sm^{3+} is less paramagnetic, compared to the other lanthanides (except La^{3+} and Lu^{3+} which are not paramagnetic) it was possible to get good quality ^{29}Si MAS NMR spectrum. Sm-AV-24 sample (Figure 6.7) displays resonances in the range -70 to -130 ppm. The spectrum can be deconvoluted into five resonances at -77.9, -89.7, -97.2, -112.8 and -115.9 ppm in a 1:1:1:1:2 intensity ratio, in accord with the crystal structure which calls for the presence of six Si local environments.

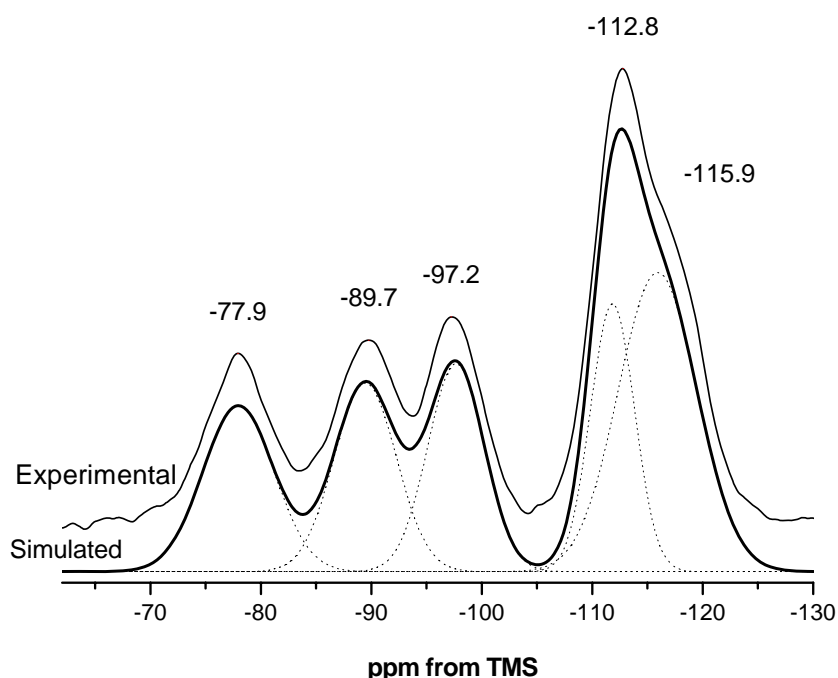


Figure 6.7 – Experimental and simulated ^{29}Si MAS NMR spectra of Sm-AV-24.

Figure 6.8 represents the three different Si chemical environments according to the crystal structure. Si2, Si3, Si5 and Si6 are of the type Q^3 , $\text{Si}[3\text{Si}; 1\text{Ln}]$ and should represent resonances at the high isotropic chemical shift. Si1 and Si4 sites have as second-nearest-neighbors 2 Si and 2 Ln atoms. Si1 is of the type Q^2 , $\text{Si}[2\text{Si}; 2\text{Ln}]$ and Si4 is of the type Q^2 , $\text{Si}[2\text{Si}; \text{Ln}, 2\text{Ln}]$.

In spite of Si2, Si3, Si5 and Si6 having the same chemical environment and considering the well-known correlation between the ^{29}Si chemical shifts and the Si-O bond

lengths in silicates (high-field shift at shorter bond lengths) [16] the peak at -115.9 ppm can be tentatively assigned to Si3 and Si6 (Si-O bond lengths =1.615 Å and average bond angles Si-O-Si =140.2 °) and the peaks at -112.8, -97.2 ppm can be tentatively assigned to Si2 and Si5 (Si-O bond lengths =1.619 Å and bond angles Si-O-Si =141.72 °). Site Si4 should have larger positive charge due to the presence of 3 Ln³⁺, because of that the peak at -89.7 ppm can be tentatively assigned to Si4. The resonance at -77.9 ppm is assigned to the remaining Si1.

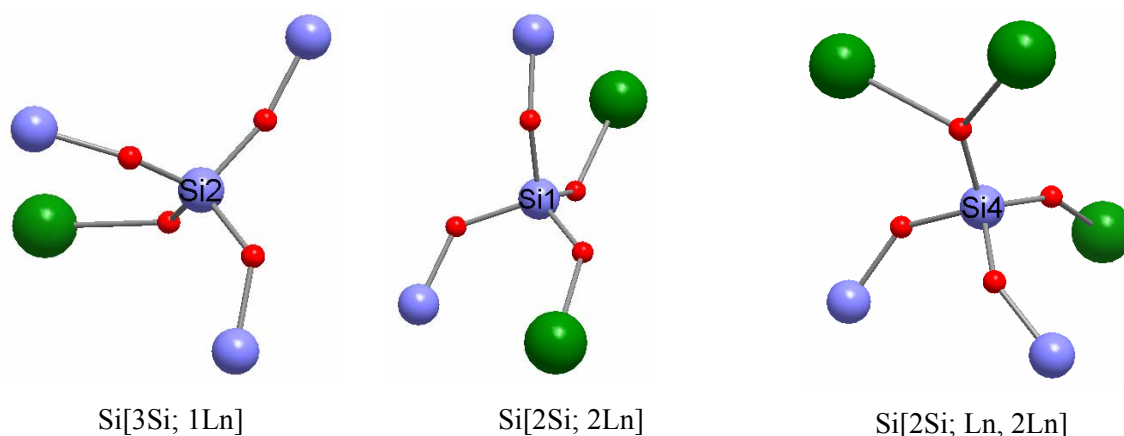


Figure 6.8 – Si local environments in the structure of Sm-AV-24. Green - Sm³⁺, blue - Si⁴⁺, red - O²⁻.

The Raman spectrum of Eu-AV-24 (Figure 6.9) shows several sharp bands between 100 and 1200 cm⁻¹. Below 400 cm⁻¹ bands are mainly caused by lattice vibrations of the framework or skeleton and cation-oxygen bonding [17]. Typical values for Ln-O stretching vibrations are around 300 cm⁻¹, located in the region of lattice vibrations [18]. Numerous bands in the low-, medium-, and high- wavenumber range were recorded. Symmetric Si – O⁻ stretching vibrations of SiO₄ groups with one, two, three, or four nonbridging oxygens emerge in alkali silicates with different contents of metal oxides in the high-wavenumber range (800-1200cm⁻¹) [17,19,20]. Bands in the intermediate-wavenumber range (400-800 cm⁻¹) result from symmetric bending vibrations of the Si-O-Si bridging oxygens between adjacent SiO₄ tetrahedra. Compared to the Raman shifts observed in silicate glasses and melts, the Raman bands in the range between 400 and 600 cm⁻¹ and below 400 cm⁻¹ can be assigned to the presence of Si–O–Si symmetric stretching vibrations and the bending of the Si–O–Si linkages [21]. In yttrium orthosilicate crystals, bands in the 500-700 cm⁻¹ range

are generally characteristic of the YO_6 octahedra [22]. For Tb-AV-22 and Tb-AV-23 materials we ascribed the bands in this region to the Tb–O stretching vibrations of TbO_6 octahedra and thus the bands at 587 and 642 cm^{-1} can be attributed to Eu–O stretching vibrations of EuO_6 octahedra.

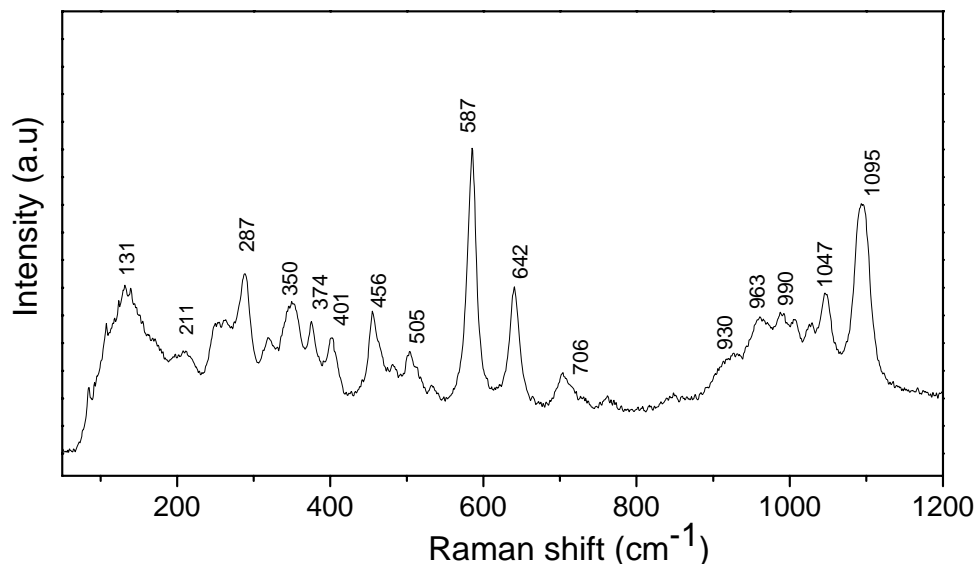


Figure 6.9 – Raman spectrum of Eu-AV-24.

6.4 Photoluminescence spectroscopy

Figure 6.10 shows the excitation spectrum of Tb-AV-24 recorded at room temperature (RT), monitored at the $\text{Tb}^{3+} \ ^5\text{D}_4 \rightarrow \ ^7\text{F}_5$ transition (541 nm). The sharp lines between 240 and 500 nm are assigned to $\ ^7\text{F}_6 \rightarrow \ ^5\text{D}_{4,0}$, $\ ^5\text{L}_{10}$ and $\ ^5\text{G}_{6-3}$ intra-configurational forbidden $4f^8 \rightarrow 4f^8$ transitions of Tb^{3+} . The broad band between 240 and 300 nm is ascribed to the spin-forbidden (high-spin, HS) inter-configurational $4f^8 \rightarrow 4f^75d^1$ (*fd*) transition of Tb^{3+} [23-25]. This type of spin-forbidden *fd* band may be observed for (heavy) lanthanide ions with more than seven *4f* electrons at an energy lower than the energy of spin-allowed (low-spin, LS) *fd* transitions. We note that the excitation spectra intensity has not been corrected for wavelengths lower than 240 nm.

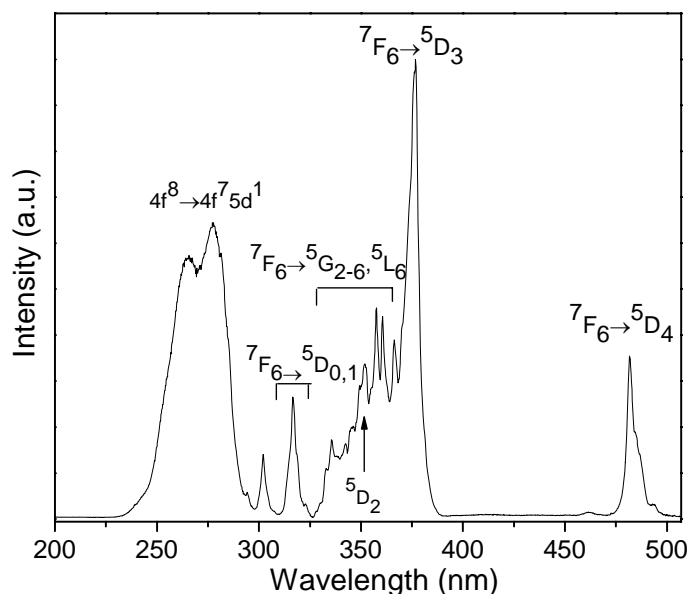


Figure 6.10 – Excitation spectrum of Tb-AV-24, monitored at the 7F_5 manifold (541 nm).

Figure 6.11 shows the RT emission spectrum of Tb-AV-24, excited at 377 nm. The emission lines are assigned to the ${}^5D_4 \rightarrow {}^7F_{2-6}$ transitions of Tb^{3+} . Luminescence from the higher (*e.g.* 5D_3) excited states is not detected, indicating a very efficient non-radiative relaxation to the 5D_4 level. The deactivation of excited states by cross-relaxation between adjacent centers (concentration quenching) may also explain the absence of emission from high-energy states (*e.g.* 5D_3). The same emission is obtained with excitation at the maximum of the HS *fd* band (277nm).

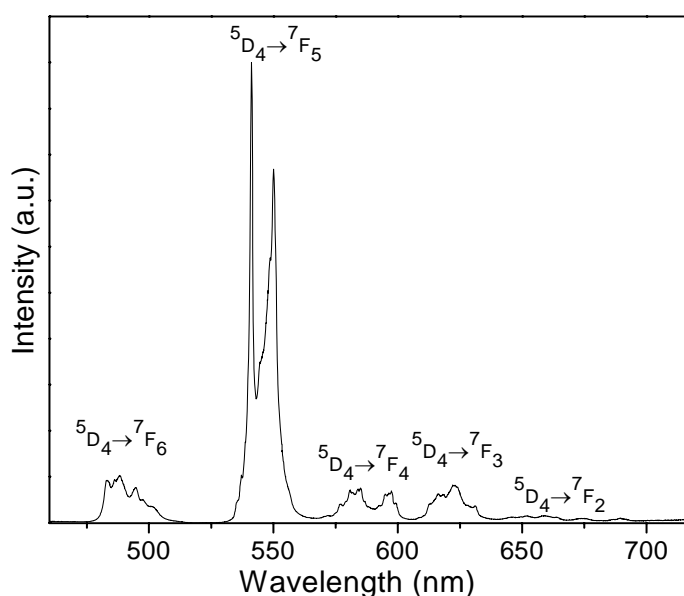


Figure 6.11 – Emission spectrum of Tb-AV-24, excited at the 5D_3 manifold (377 nm).

The 5D_4 decay curves (shown in Figure 6.12), excited at 377 or 483 nm and monitored at the $^5D_4 \rightarrow ^7F_5$ transition (542 or 552 nm), reveal the presence of more than a single local Tb^{3+} environment. Indeed, these curves are well fitted by bi-exponential functions yielding lifetimes at room temperature $\tau_1 = 1.40 \pm 0.01$ ms and $\tau_2 = 4.26 \pm 0.01$ ms and $\tau_1 = 4.26 \pm 0.03$ ms and $\tau_2 = 8.44 \pm 0.03$ ms at 10 K.

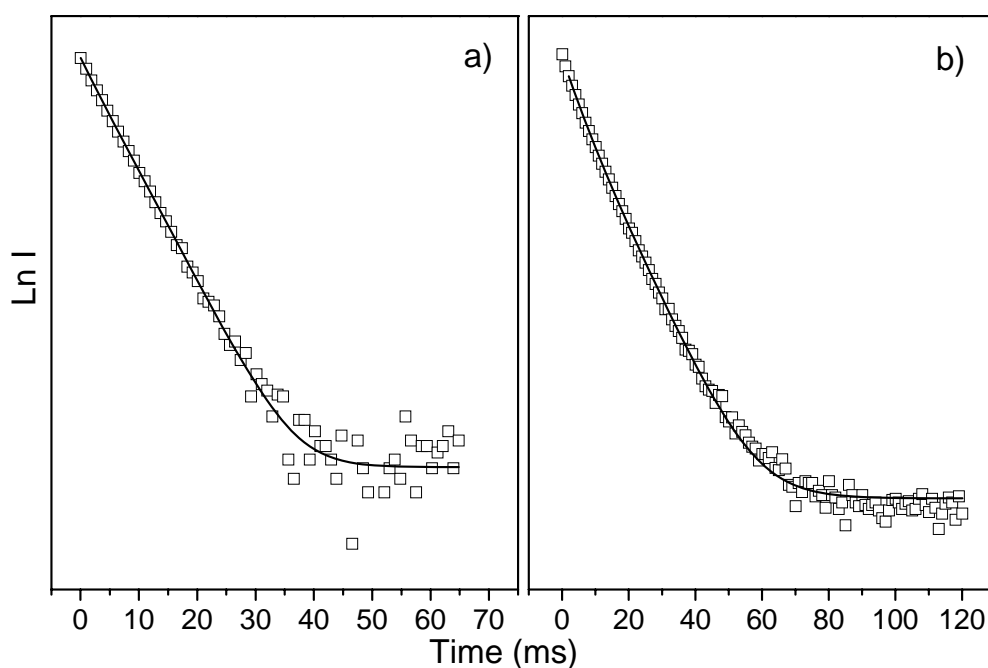


Figure 6.12 – a) Room temperature and b) 10 K 5D_4 decay curves of Tb-AV-24, monitored at 542 nm under 377 nm excitation. The black lines are the best data bi-exponential fit ($r^2 > 0.99$).

The RT and 10 K excitation spectra of $K_7Eu_3Si_{12}O_{32} \cdot 3H_2O$ (Eu-AV-24) and $K_7(Gd_{2.7}Eu_{0.3})Si_{12}O_{32} \cdot 3H_2O$ (Eu,Gd-AV-24) monitored at the $^5D_0 \rightarrow ^7F_2$ transition, 610.8 nm (Figures 6.13 and 6.14) display a series of sharp lines assigned to the $^7F_{0-1} \rightarrow ^5D_{0-0}$, 5L_6 , $^5G_{2-6}$, $^5H_{3-7}$ and $^5F_{1-5}$ intra $4f^6$ transitions. A faint broad band at 245 nm is ascribed to the low-spin inter-configurational $4f^6 \rightarrow 4f^55d^1$ transition. At 10 K, a second broad band is observed at 265 nm, attributed to O \rightarrow Eu charge-transfer transition [26].

The excitation spectra of $K_7(Gd_{2.7}Eu_{0.3})Si_{12}O_{32} \cdot 3H_2O$ also displays lines at 272-279 and 302-312 nm assigned to, respectively, the $^8S_{7/2} \rightarrow ^6I_{7/2-17/2}$ and $^6P_{3/2-7/2}$ intra- $4f^7$ transitions of Gd^{3+} , revealing the occurrence of energy transfer from the Gd^{3+} to the Eu^{3+} ions.

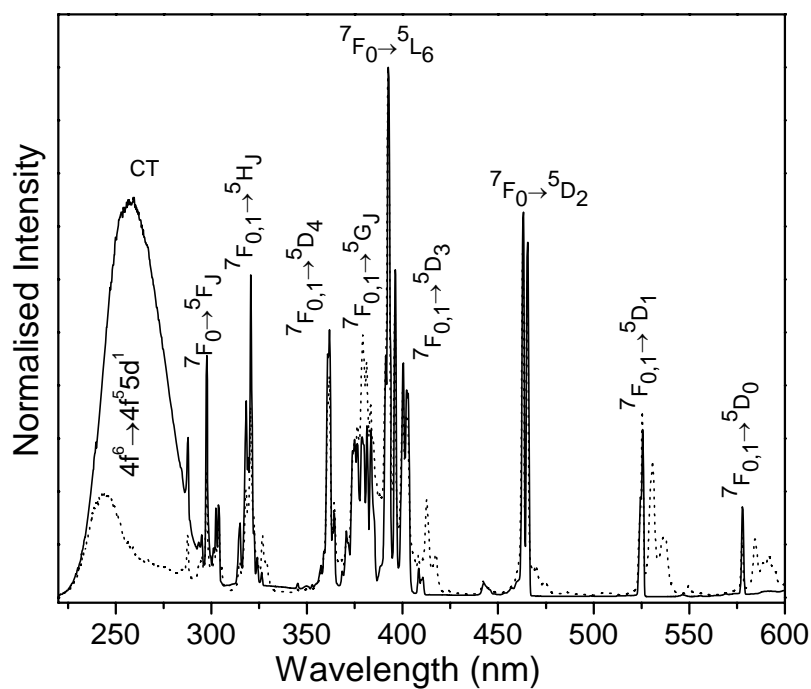


Figure 6.13 – Excitation spectra of Eu-AV-24, recorded at room temperature (dashed line) and at 10 K (solid line), monitored at the 7F_2 manifold (610.8 nm).

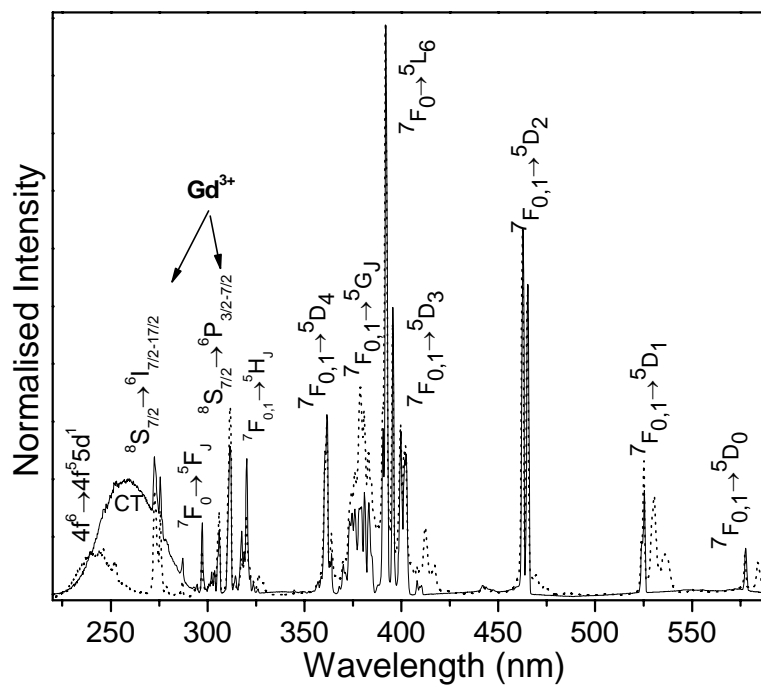


Figure 6.14 – Excitation spectra of $K_7(Gd_{2.7}Eu_{0.3})Si_{12}O_{32} \cdot 3H_2O$, recorded at room temperature (dashed line) and at 10 K (solid line) monitored at the 7F_2 manifold (610.8 nm).

The room temperature and 10 K emission spectra of Eu-AV-24 and $\text{K}_7(\text{Gd}_{2.7}\text{Eu}_{0.3})\text{Si}_{12}\text{O}_{32}\cdot 3\text{H}_2\text{O}$ (excited at 393 nm) are shown in Figures 6.15 and 6.16. The sharp emission lines are assigned to transitions between the first excited non-degenerate $^5\text{D}_0$ state and the $^7\text{F}_{0-4}$ levels of the fundamental Eu^{3+} septet. Eu^{3+} luminescence from higher excited states, such as $^5\text{D}_1$, is not detected, indicating a very efficient non-radiative relaxation to the $^5\text{D}_0$ level. The deactivation of excited states by cross-relaxation between adjacent centers may explain the absence of the $^5\text{D}_1$ emission. Except for the $^5\text{D}_0 \rightarrow ^7\text{F}_1$ lines, which have a predominant magnetic dipole character, the observed transitions are mainly of electric dipole nature. The $^5\text{D}_0 \rightarrow ^7\text{F}_1$ magnetic transition is weaker than the $^5\text{D}_0 \rightarrow ^7\text{F}_2$ forced electric-dipole transition. The local-field splitting of the $^5\text{D}_0 \rightarrow ^7\text{F}_1$ and $^5\text{D}_0 \rightarrow ^7\text{F}_2$ transitions in more than, respectively, three and five Stark components indicate the presence of two distinct Eu^{3+} environments.

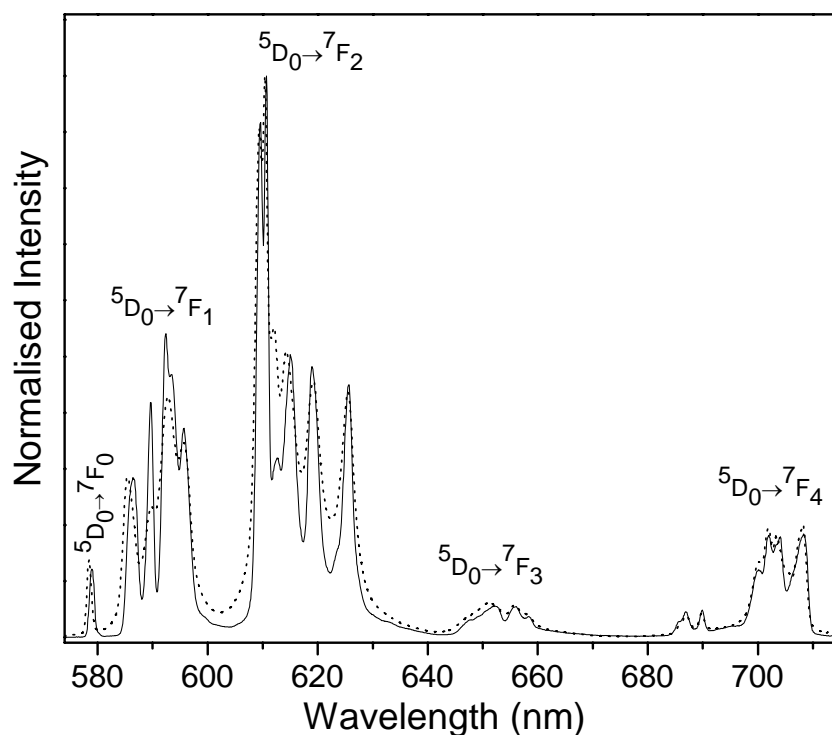


Figure 6.15 – Emission spectra of Eu-AV-24 recorded at room temperature (dashed line) and 10 K (solid line), excited at the $^5\text{L}_6$ manifold (393 nm).

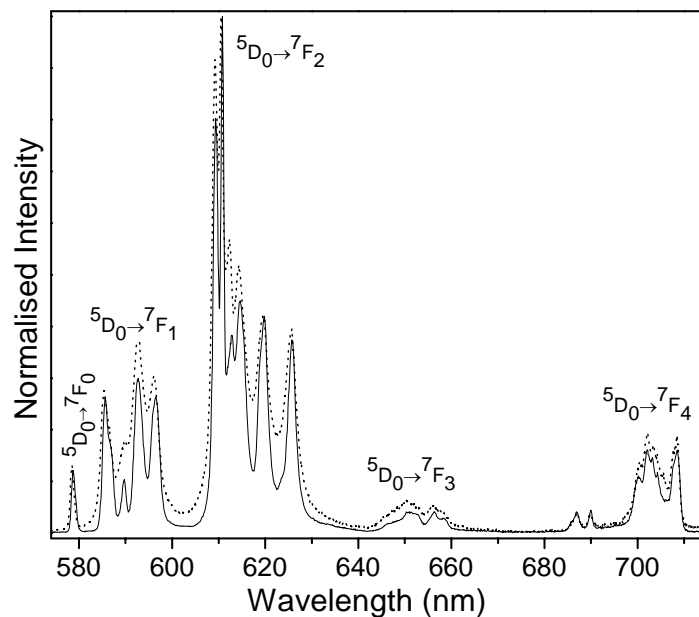


Figure 6.16 – Emission spectra of $K_7(Gd_{2.7}Eu_{0.3})Si_{12}O_{32} \cdot 3H_2O$ recorded at room temperature (dashed line) and 10 K (solid line), excited at the 5L_6 manifold (393 nm).

The changes detected in the relative intensity of the Stark levels, as the excitation wavelength varies from 393 (5L_6) to 525.5 nm (5D_1), confirm the presence of two local Eu^{3+} environments (illustrated in Figure 6.17 for Eu-AV-24).

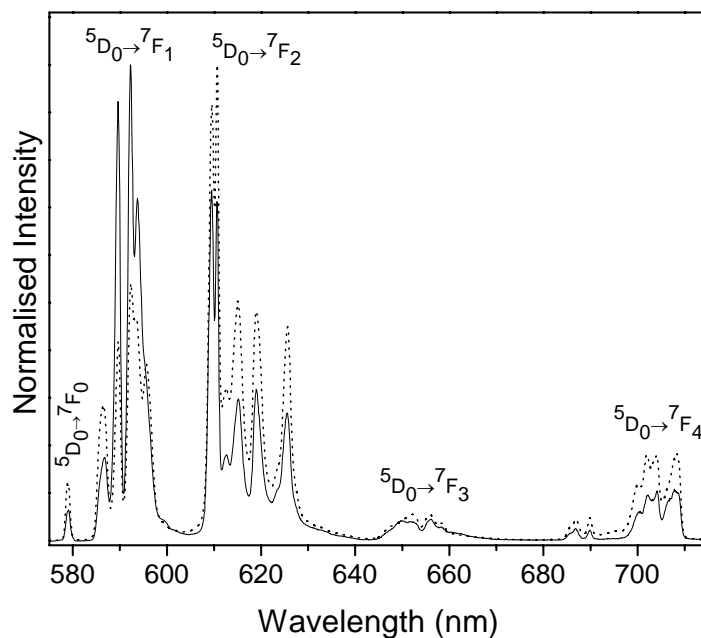


Figure 6.17 – Emission spectra of Eu-AV-24 recorded at 10 K excited at 393 nm, 5L_6 manifold (dashed line), and at 525.5 nm, 5D_1 manifold (solid line).

These local environments were further investigated by time-resolved spectroscopy. Increasing the delay time (Figure 6.18), the relative intensity of the ${}^5D_0 \rightarrow {}^7F_{0,2}$ lines decreases, while that of the ${}^5D_0 \rightarrow {}^7F_1$ lines at 589.8, 592.4 and 594.0 nm increases. Moreover, for the longest delay time (25 ms) the spectrum is dominated by the dipole-magnetic ${}^5D_0 \rightarrow {}^7F_1$ transition, exhibiting only these three Stark components, which is typical of a single Eu^{3+} local environment with an inversion centre. The detection of a Eu^{3+} emission after a 25 ms delay is also unprecedented.

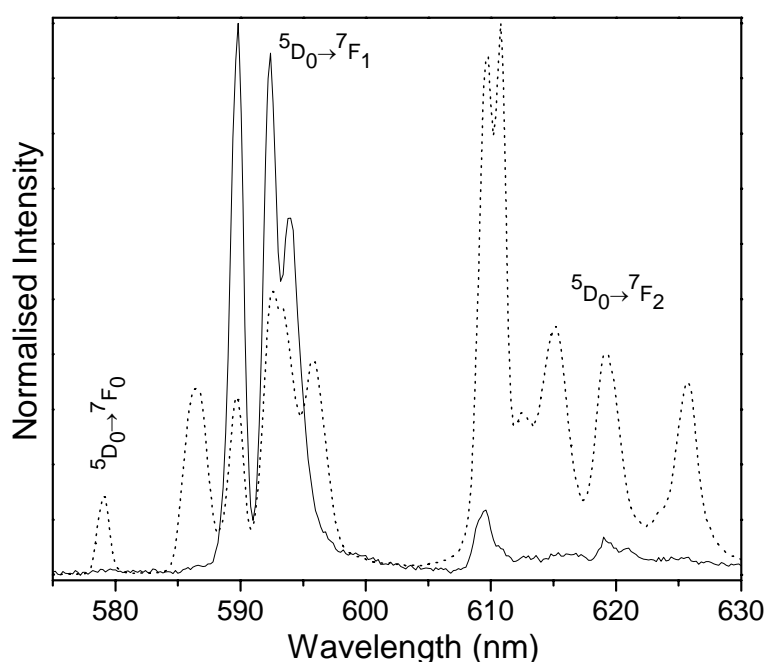


Figure 6.18 – Time-resolved emission spectra of Eu-AV-24 recorded at 10 K, with an initial delay of 0.05 ms (dashed line) and 25 ms (solid line). The excitation was performed at 393 nm.

For times up to *ca.* 4 ms, the $\text{K}_7\text{Eu}_3\text{Si}_{12}\text{O}_{32}\cdot 3\text{H}_2\text{O}$ and $\text{K}_7(\text{Gd}_{2.7}\text{Eu}_{0.3})\text{Si}_{12}\text{O}_{32}\cdot 3\text{H}_2\text{O}$ decay curves, detected at 589.8 nm (the most intense ${}^5D_0 \rightarrow {}^7F_1$ line) in the range 10–300 K, are clearly non-exponential (Figure 6.19). For $\text{K}_7\text{Eu}_3\text{Si}_{12}\text{O}_{32}\cdot 3\text{H}_2\text{O}$ sample the decay curve is characterized by a “grow-in” behavior (inset in Figure 6.19a) indicating a contribution from an energy transfer pathway. For times larger than 4 ms, the decay curves could be well-fitted with a mono-exponential function yielding at 10 K lifetimes of 10.29 ± 0.04 and 9.53 ± 0.05 ms, respectively for $\text{K}_7\text{Eu}_3\text{Si}_{12}\text{O}_{32}\cdot 3\text{H}_2\text{O}$ and $\text{K}_7(\text{Gd}_{2.7}\text{Eu}_{0.3})\text{Si}_{12}\text{O}_{32}\cdot 3\text{H}_2\text{O}$. The values measured for the other temperatures between 10 and 300 K are gathered in Table 6.3.

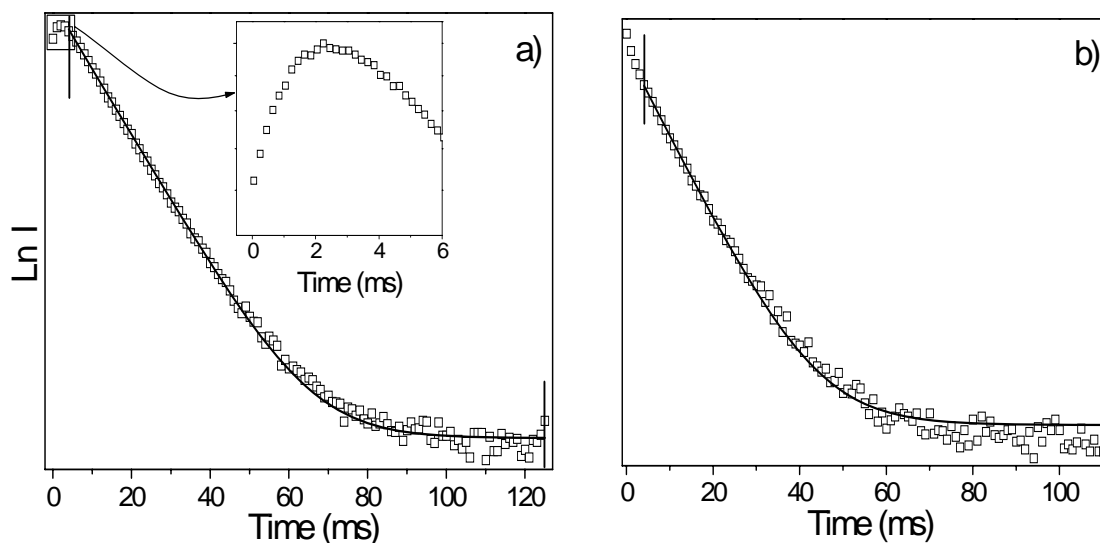


Figure 6.19 – Eu(2)-Eu(2) dimmer decay curve of a) Eu-AV-24 and b) $K_7(Gd_{2.7}Eu_{0.3})Si_{12}O_{32} \cdot 3H_2O$ detected at 10 K on the ${}^5D_0 \rightarrow {}^7F_1$ transition (589.8 nm) and excited at 229 nm. The full line correspond to the best fit to the data considering a mono-exponential function ($r^2=0.999$ and $\chi^2=2 \times 10^{-6}$). The inset shows the “grow-in” component of the luminescence emission profile.

Table 6.3 – Dimmer Eu(2)-Eu(2) lifetimes as a function of the temperature (T) for $K_7Eu_3Si_{12}O_{32} \cdot 3H_2O$ and $K_7Gd_{2.70}Eu_{0.30}Si_{12}O_{32} \cdot 3H_2O$ samples monitoring the ${}^5D_0 \rightarrow {}^7F_1$ transition (589.8 nm) (excitation of 229 nm).

T (K)	10	25	50	75	100	125	150	200	300
$K_7Eu_3Si_{12}O_{32} \cdot 3H_2O$									
τ (ms)	10.29±0.04	8.68±0.04	7.58±0.03	6.68±0.03	5.59±0.02	4.57±0.02	4.06±0.01	3.50±0.01	2.84±0.01
r^2	0.9995	0.9996	0.9996	0.9997	0.9997	0.9998	0.9999	0.9999	0.9997
χ^2	1.65×10^{-6}	1.39×10^{-6}	1.49×10^{-5}	6.56×10^{-6}	6.67×10^{-7}	5.68×10^{-6}	2.62×10^{-6}	2.58×10^{-6}	5.57×10^{-6}
$K_7Gd_{2.70}Eu_{0.30}Si_{12}O_{32} \cdot 3H_2O$									
τ (ms)	9.53±0.05	9.36±0.06	9.02±0.05	8.40±0.05	7.46±0.05	6.71±0.05	5.65±0.05	4.77±0.02	4.09±0.01
r^2	0.9993	0.9990	0.9992	0.9988	0.9989	0.9989	0.9981	0.9994	0.9997
χ^2	7.86×10^{-6}	1.11×10^{-5}	9.10×10^{-6}	1.40×10^{-5}	1.37×10^{-5}	1.08×10^{-5}	2.47×10^{-5}	1.04×10^{-5}	7.18×10^{-6}

However, when monitoring the emission within the ${}^5D_0 \rightarrow {}^7F_2$ transition (at 609 and 610.8 nm) the decay curves are complex due to the energy transfer contribution (Figure 6.20) and only at 10 K the curves could be approximately described by a single-exponential function, yielding lifetime ascribed to the Eu(1) site of 2.73 ± 0.01 ms for the Gd-containing sample, for instance.

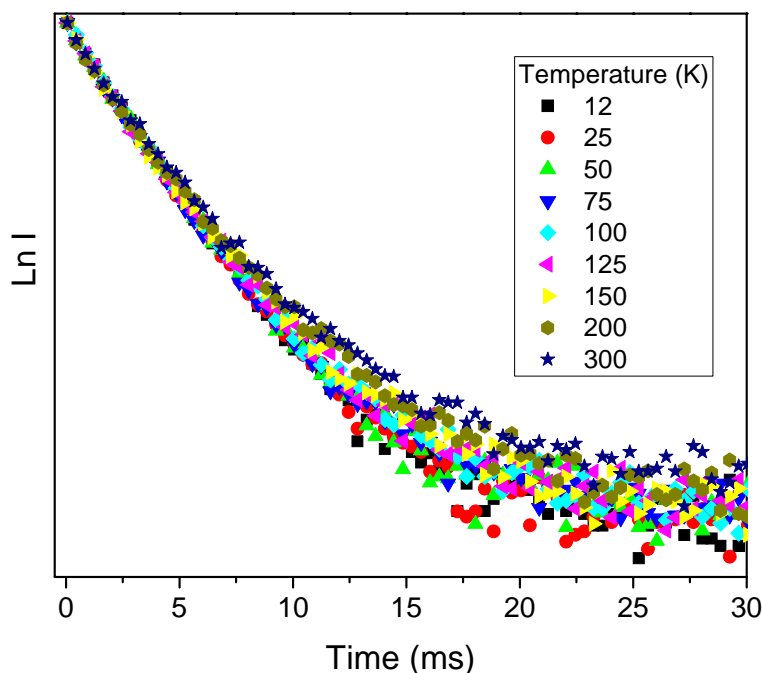


Figure 6.20 – Decay curves of $K_7(Gd_{2.7}Eu_{0.3})Si_{12}O_{32} \cdot 3H_2O$ detected at different temperatures (10–300 K) on the ${}^5D_0 \rightarrow {}^7F_2$ transition (609 nm) and excited at 393 nm.

It is possible to reconcile photoluminescence and crystallography by assuming that both $Eu(2)^{3+}$ ions in the dimmers behave as a single entity, with a pseudo point group symmetry with an inversion centre. If so, the unusually long lifetime is due to the $Eu(2)^{3+}$ - $Eu(2)^{3+}$ resonant energy transfer. These dimmers are present even at relatively low Eu^{3+} content (in $K_7[Gd_{2.85}Eu_{0.15}Si_{12}O_{32}] \cdot 3H_2O$ sample).

The temperature dependence of the $Eu(2)$ - $Eu(2)$ dimmers lifetime for $K_7Eu_3Si_{12}O_{32} \cdot 3H_2O$ and $K_7(Gd_{2.7}Eu_{0.3})Si_{12}O_{32} \cdot 3H_2O$ (Table 6.3 and Figure 6.21) is typical of thermally activated non-radiative mechanisms and may be approximately described by the Mott-Seitz model, which expresses the temperature dependence of the experimental lifetimes as

$$\tau^{-1} = \tau_0^{-1} + k \exp(-\Delta E/k_B T) \quad (6.3)$$

where τ_0 is the lifetime at $T=0$ K, k is the migration energy rate, ΔE is the energy gap between the 5D_0 level and the de-excitation states, and k_B is the Boltzmann constant. The main activation energy obtained for both samples is *ca.* 169 ± 11 cm^{-1} . However, the temperature dependence of the Eu(2)-Eu(2) dimmers lifetime for $\text{K}_7\text{Eu}_3\text{Si}_{12}\text{O}_{32}\cdot 3\text{H}_2\text{O}$ exhibits a second deactivation component with a much smaller energy (3 ± 0.3 cm^{-1}). Whereas the main thermally activated non-radiative mechanism involves Eu-O local vibrations, the much smaller second one is probably attributed to the interaction with Eu(1) ions. In accord, the excitation spectrum of $\text{K}_7\text{Eu}_3\text{Si}_{12}\text{O}_{32}\cdot 3\text{H}_2\text{O}$ monitored in the main line of the 7F_1 manifold (corresponding to the Eu(2)-Eu(2) dimmers emission, Figure 6.22), shows clearly phonon-assisted anti-Stokes (Stokes) vibronic component in the lower (higher) energy regions of the $^7F_0 \rightarrow ^5D_2$ ($^7F_1 \rightarrow ^5D_3$) transition ($\Delta J = 2$) [27,28]. The phonon energy corresponding to the observed sidebands is estimated by the energy difference relatively to the corresponding electronic transitions. The values obtained for the two vibronic lines associated with the $^7F_0 \rightarrow ^5D_2$ and $^7F_1 \rightarrow ^5D_3$ transitions are similar, *ca.* 155 cm^{-1} . This phonon energy is assigned to Eu-O local vibrational modes (similarly to the values found for other lanthanide-based materials [29-32]) and corresponds to a Raman-active vibrational mode (strong band at *ca.* 150 cm^{-1} in Fig. S11) that quenches the resonant Eu(2)-Eu(2) energy transfer decreasing therefore the dimmers lifetime.

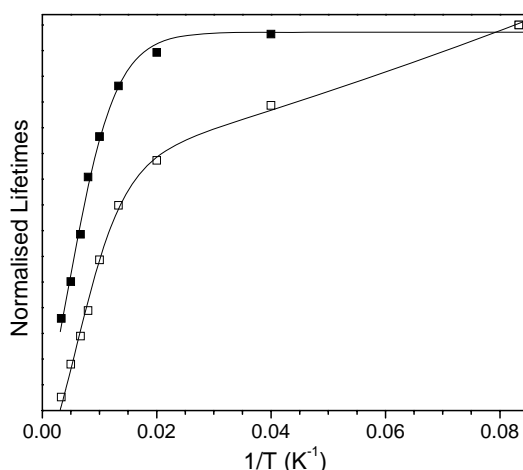


Figure 6.21 – Temperature dependence of Eu(2)-Eu(2) lifetime for samples $\text{K}_7\text{Eu}_3\text{Si}_{12}\text{O}_{32}\cdot 3\text{H}_2\text{O}$ (\square) and $\text{K}_7(\text{Gd}_{2.7}\text{Eu}_{0.3})\text{Si}_{12}\text{O}_{32}\cdot 3\text{H}_2\text{O}$ (\blacksquare). The full lines correspond to the best fit of the experimental lifetimes using the Mott-Seitz temperature-dependence.

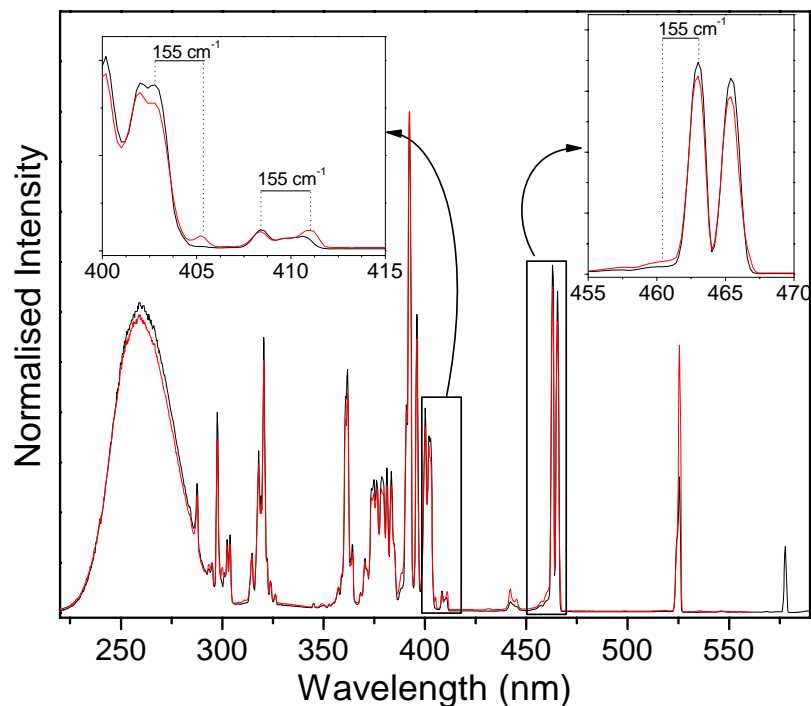


Figure 6.22 – Excitation spectra of Eu-AV-24, recorded at 10 K, monitored at the 7F_2 manifold (610.8 nm) and at the 7F_1 manifold (589.8 nm) (isolated dimmer line; red line). The insets show the phonon-assisted anti-Stokes (${}^7F_0 \rightarrow {}^5D_2$) and Stokes vibronic components (${}^7F_1 \rightarrow {}^5D_3$).

The temperature dependence of the time-resolved emission spectrum furnishes an additional evidence of the existence of thermally activated energy transfer mechanisms between the Eu(2)-Eu(2) dimmers and the Eu(1) ions (Figure 6.23). At 10 K the time-resolved emission spectrum (delay time of 25 ms) exhibits essentially the spectroscopic fingerprint of the Eu(2)-Eu(2) dimmers, as stated above. However, for temperatures up to 50 K the emission lines of the Eu(1) site are discerned even after that long delay times (much larger than the natural Eu(1) 5D_0 lifetime) supporting unequivocally energy transfer from the dimmers entity.

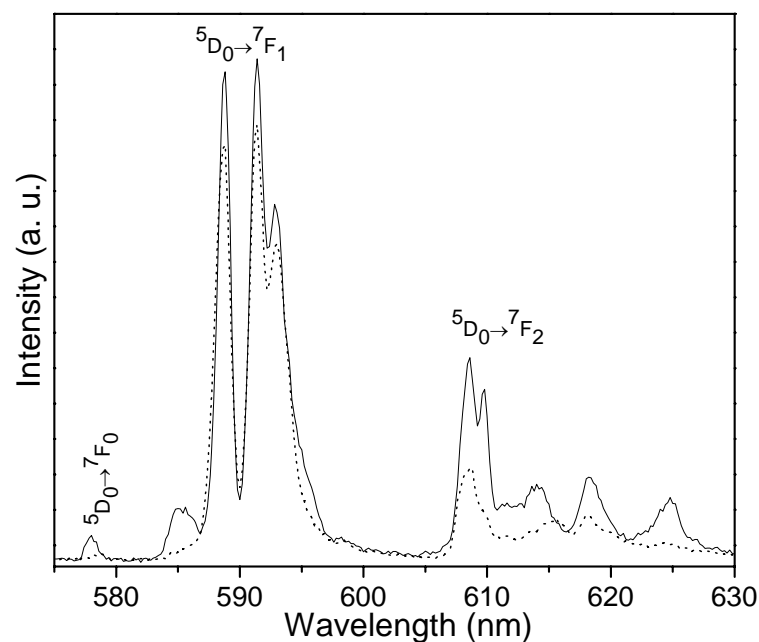


Figure 6.23 – Time-resolved emission spectra of Eu-AV-24 with initial delay of 25 ms recorded at 10 K (dashed line) and at 50 K (black line). The excitation was performed at 393 nm.

Figure 6.24 illustrates the emission spectrum of $K_7Tb_{2.94}Eu_{0.06}Si_{12}O_{32} \cdot 3H_2O$ sample excited at the Tb^{3+} (377 nm) level and showing the typical Eu^{3+} lines present in the spectrum of the pure Eu^{3+} sample (Figure 6.17) and ${}^5D_4 \rightarrow {}^7F_{5,6}$ transitions of the pure Tb^{3+} sample (Figure 6.13). Similar spectra were obtained under excitations within other Tb^{3+} levels (277nm), $4f^8 \rightarrow 4f^75d^1$ (fd) transition of Tb^{3+} which do not overlap with Eu^{3+} states. The normalized integrated intensity of ${}^5D_4 \rightarrow {}^7F_{5,6}$ Tb^{3+} transitions was calculated for various mixed $K_7Tb_{3-a}Eu_aSi_{12}O_{32} \cdot 3H_2O$ samples, as a function of the Eu content ($a = 0.06-1.50$) and is illustrated in Table 6.4. For the sample with higher ($a=0.15$) Eu^{3+} content, the intensity of the ${}^5D_4 \rightarrow {}^7F_{5,6}$ Tb^{3+} transitions decreases 50.25 %, relatively to the sample with $a=0.06$ and for the sample with $a=1.50$ the decrease is almost 100 % (no Tb^{3+} lines). This further supports the energy transfer between Tb^{3+} and Eu^{3+} and clearly indicates that the two kinds of lanthanide optical centers are in close spatial proximity.

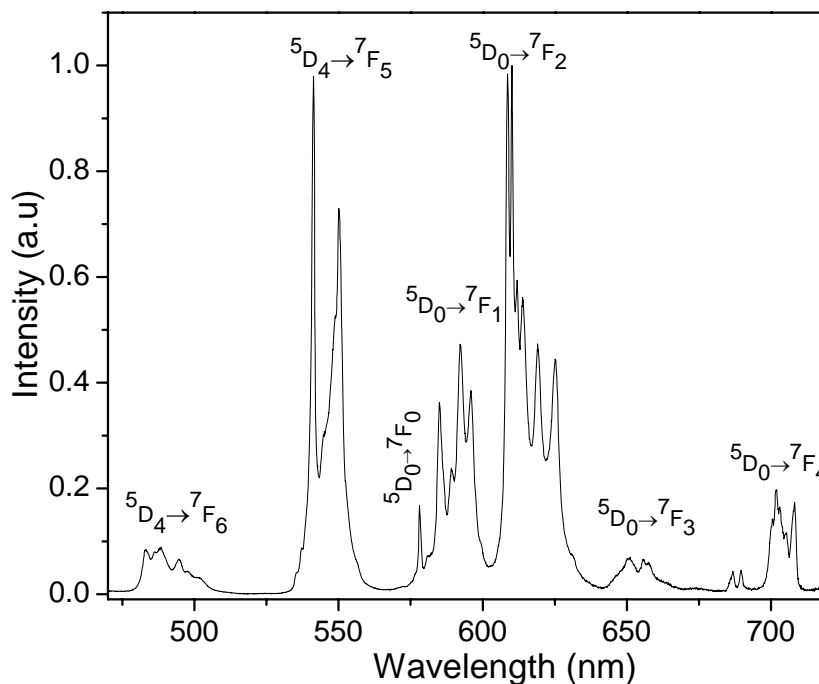


Figure 6.24 – Room temperature emission spectra of $\text{K}_7\text{Tb}_{2.94}\text{Eu}_{0.06}\text{Si}_{12}\text{O}_{32}\cdot 3\text{H}_2\text{O}$, excited at the $^5\text{D}_3$ manifold (377 nm).

Table 6.4 – The normalized integrated intensity of the $^5\text{D}_4 \rightarrow ^7\text{F}_{5,6}$ Tb^{3+} transitions (I) for $\text{K}_7\text{Tb}_{3-a}\text{Eu}_a\text{Si}_{12}\text{O}_{32}\cdot 3\text{H}_2\text{O}$ samples, $a = 0.06$ -1.50.

a	0.06	0.15	0.30	0.60	1.50
I (%)	100	49.75	20.06	5.30	0.15

The (x,y) emission color coordinates were measured according to the *Commission Internationale d'Eclairage* (CIE). For convenience, the color coordinates of AV-24 materials and the green and red standards are plotted in the CIE (1931) diagram (Figure 6.25). Clearly, the color coordinates of Tb-AV-24 and $\text{Gd}_2\text{O}_2\text{S}:\text{Tb}$, and Eu-AV-24 and $\text{Y}_2\text{O}_2:\text{Eu}$ are similar. For $\text{K}_7\text{Tb}_{3-a}\text{Eu}_a\text{Si}_{12}\text{O}_{32}\cdot 3\text{H}_2\text{O}$, $a = 0.06$ -2.70, even the sample with the lowest Eu content ($a=0.06$) exhibit a red shift of the color coordinates, due to the Eu^{3+} red-band contribution to the overall emission. The color coordinates of samples richer in Eu^{3+} overlap with those of pure Eu-AV-24 sample.

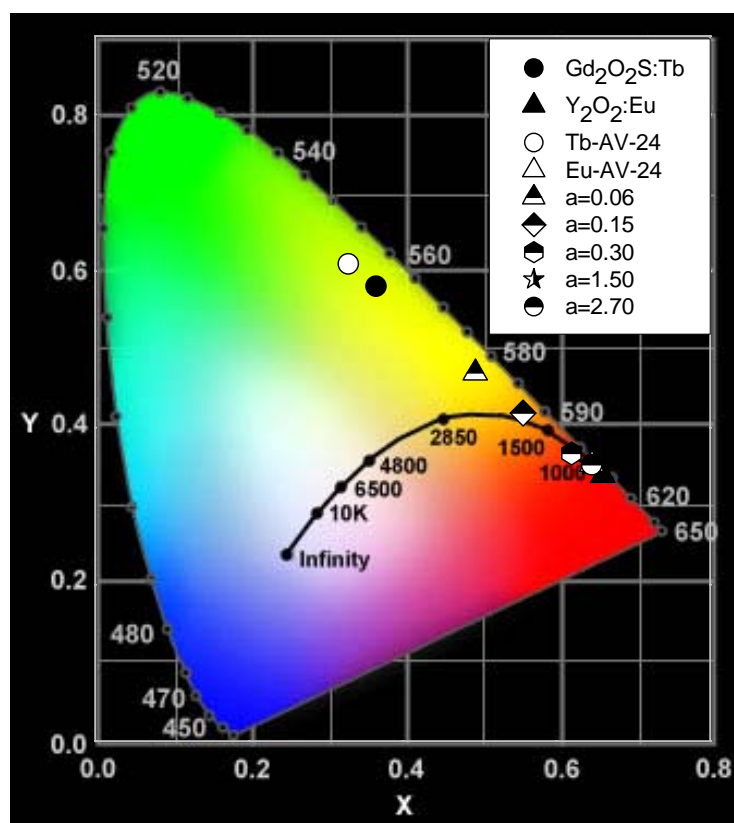


Figure 6.25 – CIE chromaticity diagram showing the RT (x,y) colour coordinates, measured at 270 nm for $\text{Gd}_2\text{O}_2\text{S:Tb}$, 264 nm for $\text{Y}_2\text{O}_2\text{:Eu}$, 393 nm for Eu-AV-24 and 377 nm for Tb-AV-24 and mixed Tb/Eu samples (the amount of Eu is depicted in the figure).

6.5 Conclusions

The synthesis and structural characterization of new microporous rare-earth silicates $\text{K}_7\text{M}_{3-a}\text{Ln}_a\text{Si}_{12}\text{O}_{32}\cdot 3\text{H}_2\text{O}$, $\text{M}^{3+} = \text{Tb}^{3+}, \text{Gd}^{3+}$; $\text{Ln}^{3+} = \text{Eu}^{3+}, \text{Sm}^{3+}, \text{Tb}^{3+}$ and Gd^{3+} , named AV-24 materials have been reported.

Microporous lanthanide silicates AV-24 are the first reported to contain Ln-O-Ln dimmers isolated in a siliceous matrix and exhibiting a unique emission feature: the lifetime of the $^5\text{D}_0$ excited state is remarkably long, *ca.* 10.29 ms at 10 K. The structure allows the inclusion of a second (or even third) type of Ln^{3+} ion in the framework and, therefore, the fine-tuning of the photoluminescence properties.

The temperature dependence of the Eu(2)-Eu(2) dimmers lifetime for $\text{K}_7\text{Eu}_3\text{Si}_{12}\text{O}_{32}\cdot 3\text{H}_2\text{O}$ and $\text{K}_7(\text{Gd}_{2.7}\text{Eu}_{0.3})\text{Si}_{12}\text{O}_{32}\cdot 3\text{H}_2\text{O}$, typical of thermally activated non-

radiative mechanisms is described by the Mott-Seitz model. It reveals main activation energy *ca.* $169 \pm 11 \text{ cm}^{-1}$ involving Eu-O local vibrations and in case of $\text{K}_7\text{Eu}_3\text{Si}_{12}\text{O}_{32}\cdot 3\text{H}_2\text{O}$ smaller deactivation energy ($3 \pm 0.3 \text{ cm}^{-1}$), probably attributed to the interaction with Eu(1) ions.

In mixed $\text{K}_7\text{Tb}_{3-a}\text{Eu}_a\text{Si}_{12}\text{O}_{32}\cdot 3\text{H}_2\text{O}$ samples, ($a=0.06-1.50$) energy transfer between Tb^{3+} and Eu^{3+} clearly indicates that the two kinds of lanthanide optical centers are in close spatial proximity. Moreover, even the sample with the lowest Eu content ($a=0.06$) exhibit a red shift of the color coordinates, due to the Eu^{3+} red-band contribution to the overall emission.

The microporous lanthanide silicate system exhibits remarkable photoluminescence properties which may be tuned by judicious choice of the Ln^{3+} ions. This has been illustrated for $\text{K}_7\text{M}_{3-a}\text{Ln}_a\text{Si}_{12}\text{O}_{32}\cdot 3\text{H}_2\text{O}$, $\text{M}^{3+} = \text{Tb}^{3+}, \text{Gd}^{3+}$; $\text{Ln}^{3+} = \text{Eu}^{3+}, \text{Sm}^{3+}, \text{Tb}^{3+}$ and Gd^{3+} and it may be extended to other lanthanides ions in the future.

6.6 References

- [1] M.H. Kostova, D. Ananias, F.A.A. Paz, L.D. Carlos, J. Rocha, (2007) in prepar.
- [2] D.I. Pushcharovskii, A.M. Dago, E.A. Pobedimskaia, N.V. Belov, Dokl. Akad. Nauk SSSR 258 (1981) 1111.
- [3] S.M. Haile, B.J. Wuensch, T. Siegrist, R.A. Laudise, Solid State Ion. 53-6 (1992) 1292.
- [4] S.M. Haile, B.J. Wuensch, T. Siegrist, J. Solid State Chem. 148 (1999) 406.
- [5] T. Kottke, D. Stalke, J. App. Cryst. 26 (1993) 615.
- [6] R. Hooft, in, Nonius B. V., Delft, The Netherlands, 1998.
- [7] Z. Otwinowski, W. Minor, in C.W. Carter Jr., R.M. Sweet (Editors), Methods in Enzymology, Academic Press, New York, 1997, p. 307.
- [8] R.H. Blessing, Acta Cryst. A 51 (1995) 33.
- [9] R.H. Blessing, J. Appl. Crystallogr. 30 (1997) 421.
- [10] G.M. Sheldrick, SHELXS-97, Program for Crystal Structure Solution, University of Göttingen (1997).
- [11] G.M. Sheldrick, SHELXL-97, Program for Crystal Structure Refinement, University of Göttingen (1997).
- [12] W.H. Baur, Acta Cryst. B B 30 (1974) 1195.
- [13] R.D. Shannon, Acta Cryst. A 32 (1976) 751.
- [14] J. Rodriguez-Carvajal, FULLPROF - A Program for Rietveld Refinement and Pattern Matching Analysis, Abstract of the Satellite Meeting on Powder Diffraction of the XV Congress of the IUCR, Toulouse, France, 1990, p.127.
- [15] A. Le Bail, H. Duroy, J.L. Fourquet, Mater. Res. Bull. 23 (1988) 447.
- [16] G. Engelhardt, D. Michel, High-resolution solid-state NMR of silicates and zeolites, John Wiley, Chichester, 1987.
- [17] J.L. You, G.C. Jiang, H.Y. Hou, H. Chen, Y.Q. Wu, K.D. Xu, J. Raman Spec. 36 (2005) 237.
- [18] H. Assaoudi, A. Ennaciri, A. Rulmont, Vibr. Spec. 25 (2001) 81.
- [19] M. Akaogi, N.L. Ross, P. McMillan, A. Navrotsky, Am. Mineral. 69 (1984) 499.
- [20] D.M. Tobbens, V. Kahlenberg, R. Kaindl, Inorg. Chem. 44 (2005) 9554.

- [21] P. McMillan, *Am. Mineral.* 69 (1984) 622.
- [22] S. Campos, A. Denoyer, S. Jandl, B. Viana, D. Vivien, P. Loiseau, B. Ferrand, J. *Phys. Cond. Matter* 16 (2004) 4579.
- [23] M. Laroche, J.L. Doualan, S. Girard, J. Margerie, R. Moncorge, *J. Opt. Soc. Am. B* 17 (2000) 1291.
- [24] L. van Pieterson, M.F. Reid, G.W. Burdick, A. Meijerink, *Phys. Rev. B* 65 (2002) 45114.
- [25] M.F. Hazenkamp, G. Blasse, *Chem. Mat.* 2 (1990) 105.
- [26] D. Ananias, F.A.A. Paz, L.D. Carlos, C. Geraldes, J. Rocha, *Angew. Chem. Int. Ed.* 45 (2006) 7938.
- [27] O.L. Malta, *J. Phys. Chem. Solids* 56 (1995) 1053.
- [28] C.D. Donega, A. Meijerink, G. Blasse, *J. Phys. Cond. Matter* 4 (1992) 8889.
- [29] S. Todoroki, K. Hirao, N. Soga, *J. Non-Cryst. Solids* 143 (1992) 46.
- [30] M. Dejneka, E. Snitzer, R.E. Riman, *J. Lumin.* 65 (1995) 227.
- [31] S.J.L. Ribeiro, R.E.O. Diniz, Y. Messaddeq, L.A. Nunes, M.A. Aegerter, *Chem. Phys. Lett.* 220 (1994) 214.
- [32] J.P. Rainho, M. Pillinger, L.D. Carlos, S.J.L. Ribeiro, R.M. Almeida, J. Rocha, *J. Mat. Chem.* 12 (2002) 1162.

7 Final conclusions and further work

Host-guest chemistry provides a wealth of opportunities for engineering new types of functional materials with tunable properties. The preparation of stoichiometric rare-earth silicates is an emerging field, rare-earth silicates are extremely promising tunable photoluminescent systems that may find applications in new types of sensors. In this context, the aim of this thesis was to prepare novel layered and microporous materials, encompassing rare-earth elements.

In this thesis I have presented the hydrothermal synthesis, structural characterization and photoluminescence studies of new layered and microporous rare-earth silicates denominated: AV-22, $K_3[(RE)Si_3O_8(OH)_2]$ $RE^{3+}=Y^{3+}, Eu^{3+}, Er^{3+}, Tb^{3+}, Gd^{3+}$ and Ce^{3+} ; AV-23, $K_3[RESi_3O_9]$, $RE^{3+}=Y^{3+}, Eu^{3+}, Er^{3+}$ and Tb^{3+} and AV-24, $K_7Ln_3Si_{12}O_{32}\cdot 3H_2O$,; $Ln^{3+}=Eu^{3+}, Sm^{3+}, Tb^{3+}$ and Gd^{3+} . The proposed structures are supported by single-crystal and powder X-ray diffraction, nuclear magnetic resonance and photoluminescence spectroscopy. Partucularly the Eu^{3+} luminescence, focused on the emission spectra allowed to study the local lanthanide ion environment in these materials, essential for the solution of the proposed structures.

The flexibility of the structure of AV-22, $K_3[(RE)Si_3O_8(OH)_2]$, $RE^{3+}=Y^{3+}, Eu^{3+}, Er^{3+}, Tb^{3+}, Gd^{3+}$ and Ce^{3+} allowed to obtain materials encompassing different lanthanides and possessing interesting properties. The Tb- and Eu-AV-22 samples are visible emitters (green and red, respectively) with output efficiency comparable to that of standards used in commercial lamps, while Er-AV-22 is a room-temperature infrared phosphor. It was possible to include a second (or even a third) type of RE^{3+} ion in the framework and, therefore, to fine-tune the photoluminescence properties. For the mixed Tb^{3+}/Eu^{3+} and Tb^{3+}/Ce^{3+} materials evidence has been found of the inclusion of Eu^{3+} and Ce^{3+} ions in the interlayer space by replacing K^+ ions, further allowing the activation of energy transfer mechanisms.

Upon calcination at 650 °C, AV-22 materials undergo a phase transformation to small-pore framework AV-23, $K_3[RESi_3O_9]$, $RE^{3+}=Y^{3+}, Eu^{3+}, Er^{3+}$ and Tb^{3+} . That gave further insight into the evolution of photoluminescence in rare-earth silicates across

dimensionality. It was interesting to bridge between the fields of layered and microporous rare-earth materials. The crystal structure of AV-23 calls for the presence of a single independent RE^{3+} environment. Despite this, detailed PL studies showed the presence of two or three RE^{3+} sites, which may be ascribed to metal centers in regular framework positions, defect regions, and in the micropores, replacing K^+ . The radiance values of Tb-AV-23 and standard Tb^{3+} green phosphors ($\text{Gd}_2\text{O}_2\text{S:Tb}$) are similar. The calcination process increases the intensity of the Er^{3+} emission (essentially due to the removing of OH groups) and the importance of the Er^{3+} - Er^{3+} interactions as a quenching emission channel.

Microporous lanthanide silicates AV-24, $\text{K}_7\text{Ln}_3\text{Si}_{12}\text{O}_{32}\cdot 3\text{H}_2\text{O}$, $\text{Ln}^{3+}=\text{Eu}^{3+}$, Sm^{3+} , Tb^{3+} and Gd^{3+} were the first reported to contain Ln-O-Ln dimmers isolated in a siliceous matrix and exhibiting a unique emission feature: the lifetime of the $\text{Eu}^{3+} \ ^5\text{D}_0$ excited state is remarkably long, *ca.* 10 ms at 10 K. The structure allows the inclusion of a second (or even third) type of Ln^{3+} ion in the framework and, therefore, the fine-tuning of the photoluminescence properties. Energy transfer between Tb^{3+} and Eu^{3+} in $\text{K}_7\text{Tb}_{3-a}\text{Eu}_a\text{Si}_{12}\text{O}_{32}\cdot 3\text{H}_2\text{O}$ samples, ($a=0.06$ -1.50) was observed. Moreover, even the sample with the lowest Eu content ($a=0.06$) exhibit a red shift of the color coordinates, due to the Eu^{3+} red-band contribution to the overall emission.

Finishing this dissertation I would like to refer to the need to continue the investigation in crystalline rare-earth silicates (layered and microporous) obtained by hydrothermal synthesis. With the advent of the nanotechnology era the obtained results are sufficiently promising to motivate the further extension to nanoparticles of crystalline layered and microporous silicates. In order to obtain nanoparticles, systematic synthetic studies for the target materials are required. The influence of parent reagents, concentration of OH⁻ and cations, water content, temperature and time have to be comprehensively studied. The particle size and its distribution can be altered by adding templates (organic cations) into parent mixture, and this effect can also be investigated.

The ovens usually used in hydrothermal synthesis could be substituted by a microwave, which poses the advantage of using microwave radiation in volumetric heating and result in homogeneous nucleation, favouring the formation of nanocrystals.

The crystals with specific size, shape, stability in solution, and functionality allow the fabrication of new families of components for the organized assembly in two dimensions, such as films, or in three dimensions, such as porous bodies with multiscale

channel structures. Nanosize particles are also used as seeds in the preparation of thin or thick films and membranes, catalysts, ion-exchangers and *etc.*

In conclusion, in this thesis are presented novel layered and microporous materials, encompassing rare-earth elements and presenting interesting photoluminescent properties, relevant for several applications (sensing, new advanced photoluminescent materials, *etc.*).

Appendices

Appendix I – Crystal data and structure refinement information for Tb-AV-22

Table AI.1 - Crystal and structure refinement data for Tb-AV-22.

formula	H ₂ K ₃ O ₁₀ Si ₃ Tb
formula weight	522.51
crystal system	orthorhombic
space group	<i>Pnma</i>
<i>a</i> /Å	13.210(3)
<i>b</i> /Å	13.543(3)
<i>c</i> /Å	5.9072(12)
Volume / Å ³	1056.8(4)
<i>Z</i>	4
<i>D_c</i> / gcm ⁻³	3.284
μ (Mo-K α) / mm ⁻¹	8.254
F(000)	984
crystal size / mm	0.16 × 0.05 × 0.02
crystal type	colorless blocks
θ range	3.76 to 27.47
index ranges	-12 ≤ <i>h</i> ≤ +17 -17 ≤ <i>k</i> ≤ +17 -6 ≤ <i>l</i> ≤ +7
reflections collected	5329
independent reflections	1257 (<i>R</i> _{int} = 0.0507)
completeness to $\theta = 27.47^\circ$	99.6 %
goodness-of-fit on <i>F</i> ²	1.085
final <i>R</i> indices [<i>I</i> > 2 σ (<i>I</i>)]	<i>R</i> 1 = 0.0339 <i>wR</i> 2 = 0.0838
final <i>R</i> indices (all data)	<i>R</i> 1 = 0.0408 <i>wR</i> 2 = 0.0876
largest diff. peak and hole / (e Å ⁻³)	1.703 and -1.935

Table AI.2 - Atomic coordinates and isotropic displacement parameters (in Å²) for Tb-AV-22 (standard deviations are in parentheses).

Atomic parameters					
Atom	X	Y	Z	U [Å ²]	Wyck.
Tb1	0.0418	01/04	0.0848		4c
K1	0.3722(1)	01/04	-0.0780(3)		4c
Si1	0.2525(2)	01/04	0.4211(3)		4c
Si2	0.0989(1)	0.3976(1)	0.5866(2)		8d
K2	0.3614(1)	0.4837(1)	0.5865(2)		8d
O1	0.2066(4)	01/04	0.1715(9)		4c
O2	0.2120(3)	0.3463(3)	0.5682(5)		8d
O3	0.1326(3)	0.5163(3)	0.5841(6)		8d
O4	0.0318(3)	0.3706(3)	0.3673(7)		8d
O5	0.0434(2)	0.3726(3)	-0.1796(7)		8d
O6	-0.1264(4)	01/04	0.0648(8)		4c
H1	0.085(5)	0.537(5)	0.600(9)	0.000(15)	8d

Table AI.3 – Main interatomic distances (in Å) for Tb-AV-22.

Connection	Distance (Å)	Connection	Distance (Å)
Tb1–O6	2.225	O1–Tb1	2.236
Tb1–O1	2.236	O2–Si2	1.651
Tb1–O5	2.280	O2–Si1	1.656
Tb1–O5	2.280	O3–H1	0.695
Tb1–O4	2.339	O3–Si2	1.668
Tb1–O4	2.339	O4–Si2	1.612
Si1–O1	1.594	O4–H1	1.996
Si1–O6	1.602	O4–Tb1	2.339
Si1–O2	1.656	O5–Si2	1.600
Si1–O2	1.656	O5–Tb1	2.280
Si2–O5	1.600	O6–Si1	1.602
Si2–O4	1.612	O6–Tb1	2.225
Si2–O2	1.651	H1–O3	0.695
Si2–O3	1.668	H1–Si2	1.898
Si2–H1	1.898	H1–O4	1.996
O1–Si1	1.594		

Table AI.4 – Main interatomic angles (in degrees) for Tb-AV-22.

Connection	Angles (°)	Connection	Angles (°)
Tb1–O6–O1	169.805	Si2–O5–O4	113.193
Tb1–O6–O5	88.446	Si2–O5–O2	112.483
Tb1–O6–O5	88.446	Si2–O5–O3	109.505
Tb1–O6–O4	88.939	Si2–O5–H1	97.477
Tb1–O6–O4	88.939	Si2–O4–O2	110.441
Tb1–O1–O5	98.504	Si2–O4–O3	110.996
Tb1–O1–O5	98.504	Si2–O4–H1	101.884
Tb1–O1–O4	83.776	Si2–O2–O3	99.405
Tb1–O1–O4	83.776	Si2–O2–H1	120.574
Tb1–O5–O5	93.497	Si2–O3–H1	21.228
Tb1–O5–O4	176.405	O1–Si1–Tb1	125.593
Tb1–O5–O4	88.897	O2–Si2–Si1	131.164
Tb1–O5–O4	88.897	O3–H1–Si2	98.401
Tb1–O5–O4	176.405	O4–Si2–H1	101.836
Tb1–O4–O4	88.589	O4–Si2–Tb1	134.499
Si1–O1–O6	115.335	O4–H1–Tb1	123.404
Si1–O1–O2	111.249	O5–Si2–Tb1	138.576
Si1–O1–O2	111.249	O6–Si1–Tb1	173.976
Si1–O6–O2	107.179	H1–O3–Si2	60.371
Si1–O6–O2	107.179	H1–O3–O4	164.925
Si1–O2–O2	103.918	H1–Si2–O4	134.609

Appendix II – Crystal data and structure refinement information for Tb-AV-23

Table AII.1 - Crystal and structure refinement data for Tb-AV-23.

formula	$K_3O_9Si_3Tb$
formula weight	504.50
crystal system	orthorhombic
space group	$Pmn2_1$
$a/\text{\AA}$	14.053(3)
$b/\text{\AA}$	5.9090(12)
$c/\text{\AA}$	12.978(3)
$\text{vol}/\text{\AA}^3$	1077.7(4)
Z	4
$D_c / (\text{gcm}^{-3})$	3.109
$\mu(\text{Mo-K}\alpha) / \text{mm}^{-1}$	8.081
F(000)	944
crystal size / mm	$0.17 \times 0.14 \times 0.10$
crystal type	colorless plates
θ range	3.74 to 26.37
index ranges	$-17 \leq h \leq +16$ $-7 \leq k \leq +7$ $-16 \leq l \leq +16$
reflections collected	8716
independent reflections	2292 ($R_{\text{int}} = 0.0430$)
data completeness	to $\theta = 26.37^\circ$, 99.7%
final R indices [$I > 2\sigma(I)$]	$R1 = 0.1099$ $wR2 = 0.2613$
final R indices (all data)	$R1 = 0.1147$ $wR2 = 0.2643$
largest diff. peak and hole/ ($e \text{\AA}^{-3}$)	4.855 and -4.695

Table AII.2 - Atomic coordinates and isotropic displacement parameters in (\AA^2) for Tb-AV-23 (standard deviations are in parentheses).

Atom	X	Y	Z	U [\AA^2]	Wyck.
Tb1	-0.25637(8)	-0.84081(18)	0.5044(3)		4b
Si1	-0.3899(5)	-1.3314(13)	0.4191(5)	0.0118(9)	4b
Si2	-0.2250(5)	-1.1799(13)	0.2918(5)	0.0118(9)	4b
Si3	-0.1130(4)	-1.3406(14)	0.4733(5)	0.0118(9)	4b
O1	-0.3728(12)	-1.125(2)	0.4963(11)	0.0212(17)	4b
O2	-0.3275(6)	-1.291(2)	0.3158(8)	0.0212(17)	4b
O3	-0.5	-1.333(4)	0.3840(13)	0.0212(17)	2a
O4	-0.3641(13)	-1.565(2)	0.4711(12)	0.0212(17)	4b
O5	-0.2228(12)	-0.9265(17)	0.3334(13)	0.0212(17)	4b
O6	-0.2007(10)	-1.192(3)	0.1731(7)	0.0212(17)	4b
O7	-0.1488(8)	-1.329(2)	0.3563(6)	0.0212(17)	4b
O8	-0.1600(11)	-1.138(2)	0.5383(11)	0.0212(17)	4b
O9	-0.1374(12)	-1.578(2)	0.5226(11)	0.0212(17)	4b
O10	0	-1.301(3)	0.4738(14)	0.0212(17)	2a
K1	-0.2271(5)	-0.6656(13)	0.1745(6)	0.0187(10)	4b
K2	-0.5	-1.662(3)	0.3471(14)	0.0187(10)	2a
K2'	-0.5	-1.850(5)	0.375(2)	0.0187(10)	2a
K3	0	-0.691(3)	0.3466(14)	0.0187(10)	2a
K3'	0	-0.853(5)	0.394(2)	0.0187(10)	2a
K4	-0.5	-1.187(3)	0.1379(15)	0.0187(10)	2a
K4'	-0.5	-0.887(4)	0.1748(17)	0.0118(9)	2a
K5	0	-1.163(3)	0.1253(15)	0.0187(10)	2a
K5'	0	-1.311(9)	0.138(4)	0.0187(10)	2a
K5''	0	-0.813(9)	0.150(4)	0.0187(10)	2a

Table AII.3 – Interatomic distances (in Å) for Tb-AV-23.

Connection	Distance (Å)	Connection	Distance (Å)
Tb1–O8	2.261	O4–Si1	1.579
Tb1–O4	2.266	O4–Tb1	2.266
Tb1–O6	2.279	O5–Si2	1.592
Tb1–O9	2.294	O5–Tb1	2.325
Tb1–O5	2.325	O6–Si2	1.580
Tb1–O1	2.347	O6–Tb1	2.279
Si1–O4	1.579	O7–Si3	1.601
Si1–O1	1.597	O7–Si2	1.620
Si1–O3	1.613	O8–Si3	1.607
Si1–O2	1.620	O8–Tb1	2.261
Si2–O6	1.580	O9–Si3	1.579
Si2–O5	1.592	O9–Tb1	2.294
Si2–O2	1.613	O10–Si3	1.605
Si2–O7	1.620	O10–Si3	1.605
Si3–O9	1.579	K2–K2'	1.168
Si3–O7	1.601	K2–O3	2.002
Si3–O10	1.605	K2'–K2	1.168
Si3–O8	1.607	K3–K3'	1.138
O1–Si1	1.597	K3'–K3	1.138
O1–Tb1	2.347	K4–K4'	1.836
O2–Si2	1.613	K4'–K4	1.836
O2–Si1	1.620	K5–K5'	0.890
O3–Si1	1.613	K5–K5''	2.093
O3–Si1	1.613	K5'–K5	0.890
O3–K2	2.002	K5''–K5	2.093

Table AII.4 – Interatomic angles (in degrees) for Tb-AV-23.

Connection	Angle (°)	Connection	Angle (°)
Tb1–O8–O4	174.843	Si2–O5–O2	109.547
Tb1–O8–O6	92.161	Si2–O5–O7	108.874
Tb1–O8–O9	93.969	Si2–O2–O7	105.614
Tb1–O8–O5	83.974	Si3–O9–O7	110.731
Tb1–O8–O1	82.562	Si3–O9–O10	110.036
Tb1–O4–O6	86.858	Si3–O9–O8	111.092
Tb1–O4–O9	91.127	Si3–O7–O10	107.966
Tb1–O4–O5	96.325	Si3–O7–O8	109.687
Tb1–O4–O1	92.310	Si3–O10–O8	107.216
Tb1–O6–O9	92.087	O1–Si1–Tb1	132.814
Tb1–O6–O5	171.597	O2–Si2–Si1	134.682
Tb1–O6–O1	85.374	O3–Si1–Si1	147.183
Tb1–O9–O5	95.615	O3–Si1–K2	94.200
Tb1–O9–O1	175.608	O3–Si1–K2	94.200
Tb1–O5–O1	86.725	O4–Si1–Tb1	149.749
Si1–O4–O1	111.414	O5–Si2–Tb1	121.646
Si1–O4–O3	109.628	O6–Si2–Tb1	151.136
Si1–O4–O2	111.000	O7–Si3–Si2	136.149
Si1–O1–O3	109.032	O8–Si3–Tb1	136.293
Si1–O1–O2	108.986	O9–Si3–Tb1	135.867
Si1–O3–O2	106.646	O1–Si3–Si3	163.229
Si2–O6–O5	111.662	K2–K2'–O3	148.109
Si2–O6–O2	111.279	K5–K5'–K5''	160.516
Si2–O6–O7	109.662		

Appendix III – Crystal data and structure refinement information for Sm-AV-24

Table AIII.1 - Crystal and structure refinement data forms Sm-AV-24.

formula	$\text{H}_6\text{K}_7\text{O}_{35}\text{Si}_{12}\text{Sm}_3$
formula weight	1627.91
crystal system	triclinic
space group	$P\bar{1}$
$a/\text{\AA}$	6.9209(14)
$b/\text{\AA}$	11.428(2)
$c/\text{\AA}$	11.612(2)
$\alpha/^\circ$	87.68(3)
$\beta/^\circ$	88.16(3)
$\gamma/^\circ$	79.50(3)
volume / \AA^3	902.0(3)
Z	1
D_c / gcm^{-3}	2.997
$\mu(\text{Mo-K}\alpha) / \text{mm}^{-1}$	6.143
F(000)	773
crystal size / mm	0.21 × 0.05 × 0.02
crystal type	colorless blocks
θ range	3.51 to 27.49
index ranges	$-8 \leq h \leq +8$ $-14 \leq k \leq +14$ $-14 \leq l \leq +15$
reflections collected	10522
independent reflections	4090 ($R_{\text{int}} = 0.0512$)
data completeness	to $\theta = 27.49^\circ$, 99.2%
final R indices [$I > 2\sigma(I)$]	$R1 = 0.0391$ $wR2 = 0.0969$
final R indices (all data)	$R1 = 0.0425$ $wR2 = 0.0997$
largest diff. peak and hole/ ($e \text{\AA}^{-3}$)	3.061 and -3.436

Table AIII.2 - Atomic coordinates and isotropic displacement parameters (in Å²) for Sm-AV-24 (standard deviations are in parentheses).

Atom	X	Y	Z	Wyck.
Sm1	0	0	1/2	1b
Sm2	0.51199(4)	0.51429(2)	0.66656(2)	2i
Si1	0.0123(2)	0.51248(14)	0.75085(13)	2i
Si2	0.3144(2)	0.30231(14)	0.84488(13)	2i
Si3	0.3346(2)	0.09378(14)	0.69367(13)	2i
Si4	0.5471(2)	0.23573(14)	0.51032(12)	2i
Si5	0.3431(2)	0.13730(14)	0.31404(13)	2i
Si6	0.3019(2)	0.32628(14)	0.11910(13)	2i
O1	0.1813(6)	0.5748(4)	0.6917(4)	2i
O2	0.1020(7)	0.3806(4)	0.8075(4)	2i
O3	-0.1542(6)	0.4983(4)	0.6624(4)	2i
O4	-0.0851(7)	0.5900(4)	0.8629(4)	2i
O5	0.4972(7)	0.3492(4)	0.7866(4)	2i
O6	0.3059(7)	0.1646(4)	0.8147(3)	2i
O7	0.3233(7)	0.2967(4)	0.9840(4)	2i
O8	0.3780(6)	0.1883(4)	0.5929(3)	2i
O9	0.1456(6)	0.0406(4)	0.6687(4)	2i
O10	0.5306(7)	-0.0064(4)	0.7135(4)	2i
O11	0.5226(6)	0.3785(4)	0.5156(3)	2i
O12	0.4846(7)	0.2150(4)	0.3761(3)	2i
O13	0.7629(6)	0.1659(4)	0.5351(4)	2i
O14	0.1452(6)	0.1304(4)	0.3830(3)	2i
O15	0.2970(7)	0.1993(4)	0.1862(4)	2i
O16	0.4749(7)	0.3878(4)	0.1594(4)	2i
K1	-0.0141(2)	0.66670(12)	0.49375(11)	2i
K2	-0.1610(2)	0.19540(13)	0.23633(13)	2i
K3	0.7377(4)	0.3932(3)	-0.0193(2)	2i

Atom	X	Y	Z	Wyck.
K4	-0.1726(4)	0.1740(4)	0.7783(2)	2i
O1W	0.802(3)	0.309(2)	0.0122(19)	2i
O2W	-0.1810(17)	0.1286(10)	1.006(1)	2i
O3W	0.4819(14)	0.0180(8)	0.0138(7)	2i

Table AIII.2 – Continuation from previous page.

Table AIII.3 – Selected angles (in degrees) for the two distinct Sm³⁺ coordination environments in Sm-AV-24.^a

Connection	Angles (°)	Connection	Angles (°)
O(13) ⁱ –Sm(1)–O(14)	95.66(15)	O(1)–Sm(2)–O(3) ⁱⁱⁱ	165.46(16)
O(13) ⁱⁱ –Sm(1)–O(14)	84.34(15)	O(1)–Sm(2)–O(5)	89.75(16)
O(13) ⁱ –Sm(1)–O(9)	93.20(16)	O(1)–Sm(2)–O(11)	101.00(16)
O(13) ⁱⁱ –Sm(1)–O(9)	86.80(16)	O(1)–Sm(2)–O(11) ^{iv}	86.37(15)
O(14)–Sm(1)–O(9)	95.17(14)	O(1)–Sm(2)–O(16) ^{iv}	83.36(16)
O(14) ^v –Sm(1)–O(9)	84.83(14)	O(3) ⁱⁱⁱ –Sm(2)–O(5)	97.11(16)
		O(3) ⁱⁱⁱ –Sm(2)–O(11)	92.45(15)
		O(3) ⁱⁱⁱ –Sm(2)–O(11) ^{iv}	93.07(15)
		O(3) ⁱⁱⁱ –Sm(2)–O(16) ^{iv}	84.60(15)
		O(5)–Sm(2)–O(11)	84.40(14)
		O(5)–Sm(2)–O(11) ^{iv}	153.06(15)
		O(5)–Sm(2)–O(16) ^{iv}	84.21(15)
		O(11)–Sm(2)–O(11) ^{iv}	70.26(16)
		O(16) ^{iv} –Sm(2)–O(11)	167.79(15)
		O(16) ^{iv} –Sm(2)–O(11) ^{iv}	121.66(15)

^a Symmetry transformations used to generate equivalent atoms: (i) $I-x, -y, I-z$; (ii) $-I+x, y, z$; (iii) $I+x, y, z$; (iv) $I-x, I-y, I-z$; (v) $-x, -y, I-z$.

Table AIII.4 –Selected bond lengths (in Å) for the two distinct Sm³⁺ coordination environments in Sm-AV-24.^a

Connection	Distance (Å)		Connection	Distance (Å)
Sm(1)–O(13) ⁱ	2.310(4)		Sm(2)–O(1)	2.280(4)
Sm(1)–O(14)	2.317(4)		Sm(2)–O(3) ⁱⁱⁱ	2.283(4)
Sm(1)–O(9)	2.333(4)		Sm(2)–O(5)	2.315(4)
			Sm(2)–O(16) ^{iv}	2.361(4)
			Sm(2)–O(11)	2.378(4)
			Sm(2)–O(11) ^{iv}	2.398(4)

^aSymmetry transformations used to generate equivalent atoms: (i) $I-x, -y, I-z$; (ii) $-I+x, y, z$; (iii) $I+x, y, z$; (iv) $I-x, I-y, I-z$; (v) $-x, -y, I-z$